Novel Cooling Design for Blade or Vane Trailing Edges



Tsun Holt Wong

Wadham College

University of Oxford

A thesis submitted for the degree of

Doctor of Philosophy

Trinity 2018

Abstract

The trailing edge of the high pressure turbine blade and vane presents significant challenges to the turbine cooling engineer. This section endures very high temperature and mechanical stresses but aerodynamic efficiency requirements dictate that it must be tapered to the end with minimal thickness, making it difficult to cool internally. Pressure side film cooling using a slot has become a common and effective method to cool the trailing edge by creating a sheet of coolant which protects the trailing edge from the mainstream gas. However, continuous cooling slots are not mechanically robust and weaken the design, necessitating the use of interrupted slots with a "bridge" internally and a "land" externally. Manufacturing constraints also dictate that the slot cannot be too thin, resulting in excessive coolant flow unless the slot or feed passage are restricted.

The current research proposes a novel cooling slot design that uses cross corrugated channels on either side of the cooling slot. These improve internal cooling and increase pressure loss, allowing the flow to be restricted without reducing the slot height or introducing a restrictor into the feed passage which could be vulnerable to blockage. However, this design potentially has very poor film cooling performance due to the complex flow structures that exit the corrugated channels. Thus, it was necessary to investigate this weakness and recommend strategies to combat it.

The pressure sensitive paint technique for measuring adiabatic film cooling effectiveness was developed for use in a large scale simplified model of the trailing edge. Initial experiments were conducted to choose an appropriate land shape to be used with the slot and then a series of eight different cross corrugated geometries were tested at five blowing ratios ranging from 0.6 to 1.4 in increments of 0.2. These geometries encompassed

two included angles of $90°$ and $120°$ and four different exit alignments. The experiments showed that the cross corrugated geometries did indeed perform very poorly in terms of film cooling effectiveness across the board. In an effort to remedy this, the cross corrugated slot designs were modified with exit shaping in such a way as to create a more uniform coolant flow at the slow exit.

In total, five slots with exit shaping were designed and tested in the facility. Exit shaping proved to be an effective solution to the issue of film cooling performance, increasing the effectiveness significantly on the cutback surface and increasing spanwise consistency across the slot as well. The best performing geometry was selected as the most optimised cross corrugated slot geometry with exit shaping and tested further using a more engine representative coolant to mainstream density ratio.

Overall film cooling performance using the optimised cross corrugated slot was improved beyond that of a simple rectangular slot by $6.6\,\%$ up to a blowing ratio of 1.0. Trailing edge effectiveness was improved by $16.3\,\%$ up to a blowing ratio of 1.0 and $5.4\,\%$ up to a blowing ratio of 1.2. Simultaneously, pressure losses were significantly increased by the cross corrugated slots. Fanning friction factor was enhanced by between 15 and 25 times for an included angle of $90°$ and 50 to 90 times for an included angle of $120°$. This shows that the cross corrugated slot geometry is a viable candidate for use in trailing edge slot cooling and can achieve great pressure losses without sacrificing film cooling performance.

Acknowledgements

The first to be acknowledged must be Prof. Peter Ireland, an inspiring role model of a supervisor, an engineer, and a friend. Without his encouragement, support and *enduring* patience, I would never have been able to complete this research.

Next should be my parents, who I thank for much more than just their support during my studies. In particular my mother who must have the patience of a saint. She warned me how difficult it would be and she was so very right, but she always held back the brunt of her admonishments and together with my father did everything they could do make my life easier. I cannot fail to mention also my brother, my best friend throughout my life and together with my sister-in-law, my favourite travelling companions.

I must recognise two of the best things to have ever come out of the Osney lab: Doctors Irene Cresci and Inés Usandizaga Forés , the greatest friends a person could ever ask for. Your presence at the lab and at the flat have been sorely missed. Also my buddies back "home", Rob Syratt and Muzher Sharif, who I could always talk to now matter how far away we were and could be relied upon for a good laugh. My colleagues Doctors Jack Nicholas, Rob Pearce and Andrew van Paridon also deserve a mention — their encouragement, advice and friendship have helped to keep me sane during the final home straight.

I would be remiss if I did not mention all of the people without whom this research would not have been possible: including, but not limited to, Gerald Walker, Leo Verling, Duncan Blake, David Mountain, Craig Parsons, Trevor Godfrey, Michael Japp, Gregory King, Paul Cox, Hal Surtell, Bill Godfrey, Jason McCluskey. At one point or another, they each had to deal with my last minute requests and always went above and beyond to

help me get things done.

Special thanks goes to Kaz Self of Rolls-Royce for her assistance throughout the project as well as to Rolls-Royce and the EPSRC who funded the research project and my studentship. I would also like to acknowledge the use of the University of Oxford Advanced Research Computing (ARC) facility in carrying out this work.

http://dx.doi.org/10.5281/zenodo.22558

Contents

Abstract i

Acknowledgements iii

List of Figures xvi

List of Tables xvii

Nomenclature xviii

1 Introduction 1

1.1 Civil turbofan engines 1

1.1.1 Background 1

1.1.2 The Trent extra wide body 3

1.2 The need for cooling 3

1.3 Air cooling 4

1.4 Trailing edge cooling 5

1.5 Objectives of research 6

1.6 Thesis outline 7

1.7 Summary of achievements and publications 8

2 Literature Review 9

2.1 Introduction 9

2.2 Film cooling 9

2.2.1 General film cooling 9
2.2.2 Slot film cooling 11
2.2.3 Density ratio effects 13
2.2.4 Numerical modelling 15
2.3 Lattice internal cooling 16
2.4 Cross corrugated heat exchangers 17
2.5 Summary 19

3 Novel Cooling Design 21
3.1 Introduction 21
3.2 Geometry 21
3.3 Potential features 23
3.3.1 Flow control 23
3.3.2 Internal cooling 25
3.3.3 Film cooling 26
3.3.4 Land cooling 27
3.3.5 Other potential benefits 29
3.4 Patent 30
3.5 Deciding on test geometries 32

4 Experimental Methods 34
4.1 Introduction 34
4.2 Pressure sensitive paint 34
4.2.1 Limitations of pressure sensitive paint 37
4.3 PSP mass transfer analogy to determine film cooling effectiveness 38
4.3.1 Using different gases as the coolant 41
4.4 Comparison with the thermochromic liquid crystals 44

5 Experimental Set-up 48
5.1 Introduction 48

5.2 Initial experimental set-up 49
5.2.1 Experimental facility 49
5.2.2 Effectiveness measurement technique 52
5.2.3 Pressure loss measurements 53
5.2.4 Data acquisition 55
5.2.5 Calibration of PSP 56
5.2.6 Calculating effectiveness 58
5.2.7 Operating conditions 58
5.2.8 Uncertainties 59
PSP lighting and paint degradation 59
PSP temperature sensitivity 60
Uncertainty analysis 60
5.2.9 Limitations 64
5.3 Phase 1 geometries 64
5.4 Modifications to set-up 66
5.5 Phase 2 geometries 69
5.6 Phase 3 geometries 72
5.7 Coolant feed modifications for carbon dioxide 77
5.7.1 Operating conditions 81
5.8 Phase 4 geometries 82

6 Effectiveness Measurements — Land Shapes 83
6.1 Introduction 83
6.2 2D film cooling effectiveness distributions 83
6.3 Discussion 91
6.3.1 Land effectiveness 91
Comparison with literature 93
6.3.2 Effectiveness downstream of lands 94
6.3.3 Centreline effectiveness 95

Comparison with literature 98
6.3.4 Spanwise averaged effectiveness 99
6.3.5 Spanwise variation of effectiveness at end of lands 102
6.3.6 Area averaged effectiveness 104
6.4 Summary and conclusions 106

7 Effectiveness Measurements — Cross Corrugated Slots 109
7.1 Introduction 109
7.2 2D film cooling effectiveness distributions 109
7.3 Discussion 120
7.3.1 Baseline geometry G0 inconsistency with phase 1 120
7.3.2 Cutback effectiveness 122
G1–4, 90° included angle 122
G5–8, 120° included angle 124
7.3.3 Land effectiveness 125
7.3.4 Effectiveness downstream of lands 127
7.3.5 Centreline effectiveness 128
7.3.6 Spanwise averaged effectiveness 131
7.3.7 Spanwise variation of effectiveness at end of lands 134
7.3.8 Area averaged effectiveness 138
7.4 Summary and conclusions 140

8 Effectiveness Measurements — Exit Shaping 143
8.1 Introduction 143
8.2 2D film cooling effectiveness distributions 144
8.3 Discussion 145
8.3.1 Cutback effectiveness 145
Addition of ramp down section 145
Further addition of straightening section 151

8.3.2 Land effectiveness 153
8.3.3 Effectiveness downstream of lands 154
8.3.4 Centreline effectiveness 155
8.3.5 Spanwise averaged effectiveness 160
8.3.6 Spanwise variation of effectiveness at end of lands 163
8.3.7 Area averaged effectiveness 165
8.3.8 Most optimised geometry 167
8.4 Summary and conclusions 168

9 Effectiveness Measurements — Density Ratio Effects 171
9.1 Introduction 171
9.2 2D film cooling effectiveness distributions 172
9.3 Discussion 173
9.3.1 Cutback effectiveness 173
9.3.2 Land effectiveness 176
9.3.3 Effectiveness downstream of lands 177
9.3.4 Centreline effectiveness 178
9.3.5 Spanwise averaged effectiveness 181
9.3.6 Spanwise variation of effectiveness at end of lands 186
9.3.7 Area averaged effectiveness 188
9.4 Summary and conclusions 189

10 Pressure Loss Measurements 192
10.1 Introduction 192
10.2 Pressure loss characteristics 193
10.3 Cross corrugated slots with $90°$ included angle 194
10.4 Cross corrugated slots with $120°$ included angle 197
10.5 Cross corrugated slots with exit shaping 198
10.6 Summary and conclusions 200

11 Numerical Analysis **204**

11.1 Introduction 204

11.2 Numerical methods 205

11.2.1 Computational domain 205

11.2.2 Simulation settings 206

11.3 Results 208

11.4 Summary and conclusions 213

12 Conclusions **215**

12.1 Suggestions for further work 218

Bibliography **220**

Appendices **232**

A Isenthalpic Expansion of Gases **233**

A.1 Nitrogen 233

A.2 Carbon dioxide 233

List of Figures

1.1 Effect of temperature and pressure ratio on efficiency (Cumpsty, 2003) . . 2

1.2 Turbine entry temperatures over the decades (Cumpsty, 2003) 2

1.3 Diagram of Trent 1000 air systems (Rolls-Royce, 2009) 4

2.1 Cooling systems in HP blades and vanes (Rolls-Royce, 2005) 10

2.2 Lattice cooled blade (Goreloff et al., 1990) 16

2.3 Cross corrugated geometry 18

3.1 Cut HP blade with cross corrugated trailing edge slot 21

3.2 Cut HP blade showing internal corrugations 22

3.3 Close-up cut view of cross corrugated trailing edge slot 23

3.4 Coolant flow in cross corrugated slot with $\theta_{cc} = 90°$ 23

3.5 Coolant flow in cross corrugated slot with $\theta_{cc} = 105°$ 24

3.6 Different corrugation alignments at the bridge wall 25

3.7 Radial passage cooling with cross corrugations 26

3.8 Different slot exit configurations 28

3.9 Cross corrugated slot with exit shaping 29

3.10 Patent geometries 31

4.1 Emission spectra of UniFIB PSP (Innovative Scientific Solutions Inc., 2016) 35

4.2 Basic PSP experimental set-up (Quinn et al., 2013) 36

4.3 PSP calibration curves (Han and Rallabandi, 2010) 37

4.4 2D Film cooling model (Han and Rallabandi, 2010) 38

4.5 Diagram of layered TLC structure (Ireland and Jones, 2000) 44

5.1 Rig schematic 49
5.2 Cross-sectional views of test section 50
5.3 Coolant mass flow control 51
5.4 Dimensions and placement of slot geometry 52
5.5 LED lighting positions 54
5.6 Full image mean calibration curve 57
5.7 Plain rectangular slot geometry 65
5.8 Phase 1 land geometries 66
5.9 Cross-sectional views of phase 2 test section 67
5.10 Dimensions and placement of cross corrugated slot geometry 67
5.11 UV LED array 68
5.12 Test section under UV light 68
5.13 200 pixels square sample mean calibration curve 69
5.14 Cross corrugated slot plates 70
5.15 Exit corrugation alignments 71
5.16 X-ray view of coolant flow path through a cross corrugated slot 71
5.17 Exit shaped bottom plates 73
5.18 Exit shaped top plates 74
5.19 Ramp down exit shaping 76
5.20 Combined channel straightening and ramp down exit shaping 77
5.21 G13 cross corrugated geometry 78
5.22 Joule-Thomson coefficients for nitrogen and carbon dioxide 79
5.23 Rig schematic with intermediate reservoir 81
5.24 Intermediate reservoir 81

6.1 Approximate view area and coordinate system 84
6.2 2D η distributions, L1: No lands 85
6.3 2D η distributions, L2: Block 86

6.4 2D η distributions, L3: Rounded 87
6.5 2D η distributions, L4: Tapered 88
6.6 2D η distributions, L5: Diffuser 89
6.7 2D η distributions, L6: Tapered diffuser 90
6.8 2D land η distributions, L1 91
6.9 2D land η distributions, L2 92
6.10 2D land η distributions, L3–6, $M \approx 0.6$ 92
6.11 Centreline η, all land shapes 96
6.12 Potential core length, all land shapes 97
6.13 Potential core length comparison with literature 99
6.14 Spanwise averaged η, all land shapes 100
6.15 Spanwise varation of η, all land shapes 103
6.16 Area averaged η, all land shapes 105

7.1 2D η distributions, G0 111
7.2 2D η distributions, G1 112
7.3 2D η distributions, G2 113
7.4 2D η distributions, G3 114
7.5 2D η distributions, G4 115
7.6 2D η distributions, G5 116
7.7 2D η distributions, G6 117
7.8 2D η distributions, G7 118
7.9 2D η distributions, G8 119
7.10 Centreline effectiveness comparison between phase 1 and 2 120
7.11 Spanwise averaged effectiveness comparison between phase 1 and 2 . . . 120
7.12 Centreline effectiveness comparison between phase 2 and repeat 121
7.13 Spanwise averaged effectiveness comparison between phase 2 and repeat 122
7.14 2D land η distributions, G0 125
7.15 2D land η distributions, G1 126

7.16 2D land η distributions, G0–4, $M \approx 0.6$ 126
7.17 2D land η distributions, G5–8, $M \approx 0.6$ 127
7.18 Centreline η, slots without exit shaping, G0–4 129
7.19 Centreline η, slots without exit shaping, G5–8 130
7.20 Spanwise averaged η, slots without exit shaping, G0–4 132
7.21 Spanwise averaged η, slots without exit shaping, G5–8 133
7.22 Spanwise variation of η, slots without exit shaping, G0–4 135
7.23 Spanwise varation of η, slots without exit shaping, G5–8 136
7.24 Area averaged η, slots without exit shaping, G0–8 138

8.1 2D η distributions, G9 146
8.2 2D η distributions, G10 147
8.3 2D η distributions, G11 148
8.4 2D η distributions, G12 149
8.5 2D η distributions, G13 150
8.6 2D land η distributions, G9 153
8.7 2D land η distributions, G10–13, $M \approx 0.6$ 153
8.8 Centreline η, slots with exit shaping, G9–13 156
8.9 Determining potential core length with cross corrugated slot using logarithmic plot 157
8.10 Determining potential core length with cross corrugated slot using filtered data 158
8.11 Potential core length, cross corrugated geometries with exit shaping . . . 159
8.12 Spanwise averaged η, slots with exit shaping, G9–13 161
8.13 Peak η, slots with exit shaping, G0 and G9–13 162
8.14 End of lands η, slots with exit shaping, G0 and G9–13 163
8.15 Spanwise varation of η, slots with exit shaping, G9–13 164
8.16 Area averaged η, slots with exit shaping, G0 and G9–13 166
8.17 Comparison of η between G0 and G13 167

9.1 2D η distributions using carbon dioxide coolant, G0 174
9.2 2D η distributions using carbon dioxide coolant, G13 175
9.3 2D land η distributions using carbon dioxide coolant, G0 176
9.4 2D land η distributions using carbon dioxide coolant, G13 176
9.5 Centreline η using carbon dioxide coolant, G0 178
9.6 Centreline η using carbon dioxide coolant, G13 179
9.7 Potential core length of G0 and G13 using carbon dioxide coolant 180
9.8 Potential core length against momentum flux ratio, G0 and G13 181
9.9 Spanwise averaged η using carbon dioxide coolant, G0 182
9.10 Spanwise averaged η using carbon dioxide coolant, G13 183
9.11 Peak η, G0 and G13 using carbon dioxide coolant 184
9.12 End of lands η, G0 and G13 using carbon dioxide coolant 185
9.13 Spanwise varation of η using carbon dioxide coolant, G0 186
9.14 Spanwise varation of η using carbon dioxide coolant, G13 187
9.15 Area averaged η, G0 and G13 using carbon dioxide coolant 188

10.1 Pressure losses with included angle of $90°$, G0–4 194
10.2 Enhancement in Fanning friction factor relative to G0, G1–4 195
10.3 Bridge wall flow reflection 196
10.4 Pressure losses with included angle of $120°$, G0, G5–8 197
10.5 Enhancement in Fanning friction factor relative to G0, G5–8 198
10.6 Pressure losses with exit shaping, G0, G9–13 198
10.7 Enhancement in Fanning friction factor, G9–13 199
10.8 Bridge wall alignment, G9–11 200
10.9 Parallel coordinates summary of all friction factor results 203

11.1 Computational domains 206
11.2 Mesh detail 207
11.3 Pressure losses with included angle of $120°$, G0, G5–8 207
11.4 Unsteady simulation monitoring data for G0 209

11.5 Flow visualisation on midslot plane 210
11.6 Unsteady simulation monitoring data for G13 211
11.7 Effectiveness on cutback and lands 212
11.8 Comparison of η between experiment and CFD, G0 213
11.9 Comparison of η between experiment and CFD, G13 214

A.1 Pressure-enthalpy chart for nitrogen (Reynolds, 1979) 235
A.2 Temperature-entropy chart for carbon dioxide (Reynolds, 1979) 236

List of Tables

5.1 Pressure transducer model numbers 56

5.2 Target operating conditions 59

5.3 Uncertainty in p/p_{ref} evaluated at 0.496 62

5.4 Uncertainty in blowing ratio evaluated at $M = 0.969$ 62

5.5 Uncertainty in effectiveness evaluated at $\eta = 0.081$ 63

5.6 Uncertainty in effectiveness evaluated at $\eta = 0.919$ 63

5.7 Uncertainty in Fanning friction factor evaluated at $f = 0.431$ 63

5.8 Cross corrugated plate combinations and dimensions 72

5.9 Exit shaped plate combinations and dimensions 75

5.10 Exit shaping dimensions 78

5.11 Target operating conditions using carbon dioxide coolant 82

9.1 Comparison of momentum flux ratio using nitrogen and carbon dioxide coolant compared to a real engine 172

Nomenclature

Acronyms

1D	One-dimensional
2D	Two-dimensional
3D	Three-dimensional
CCD	Charge-coupled device
CFD	Computational fluid dynamics
FIB	Fluoro/Isopropyl/Butyl polymer
HP	High pressure
HTC	Heat transfer coefficient
ISSI	Innovative Scientific Solutions, Incorporated
LED	Light-emitting diode
MFC	Mass flow controller
MR	Multifaceted reflector
MTO	Maximum take-off
NI	National Instruments
PIV	Particle image velocimetry
PSP	Pressure sensitive paint
PtTFPP	Platinum tetra(pentafluorophyenyl)porphine
RANS	Reynolds-averages Navier-Stokes
SLM	Standard litres per minute
TLC	Thermochromic liquid crystals
UK	United Kingdom

USA	United States of America	
UV	Ultraviolet	
XWB	Extra wide body	

Dimensionless Numbers

f	Fanning friction factor	
Le_{T}	Turbulent Lewis number	
Re	Reynolds number	
St	Strouhal number	

Greek Symbols

α	Thermal diffusivity	$\mathrm{m^2\,s^{-1}}$
δ_{f}	Film thickness	mm
ϵ_M	Turbulent mass diffusivity	$\mathrm{m^2\,s^{-1}}$
ϵ_T	Turbulent thermal diffusivity	$\mathrm{m^2\,s^{-1}}$
η	Adiabatic film cooling effectiveness	
Γ	Mass Diffusion Coefficient	$\mathrm{m^2\,s^{-1}}$
Δp	Pressure loss	Pa
μ	Dynamic viscosity	$\mathrm{Pa\,s}$
ρ	Density	$\mathrm{kg\,m^{-3}}$
θ	Angle	$^\circ$
θ_{cc}	Included angle	$^\circ$

Roman Symbols

R	Radius of curvature	mm
Z	Density ratio factor	
$\mathrm{A}(T)$	Stern-Volmer coefficient	
A	Area	$\mathrm{mm^2}$
A_{HT}	Unitary cell heat transfer area	$\mathrm{mm^2}$
$\mathrm{B}(T)$	Stern-Volmer coefficient	
C	Mass fraction	
D	Diameter	mm

D_{h}	Hydraulic diameter	m
D_{ori}	Orifice meter hole diameter	mm
D_{pipe}	Orifice meter pipe diameter	mm
G	Mass flux	$\mathrm{kg\,m^{-2}\,s}$
H	Height	mm
H_{cc}	Corrugation height	mm
H_{lip}	Minimum lip thickness	mm
H_{se}	Maximum slot exit height	mm
H_{si}	Maximum slot internal height	mm
I	Image intensity	
J	Momentum flux ratio	
L	Length or thickness	mm
L_{coff}	Offset distance of channel straightening section from slot exit	mm
L_{roff}	Offset distance of ramp down section from slot exit	mm
$\dot{\mathrm{M}}$	Molar flow rate	$\mathrm{kmol\,s^{-1}}$
M	Blowing ratio	
$\dot{m}$	Mass flow rate	$\mathrm{kg\,s^{-1}}$
$\dot{m}$	Mass flow rate	$\mathrm{kg\,s^{-1}}$
$\mathrm{MIX_N}$	Sturgess geometric parameter	
MW	Molecular weight	$\mathrm{kg\,kmol^{-1}}$
n	Mole fraction of oxygen	
P	Pitch	mm
p	Pressure	Pa
$p(\mathrm{O_2})$	Partial pressure of oxygen	Pa
P_{se}	Slot exit perimeter	mm
P_{span}	Spanwise pitch	mm
p_{tot}	Total pressure of gas mixture	
P_{true}	True perpendicular pitch	mm
T	Temperature	K

u	Flow velocity	$\mathrm{m\,s^{-1}}$
u_T	Spanwise cut plane area averaged flow velocity	$\mathrm{m\,s^{-1}}$
$\bar{u}$	Bulk flow velocity	$\mathrm{m\,s^{-1}}$
V	Volume	$\mathrm{m^3}$
V_unit	Unitary cell volume	$\mathrm{m^3}$
W	Width	mm
X	Mole fraction	
x	Downstream distance from coolant exit	mm
x_p	Potential core length	mm
y	Perpendicular distance from wall	mm
z	Spanwise displacement from centreline	mm

Subscripts

∞	Mainstream flow
air	Air
atm	At atmospheric conditions
aw	Adiabatic wall
cc	Pertaining to the cross corrugations
coff	Channel straightening section offset
c	Coolant flow
curve	Pertaining to the channel straightening section
dark	In darkness
fg	Foreign gas
f	Fluid
lip	Pertaining to the lip
land	Pertaining to the land
m	Mainstream flow
mix	Gas mixture
N_2	Nitrogen
O_2	Oxygen

ramp	Pertaining to the ramp down section
ratio	Ratio
ref	At reference conditions
roff	Ramp down section offset
s	Static
se	Pertaining to the slot exit
si	Pertaining to the slot internals
slot	Pertaining to the slot
span	In the spanwise direction
surf	On the surface
tot	Combined mainstream and coolant flow
true	True or actual
w	Wall
gauge	Gauge (relative to atmospheric)
i	A specific substance
ori	Pertaining to the orifice meter

Chapter 1

Introduction

1.1 Civil turbofan engines

In the civil aircraft industry, rising fuel costs and environmental concerns have emphasised the importance of the overall fuel efficiency of an aircraft. This means reducing the specific fuel consumption (SFC) which defines the fuel usage per unit of thrust. From the turbofan engine designer's point of view, this can be achieved by increasing the pressure ratio and turbine entry temperature of the engine. An analysis of the idealised gas turbine cycle, accounting for the non-perfect isentropic efficiency of the compressor and turbine as shown in Cumpsty (2003), shows that at high pressure ratios better thermal efficiency can only be achieved with higher turbine entry temperature (TET) (Figure 1.1). For this reason, engine manufactures including Rolls-Royce have been steadily increasing the turbine entry temperature in their engines for decades (Figure 1.2).

1.1.1 Background

The Rolls-Royce company began in 1906 when Sir Henry Royce and Charles Rolls joined forces to sell motor cars bearing the Rolls-Royce badge. 9 years later, soon after the outbreak of war, the company developed its first aero engine named the Eagle. This was quickly followed by other aero engine designs and by the end of the First World War,

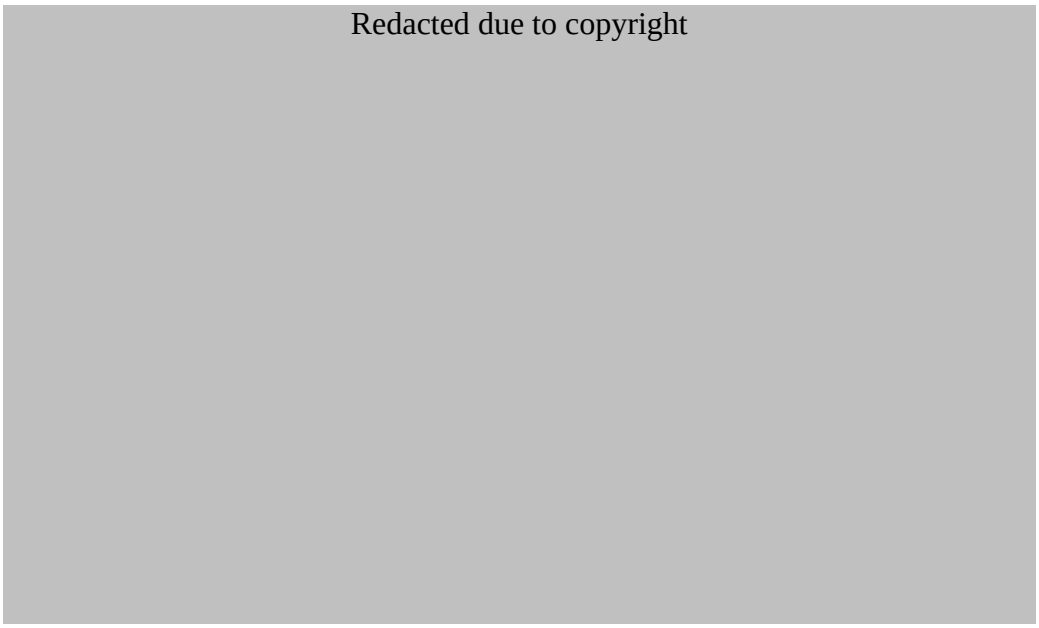


Figure 1.1: Effect of temperature and pressure ratio on efficiency (Cumpsty, 2003)

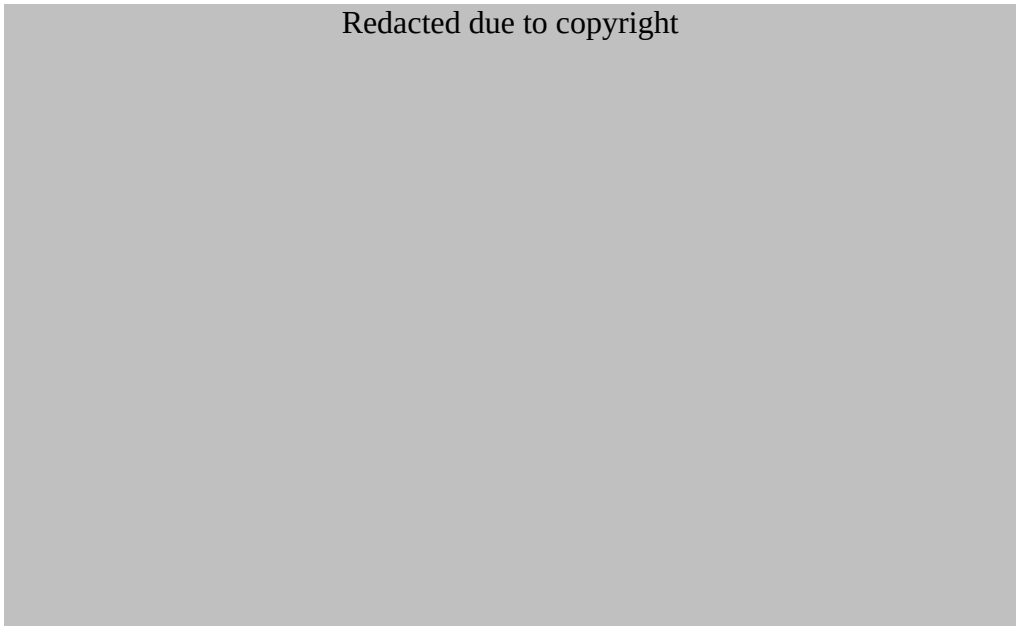


Figure 1.2: Turbine entry temperatures over the decades (Cumpsty, 2003)

Rolls-Royce engines were propelling half the Allied air power. In the late 1920s, aero engines became Rolls-Royce's core business and when Sir Henry Royce passed away in 1933, he left one final gift to the world of aviation in the form of the Merlin engine. Towards the end of the Second World War, Rolls-Royce began work on jet engines and during the post war period, significant advances in gas turbine engine production for civil aviation were made. Unfortunately, financial difficulties in developing the RB211 turbofan eventually forced the company into receivership and nationalisation in 1971. Nevertheless, development of the RB211 continued and Rolls-Royce produced the first triple shaft turbofan engine in 1972. In 1987, Rolls-Royce was privatised and has since used its experience with the RB211 to launch the Trent family of turbofan engines, beginning with the highly successful Trent 700. The success of the Trent family of engines has propelled Rolls-Royce to the position of the world's second largest aero engine producer.

1.1.2 The Trent extra wide body

The Trent extra wide body (XWB) is the latest large civil engine to be designed and manufactured by Rolls-Royce. It is designed for the Airbus A350 XWB and features up to 97,000 lb of Thrust (Rolls-Royce, 2012). Since the results of this project may be applicable to current or future Rolls-Royce HP turbine blade designs, it was decided to use the geometry and maximum take-off (MTO) operating conditions of the Trent XWB 97k HP Turbine Demo 2 Blade as the basis for all designs in this project.

1.2 The need for cooling

Aside from engine efficiency, the other major concern for the turbofan engine designer is the ability of the engine to continue operating at high efficiency while maximising the time between servicing or replacement. In particular, the high pressure (HP) turbine disc and blades must operate under extreme temperature and mechanical loading for extended periods of time. The durability of any component under its operating conditions is referred

to as its "life" which is usually expressed as a number of hours, test cycles or flight cycles it can be expected to endure before requiring a service or replacement. Running components at high temperatures lowers the life, so air cooling is used to reduce the temperature of the components while increasing the gas temperature.

1.3 Air cooling

In modern aircraft engines, the HP turbine components are cooled by taking air from the final stage of the HP compressor, bypassing the combustor through a cavity and feeding it to the components (Figure 1.3). However, some of this cooling air bypasses the HP blade without useful work being extracted from it. Furthermore, the cooler air is ejected back into the mainstream gas via film cooling holes, reducing the mainstream gas temperature, thereby reducing the amount of thrust relative to an engine where the same air did not bypass the combustor. This detriment to the engine efficiency is established in Horlock (2001) but is normally small where low cooling flows are required.

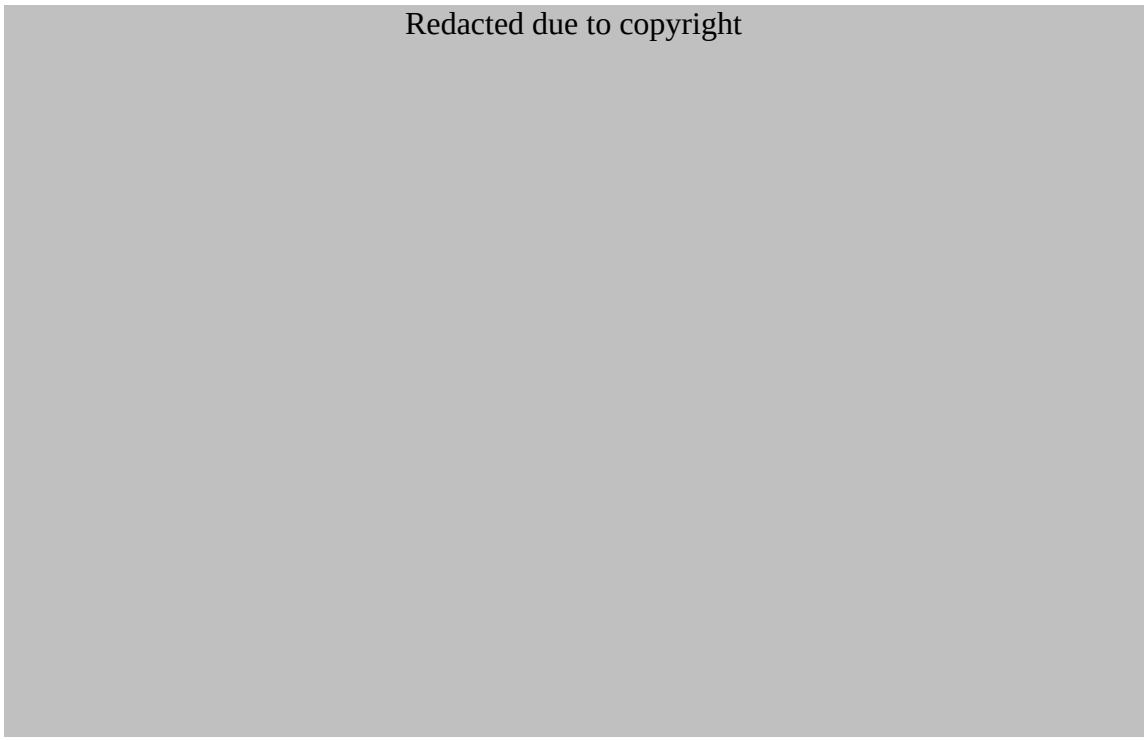


Figure 1.3: Diagram of Trent 1000 air systems (Rolls-Royce, 2009)

With higher TET however, comes higher required cooling flows. As Cumpsty (2003)

explains, there are diminishing returns on efficiency as TET increases. This is because the amount of cooling air required becomes so large that the reduction of efficiency due to cooling outweighs the increase in efficiency due to having a higher TET. Current engine designs have reached this point with TETs of over 2000 K as well as high operating pressures. Thus, new inventions in cooling technology are required to continue increasing TET while minimising cooling flows, allowing reductions in SFC.

1.4 Trailing edge cooling

A particularly challenging part of the high pressure blade is the trailing edge. This section endures very high temperatures and mechanical stresses but aerodynamic efficiency requirements dictate that it must be tapered to the end with minimal thickness. The thin profile makes it difficult to feed directly with coolant internally and necessitates the use of film cooling. A common method of film cooling the trailing edge is to position film cooling holes or slots just upstream of the trailing edge on the pressure surface side of the blade. Modern designs may include a cutback region where material is removed from the pressure surface between the film hole exits and the trailing edge to allow the coolant to exit almost tangentially to the mainstream and also reduce the risk of blockage. Cooling slots have an advantage over cooling holes in that the film is uniform along the spanwise width which provides even surface coverage and the film sticks to the surface more readily, rather than lifting off into the mainstream gas.

However, continuous cooling slots are not mechanically robust as the slot weakens the design. This necessitates the use of interrupted cooling slots which have an internal "bridge" connecting the two sides and dividing the continuous slot into discrete slots, as well as an external protuberance, or "land", which extends from the bridge to the trailing edge, dividing and stiffening the cutback area. Furthermore, manufacturing constraints dictate the minimum slot height, resulting in excessive coolant usage if a plain, unobstructed slot is used. Various methods are used by blade cooling designers to restrict coolant flow, including pedestal banks and internal ribs. The cross corrugated slot is one

such design under investigation in the current research project.

1.5 Objectives of research

The aim of this research was to conceive of a novel blade trailing edge cooling geometry capable of controlling coolant flow while also providing good film cooling performance. Its performance was assessed relative to a baseline geometry and then modifications were made to the geometry to improve its performance. The steps taken to accomplish this were:

1. Conceive of the cross corrugated slot cooling design and demonstrate its novelty.

2. Develop the capability to use the pressure sensitive paint technique to measure adiabatic film cooling effectiveness while eliminating conduction effects.

3. Compare land shapes for trailing edge slot film cooling and recommend the optimal shape.

4. Measure the film cooling performance of the cross corrugated slot design and compare with the baseline geometry.

5. Modify and optimise the cross corrugated design to improve film cooling performance and compare with the baseline geometry.

6. Determine whether or not density ratio has a significant effect on the film cooling performance of the optimised design.

7. Characterise the pressure loss characteristics of the cross corrugated slot and compare with the baseline geometry.

8. Investigate the ability of numerical simulations to model the cross corrugated slot film cooling flow.

1.6 Thesis outline

- Chapter 2 contains a review of the current methods of film cooling and the issues that could be helped with the use of cross corrugated slot geometries.
- Chapter 3 outlines the basic concept of the geometry of the novel cross corrugated cooling slot design, identifies the potential advantages and potential disadvantages of the design and justifies the novelty of the design concept.
- Chapter 4 explains the experimental methods used for measuring adiabatic film cooling effectiveness and pressure losses.
- Chapter 5 details the experimental set-up and the evolution of the geometries as well as the facility itself throughout the research.
- Chapter 6 presents the adiabatic effectiveness results regarding the selection of the optimal land geometry.
- Chapter 7 produces the first adiabatic effectiveness results for cross corrugated slot geometries and how they adversely affect film cooling performance.
- Chapter 8 tests a series of modified cross corrugated slot geometries in order to improve the film cooling performance and recommend the best geometry.
- Chapter 9 tests the best geometry using a higher density ratio to assess the effect on cooling performance.
- Chapter 10 records the hydraulic performance of the cross corrugated geometries.
- Chapter 11 assesses the ability of unsteady numerical simulations to model the complex flow from the cross corrugated geometry.
- Chapter 12 summarises the research and presents the conclusions and suggestions for future work.

1.7 Summary of achievements and publications

- This research has conceived of a novel trailing edge slot cooling design that has the potential to allow cooling designers great control over the cooling performance and efficiency of high pressure turbine blades and vanes. In particular, it allows the coolant flow through the trailing edge to be limited without compromising the blade rigidity and strength.

- The greatest disadvantage of the cross corrugated design, namely the poor film cooling performance relatively to an unobstructed slot, has been identified and quantified, and modifications to the geometry have been proposed to solve this issue.

- These modifications have been experimentally proven to improve the film cooling performance of the cross corrugated slot to the point that it was on par with, and in some aspects better than, the unobstructed slot.

- Four papers have been published thus far from the research conducted: Wong et al. (2015), Wong et al. (2016a), Wong et al. (2016b) and Wong et al. (2017).

- A patent application was submitted in 2014 by Rolls-Royce with application number GB1422322.6 and granted in 2016 with publication number GB2533315.

- The development of the pressure sensitive paint method has led to its adoption in other research projects at Oxford and directly contributed to three related papers: Gurram et al. (2016), Murray et al. (2018) and Saul et al. (2018).

Chapter 2

Literature Review

2.1 Introduction

This chapter provides a brief overview of the available methods of cooling the turbine blade trailing edge, discusses their strengths and weaknesses and how the cross corrugated slot design aims to solve these issues.

It then goes on to identify relevant studies in the literature that were used to verify the experimental technique used and inform the creation of the baseline geometry which the cross corrugated slot was compared against and required to match or exceed the performance of in order to achieve the objectives of the research.

2.2 Film cooling

2.2.1 General film cooling

There are a number of methods used to cool HP turbine blades and vanes (Figure 2.1). The trailing edge is usually cooled externally since this portion of the blade is too thin to cool internally. External cooling involves ejecting coolant from holes or slots such that they form a protective layer of relatively cool air on the outer walls, acting as a buffer between the blade metal and the extremely hot mainstream gas.



(a) HP blade (b) HP vane

Figure 2.1: Cooling systems in HP blades and vanes (Rolls-Royce, 2005)

The most commonly used method of film coolant ejection is using rows of discrete drilled holes. Due to their prevalence in blade and vane cooling, a large body of research is available on film cooling holes. Goldstein et al. (1968) first investigated holes exhausting perpendicular and at a 35° angle to the flow. Ekkad et al. (1997a,b) followed this with film exhausted at a compound angle to the flow and Ligrani et al. (1994), and Kusterer et al. (2006) took this further with double staggered rows. Unfortunately, the coolant jets from film holes are discrete and therefore do not provide as good coverage as a slot for the same cooling flow. They also tend to lift-off from the surface at high momentum flux ratios of approximately 1 and above (Sargison, 2001), leading to mixing with the mainstream flow, reducing the cooling effectiveness. Jet lift-off and penetration into the mainstream flow also creates significant aerodynamic losses greater than that of a slot (Denton, 1993, Young and Wilcock, 2002a,b). It is for these reasons that slot cooling is preferred where possible.

2.2.2 Slot film cooling

Cooling slots have the advantages that the film is uniform along the spanwise width which provides even surface coverage and the Coanda effect causes the film to stick to the surface more readily rather than lifting off into the mainstream gas (Sargison, 2001). Slots can exhaust tangentially to the external flow, as investigated by Hartnett et al. (1961). Alternatively, they may be inclined to the external flow, as in the study by Metzger et al. (1968). The slot could also be covered with a porous material to enable transpiration cooling as well as film cooling, as studied by Goldstein et al. (1965).

However, slots are not without their disadvantages. They are not as mechanically robust as film holes since the two sides of the slot are completely disconnected. Furthermore, manufacturing constraints dictate a minimum slot height in order to be able to cast the core correctly, resulting in excessive and wasteful coolant flow through the slot. This means they are only suited for use in areas where structural integrity is not as much of an issue and high cooling flow is necessary, for example at the vane TE. Even there, it is necessary to use interrupted slots with internal bridges and external cutback lands, as well as internal structures like pin-fin arrays to both maintain structural integrity and control the coolant flow rate. However, pin-fin arrays like that shown in Figure 2.1b create long lasting wakes that disrupt the even film coverage, resulting in a non-uniform film and poor film effectiveness.

The cross corrugated slots would accomplish the same goal of maintaining structural integrity and coolant flow control, since the opposing sides of the slot are in physical contact, and the corrugations act as flow restriction. Just like the pin-fin arrays, the corrugations would create wakes that result in poor film effectiveness. However, unlike pin-fin arrays, cross corrugated slots may incorporate exit shaping as described in Section 3.3.3 which could provide better film coverage than the pin-fin arrays, comparable to the ideal of a plain unobstructed slot.

There have been many studies investigating general film cooling slots experimentally. Goldstein (1971) provided a review of much relevant work up to that year on various

slot designs including tangential and angled slots. Kacker and Whitelaw (1967) showed that the effect of mainstream boundary layer thickness on adiabatic film effectiveness is small, so the present study does not need to replicate the incoming mainstream boundary layer. Mukherjee (1976) performed a literature survey to form a number of correlations for predicting film effectiveness and the length of the initial "potential core" region of unity effectiveness. These correlations were used in the present study to verify that the effectiveness measurements taken are consistent with the literature. Sturgess (1986) and Sturgess and Pfeifer (1986) investigated the film cooling of practical combustor slots, detailing a process for measuring potential core length which was used in the current study. They formed a geometric parameter, MIXN (where $\mathrm{MIX_N} = 0$ corresponds to a clean slot with realistically thick lip), for characterising practical combustor slot geometries and reported the relation between potential core length, blowing ratio, and MIXN. This data was also used to compare effectiveness measurements with the literature.

Several studies have focused on slots applied to the turbine blade trailing edge, where the slot is interrupted and external lands are usually present. The studies most relevant to the present study due to the similarity of geometry and measurements taken are summarised here:

Taslim et al. (1992) studied the film cooling effectiveness on the cutback surface downstream of the slot with straight bridges and lands dividing the slots. They varied injection angle, lip thickness to slot height ratio, slot width to slot height ratio, blowing ratio and density ratio. Martini et al. (2005a) investigated how three different slot designs used in modern blades affect the film cooling effectiveness, heat transfer coefficients and discharge coefficients in the near slot region of the cutback. These geometries featured different internal slot geometries but no external lands on the cutback surface. Murata et al. (2012) used the transient infrared thermography method to compare four different slot geometries for film cooling effectiveness and heat transfer coefficients. Two of these featured plain slots with straight lands and tapered lands respectively. Yang and Hu (2011) and Yang and Hu (2012) used stereoscopic particle image velocimetry (PIV) to take flow field measurements of an interrupted slot geometry with and without tapered

diffuser lands and compared these with film cooling effectiveness maps acquired using the pressure sensitive paint (PSP) technique. Ling et al. (2015a) used an MRI technique to take velocity field and film effectiveness measurements using tapered straight and diffuser lands.

The aforementioned studies have been used to inform the specification of the baseline rectangular slot geometry and land shape used to compare the cross corrugated slot design against. While slots with pin-fin arrays are common in trailing edge cooling, it was decided that a plain, unobstructed slot aside from internal bridges would be used as the baseline since there is a large body of literature available to compare against and it represents the best-case scenario for the film cooling effectiveness downstream of a slot. The pressure losses through the slot were also compared with a study using pin-fin arrays by Lau et al. (1989) to show how the pressure losses compare to a typical pin-fin array.

While there have been various land geometries investigated in the literature, the research has been sporadic, with insufficient evidence to choose one design over the others, all other geometric and flow parameters being equal. Therefore, it was necessary to investigate a number of land designs already used in the literature and variations on them and select one design to be used in all subsequent cross corrugated slot cooling tests.

2.2.3 Density ratio effects

Two important parameters in film cooling are the blowing ratio, denoted as M and defined in Equation 2.1, and the momentum flux ratio, denoted as J and defined in Equation 2.2. It can be seen that both are function of coolant to mainstream density ratio.

$$M = \frac{\rho_{\mathrm{c}} u_{\mathrm{c}}}{\rho_{\mathrm{m}} u_{\mathrm{m}}} \tag{2.1}$$

$$J = \frac{\rho_{\mathrm{c}} u_{\mathrm{c}}^2}{\rho_{\mathrm{m}} u_{\mathrm{m}}^2} \tag{2.2}$$

If the density ratio is increased by a factor Z, but the blowing ratio M is kept constant, then the velocity ratio must be reduced by the same factor Z. Therefore, momentum flux

ratio is increased by factor of Z from the density ratio but also reduced by a factor of Z^2 from the velocity ratio, resulting in an overall reduction by a factor of Z.

For a typical HP turbine blade, the mainstream air temperature is approximately $1900\,\mathrm{K}$ and the cooling air is taken from the HP compressor exit at approximately $1000\,\mathrm{K}$ (Rolls-Royce, 2005). The resulting density ratio for HP blade film cooling is then in the region of 1.9. However, experimental studies of film cooling frequently use density ratios as low as 1. This is because achieving the same density ratio outside of a running engine requires some combination of three elements:

- Heating of the mainstream flow to extreme temperatures which is expensive and can be dangerous.
- Cooling of the coolant flow which is also expensive and can cause icing issues in the feed system.
- Use of higher density gases as coolant or lower density gases as mainstream which adds complexity and expense to the gas supply systems.

Without matching density ratio, it is impossible to match both blowing ratio and momentum flux ratio simultaneously in the same film effectiveness experiment. If a density ratio is halved for the experiment and blowing ratio is matched, then the momentum flux ratio will be double that of the engine. Therefore, experiments using low density ratios must choose which parameter to match out of the two.

U.S. Department of Energy-National Energy Technology Laboratory (NETL) and Bogard (2006) observed that in general, for situations where momentum flux ratio is low and the coolant flows are fully attached to the surface, the film effectiveness measurements taken at low density ratio are similar to those taken at high density ratio for the same blowing ratio. However, where momentum flux ratio is high and the coolant flows begin to detach from the surface (Typically at $J > 0.4$), the film effectiveness measurements at low density ratio and at high density ratio are most similar for the same momentum flux ratio. In the case of a tangentially fed slot, the coolant flow is likely

to remain attached to the surface. Therefore, it is more important in this case to match blowing ratio than momentum flux ratio.

2.2.4 Numerical modelling

In order to optimise a cooling design for a particularly application, the design is usually modelled numerically so that geometric and flow parameters may be modified and simulated rather than having to experimentally test every possible variation on the design. Modelling trailing edge slots in numerical simulations has proven to be difficult. Holloway et al. (2002a) showed that steady Reynolds-averaged Navier-Stokes (RANS) simulations consistently over-predicted effectiveness due to not resolving the vortex shedding from the lip. Ravelli and Barigozzi (2013) confirmed this with a complex geometry including both trailing edge slots and upstream film rows. Holloway et al. (2002b) was able to significantly improve the accuracy of the predictions using unsteady RANS simulations. Ravelli and Barigozzi (2014) took this further by using a scale adaptive simulation method and went on to compare this with a detached eddy simulation and experimental data in Ravelli and Barigozzi (2015). Martini et al. (2005b) also used unsteady detached eddy simulations to gain insight into the unsteady mixing process on the cutback. Other studies including numerical simulations include Cakan and Taslim (2006), Ling et al. (2014) and Ling et al. (2015a,b).

All of the aforementioned studies have affirmed that in order to predict film effectiveness from a slot with any level of accuracy, unsteady simulations are the bare minimum requirement. The same is likely to hold for the cross corrugated slot design, thus, the current study has attempted to model the cross corrugated slot numerically using unsteady RANS based on the method used by Holloway et al. (2002b).

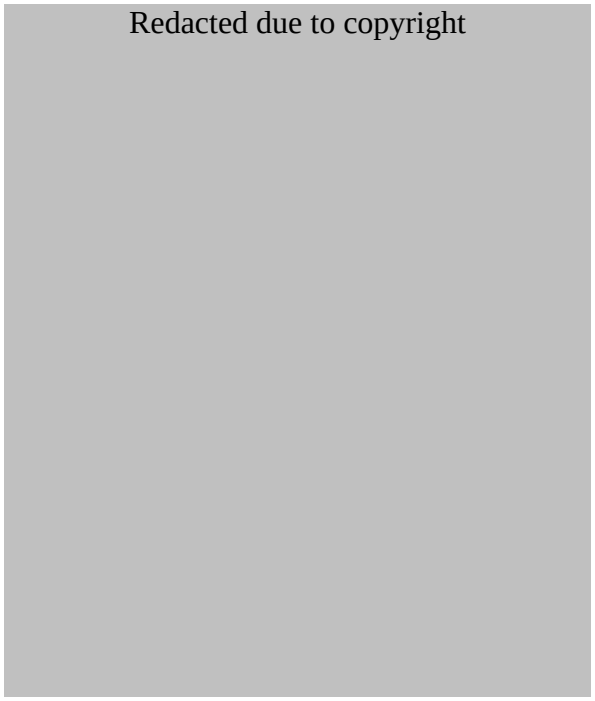


Figure 2.2: Lattice cooled blade (Goreloff et al., 1990)

2.3 Lattice internal cooling

Lattice cooling is a method of internal cooling similar in shape to the cross corrugated slot design. The use of lattice cooling in blades and vanes is most recognisable in Soviet-era designs, where it has been developed over the last few decades, an example of which is shown in Figure 2.1a. In a typical lattice design, each side of the passage has a set of parallel channels. The channels on one side are at a different angle to the channels on the other side, such that they cross over each other periodically. These channels are separated by ribs spanning half the passage height so that the tops of the ribs meet periodically in the middle of the passage. This forms a vortex where the flow moves along the channels on one side, reflect from the side wall and continue in the opposing channels.

A number of studies have been conducted on lattice geometries to obtain heat transfer and pressure loss characteristics of lattice cooling systems. These include stationary experiments by Bunker (2004) and rotating experiments by Acharya et al. (2004). Experiments with lattice cooling applied to the radial passage feeding the TE of the blade were conducted by Gillespie and Ireland (1997). The advantages in high heat transfer, low pres-

sure loss, high structural integrity and suitability for investment casting are summarised by Bunker (2008).

Lattice cooling looks quite similar to cross corrugations but has been used and studied exclusively as an internal cooling method for blades, rather than a cooling and flow restriction method for trailing edge slot cooling. Therefore, although it is worth noting as an inspiration for the creation of the cross corrugated slot geometry, there is no available data on how it would perform as a trailing edge slot cooling design.

2.4 Cross corrugated heat exchangers

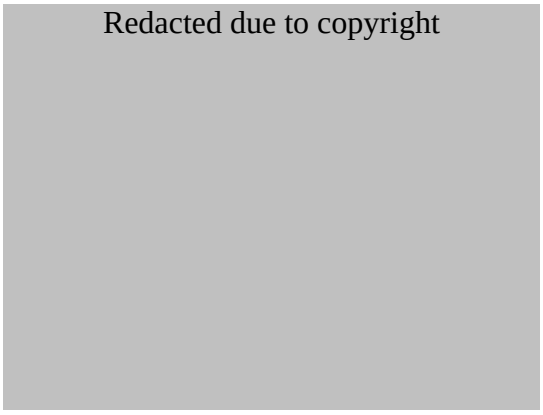
The cross corrugated geometry is frequently found in heat exchanger designs. These consist of plates with sinusoidal corrugations closely packed one of top of another with the direction of the corrugation channels alternating between layers (Figure 2.3a). As a heat exchanger it has excellent heat transfer properties and low pressure losses in a very compact arrangement. The flow properties can be adjusted by altering the geometric properties, i.e. the included angle, pitch and height (Figure 2.3b). The convention in the literature is to define the cross corrugated Reynolds number (Re_{cc}) as:

$$Re_{\mathrm{cc}} = \frac{\rho u_{\mathrm{T}} D_{\mathrm{h,cc}}}{\mu} \tag{2.3}$$

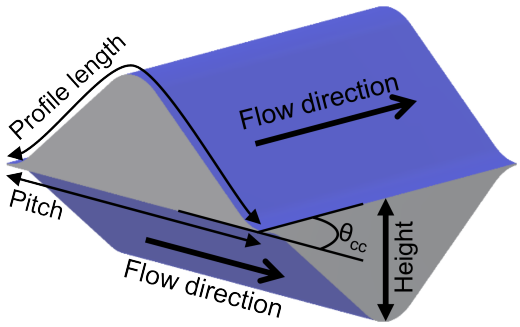
$$\text{Where the cross corrugated hydraulic diameter } D_{\mathrm{h,cc}} = \frac{4V_{\mathrm{unit}}}{A_{\mathrm{HT}}} \tag{2.4}$$

u_{T} is the spanwise cut plane area averaged flow velocity, V_{unit} is the unitary cell volume (Figure 2.3b) and A_{HT} unit is the unitary cell heat transfer area (coloured blue in Figure 2.3b).

A large body of research has been conducted on cross corrugated heat exchanger geometries. Savostin and Tikhonov (1970), and Okada et al. (1972) both obtained heat transfer measurements at a variety of included angles and pitch-to-height ratios based on the temperature change between the inlet and outlet of the test section. Focke et al.



(a) Heat exchanger (Ciofalo et al., 1996)



(b) Unitary cell

Figure 2.3: Cross corrugated geometry

(1985) used a mass transfer analogy technique with water as the working fluid to obtain local heat transfer measurements at a large range of *Re* from 10^2 to 10^5 and included angle. Focke and Knibbe (1986) used another water based method to visualise flow patterns in the same geometry at low *Re*. Rosenblad and Kullendorff (1975), and Gaiser and Kottke (1989) used the mass transfer analogy technique with air as the working fluid to confirm previous findings at low to mid-range *Re*.

More recently, thermochromic liquid crystals have been used to obtain more accurate local heat transfer measurements by Stasiek et al. (1996). The geometry used had a specific pitch-to-height ratio of 2 and the included angle varied from $30°$ to $79°$. Experiments were run with $500 < Re < 5000$. A concurrent numerical analysis was performed by Ciofalo et al. (1996) using the same geometry which found the best match for $Re < 5000$ using the low *Re* k-epsilon or large eddies simulation turbulence models. Adams (2004) obtained both experimental and numerical results for included angles of $60°$ and $90°$ with a pitch-to-height ratio of 2.2 and $1066 < Re < 5743$. Kwan (2011) used the same $90°$ included angle geometry as Adams and performed both experiments and numerical analyses at $1400 < Re < 8200$ but also took detailed heat transfer measurements at the side wall where the flow is reflected into the opposing corrugation channels.

All the aforementioned studies allow the prediction of the internal cooling performance of the cross corrugated slot geometry. However, none have applied this concept to a trailing edge slot and therefore there are no relevant studies investigating how this would

affect film cooling performance. Therefore, the present research has focused only on film cooling performance following a cross corrugated trailing edge slot and how it might be improved.

2.5 Summary

The current ideal for trailing edge cooling is the plain unobstructed slot. However, manufacturing and robustness considerations have meant that in practice, interrupted slots with some form of internal flow restriction like pin-fin arrays are used, resulting in reduced film cooling performance relative to the ideal plain slot.

The cross corrugated slot geometry that will be described in further detail in Chapter 3 has been proposed as a potential alternative flow restriction feature. Without exit shaping, this would like have the same or worse film cooling performance found in other flow restriction designs. However, unlike those other designs, cross corrugated geometries have the added benefit of being able to incorporate exit shaping to improve film cooling effectiveness.

The related geometry in lattice internal cooling was discussed but this has so far not been used as a flow restriction method for cooling the trailing edge and little relevant literature was available. Similarly, cross corrugated geometries were found to be commonly used in heat exchangers and the literature is abundant with internal heat transfer studies. However, the geometry has never been applied to a trailing edge slot and thus there is no relevant literature on film cooling effectiveness downstream of a cross corrugated slot, necessitating the current research.

A review of the literature has identified several studies that have been used to verify the experimental methods used in the present research and inform the creation of a baseline geometry to compare the novel cross corrugated slot design against. It was decided that a plain slot with only internal bridges and external lands would be used as an idealised, best-case scenario cooling design for the cross corrugated slot design to beat. The lack of sufficient evidence to choose the external land shape necessitated the preliminary

investigation of land shapes in phase 1.

Chapter 3

Novel Cooling Design

3.1 Introduction

In this chapter, the generalised novel cross corrugated slot cooling geometry is elaborated upon and the various parameters and possibilities for variations are detailed. Potential advantages and disadvantages of the general concept are discussed and a summary of the patent review demonstrates the novelty of this design, leading to the granting of a patent. Finally, the specific design choices tested in this research are defined.

3.2 Geometry

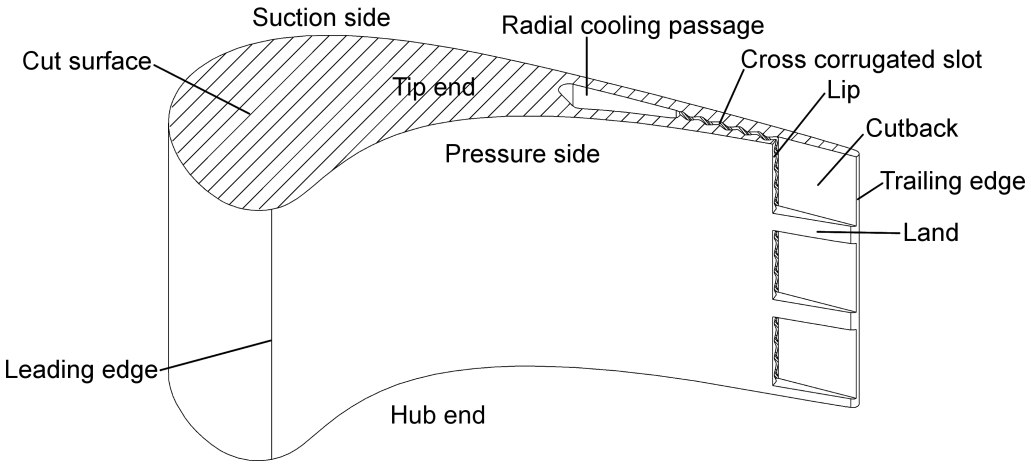
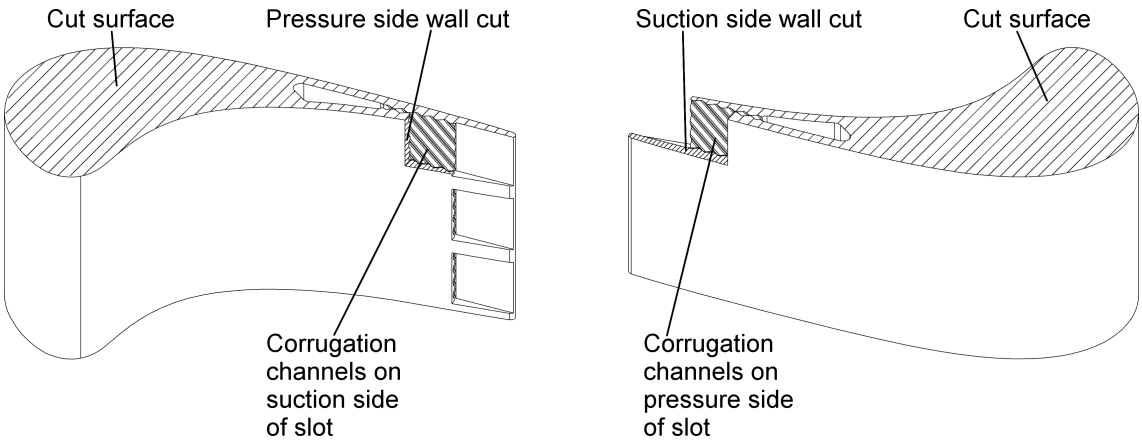


Figure 3.1: Cut HP blade with cross corrugated trailing edge slot



(a) Suction side corrugations (b) Pressure side corrugations

Figure 3.2: Cut HP blade showing internal corrugations

The geometry being investigated involves the use of a cross corrugated pattern within the trailing edge cooling slot of a high pressure (HP) blade although it is also applicable to any air cooled blade or vane. Figure 3.1 shows an isometric view of a constant-cross-section HP blade with a cross corrugated trailing edge slot. The blade shown has been cut in the streamwise direction such that the internal cross corrugated slot geometry is visible and the key blade nomenclature labelled.

Figures 3.2a and 3.2b show the same blade but with the slot wall cut away to reveal the internal corrugations. Figure 3.2a shows the corrugations on the suction side wall channelling the flow in a tip-to-hub direction at $45°$ to the mainstream. Figure 3.2b shows the corrugations on the pressure side wall channelling the flow in a hub-to-tip direction at $45°$ to the mainstream.

The design is comprised of a set of repeated, parallel corrugations on the suction surface side of the slot along with a second set of repeated, parallel corrugations on the pressure surface side of the slot. The first set is at an inclined angle and the opposing set is at an angle different to the first set such that the tops of the ridges of one set periodically cross the tops of the ridges of the other set. The angle between the corrugations on opposing sides of the slot is defined as the included angle θ_{cc}, and the corrugation channel geometry is defined by the corrugation height H_{cc}, the spanwise pitch P_{span}, and the true pitch P_{true}. At the slot exit, the lip has minimum thickness H_{lip} and the maximum slot exit

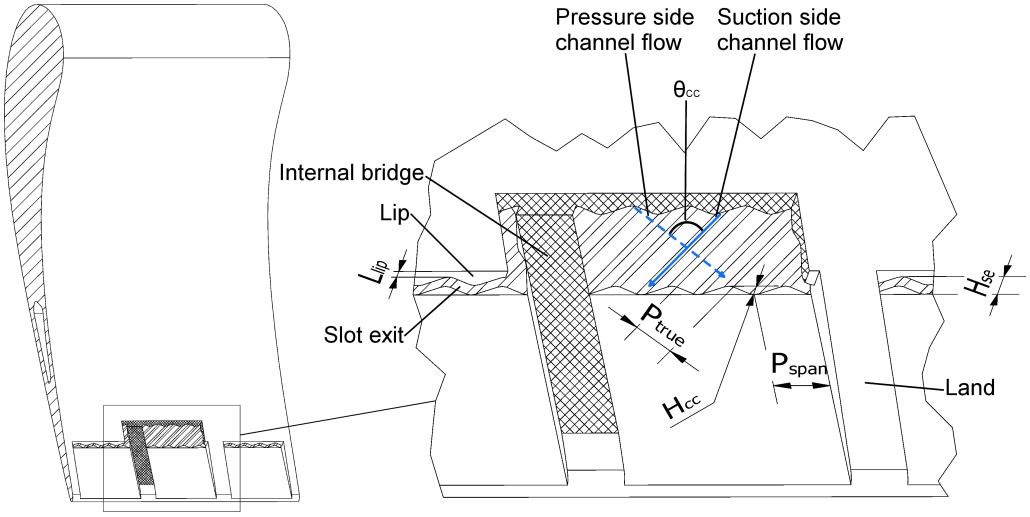


Figure 3.3: Close-up cut view of cross corrugated trailing edge slot

height H_{se}. Figure 3.3 shows a close-up view of the trailing edge with part of the pressure side wall cut out. Key features are labelled and dimensions defined. The profile shape is approximately sinusoidal in shape but can be any manufacturable shape which results in a reasonable flow area and has rounded edges to avoid stress concentrations.

3.3 Potential features

3.3.1 Flow control

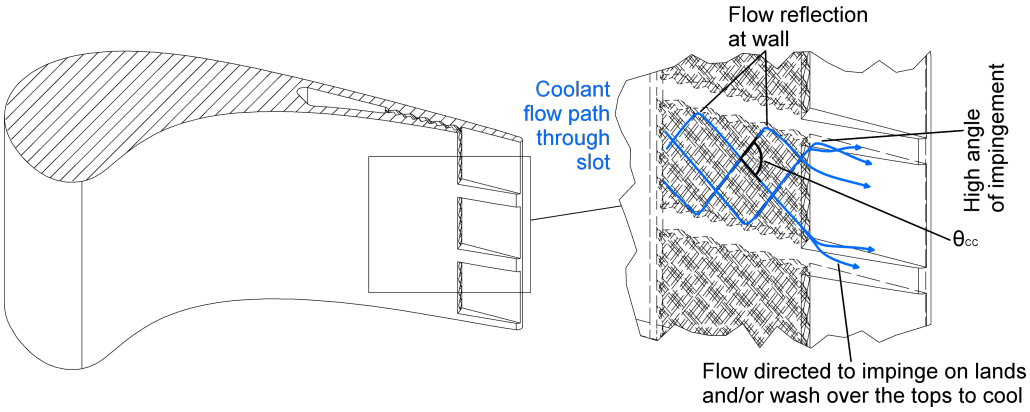


Figure 3.4: Coolant flow in cross corrugated slot with $\theta_{cc} = 90°$

The key benefit of the cross corrugated slot design is the high pressure losses through the slot. This occurs because the flow within the slot follows roughly the corrugation

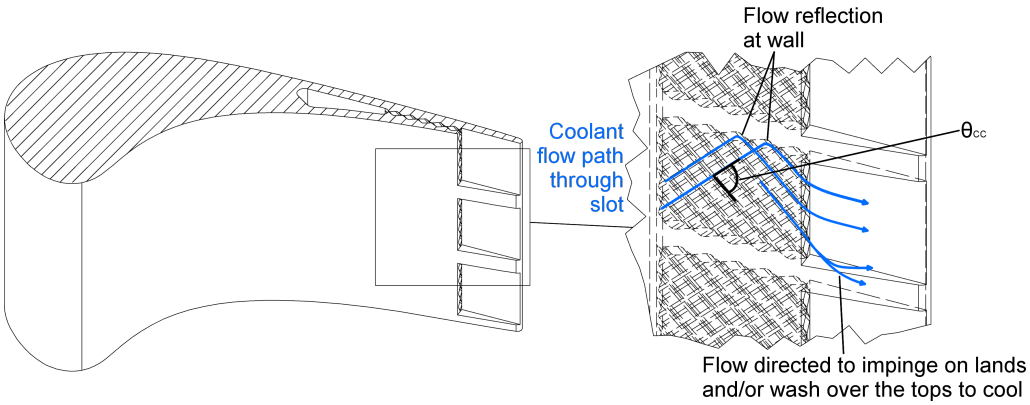
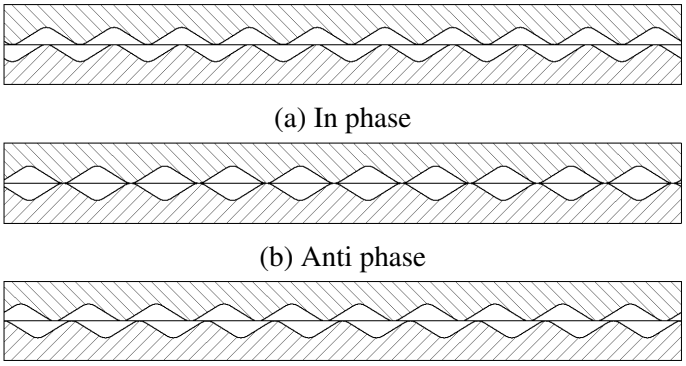


Figure 3.5: Coolant flow in cross corrugated slot with $\theta_{cc} = 105°$

channels, increasing the effective length of the flow path and restricting the effective flow area. The pressure drop is also enhanced when the flow meets the walls of the internal bridges separating the individual slots and changes direction. Upon meeting the bridge walls, the flow "reflects" from the wall and swaps from one set of passages to the other, resulting in further inertial pressure losses. An example of this design is shown in Figure 3.4 with the coolant flow path shown in blue. With an included angle of $90°$, the coolant reflects against the bridge walls once or twice before exiting on to the cutback surface.

The increased pressure loss is useful because excessive coolant flow is one of the main issues with the use of slots for cooling the HP turbine blade trailing edge. Slots are manufactured by casting, and if the slot is designed to be too thin (the slot height is too small), then the core used in the casting process will be too fragile, making it difficult and expensive to manufacture reliably. Because of this, the designer is restricted with a minimum slot height which, when combined with the high pressure margin that the slots are fed with, results in excessive coolant flow through the slots. The cross corrugated slot increases the pressure losses through the slot, allowing the use of a larger slot height while decreasing coolant flow. This translates into a thicker casting core which could make manufacturing easier.

Furthermore, by having several parameters that can be adjusted independently, the cross corrugated slot can be finely tuned to achieve the pressure losses required by the blade designer in each specific application. For example, an increase in the included angle



(a) In phase

(b) Anti phase

(c) 90° out of phase

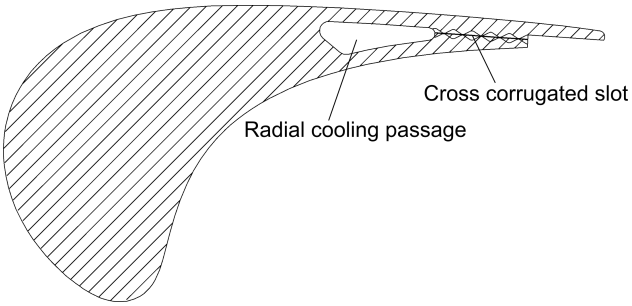
Figure 3.6: Different corrugation alignments at the bridge wall

can be used to reduce the flow rate by effectively reducing the true pitch and therefore the flow area perpendicular to the corrugations (maintaining the same spanwise pitch). This causes extra pressure losses due to the interaction between the flows in the two sets of channels. Figure 3.5 shows an example where the pressure side corrugations are set at a steeper angle of $60°$ from the mainstream while the suction side corrugations are set at the same angle of $45°$, resulting in an included angle of $105°$. This results in the coolant flow path becoming more restricted while also introducing more flow reflections at the bridge walls. The corrugation alignment at the interaction with the bridge walls can also be changed as indicated in Figure 3.6 to fine tune the pressure losses as necessary. These solid sections also act to increase the mechanical strength of the trailing edge as well as increase heat flux from the pressure surface to the suction surface or vice versa to reduce thermally induced stresses.

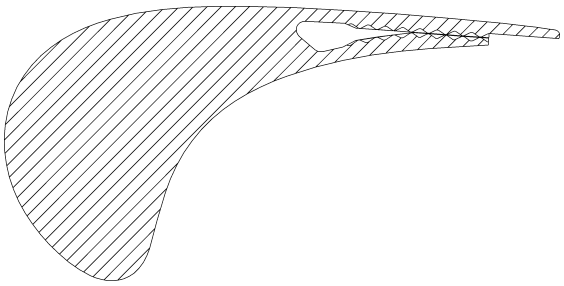
3.3.2 Internal cooling

Blade cooling is carried out by a combination of internal convective cooling in the serpentine passages within the blade and protective film cooling on the external surface. Typically, internal cooling is enhanced by the addition of ribs in the coolant passages (See Figure 2.1a). These enhance heat transfer on the internal walls, reducing the metal temperature from within. A cross corrugated slot achieves the same effect within the trailing edge slot by enhancing internal heat transfer. This effect can be applied within

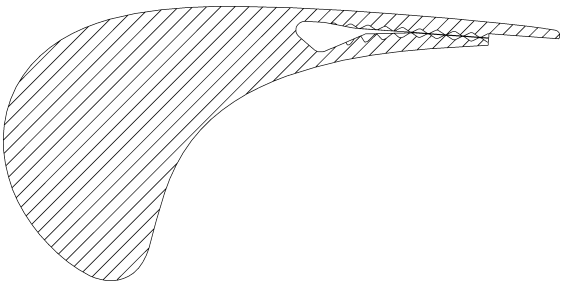
the radial cooling passage by extending the corrugations into the passage. Figure 3.7a shows the basic cross corrugated slot as it joins with the radial cooling passage. Figure 3.7b shows the cross corrugations extended part way into the radial cooling passage to enhance heat transfer. Figure 3.7c shows how the corrugation height can be increased within the radial cooling passage to further enhance heat transfer.



(a) Cross corrugated slot



(b) Extended cross corrugations into radial cooling passage



(c) Corrugation height increased in cooling passage

Figure 3.7: Radial passage cooling with cross corrugations

3.3.3 Film cooling

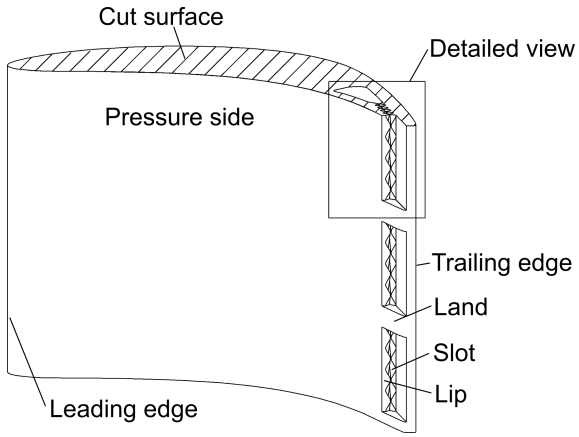
Protective film cooling of the trailing edge is the main purpose of the slot, since the trailing edge cannot be reached with internal cooling. The flow control benefits of the cross corrugated slots are therefore unusable if film cooling performance is not on par with a regular slot. Poor film effectiveness and high aerodynamic losses after the slot exit are possible issues with the cross corrugated design, due to the flow leaving the slot with a significant amount of momentum unaligned to the mainstream flow. The alignment at the inlet and outlet of the slot can be adjusted to modify the flow properties and entry or exit losses. Figure 3.8a shows a detailed view of the slot exit viewed from downstream.

Figures 3.8b, 3.8c and 3.8d show various possible exit alignments that could be used. Figures 3.8e and 3.8f show how the corrugation height could be adjusted to either leave a gap between the two sides or combine in the middle to adjust the exit flow properties. These two designs would also have an effect on pressure losses through the slot. The design shown in Figure 3.8e would have lower pressure losses and a more uniform spanwise film effectiveness profile. It would also likely be easier to manufacture since it would allow for a more robust core for casting. The design shown in Figure 3.8f would have the opposite effect.

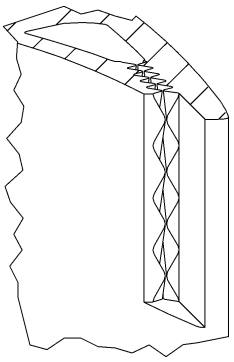
If the film cooling performance on the cutback surface is found to be unacceptable, modifications to the slot exit will be necessary. In order to achieve greater film cooling effectiveness after the flow leaves the slot, the channels can be redirected such that the flow exhausts at a an angle parallel to the mainstream flow as shown in Figure 3.9. This would like increase effectiveness further from the slot exit and reduce aerodynamic losses. Straightening the channels while remaining continuous also increases the corrugation pitch as defined perpendicular to the channel flow, increasing the channel flow area and reducing blockage. Furthermore, the corrugations close to the exit can be shaped to create a more uniform continuous slot at the exit, for example by chamfering the tops of of the ridges, creating a gradual ramp down to the cutback surface as in Figure 3.9.

3.3.4 Land cooling

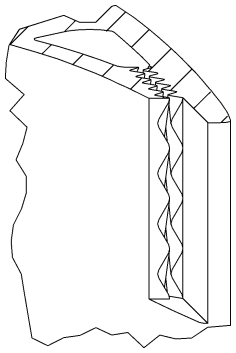
The lands on the cutback surface are a challenge to cool since they are not covered by the film leaving the slot. Cross corrugated slots without exit shaping would direct some of the flow at exit towards the lands, possibly improving land cooling either through impingement against the sides of the lands or by directing coolant to wash over the tops and displace the hot mainstream gas. Increasing the included angle might result in greater impingement and better cooling on the lands (as shown in Figure 3.5). However, as mentioned previously, this flow non-parallel to the mainstream flow direction would likely reduce effectiveness on the cutback region and increase aerodynamic losses. A compro-



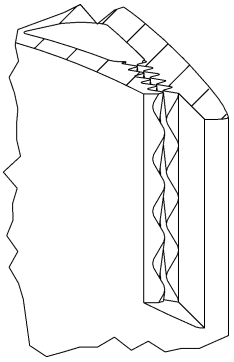
(a) View of slot exit from downstream



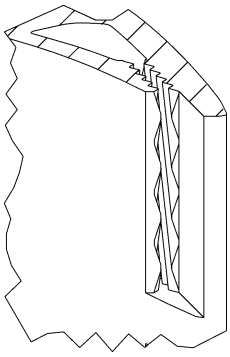
(b) Anti phase



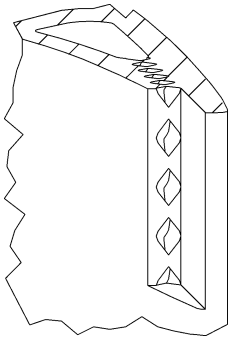
(c) In phase



(d) 90° out of phase



(e) Gap left between the two corrugation sides



(f) Corrugation ridges combine in the middle

Figure 3.8: Different slot exit configurations

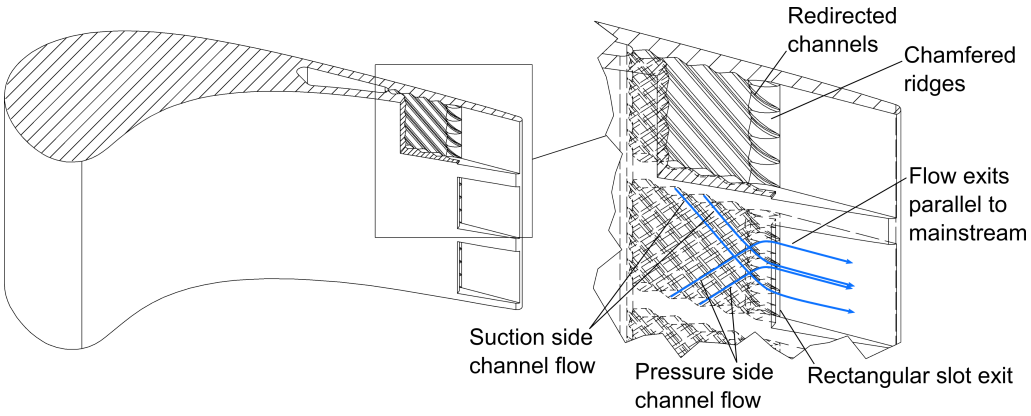


Figure 3.9: Cross corrugated slot with exit shaping

mise must be made between more effectively cooling the lands by using a exit flow angle and more effectively cooling the cutback by straightening the exit flow. Since spanwise consistency of the film is beneficial in terms of reducing thermal stresses, this compromise should be made such that the degree of straightening results in fairly even effectiveness both on or near the lands and across the slot.

3.3.5 Other potential benefits

Some other potential benefits of using the cross corrugated slot are:

- The extra pressure loss caused by the interaction between the flows in the two sets of channels and the inertial pressure loss where the flow changes directions at the bridge walls, mean that a channel with larger dimensions can be used for a particular flow rate and pressure difference when compared to a rectangular slot. This permitted increase in the passage dimensions reduces the susceptibility to blockage.

- Finally, the cross corrugated slot has a robust, smooth walled structure and lacks sharp edges along the slot. This results in a stronger ceramic core to be used for investment casting.

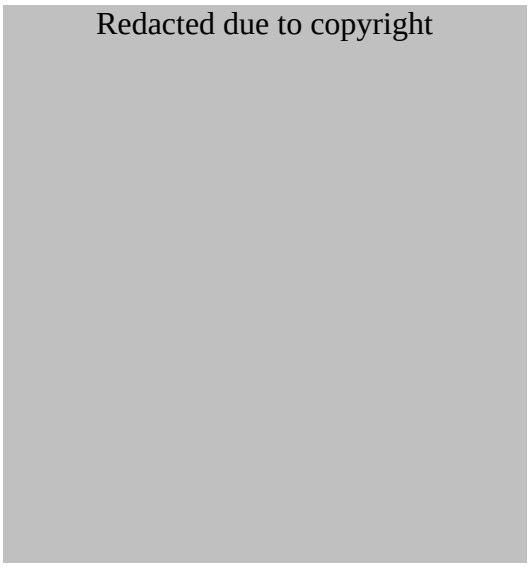
3.4 Patent

Numerous patents including lattice cooling and similar designs have been filed and some of those most similar to the cross corrugated slot design are summarised here.

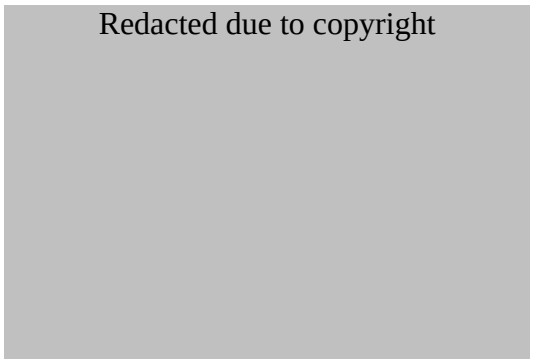
Patent US 3,819,295 (Hauser et al., 1974) describes two sets of drilled holes along the TE such that they intersect, forming a lattice with the intersecting nodes acting as turbulence promoters and area increasers for improved convective heat transfer from blade to cooling fluid (Figure 3.10a). This design is difficult to manufacture since it requires heavily inclined drilled holes. Furthermore, the design leaves large areas of uncooled metal near the hub and tip of the blade where holes cannot be drilled because they would start and end inside the blade. Such holes would be too small and fragile for casting.

Patent US 4,407,632 (Liang, 1983) describes a TE slot with an array of pedestals extending across it wherein selected pairs of pedestals are connected by a barrier wall attached to either the pressure side or suction side of the slot. The barriers extend only part of the way across the slot to trip the thermal boundary layer of cooling air flow, allowing improved heat transfer from blade to cooling fluid (Figure 3.10b). However, the sharp edges of the design may create issues with manufacturability and mechanical durability.

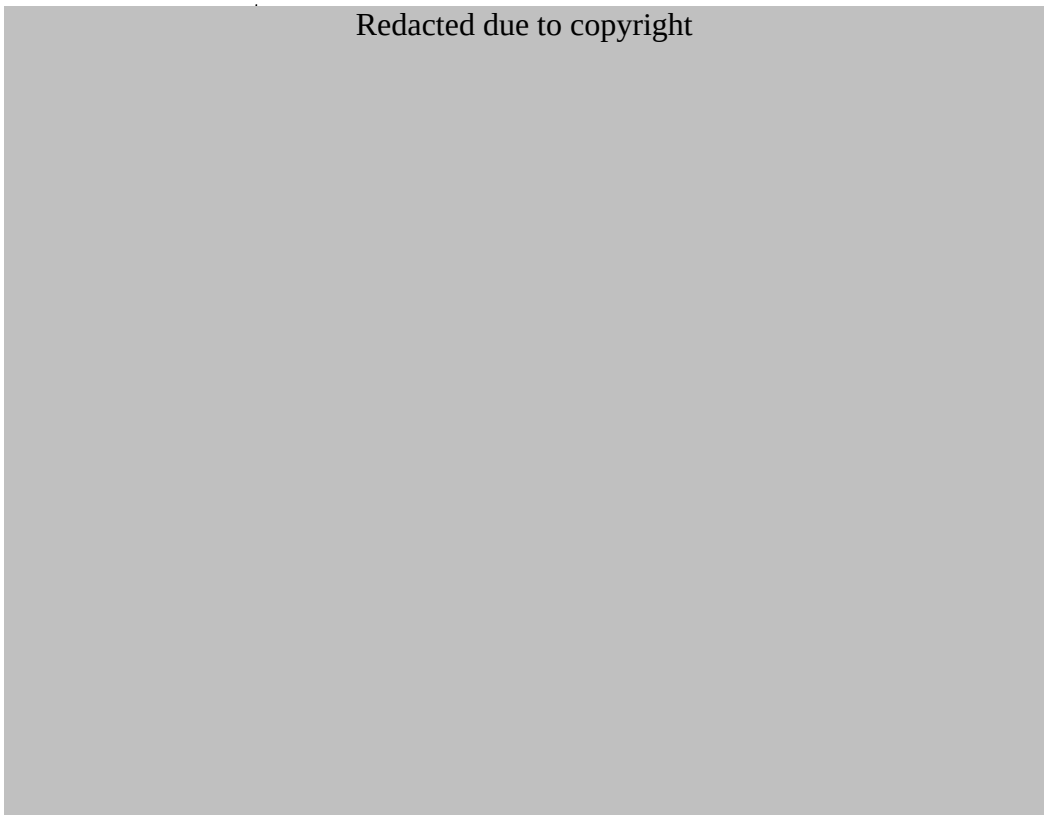
Patent WO 2005/083236A1 (Annerfeldt et al., 2005) is a derivative of lattice cooling with special geometry modifications near the TE. The internal area between the pressure surface and suction surface walls forms a passage for cooling fluid to flow through and contains two sets of ribs (Figure 3.10c, numbers 21 & 22). These ribs form a lattice just as in Figure 2.2. However, in this case, the fluid flows from the leading edge to the TE and near the TE, the two sets of ribs curve smoothly to become substantially parallel with each other. They are aligned such that they finish at an intersection (Figure 3.10c, number 26) and combine to span the entire width of the inner space, thus combining the two sets of smaller channels into one set of larger channels (Figure 3.10c, number 27'). The exit angle of these larger channels may be parallel to the axis of rotation or vary along the span of the blade. The ribs at the final intersection may be thickened to create



(a) Patent US 3,819,295



(b) Patent US 4,407,632



(c) Patent WO 2005/083236A1

Figure 3.10: Patent geometries

a flow restriction (Figure 3.10c, number 26) and additional divider ribs may be inserted near the TE to control flow area and increase surface area (Figure 3.10c, numbers 21' & 22'). This design would also have issues with manufacturability due to the rib shape and core manufacturing constraints in the limited space of the TE. It also does not have the versatility to control the coolant mass flow, pressure losses and heat transfer at specific regions of the TE of the blade or vane which arise from the addition of solid section "lands" in the cross corrugated slot design.

The cross corrugated slot design patent application was submitted in 2014 by Rolls-Royce with application number GB1422322.6 and granted in 2016 with publication number GB2533315.

3.5 Deciding on test geometries

With such a large number of parameters defining the geometry and possible variations, it was necessary to arbitrarily select specific geometric features to be tested in the current research.

It was decided that the internal design of the cross corrugated slot would be kept simple. The spanwise profile was kept consistent throughout all test geometries. The maximum internal slot height was $50\,\%$ larger than the baseline rectangular slot height and the corrugations on opposing sides were symmetrical and just touching, with a pitch such that four corrugations fit across the slot. This made it relatively straightforward to model in computer-aided design software. The dimensions of the slots are detailed in Section 5.5.

The corrugations on either side were set at the same angle from the mainstream, and only two included angles were investigated — $90°$ representing an "intermediate" flow restricting design, and $120°$ representing an "extreme" flow restricting design.

The principle aim of the present research was to investigate the effect on film cooling performance of the cross corrugated slots and how to improve it. Therefore, aside from the included angle, only the exit features of the slot were modified across the geometries,

first investigating different corrugation alignments at exit (Detailed in Section 5.6) and then five proposed exit shaping modifications (Detailed in Section 5.6).

Chapter 4

Experimental Methods

4.1 Introduction

In order to measure adiabatic film cooling effectiveness, the pressure sensitive paint technique was used. This chapter covers the specifications of the paint used and how the mass transfer analogy is applied to allow oxygen pressure measurements to be translated into film effectiveness. The limitations of PSP and a comparison with alternative measurement techniques are also discussed here.

4.2 Pressure sensitive paint

Pressure sensitive paint (PSP) contains luminophores —chemical compounds that become excited to an electronic state higher than its ground state by absorbing a specific wavelength of light in the range from $380\,\mathrm{nm}$ to $520\,\mathrm{nm}$. The excited luminophores normally return to their ground state by emitting photons with another specific wavelength in the range from $620\,\mathrm{nm}$ to $750\,\mathrm{nm}$. Alternatively, the luminophores can follow a non-radiative process to return to their ground state if they are in contact with an external molecule of oxygen. This is known as oxygen quenching as explained by Quinn et al. (2013). The intensity of the emitted light reduces with an increase in partial pressure of oxygen in contact with the painted surface. This feature can be used to measure the partial

pressure of oxygen at all points on the painted surface.

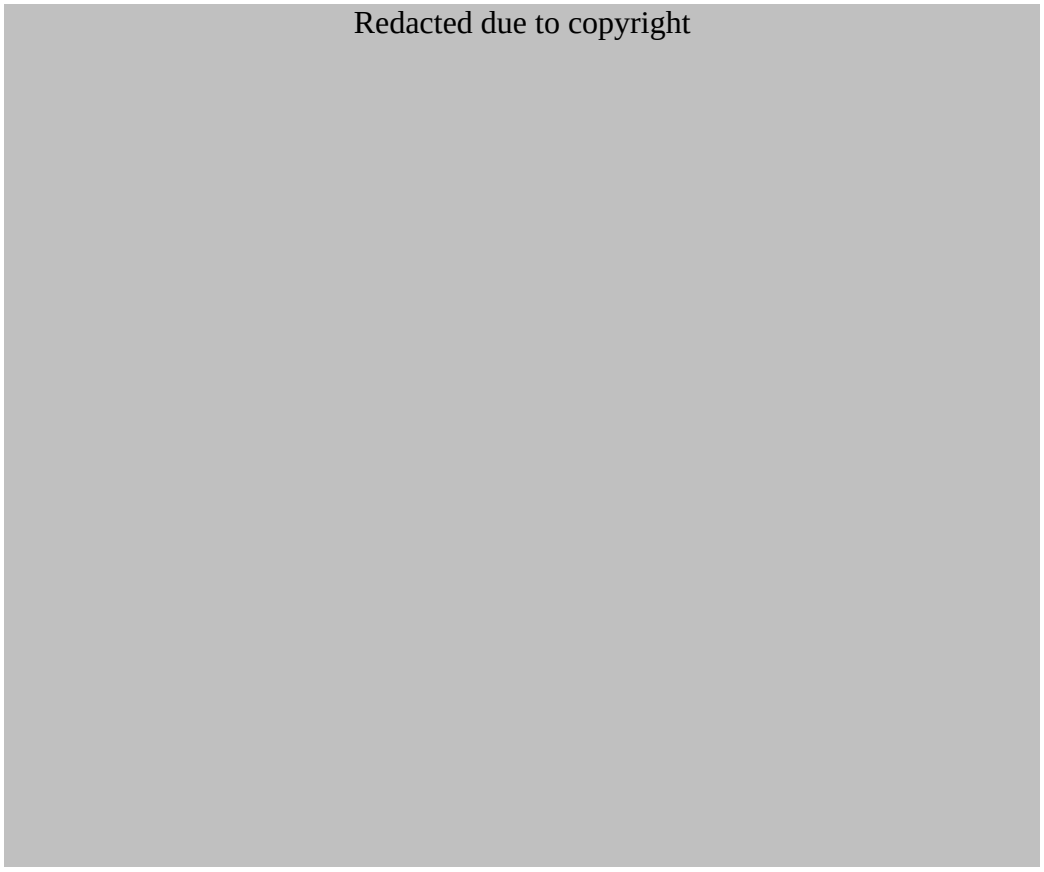


Figure 4.1: Emission spectra of UniFIB PSP (Innovative Scientific Solutions Inc., 2016)

The PSP used in the current research is called UniFIB and is manufactured by Innovative Scientific Solutions, Incorporated (ISSI) based in Dayton, Ohio, USA. UniFIB contains a blend of Fluoro / Isopropyl / Butyl polymer (FIB), platinum tetra(pentafluorophyenyl)porphine (PtTFPP) and white pigment. PtTFPP is the luminophore, the active component sensitive to oxygen. FIB is a gas-permeable polymer binder used to suspend the luminophore on the painted surface while allowing oxygen molecules to diffuse into the polymer and interact with the luminophore. When exposed to light of wavelength $400\,\mathrm{nm}$, it emits light of wavelength $620\,\mathrm{nm}$ to $750\,\mathrm{nm}$ (Figure 4.1).

The intensity of the emitted light can be recorded using a camera equipped with a red filter (Figure 4.2) at reference (wind-off or atmospheric) and test (wind-on) conditions. The intensity, I of the emitted light for each pixel at reference and test conditions can be related to the partial pressure of oxygen, $p(\mathrm{O}_2)$ on the surface at that point by the



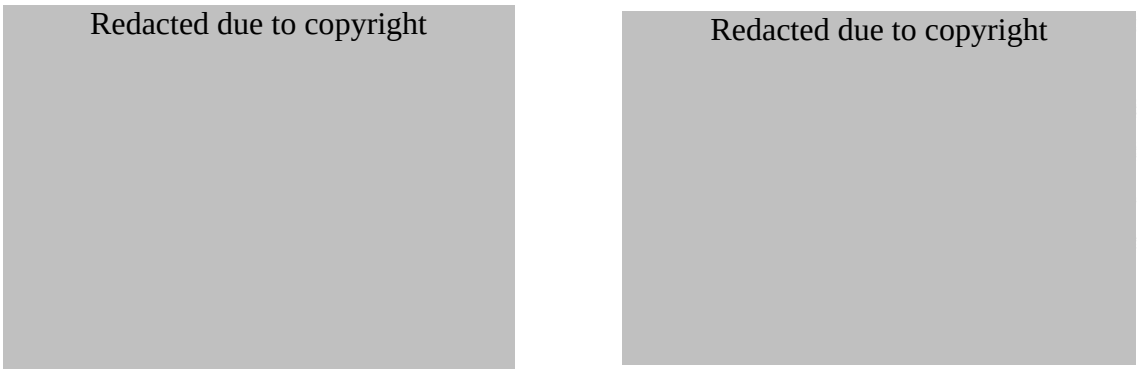
Figure 4.2: Basic PSP experimental set-up (Quinn et al., 2013)

Stern-Volmer equation (Quinn et al., 2013):

$$\frac{I_{\text{ref}}}{I} = \text{A}(T) + \text{B}(T)\frac{p(\text{O}_2)}{p(\text{O}_2)_{\text{ref}}} \tag{4.1}$$

An example of the relationship is shown in Figure 4.3a. It can be seen that the emitted light intensity varies with both the absolute partial pressure of oxygen and the temperature of the paint. The temperature sensitivity is due to thermal quenching of the luminescent molecules as well as the temperature dependent oxygen permeability within the binder. The result of this is a reduction in emitted light intensity at higher temperature under the same oxygen partial pressure. The effect of temperature can be reduced by ensuring that a reference image is taken at the same temperature as each test image, as shown in Figure 4.3b.

Air has a constant mole fraction of oxygen of $21\,\%$, so if air is used throughout an experiment, PSP allows the measurement of the absolute static pressure on any painted surface. This is an improvement over the traditional method of distributing pressure tappings connected to transducers over the surface since the pressure tappings can only provide discrete data and can miss small-scale flow features. Painting a surface with PSP effectively turns every pixel viewed by the camera into a pressure transducer, providing



(a) T_{ref} is constant at 295K (b) T_{ref} is equal to the test temperature

Figure 4.3: PSP calibration curves (Han and Rallabandi, 2010)

much higher special resolution.

Alternatively, if a foreign gas not containing oxygen is used in part of the experiment, the mole fraction of oxygen changes as the two gases mix. This allow PSP to be used for measuring film cooling effectiveness using the PSP mass transfer analogy.

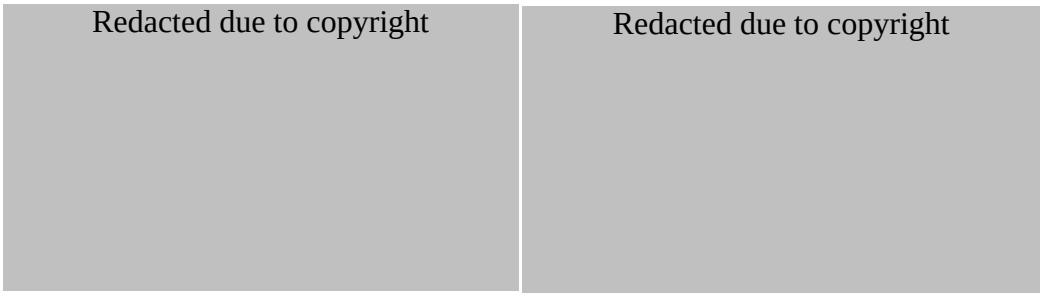
4.2.1 Limitations of pressure sensitive paint

PSP has some operational limitations (Quinn et al., 2013, Innovative Scientific Solutions Inc., 2016):

- UniFIB has a pressure sensitivity of $0.7\,\%$ intensity per kPa.
- It can operate in the pressure range $1\,\mathrm{kPa}$ to $200\,\mathrm{kPa}$.
- It is sensitive to temperature, with an error of $0.5\,\%$ per $^{\circ}\mathrm{C}$.
- It can operate in the pressure range $0\,^{\circ}\mathrm{C}$ to $50\,^{\circ}\mathrm{C}$.
- It has a response time of $300\,\mathrm{ms}$.
- When exposed to UV, the paint photo-degrades with time at a rate of $1\,\%$ per hour due to photo bleaching.
- The excitation light intensity must be constant between reference and test conditions.

- The model, lights and camera must remain in position between reference and test conditions.

4.3 PSP mass transfer analogy to determine film cooling effectiveness



(a) Heat transfer (b) Mass transfer analogy

Figure 4.4: 2D Film cooling model (Han and Rallabandi, 2010)

Han and Rallabandi (2010) provide an excellent explanation of the mass transfer analogy which this technique is based upon. Their explanation is summarised here.

Consider the case where a coolant at temperature T_{c} is ejected into a hot mainstream at temperature T_∞ as shown in Figure 4.4a. The resulting fluid temperature at any point in the film is T_{f} and the fluid temperature at the wall is T_{w}. For an adiabatic wall, this is equal to T_{aw}. The adiabatic film cooling effectiveness on the wall is defined by:

$$\eta = \frac{T_{\mathrm{aw}} - T_\infty}{T_{\mathrm{c}} - T_\infty} \tag{4.2}$$

The 2D turbulent boundary layer heat transfer equation for a homogenous fluid is (Kays, 2005):

$$G_x \frac{\partial T}{\partial x} + G_y \frac{\partial T}{\partial y} = \rho \left(\epsilon_T + \alpha\right) \frac{\partial^2 T}{\partial y^2} \tag{4.3}$$

Where G is the mass flux, α is the thermal diffusivity and ϵ_T is the turbulent thermal

diffusivity. Since the wall is adiabatic, the boundary conditions are:

$$\text{at } y = 0, \frac{\partial T}{\partial y} = 0, T = T_{\text{aw}} \tag{4.4}$$

$$\text{at } y > \delta_{\text{f}}, T = T_{\infty} \tag{4.5}$$

$$\text{at } x = 0, T = T_{\text{c}} \tag{4.6}$$

In the analogous case, the mainstream includes a specific gas with a mass fraction of C_{∞}, the coolant includes the same gas with a mass fraction of C_{c} and the mass fraction of the gas at the surface is C_{w}, as shown in Figure 4.4b. The corresponding 2D turbulent boundary layer mass transfer equation is (Han and Rallabandi, 2010):

$$G_x \frac{\partial C}{\partial x} + G_y \frac{\partial C}{\partial y} = \rho \left(\epsilon_M + \Gamma\right) \frac{\partial^2 C}{\partial y^2} \tag{4.7}$$

Where Γ is the mass diffusion coefficient and ϵ_M is the turbulent mass diffusivity. Since the wall is impenetrable, the boundary conditions are:

$$\text{at } y = 0, \frac{\partial C}{\partial y} = 0, C = C_{\text{w}} \tag{4.8}$$

$$\text{at } y > \delta_{\text{f}}, C = C_{\infty} \tag{4.9}$$

$$\text{at } x = 0, C = C_{\text{c}} \tag{4.10}$$

It can be seen that the form of Equations 4.3 and 4.7 are similar, as are their boundary conditions. Provided that the turbulent Lewis number as defined in Equation 4.11 is equal to 1, then the non-dimensionalised solutions to the two cases are identical. The work of Jones (1999) and Kays (2005) showed that this assumption holds for turbulent gaseous flow fields, which applies to most of the surface of a gas turbine blade due to the high Reynolds numbers involved. However, Han and Rallabandi (2010) showed that this does not necessarily apply to the leading edge portion of the where flow can be laminar or

intermittent.

$$Le_{\mathrm{T}} = \frac{\epsilon_T + \alpha}{\epsilon_M + \Gamma} \tag{4.11}$$

Provided that the flow fields are turbulent, then it can be shown that the adiabatic film cooling effectiveness η, at any point can be measured using mass fraction like so:

$$\eta = \frac{T_{\mathrm{aw}} - T_\infty}{T_{\mathrm{c}} - T_\infty} \approx \frac{C_{\mathrm{w}} - C_\infty}{C_{\mathrm{c}} - C_\infty} \tag{4.12}$$

If the mainstream gas used is air, the coolant gas used is pure nitrogen, and the gas being measure is oxygen, then the following substitutions for the terms in Equation 4.12 can be made:

$$\eta \approx \frac{C_{\mathrm{O_2,w}} - C_{\mathrm{O_2,air}}}{C_{\mathrm{O_2,N_2}} - C_{\mathrm{O_2,air}}} \tag{4.13}$$

Naturally, $C_{\mathrm{O_2,N_2}} = 0$. $C_{\mathrm{w}} = C_{\mathrm{O_2,w}}$ varies locally over the PSP surface, depending on the mixture of nitrogen and air at any local point. Thus, the local film cooling effectiveness at any point can be simplified as:

$$\eta \approx 1 - \frac{C_{\mathrm{O_2,w}}}{C_{\mathrm{O_2,air}}} \tag{4.14}$$

The mass fraction C of substance i can be expressed in terms of mole fraction X and molecular weight MW using the formula:

$$C_i = X_i \times \frac{\mathrm{MW}_i}{\mathrm{MW}_{\mathrm{mix}}} \tag{4.15}$$

Where $\mathrm{MW}_{\mathrm{mix}}$ is the average molecular weight of the mixture of gases, defined as:

$$\mathrm{MW}_{\mathrm{mix}} = \sum_i X_i \mathrm{MW}_i \tag{4.16}$$

The molecular weights of nitrogen and air are similar: $\mathrm{MW}_{\mathrm{N_2}} = 28.01\,\mathrm{kg\,kmol^{-1}}$, $\mathrm{MW}_{\mathrm{air}} = 28.96\,\mathrm{kg\,kmol^{-1}}$ (Howatson et al., 1991). Therefore, the mass fraction of oxygen $C_{\mathrm{O_2}}$ is approximately equal to the mole fraction of oxygen $X_{\mathrm{O_2}}$. This in turn is equal

to the ratio of the partial pressure of oxygen to the total pressure of the mixed gases $p(O_2)/p_{tot}$. Note that "total pressure" refers to the sum of each gas's partial pressure in a mixture of gases, as opposed to the sum of static pressure and dynamic pressure, which will be referred to as "stagnation pressure" to avoid confusion. Equation 4.14 becomes:

$$\eta \approx 1 - \frac{X_{O_2,w}}{X_{O_2,air}} = 1 - \frac{p(O_2)_w/p_{tot}}{p(O_2)_{air}/p_{tot}} = 1 - \frac{p(O_2)_w}{p(O_2)_{air}} \tag{4.17}$$

The numerator and denominator can then be referenced to the partial pressure of oxygen at a reference condition, leading to the final equation:

$$\eta \approx 1 - \frac{p(O_2)_w/p(O_2)_{ref}}{p(O_2)_{air}/p(O_2)_{ref}} \tag{4.18}$$

The numerator, $p(O_2)_w/p(O_2)_{ref}$, can be measured by performing the test with nitrogen as the coolant. The measured intensity under test (wind-on) conditions can form a ratio with the reference intensity at reference (wind-off) conditions and this intensity ratio can be converted to pressure ratio via the PSP calibration curve. The denominator, $p(O_2)_{air}/p(O_2)_{ref}$, can be measured by repeating the test but with air as the coolant instead. This effectively accounts for the local changes in $p(O_2)_w$ caused by the geometry and flow field rather than by the nitrogen mixing. In a low speed test, where local pressure variations are very small, and at near atmospheric conditions, $p(O_2)_{w,air}/p(O_2)_{ref}$ is close to 1.

The PSP mass transfer analogy technique has been used to measure film cooling effectiveness in many studies, including papers by Ahn et al. (2006), Caciolli et al. (2013), Mhetras et al. (2011), Yang and Hu (2012), Zhang et al. (2013) and Zhang and Jaiswal (2001).

4.3.1 Using different gases as the coolant

The use of nitrogen as the coolant simplifies the calculation of film cooling effectiveness due to its similar molecular weight to air. However, if the nitrogen coolant is at the

same temperature as the mainstream air, then the coolant to mainstream density ratio is approximately equal to one, far from the typical engine density ratio of 1.9 (Rolls-Royce, 2005). Section 2.2.3 discusses the effects of different density ratios on film cooling effectiveness.

Without cooling the coolant flow or heating the mainstream flow, the density ratio can be increased by using an alternative gas with a higher molecular weight than air as the coolant. Examples that have been used in the past include carbon dioxide (MW $= 44.01\,\mathrm{kg\,kmol^{-1}}$ (Howatson et al., 1991)) and sulphur hexafluoride (MW $= 146.06\,\mathrm{kg\,kmol^{-1}}$ (National Institute of Standards and Technology, 2016)).

If a coolant with a different density to air is used, the equations for calculating effectiveness using the mass transfer analogy become more complicated. Han and Rallabandi (2010) again provide a clear explanation of the analysis using gases with different molecular weights.

In this case, there is a mixture of the mainstream gas and the coolant gas. The mainstream gas consists entirely of air and the coolant gas consists entirely of a foreign gas that contains no oxygen, denoted with subscript "fg".

Returning to Equation 4.14 and without using an approximation for the molecular weights, effectiveness can be expressed fully in terms of mole fractions:

$$\eta \approx 1 - \frac{C_{\mathrm{O_2,w}}}{C_{\mathrm{O_2,air}}} = 1 - \frac{X_{\mathrm{O_2,w}}(\mathrm{MW_{O_2}}/\mathrm{MW_{mix}})}{X_{\mathrm{O_2,air}}(\mathrm{MW_{O_2}}/\mathrm{MW_{air}})} = 1 - \frac{X_{\mathrm{O_2,w}}\mathrm{MW_{air}}}{X_{\mathrm{O_2,air}}\mathrm{MW_{mix}}} \tag{4.19}$$

The average molecular weight of the mixture of air and foreign gas can be calculated from its constituent gases as follows:

$$\mathrm{MW_{mix}} = X_{\mathrm{air}}\mathrm{MW_{air}} + X_{\mathrm{fg}}\mathrm{MW_{fg}} \tag{4.20}$$

$$\text{where } X_{\mathrm{air}}\mathrm{MW_{air}} = X_{\mathrm{O_2}}\mathrm{MW_{O_2}} + X_{\mathrm{N_2}}\mathrm{MW_{N_2}} \tag{4.21}$$

The approximate composition of air by volume is nitrogen and oxygen in a ratio of 79 to 21 (Howatson et al., 1991) i.e. $X_{\mathrm{N_2}} = \frac{79}{21}X_{\mathrm{O_2}}$. Furthermore, the molecular weights

of nitrogen, oxygen and air are: $\mathrm{MW}_{\mathrm{N_2}} = 28.01\,\mathrm{kg\,kmol^{-1}}$, $\mathrm{MW}_{\mathrm{O_2}} = 32.00\,\mathrm{kg\,kmol^{-1}}$, $\mathrm{MW}_{\mathrm{air}} = 28.96\,\mathrm{kg\,kmol^{-1}}$ (Howatson et al., 1991). Substituting in, Equation 4.21 can be simplified to:

$$X_{\mathrm{air}} = 4.74 X_{\mathrm{O_2}} \tag{4.22}$$

In Equation 4.20, all mole fractions must add up to 1:

$$X_{\mathrm{air}} + X_{\mathrm{fg}} = 4.74 X_{\mathrm{O_2}} + X_{\mathrm{fg}} = 1 \tag{4.23}$$

$$\text{therefore } X_{\mathrm{fg}} = 1 - 4.74 X_{\mathrm{O_2}} \tag{4.24}$$

Substituting this result back in to 4.20 gives:

$$\mathrm{MW}_{\mathrm{mix}} = 4.74 X_{\mathrm{O_2}} \mathrm{MW}_{\mathrm{air}} + (1 - 4.74 X_{\mathrm{O_2}}) \mathrm{MW}_{\mathrm{fg}} \tag{4.25}$$

Which can in turn be substituted into Equation 4.19 (noting that on the surface, $X_{\mathrm{O_2}} = X_{\mathrm{O_2,w}}$):

$$\begin{aligned} \eta &= 1 - \frac{X_{\mathrm{O_2,w}} \mathrm{MW}_{\mathrm{air}}}{X_{\mathrm{O_2,air}} (4.74 X_{\mathrm{O_2,w}} \mathrm{MW}_{\mathrm{air}} + (1 - 4.74 X_{\mathrm{O_2,w}}) \mathrm{MW}_{\mathrm{fg}})} \\ &= 1 - \frac{1}{4.74 X_{\mathrm{O_2,air}} + \left(\dfrac{X_{\mathrm{O_2,air}}}{X_{\mathrm{O_2,w}}} - 4.74 X_{\mathrm{O_2,air}} \right) \dfrac{\mathrm{MW}_{\mathrm{fg}}}{\mathrm{MW}_{\mathrm{air}}}} \end{aligned} \tag{4.26}$$

From Equation 4.22, $4.74 X_{\mathrm{O_2,air}} = X_{\mathrm{air,air}}$, the mole fraction of air in air, which is obviously equal to 1. The mole fraction of oxygen $X_{\mathrm{O_2}}$ is equal to the ratio of the partial pressure of oxygen to the total pressure of the mixed gases $p(\mathrm{O_2})/p_{\mathrm{tot}}$. Finally, these can be taken referenced to the partial pressure of oxygen at a reference condition as before.

Equation 4.26 becomes:

$$\begin{aligned}\eta &= 1 - \frac{1}{1 + \left(\dfrac{p(\mathrm{O_2})_{\mathrm{air}}/p_{\mathrm{tot}}}{p(\mathrm{O_2})_{\mathrm{w}}/p_{\mathrm{tot}}} - 1\right)\dfrac{\mathrm{MW_{fg}}}{\mathrm{MW_{air}}}} \\ &= 1 - \frac{1}{1 + \left(\dfrac{p(\mathrm{O_2})_{\mathrm{air}}/p(\mathrm{O_2})_{\mathrm{ref}}}{p(\mathrm{O_2})_{\mathrm{w}}/p(\mathrm{O_2})_{\mathrm{ref}}} - 1\right)\dfrac{\mathrm{MW_{fg}}}{\mathrm{MW_{air}}}}\end{aligned} \tag{4.27}$$

As before, $p(\mathrm{O_2})_{\mathrm{w}}/p(\mathrm{O_2})_{\mathrm{ref}}$, can be measured by performing the test with the foreign gas as the coolant. The measured intensity under test (wind-on) conditions can form a ratio with the reference intensity at reference (wind-off) conditions and this intensity ratio can be converted to pressure ratio via the PSP calibration curve. $p(\mathrm{O_2})_{\mathrm{air}}/p(\mathrm{O_2})_{\mathrm{ref}}$, can be measured by repeating the test but with air as the coolant instead.

The PSP mass transfer analogy technique has been used with carbon dioxide, argon and sulphur hexafluoride by Narzary et al. (2011), Rallabandi et al. (2012) and Li et al. (2012).

4.4 Comparison with the thermochromic liquid crystals

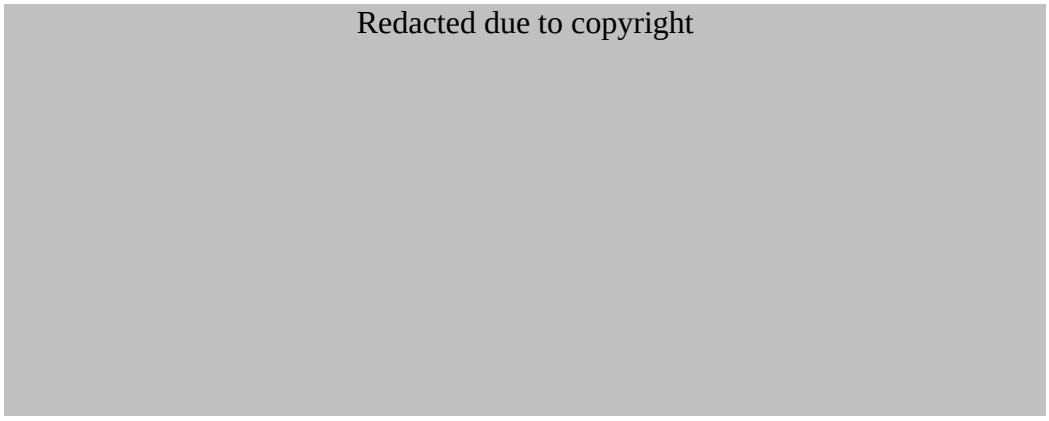


Figure 4.5: Diagram of layered TLC structure (Ireland and Jones, 2000)

Thermochromic liquid crystals (TLC) are organic compounds derived from esters of cholesterol and made up of several layers of molecules (Ekkad and Han, 2000). Within each layer, the molecules are aligned such that the direction of alignment within each

layer can be identified as the director. In the optically active phase, the director in adjacent planes is rotated through a specific angle, tracing out a helix as shown in Figure 4.5. When the TLC coating is subjected to a temperature change, the angle between the directors changes in a predictable manner, changing the pitch of the director helix. Thus, the TLC becomes optically active when the pitch is of the order of the wavelength of visible light (Ireland and Jones, 2000). This is visible as a continuous colour change across the temperature spectrum of optical activity. It is this special property of TLC that has led to it becoming the most widely used method for measuring surface temperature distributions at high resolution and high accuracy.

However, TLC have some operational limitations:

- TLC material is available to operate in temperatures from $-30\,^{\circ}\mathrm{C}$ to $115\,^{\circ}\mathrm{C}$ (Ireland and Jones, 2000).
- It can display a full scale colour change over a specified range of at least $1\,^{\circ}\mathrm{C}$ (narrow band) or at most $20\,^{\circ}\mathrm{C}$ (wide band) (Ireland et al., 1999).
- It is insensitive to pressure, with a transition shift of approximately $0.03\,^{\circ}\mathrm{C\,bar}^{-1}$ up to $133\,\mathrm{bar}$ (Bonnet, 1989).
- The optical response time is approximately $3\,\mathrm{ms}$ (Ireland and Jones, 1987).
- The established limit for heat flux across the TLC is $20\,\mathrm{kW\,m}^{-2}$ (Ireland and Jones, 2000).

In order to measure film effectiveness using TLC, the experiment is run with a mainstream flow temperature T_∞ set higher than the coolant flow temperature T_c. As shown in Figure 4.4a, this results in a wall temperature T_w which can be measured by recording the colour and intensity of the TLC painted wall. If the walls were adiabatic, then $T_\mathrm{w} = T_\mathrm{aw}$, allowing direct computation of the adiabatic film cooling effectiveness with Equation 4.2. However, since it is impossible to create a fully adiabatic wall even with very low conductivity materials, there is inevitably heat transfer between the mainstream flow, the coolant

flow and the walls of the experiment, as well as lateral conduction across the wall of interest that must be taken into account. The need to consider lateral conduction is a significant disadvantage when measuring adiabatic film cooling effectiveness since there will be abrupt changes in effectiveness across the wall that will become smoothed out by lateral conduction if not corrected. This is a difficult and complicated process and can be completely avoided by using PSP.

Caciolli et al. (2013) performed a comparative study between the PSP technique and the TLC technique for measuring film cooling effectiveness on a multi-perforated plate modelling an effusion array in a combustor liner. They identified three heat losses that had to be taken into account:

- Heat transfer due to convection between the mainstream and the effusion plate.
- Lateral conduction across the effusion plate.
- Convection between the effusion plate and the coolant, both in the annulus and inside the holes.

In order to account for heat transfer between the mainstream and the effusion plate, they used a 1D correlative procedure using previously measured HTC values. Convection between the effusion plate and the coolant, was found to be negligible as the temperature rise between the inlet and outlet of the coolant annulus was less than $1\,^{\circ}\mathrm{C}$ for all testing conditions. Lateral conduction across the effusion plate was not taken into account.

They found that although the two techniques largely agree in terms of average values, the PSP technique was able to give significantly better spatial detail and accuracy under truly adiabatic conditions, without the need for particularly complicated post-processing. This was due to the lateral conduction issue previously mentioned when using TLC.

However, they did note some disadvantages with the PSP technique when compared with the TLC technique:

- Higher cost of experiments due to the price of PSP and the required optical equipment (Scientific grade low-light camera, lens filters, Ultraviolet (UV) illumination

system).

- Foreign gas storage capacity limits the coolant mass flow.
- Limitations of the mass transfer analogy (See Section 4.3).
- Cannot be used to take heat transfer measurements.

Since this research is focused on adiabatic film cooling effectiveness measurements, PSP was used instead of TLC in order to be able to eliminate any lateral conduction issues.

Chapter 5

Experimental Set-up

5.1 Introduction

This chapter describes the experimental set-up for low speed film cooling effectiveness measurements on a simplified model of the blade trailing edge slot and details the geometries tested.

The experiments were split into four phases with the following objectives:

1. Recommend the optimal land shape for trailing edge slot film cooling.

2. Determine whether or not the novel cross corrugated slot design is suitable for slot film cooling.

3. Attempt to optimise the cross corrugated design to improve film cooling performance.

4. Determine the effects of density ratio on film cooling performance of the optimised design.

This was accomplished by using the PSP technique to measure adiabatic film cooling effectiveness on the cutback region downstream of the slots and on top of the lands for a variety of land and slot geometries. The theory behind the use of the pressure sensitive paint technique to measure film effectiveness is detailed in Section 4.2.

As this was the first use of PSP in the Osney Thermo-Fluids Laboratory, the experiment was designed to be relatively simple. It models the trailing edge pressure side slot ejection and cutback as a flat plate with tangential coolant exhaust. The dimensions of the slot are scaled up by a factor of approximately 11.5 from the Trent XWB blade design supplied by Rolls-Royce.

5.2 Initial experimental set-up

5.2.1 Experimental facility

The experiments were conducted in one of the low speed facilities of the Osney Thermo-Fluids Laboratory, University of Oxford. A large scale model of a portion of the trailing edge pressure side slot and cutback was manufactured mostly in-house by the technicians. A schematic of the rig is shown in Figure 5.1. Detailed cross-sectional plan and side views of the test section are shown in Figure 5.2.

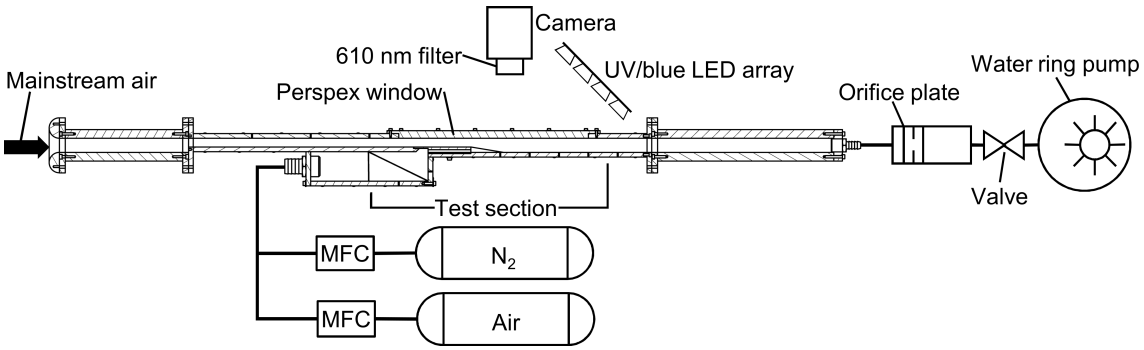


Figure 5.1: Rig schematic

The mainstream flow was ambient air drawn in through the open intake by a water ring vacuum pump. The air passed through an air filter at the intake, a flow restriction and a settling section before entering the test section. The settling section was sufficiently long to reduce the influence of the inlet restrictions on the velocity profile at the test section. Following the test section, the mixed flow entered an outlet plenum before exiting through five hoses. The hoses combined into a single long pipe with an orifice plate for mass flow measurement and a valve for total mass flow control before going to the vacuum

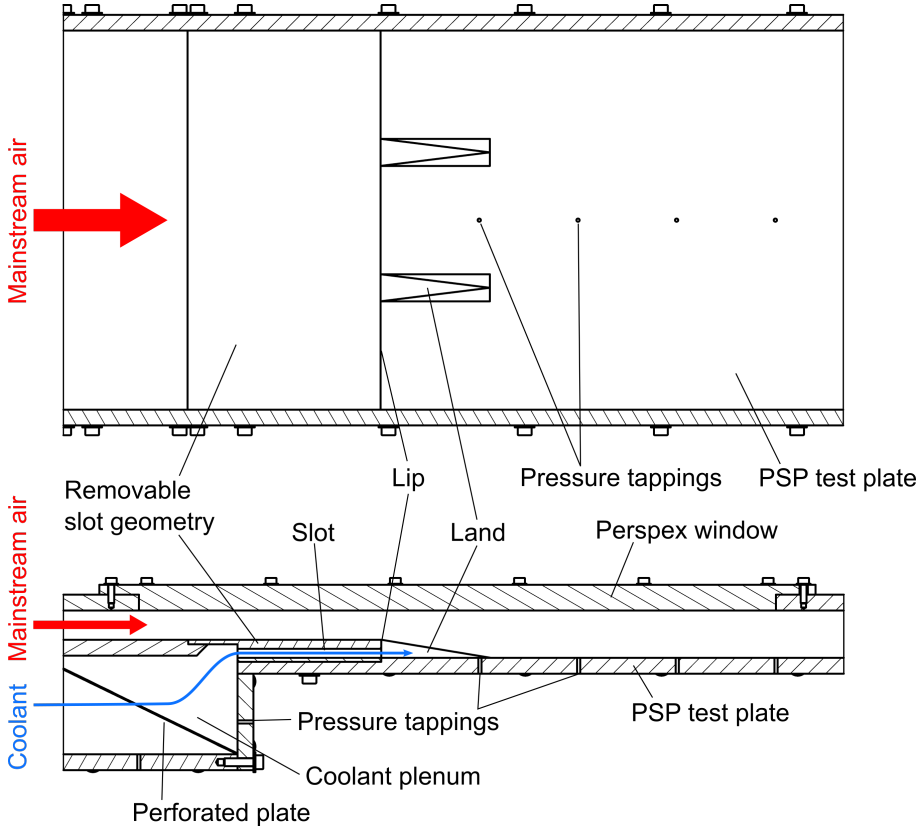
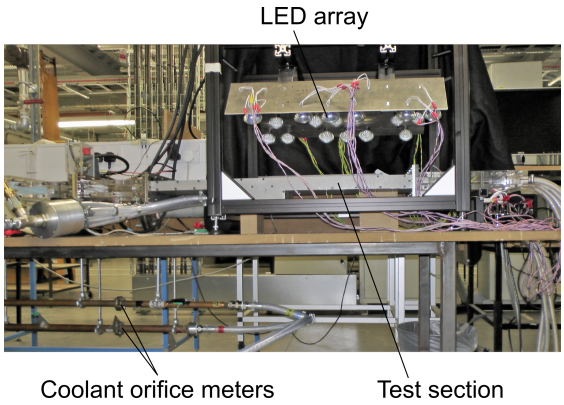


Figure 5.2: Cross-sectional views of test section

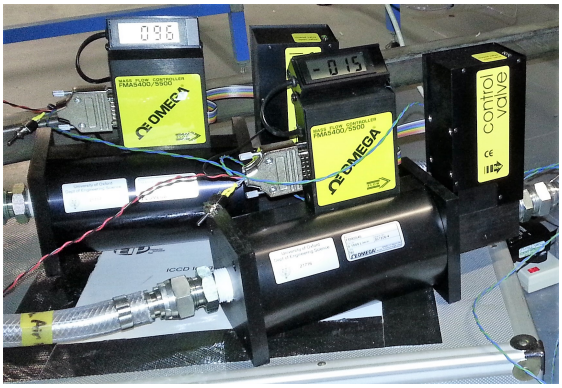
pump. The orifice plate was manufactured in accordance with ISO 5167 (ISO, 2003a,b). It used a pipe diameter D_{pipe} of $50.8\,\text{mm}$ and a hole diameter of D_{ori} $30\,\text{mm}$, with pressure tappings at one pipe diameter upstream and half a pipe diameter downstream measuring p_{ori} upstream of the orifice plate and Δp_{ori} across the orifice plate respectively.

The coolant flow was made up of a mixture of air from the $689\,\text{kPa}$ laboratory compressed air supply and nitrogen from a $20\,\text{MPa}$ compressed nitrogen bottle, both at ambient temperature. The coolant air-nitrogen ratio and flow rate were initially controlled using an orifice plate for each source, visible in Figure 5.3a. However, this was found to be difficult and time consuming to control, extending the duration of nitrogen usage in each experiment and causing significant cooling of the feed system due to the Joule-Thomson effect. These were replaced by Omega FMA5545 1000 SLM (standard litres per minute) automatic mass flow controllers (MFC) supplied by Omega Engineering Limited in Manchester, UK (Figure 5.3b) to allow for quick response, computer controlled mass flow setting. Two controllers were used, one for each source. The two streams were

mixed in a hose manifold system before entering the coolant plenum, which contained a perforated plate to dissipate the jets from the hose inlets. The coolant then passed through the slot and onto the test plate where it mixed with the mainstream flow.



(a) Dual orifice plate meters



(b) Dual mass flow controllers

Figure 5.3: Coolant mass flow control

The permanent portion of the test section was made up of stainless steel plates, laser cut by Microkerf in Leicester, UK. The removable Perspex window was positioned above the test plate and slot to allow for easy removal of the slot geometry and lands while also allowing full optical access. The test plate and lands were made from aluminium and removable to allow painting and testing of different geometries. The land length, L_{land}, was $55.4\,\text{mm}$ with a height of $9.1\,\text{mm}$ and a width, W_{land}, of $13.7\,\text{mm}$. The length was equivalent to the scaled up distance from the slot exit to the trailing edge on the real blade design. The height was equal to the sum of the slot exit height, H_{se}, and lip thickness, H_{lip}. The width was equivalent to 3 slot heights for the plain rectangular slot.

The slot geometries were manufactured by stereolithography by the Rolls-Royce rapid prototyping facility in Bristol, UK. Three slots divided by bridges and lands were included so that any lateral effects due to the boundary layers of the test section walls would not significantly affect the central slot where the measurements were taken. The slot width, W_{slot}, for all geometries was $54.9\,\text{mm}$, equivalent to 12 slot heights for the plain rectangular slot. The slot length, L_{slot}, was $72.8\,\text{mm}$, equivalent to the scaled up slot length of the real blade design. The combined slot height and lip thickness was $9.1\,\text{mm}$. The mainstream channel height was $14.9\,\text{mm}$, with a low aspect ratio to allow easy access to the

removable components inside. The slot placement and principle dimensions are shown in isometric view in Figure 5.4.

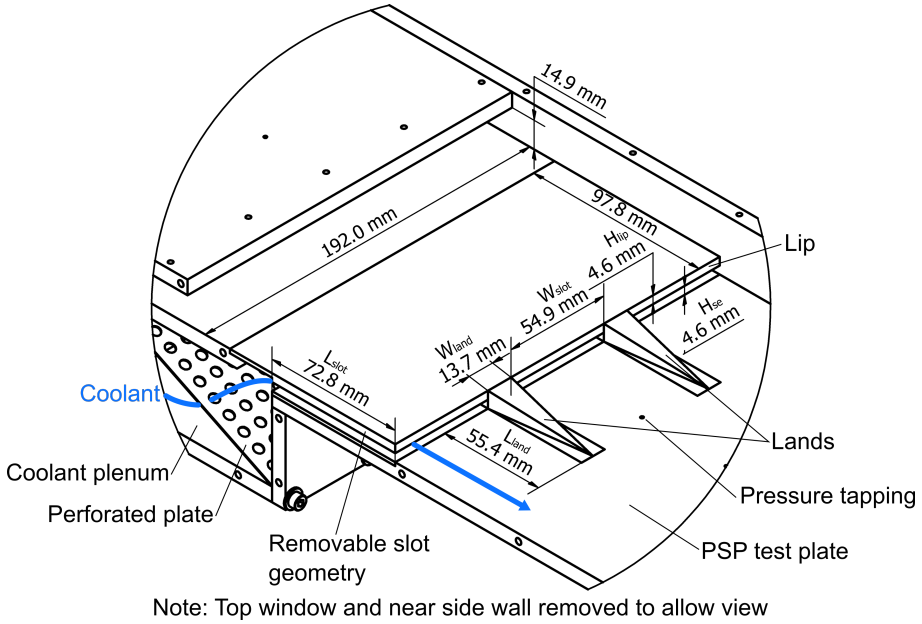


Figure 5.4: Dimensions and placement of slot geometry

5.2.2 Effectiveness measurement technique

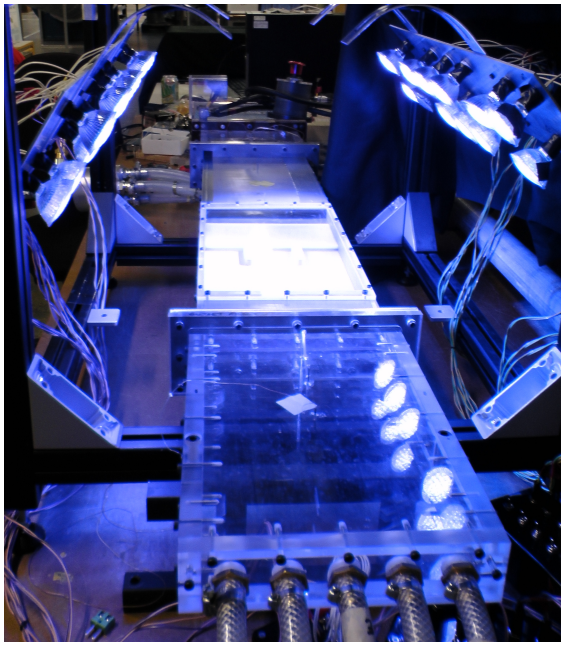
The PSP technique described in Chapter 4 was used to measure adiabatic film cooling effectiveness. The UniFIB paint used was manufactured by ISSI and supplied by Aircraft Research Association Limited based in Bedford, UK. When excited by light with wavelength in the range from $380\,\mathrm{nm}$ to $520\,\mathrm{nm}$, it emits light with wavelength in the range from $620\,\mathrm{nm}$ to $750\,\mathrm{nm}$. The intensity of the emitted light reduces with an increase in partial pressure of oxygen in contact with the painted surface. This feature can be used to measure the partial pressure of oxygen at all points on the painted surface. If the concentration of oxygen in the fluid is known, then the absolute pressure on the surface can be found. Alternatively, if two streams of fluid with different, known concentrations are used, then PSP can be used to determine the proportions of the two streams present in the mixed gas at any particular location. In the case of a film cooled surface, the adiabatic film cooling effectiveness can be calculated using the mass transfer analogy as explained in Section 4.2.

In the present research, the test plate and lands were painted with UniFIB by airbrushing and illuminated by a grid of blue LED lamps. These were Orbitec (Clichy, France) MR16 sized cluster lamps with 20 blue LEDs per lamp illuminating at a wavelength of approximately $470\,\mathrm{nm}$.

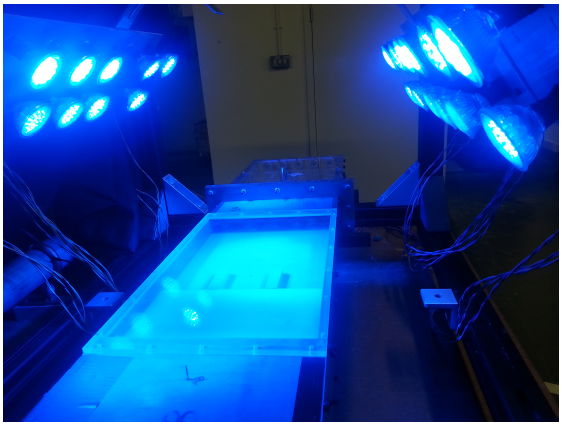
Initially, 24 blue LED lamps were used positioned on either side of the test section as shown in Figure 5.5a with the flow direction coming from far to near. This was found to create large shadows next to the lands, visible in Figure 5.5b, so instead, 12 LED lamps were positioned downstream of the slot pointing at the slot as shown in Figure 5.5c with the flow direction going from left to right. This reduced the shadows significantly as shown in Figure 5.5d.

5.2.3 Pressure loss measurements

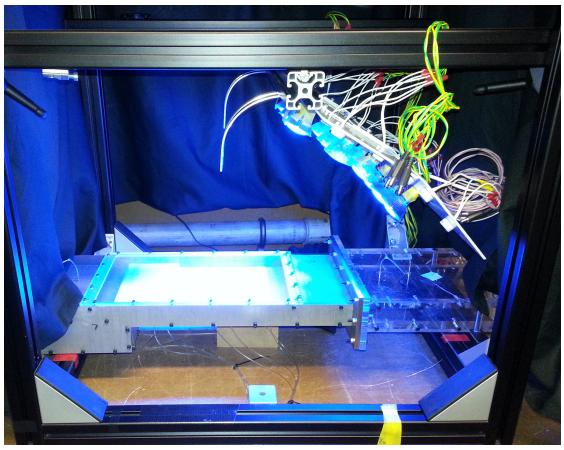
Pressure measurements were taken on both the PSP test plate surface (p_{surf}) and on the wall of the coolant plenum (p_{c}), as shown in Figure 5.2. In the coolant plenum, it was not feasible to measure directly the stagnation pressure of the coolant. However, the flow velocities within the plenum and through the slots were always well below sonic velocity, allowing the flow to be considered practically incompressible. By placing the pressure tapping within the coolant plenum and some distance from the slot entry point, it was deemed reasonable to take the measured pressure as a good approximation for the stagnation pressure of the coolant entering the slots. On the PSP test plate surface, due to the very low flow speeds, static pressure did not vary significantly with position. Thus, the precise position of the pressure tapping was not important. These measurements were used to calculate the Fanning friction factors for the various slot geometries using Equations 10.2, 10.3 and 10.5. Note that in these calculations, $D_{\mathrm{h,se}}$, L_{slot} and P_{se} were entered in and A_{se} was entered in .



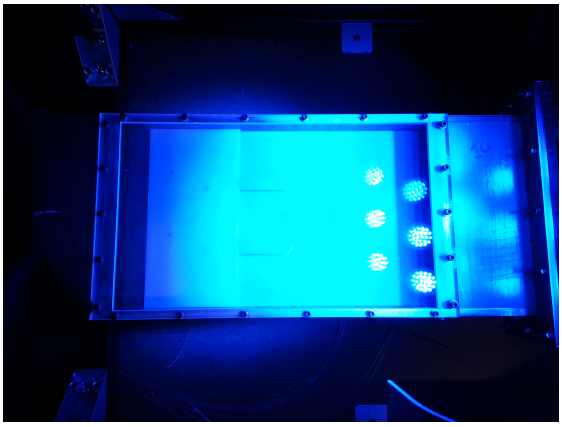
(a) Side-on LED lighting



(b) Shadows in view



(c) Downstream LED lighting



(d) Shadows reduced

Figure 5.5: LED lighting positions

5.2.4 Data acquisition

The intensity images were taken using an Allied Vision Technologies Bigeye G-283B Cool monochrome CCD camera with a Schott RG610 ($610\,\mathrm{nm}$ long pass) filter at a resolution of 1928 x 1452 pixels. The camera was supplied by Stemmer Imaging (Tongham, UK) and the filter by Edmund Optics(York, UK). The entire test section, lights and camera were surrounded by black sheets to maintain as dark an environment as possible and reduce PSP degradation over time. In order to reduce the effects of noise in the image, 30 frames were taken for every experimental condition and each pixel was averaged over the 30 frames to create the intensity images used for post processing. A dark image was also taken with the blue LEDs turned off to take into account any remaining ambient light and sensor inconsistencies. The camera interfaced with the data acquisition computer via Ethernet cable and the images were captured using MATLAB's Image Acquisition Toolbox Version 4.6 (R2013b).

All other data was captured through a modular CompactDAQ system supplied by National Instruments (NI), Newbury, UK. NI modules were held in a C series CompactDAQ chassis connected to the data acquisition computer via USB and recorded using a bespoke LabVIEW virtual instrument. Temperature measurements at the mainstream inlet, mainstream outlet, orifice meter and in the coolant plenum were taken using K-type thermocouples connected to a National Instruments (NI) 9213 thermocouple module. Pressure measurements were taken using Sensor Technics HCX series pressure transducers (Supplied by First Sensor Technics, Rugby, UK) connected to a NI 9220 voltage measurement module. In order to have a high level of accuracy in pressure measurement across a broad range of pressures, a combination of pressure transducers with different measurement ranges were used. These are listed in Table 5.1. The transducers were calibrated on-site using a Fluke 718 1G pressure calibrator for transducers with a range up to $5\,\mathrm{kPa}$ and a Fluke 718 100G pressure calibrator for transducers with higher ranges. The mass flow controllers were current controlled using a NI 9265 current output module and the mass flow rates were read using a NI 9203 current input module.

Transducer model number	Pressure range [kPa]
HCXM010D6V	0 to 1
HCXM020D6V	0 to 2
HCXM050D6V	0 to 5
HCXM100D6V	0 to 10
HCXM350D6V	0 to 35
HCXM001D6V	0 to 100

Table 5.1: Pressure transducer model numbers

5.2.5 Calibration of PSP

The PSP was calibrated in-situ by taking 11 intensity images at known partial pressures of oxygen I_{mix}, 11 corresponding reference intensity images at ambient conditions I_{ref}, and 1 dark image I_{dark}. The partial pressure was set by flushing the test section with a steady mixture of air and nitrogen at known mass flow rates. The mass flow rate was kept low, at only several $\mathrm{g\,s^{-1}}$ and maintained for a few minutes to ensure full coverage without significant local pressure variations. The absolute pressure on the painted surface $p_{\text{s,surf}}$, was measured using a static pressure tapping on the surface. The ambient pressure p_{atm}, was measured using a mercury barometer situated nearby.

Air and nitrogen have known molecular weights, $\text{MW}_{\text{air}} = 28.95\,\mathrm{kg\,kmol^{-1}}$ and $\text{MW}_{\text{N}_2} = 28.01\,\mathrm{kg\,kmol^{-1}}$ respectively. The molecular flow rate of the air and nitrogen streams at each calibration point was calculated using Equation 5.1. The streams were mixed before entering the test section and the mole fraction of oxygen in the combined air and nitrogen mixture, n_{mix}, was calculated using Equation 5.2, where the mole fraction of oxygen in the air stream $n_{\text{air}} = 20.95\,\%$. The partial pressure of oxygen on the painted surface $p(\text{O}_2)_{\text{surf}}$, was calculated by multiplying with the measured surface pressure from the pressure tappings using Equation 5.3. The partial pressure of oxygen under reference (ambient) conditions $p(\text{O}_2)_{\text{ref}}$, was simply the ambient pressure multiplied by the mole fraction of oxygen in air, Equation 5.4. The ratio of intensities was adjusted for dark as in Equation 5.5 and averaged over the entire investigated area to give 11 mean values of intensity ratio, I_{ratio}. This was then plotted against the ratio of the two partial pressures,

$p(O_2)_{surf}/p(O_2)_{ref}$ to create a mean calibration curve using a cubic fit as shown in Figure 5.6. A cubic fit was chosen following the procedure used by Han and Rallabandi (2010). This was able to conform fairly well to the steeper gradient at low pressure ratio but close to the pressure ratio of 1, it can be seen that the cubic fit line unexpectedly curves upwards when it should be fairly straight passing through 1. This may have been due to the blue LED lighting being insufficiently distinct from the emission spectrum of the PSP. The lighting setup is changed in Section 5.4 and this issue is improved somewhat.

$$\dot{M} = \frac{\dot{m}}{MW} \tag{5.1}$$

$$n_{mix} = n_{air} \times \frac{\dot{M}_{air}}{\dot{M}_{air} + \dot{M}_{N_2}} \tag{5.2}$$

$$p(O_2)_{surf} = n_{mix} \times p_{s,surf} \tag{5.3}$$

$$p(O_2)_{ref} = n_{air} \times p_{atm} \tag{5.4}$$

$$I_{ratio} = \frac{I_{ref} - I_{dark}}{I_{mix} - I_{dark}} \tag{5.5}$$

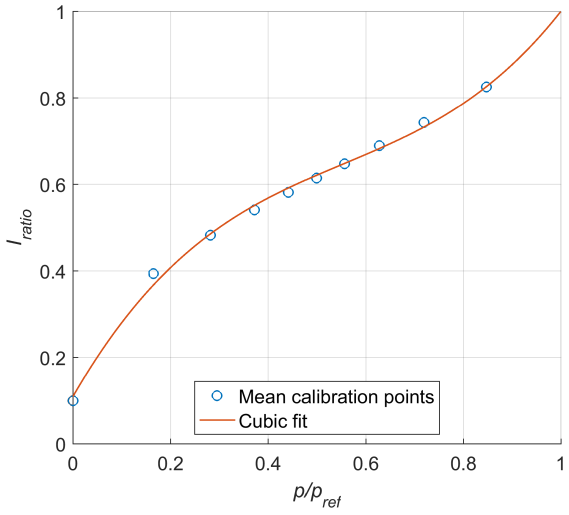


Figure 5.6: Full image mean calibration curve

The test section was flushed with air in between taking each calibration point to return the surface to ambient conditions. During each test phase, the test section was also flushed with air in order to account for local pressure fluctuations. Therefore it is unlikely that

there was any hysteresis effect with the PSP.

5.2.6 Calculating effectiveness

The film cooling effectiveness measurements were taken by running the experiment twice for each geometry at each blowing ratio. Once using nitrogen as the coolant, and once using air as the coolant. Intensity images were taken at each condition just as in the calibration and converted to values of $p(O_2)_{surf}/p(O_2)_{ref}$ for each pixel with nitrogen and with air as the coolant. This was related to film effectiveness by Equation 5.6 where the coolant gas has a similar molecular weight as air.

$$\eta \approx 1 - \frac{p(O_2)_{surf,N_2}/p(O_2)_{ref}}{p(O_2)_{surf,air}/p(O_2)_{ref}} \tag{5.6}$$

The second run with air as the coolant is necessary in order to account for the local changes in $p(O_2)_{surf}$ caused by the geometry and flow field rather than by nitrogen mixing. In a low speed test like this, where local pressure variations are very small, $p(O_2)_{surf,air}/p(O_2)_{ref}$ is close to 1.

Image processing and data post processing was performed using MATLAB scripts written specifically for this series of experiments using the equations from Section 4.3. The versions of MATLAB used for processing data were R2013b, R2016a and R2017a.

5.2.7 Operating conditions

The total exit flow including both mainstream and coolant gas, $\dot{m}_{tot}$, was set at $31\,\mathrm{g\,s^{-1}}$ and the blowing ratio was set by adjusting the mass flow ratio between the mainstream and coolant streams using the mass flow controllers. Mainstream air was at ambient conditions of approximately $293\,\mathrm{K}$, $101\,\mathrm{kPa}$, with a mean flow velocity in the range from $6.6\,\mathrm{m\,s^{-1}}$ to $7.8\,\mathrm{m\,s^{-1}}$ (calculated from the measured mainstream mass flow rate, density and area). Coolant gas was also at ambient temperature, giving a density ratio of approximately 1. The coolant stream velocity varied from $4.8\,\mathrm{m\,s^{-1}}$ to $9.5\,\mathrm{m\,s^{-1}}$ depending on the blowing

ratio. The Reynolds number of the coolant stream Re_c, based on the slot height, varied from 1400 to 2750. Blowing ratio M, was defined as in Equation 5.7 and in this study varied from 0.6 to 1.4 in increments of 0.2. The target mass flow rates, velocities and Re_c values are presented in Table 5.2. The momentum flux ratios were also calculated as defined in 2.2 and included.

$$M = \frac{\rho_c u_c}{\rho_m u_m} = \frac{\dot{m}_c A_{m,inlet}}{\dot{m}_m A_{slot}} \tag{5.7}$$

Due to the complex flow within the cross corrugated slots resulting in an exit flow that is neither parallel to the mainstream or to the corrugation channels, it was difficult to estimate the true coolant flow velocity as it leaves the slot. Since the key purpose of the cross corrugated design is to control mass flow while maintaining film cooling effectiveness, the slot area of G0 was used so that the mass flow ratio is the same for all geometries at each value of M. The hydraulic diameter and slot area of G0 were also used for all geometries in the pressure loss calculations.

M	J	$\dot{m}_c$ [$g\,s^{-1}$]	$\dot{m}_m$ [$g\,s^{-1}$]	$\dot{m}_{tot}$ [$g\,s^{-1}$]	u_c [$m\,s^{-1}$]	u_m [$m\,s^{-1}$]	Re_c	Re_{se}
0.6	0.37	4.2	26.8	31.0	4.8	7.8	1394	2574
0.8	0.66	5.4	25.6	31.0	6.1	7.4	1778	3282
1.0	1.03	6.5	24.5	31.0	7.3	7.1	2130	3931
1.2	1.49	7.5	23.5	31.0	8.5	6.8	2453	4528
1.4	2.02	8.4	22.6	31.0	9.5	6.6	2752	5080

Table 5.2: Target operating conditions

5.2.8 Uncertainties

PSP lighting and paint degradation

To ensure as consistent lighting as possible, the position and intensity of the lighting was not changed throughout the calibration and tests. The camera aperture and exposure was set such that the majority of the sensor's intensity range was used without causing saturation at any local point. Maximum local intensity was over $90\,\%$ and maximum

mean intensity was over $60\,\%$ for zero p/p_{ref}. Calibration showed a maximum deviation of recorded data from the cubic fit curve to be less than $3\,\%$.

PSP degrades under UV light, so the painted parts were kept in darkness at all times except when in use. Due to this degradation over time, the emission intensity reduces and the calibration may drift over time. An attempt to re-calibrate a part with 3-month old paint showed a deviation of recorded data from the cubic fit curve of $15\,\%$. In order to check that the calibration curve did not shift significantly between tests, a re-calibration was conducted every 10 days. Following the procedure of Han and Rallabandi (2010), the parts were also repainted if the paint was older than 1 month.

PSP temperature sensitivity

In order to take into account temperature effects on the response of the PSP, a gas thermocouple was used to measure the coolant temperature just before entry into the slot. Han and Rallabandi (2010) showed that the temperature effects could be reduced by ensuring that a reference image is taken at the same temperature as each test image during calibration and during the experiments. By monitoring the coolant temperature and taking a separate reference image immediately after each test image, the temperature effects were minimised for the current study.

Uncertainty analysis

Calibration pressure ratio, calibration intensity ratio, film effectiveness, blowing ratio and pressure drop uncertainties were quantified following the perturbation method of Moffat (1988). According to this method, a result R is calculated from a set of measurements represented by S_j:

$$R(S_1, S_2, S_3, \ldots, S_N) \tag{5.8}$$

If δS_j is the uncertainty in any particular measurement, then the uncertainty in the

result due to only that one measurement, known as the sensitivity coefficient, is:

$$\delta R_{S_j} = \frac{\delta R}{\delta S_j}\delta S_j \tag{5.9}$$

Therefore, the uncertainties caused by all of the measurements used in the calculation of R can be combined by a root-sum-square method:

$$\delta R = \left\{ \sum_{j=1}^{N} \left(\frac{\delta R}{\delta S_j}\delta S_j \right)^2 \right\}^{1/2} \tag{5.10}$$

In the current study, the results and their respective measurements were:

$$M(D_{\text{ori}}, D_{\text{pipe}}, H_{\text{se}}, W_{\text{se}}, H_{\text{m}}, W_{\text{m}}, p_{\text{atm}}, p_{\text{ori}}, \Delta p_{\text{ori}}, T_{\text{ori}}, \dot{m}_{\text{c}}) \tag{5.11}$$

$$\eta(I_{\text{ratio}}) \tag{5.12}$$

$$f(H_{\text{se}}, W_{\text{se}}, L_{\text{slot}}, p_{\text{atm}}, p_{\text{c}}, p_{surf}, T_{\text{c}}, \dot{m}_{\text{c}}) \tag{5.13}$$

Applying the perturbation method to the calibration p/p_{ref} at a nominal value of 0.496 resulted in an uncertainty of $6.16\,\%$. This calculation is shown in Table 5.3. The uncertainty in I_{ratio} was calculated by taking the images corresponding to the nominal p/p_{ref} value, computing the intensity ratio using Equation 5.5 and calculating the standard deviation across all pixels in the sample image. This was found to be 0.0071 for the nominal $I_{\text{ratio}} = 0.631$.

The uncertainty for blowing ratio M was calculated using a nominal value of 0.97 resulting in an uncertainty of $8.51\,\%$. This calculation is shown in Table 5.4.

For effectiveness η, the uncertainty varies, with the greatest uncertainty at lower effectiveness when the difference in intensity between the reference and test images is smaller. Therefore, uncertainty was calculated for a low effectiveness value of 0.081 and a high effectiveness value of 0.919 by taking sample images at each nominal effectiveness value, computing the intensity ratio using Equation 5.5 and calculating the standard deviation

across all pixels in the sample image. The standard deviation was then used as the measurement uncertainty for the intensity ratio for the perturbation method. This resulted in an uncertainty of $11.29\,\%$ at $\eta = 0.081$ and an uncertainty of $0.27\,\%$ at $\eta = 0.919$. These calculations are shown in Tables 5.5 and 5.6.

The uncertainty for Fanning friction factor was calculated for a nominal value of 0.431 resulting in an uncertainty of $15.19\,\%$. This calculation is shown in Table 5.7.

Nominal p/p_{ref}	0.496			
Measurement	Nominal value	Measurement uncertainty	Sensitivity coefficient	Normalised by nominal p/p_{ref}
p_{atm}	$101\,890$	100	0.0000	$0.00\,\%$
$p_{\text{surf,gauge}}$	954	$0.35\,\%$	0.0000	$0.00\,\%$
$\dot{m}_{\text{N}_2}$	$0.004\,97$	$2\,\%$	0.0212	$4.28\,\%$
$\dot{m}_{\text{air}}$	$0.004\,95$	$2\,\%$	0.0220	$4.44\,\%$
			p/p_{ref} uncertainty (absolute)	0.031
			p/p_{ref} uncertainty	$6.16\,\%$

Table 5.3: Uncertainty in p/p_{ref} evaluated at 0.496

Nominal M	0.969			
Measurement	Nominal value	Measurement uncertainty	Sensitivity coefficient	Normalised by nominal M
D_{ori}	30	0.1	0.0093	$0.96\,\%$
D_{pipe}	50.8	0.1	0.0007	$0.07\,\%$
H_{se}	4.571	0.1	0.0212	$2.19\,\%$
W_{se}	54.857	0.1	0.0018	$0.18\,\%$
H_{m}	14.857	0.1	0.0065	$0.67\,\%$
W_{m}	192	0.1	0.0005	$0.05\,\%$
p_{atm}	$102\,320$	100	0.0001	$0.01\,\%$
$p_{\text{ori,gauge}}$	-9843	$0.0412\,\%$	0.0000	$0.00\,\%$
Δp_{ori}	2090	$0.0369\,\%$	0.0002	$0.02\,\%$
T_{ori}	290.8	1	0.0020	$0.21\,\%$
$\dot{m}_{\text{c}}$	$0.006\,43$	$2\,\%$	0.0789	$8.14\,\%$
			M uncertainty (absolute)	0.083
			M uncertainty	$8.51\,\%$

Table 5.4: Uncertainty in blowing ratio evaluated at $M = 0.969$

Nominal η	0.081			
Measurement	Nominal value	Measurement uncertainty	Sensitivity coefficient	Normalised by nominal η
I_{ratio}	0.8979	0.0102	0.0091	$11.29\,\%$
			η uncertainty (absolute)	0.0091
			η uncertainty	$11.29\,\%$

Table 5.5: Uncertainty in effectiveness evaluated at $\eta = 0.081$

Nominal η	0.919			
Measurement	Nominal value	Measurement uncertainty	Sensitivity coefficient	Normalised by nominal η
I_{ratio}	0.2519	0.0039	0.0025	$0.27\,\%$
			η uncertainty (absolute)	0.0025
			η uncertainty	$0.27\,\%$

Table 5.6: Uncertainty in effectiveness evaluated at $\eta = 0.919$

Nominal f	0.431			
Measurement	Nominal value	Measurement uncertainty	Sensitivity coefficient	Normalised by nominal f
H_{se}	4.571	0.1	0.0276	$6.39\,\%$
W_{se}	54.857	0.1	0.0016	$0.38\,\%$
L_{slot}	72.811	0.1	0.0006	$0.15\,\%$
p_{atm}	$101\,480$	100	0.0004	$0.10\,\%$
$p_{\text{c,gauge}}$	-183.98	$0.35\,\%$	0.0006	$0.15\,\%$
$p_{surf,\text{gauge}}$	-621.78	$0.35\,\%$	0.0021	$0.49\,\%$
T_{c}	292.6	1	0.0015	$0.34\,\%$
$\dot{m}_{\text{c}}$	$0.006\,32$	$2\,\%$	0.0593	$13.76\,\%$
			f uncertainty (absolute)	0.066
			f uncertainty	$15.19\,\%$

Table 5.7: Uncertainty in Fanning friction factor evaluated at $f = 0.431$

5.2.9 Limitations

The density ratio used in the current study was different to a typical real engine density ratio of 1.9. However, relative effectiveness comparisons between the different geometries in the current study as well as other studies conducted at similar density ratios is still possible and the data forms a basis for co-validation with numerical simulations.

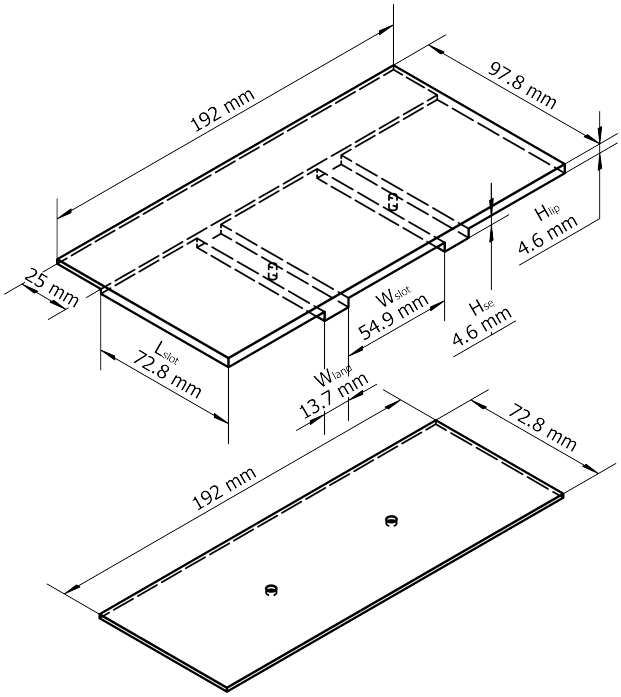
The low height of the mainstream channel at 3.25 slot heights potentially causes suppression of the vortex shedding from the slot lip, while the lack of an accelerating mainstream flow as in a full turbine blade will also have an effect on coolant mixing. This limits the direct applicability of the effectiveness measurements taken in this study to a real blade model. However, by comparing to the baseline plain slot geometry, it is still possible to make back-to-back comparisons and judge the suitability of each design when applied to trailing edge cooling designs, reducing the number of geometries that must be tested in a more expensive and more complicated high speed facility.

5.3 Phase 1 geometries

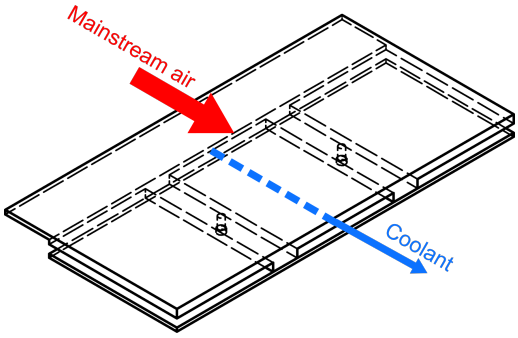
The objective of the first set of experiments was to measure the effect of land shapes on film cooling effectiveness, both on the cutback surface after the slot and on top of the lands themselves. To allow back-to-back comparisons between the land shapes, the slot geometry was kept constant, using a plain rectangular slot with no internal obstructions.

The top and bottom plates for the slot geometry are shown in Figure 5.7a with principle dimensions labelled. These were placed one on top of the other and screwed into place to form the three rectangular slots and two bridges, show in Figure 5.7b. Photographs of the topside of the bottom plate and the underside of the top plate are shown in Figures 5.7c and 5.7d respectively.

The six land geometries tested were denoted L1–6 and are shown in Figure 5.8. The "no lands" configuration, L1, was just a $2\,\mathrm{mm}$ base plate which lied flush with the test plate surface. The other five geometries, L2–6, all had the same height, width and length



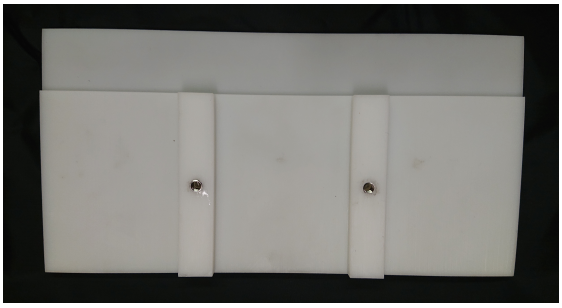
(a) Top and bottom plates A, rectangular slot



(b) Combined rectangular slot



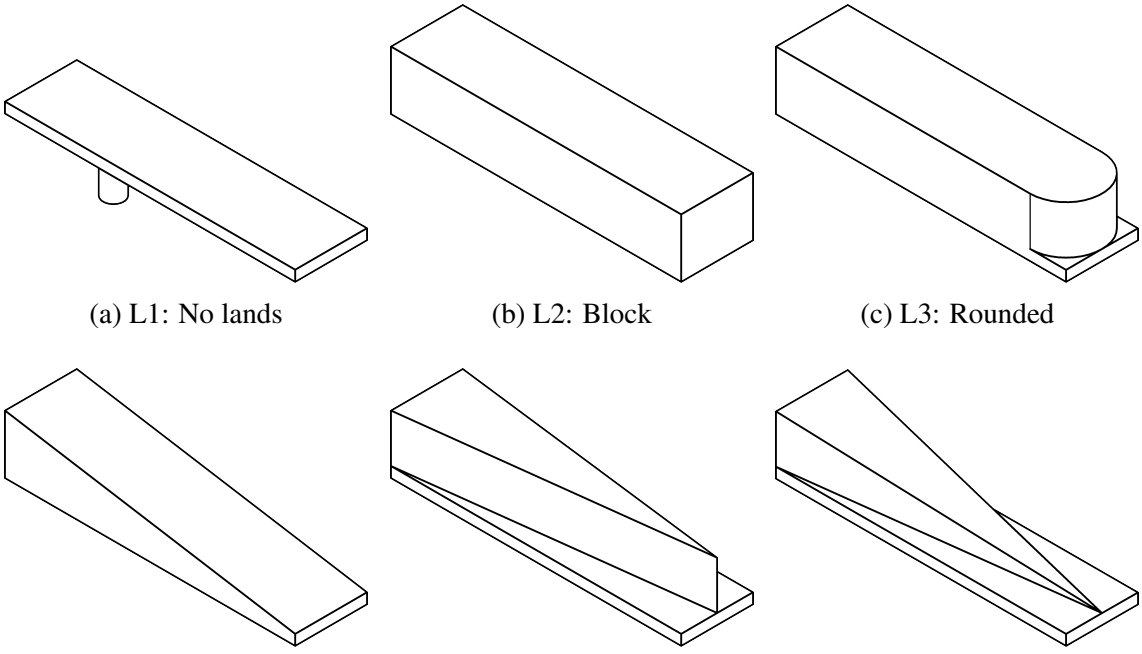
(c) Bottom plate A, rectangular slot



(d) Top plate A, rectangular slot

Figure 5.7: Plain rectangular slot geometry

of $9.1\,\mathrm{mm}$, $13.7\,\mathrm{mm}$ and $55.4\,\mathrm{mm}$ respectively. The land width and length were equivalent to 3 and 12.1 slot heights respectively for the plain rectangular slot. The block lands, L2, represent the most basic rectangular land design. The rounded lands, L3, have a semicircular end profile. The tapered lands, L4, have rectangular profile with a constant gradient ramp down from the upper edge of the lip to the cutback surface. The diffuser lands, L5, have an isosceles triangle shaped profile, allowing a gradual expansion of the cutback width. The tapered diffuser lands, L6, combine the ramp down of L4 and the isosceles shape of L5.



(a) L1: No lands (b) L2: Block (c) L3: Rounded

(d) L4: Tapered (e) L5: Diffuser (f) L6: Tapered diffuser

Figure 5.8: Phase 1 land geometries

5.4 Modifications to set-up

After the completion of phase 1, the experimental set-up was modified as follows:

The Perspex window was replaced due to the accumulation of scratches on the surface over time which are visible in the results in chapter 6.

The PSP test plate which previously formed part of the test section outer structure required dismantling the test section to remove and repaint. This was replaced with a permanent plate which formed part of the test section outer structure and a smaller removable plate placed flush on the surface. The permanent plate was unpainted and the smaller plate could be easily removed by hand through the window for painting. This new layout is shown in Figure 5.9. Figure 5.10 shows the dimensions and placement of the cross corrugated slots in the updated experimental set-up. A new dimension, H_{si}, is defined here as the maximum slot internal height.

The blue LED lamps were replaced by a grid of eight $5\,\text{W}$ UV LEDs emitting light at a wavelength of approximately $400\,\text{nm}$, shown in Figure 5.11. This was done to increase the intensity and uniformity of the incident light on the PSP in a narrower wavelength

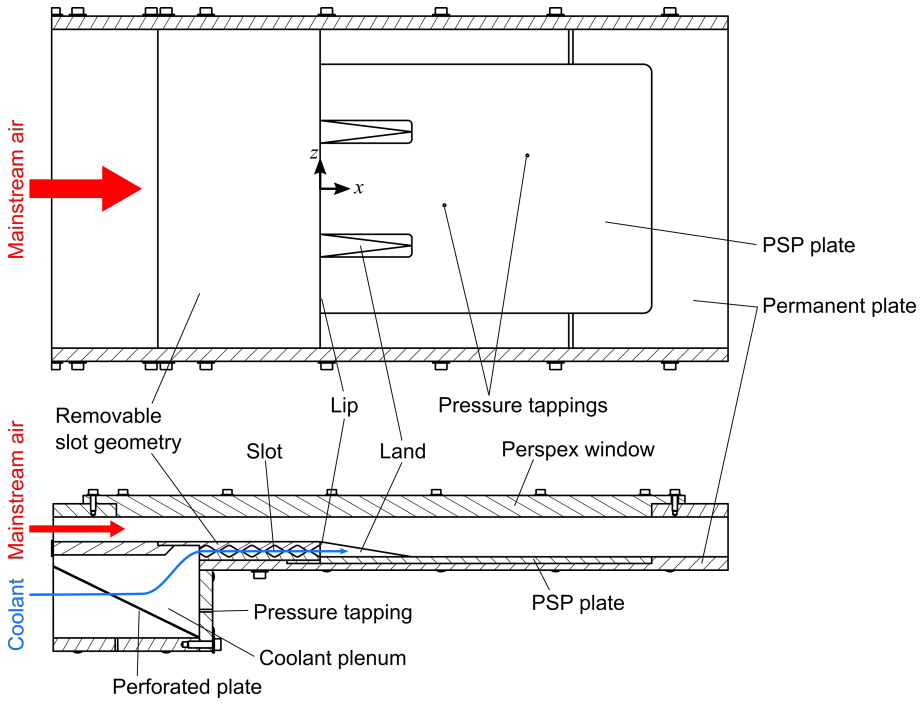


Figure 5.9: Cross-sectional views of phase 2 test section

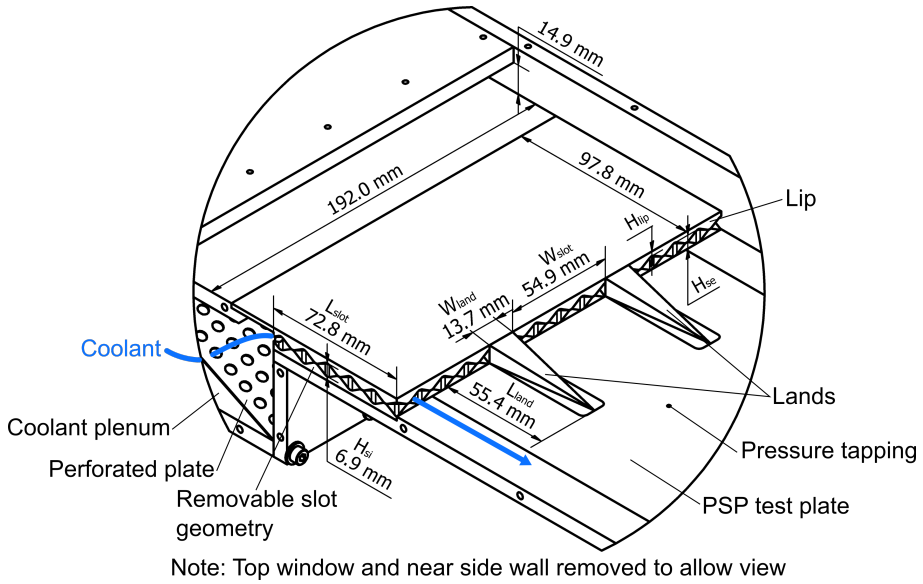


Figure 5.10: Dimensions and placement of cross corrugated slot geometry

range. This was expected to increase the emission intensity and reduce the effect of noise and background light in the image. Since the UV LEDs emit light at a wavelength on the edge of the visible spectrum, this had the added benefit of making the red light emission clearly visible to the human eye. This is shown by the photos in Figure 5.12 where Figure 5.12a shows the test section without coolant flow and Figure 5.12b shows the test section with nitrogen coolant flow. Both photos were captured using a standard digital camera. Bright streaks of coolant are clearly visible on the PSP plate with nitrogen coolant flowing.

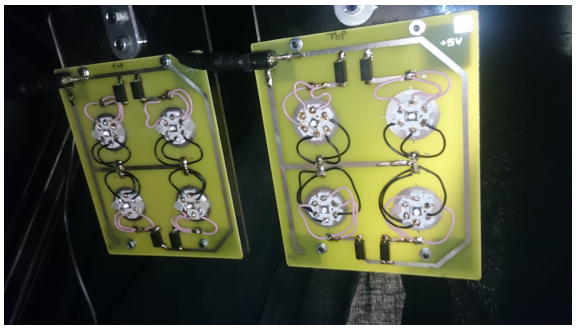
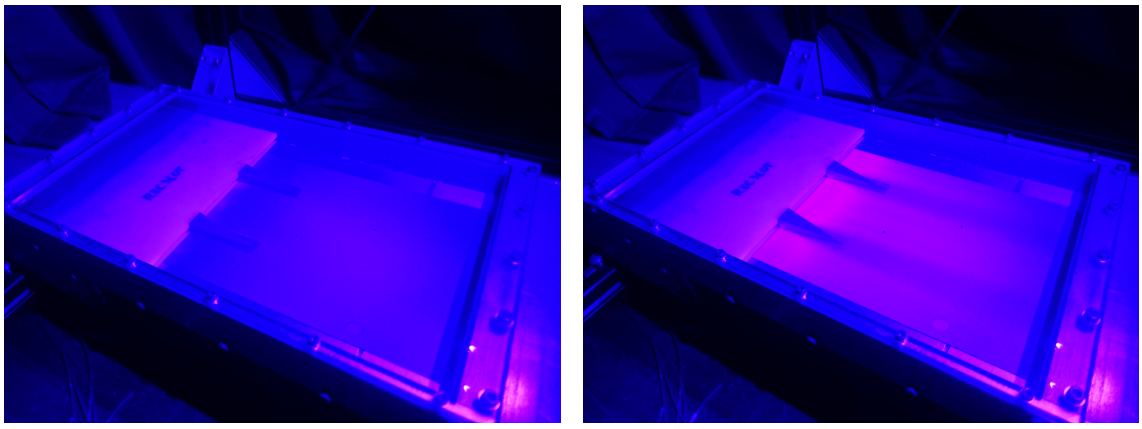


Figure 5.11: UV LED array



(a) Without coolant (b) With nitrogen coolant

Figure 5.12: Test section under UV light

The calibration procedure was changed to include 15 calibration points instead of 11, with a more even distribution and more points at low $p(O_2)_{surf}/p(O_2)_{ref}$ in order to increase the resolution of the calibration curve, especially at higher effectiveness levels that correspond with low $p(O_2)_{surf}/p(O_2)_{ref}$. The calibration curve fit method was also changed from cubic to smoothing spline fit as this was able to better conform to the

calibration points. Finally, since the calibration was shown to be insensitive to whether the whole image or a sample was used, a 200 pixels square sample next to the pressure tapping was used to reduce processing time. An example of a calibration curve used in phase 2 is shown in Figure 5.13.

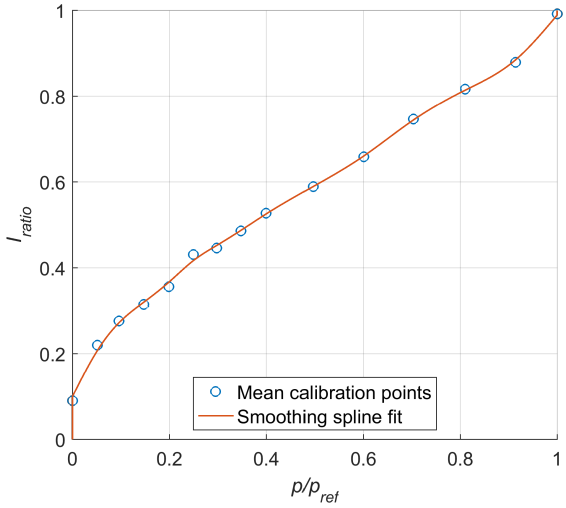
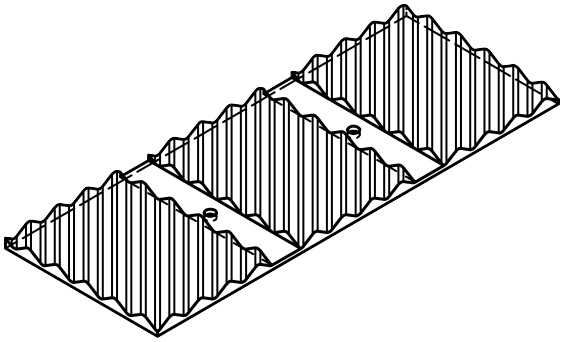


Figure 5.13: 200 pixels square sample mean calibration curve

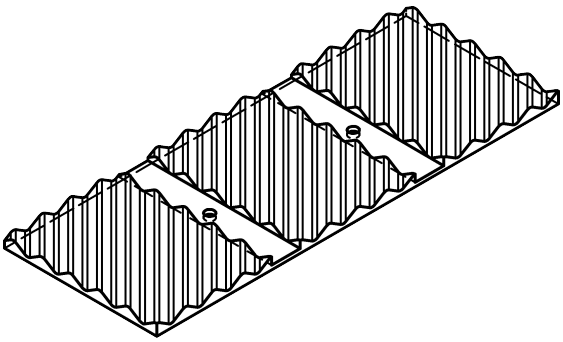
5.5 Phase 2 geometries

The objective of the second set of experiments was to measure the effect of cross corrugated slots on film cooling effectiveness, both on the cutback surface after the slot and on top of the lands. To allow back-to-back comparisons between the geometries, the land shape was kept constant, using the tapered diffuser land used in phase 1 and shown in Figure 5.8f. The baseline slot geometry was the plain rectangular slot as used in phase 1 and shown in Figure 5.7. This geometry was denoted as G0 and re-tested since the experimental set-up was modified.

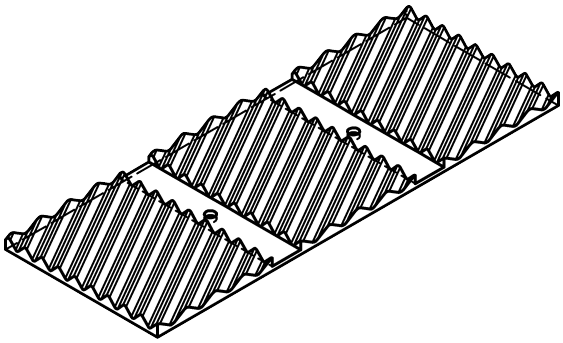
The cross corrugated geometries comprised eight pairings of top and bottom plates, all with the same spanwise corrugation profile. These plates are shown in Figure 5.14 and the pairings are tabulated in Table 5.8. Four pairs, denoted as G1–4, used an included angle of 90° with different exit alignments. Figure 5.15 shows a view of each alignment looking upstream at the slot exit with the coolant exit filled in blue. Four more pairs,



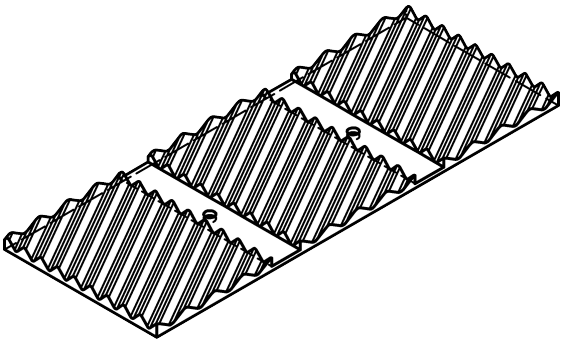
(a) Bottom plate B, $\theta_{cc} = 90°$



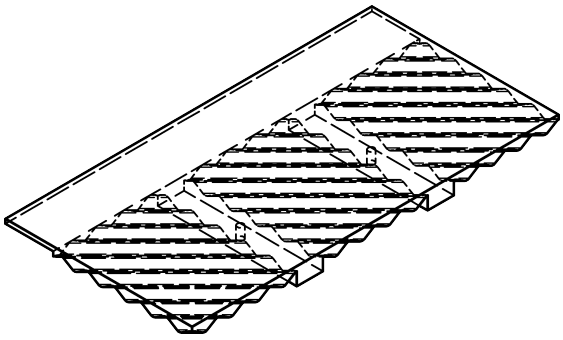
(b) Bottom plate C, $\theta_{cc} = 90°$



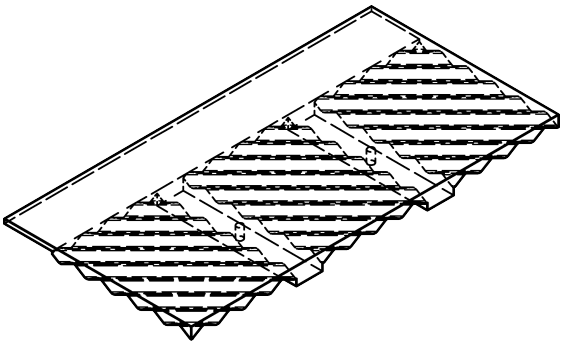
(c) Bottom plate D, $\theta_{cc} = 120°$



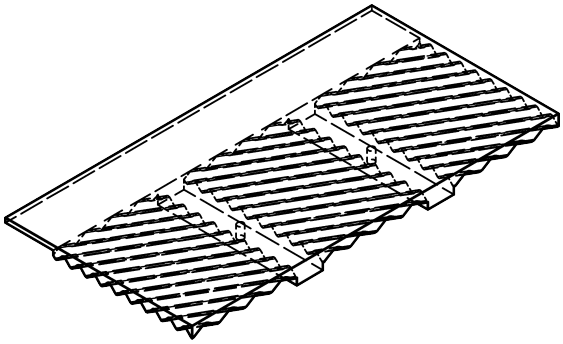
(d) Bottom plate E, $\theta_{cc} = 120°$



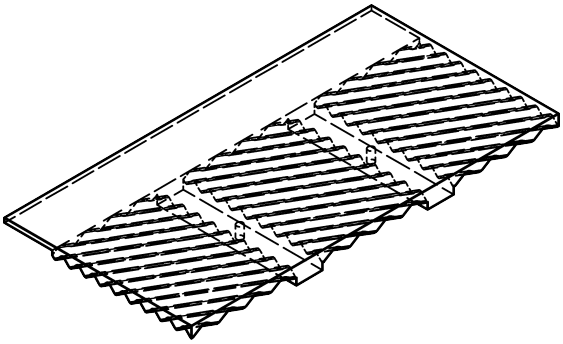
(e) Top plate B, $\theta_{cc} = 90°$



(f) Top plate C, $\theta_{cc} = 90°$

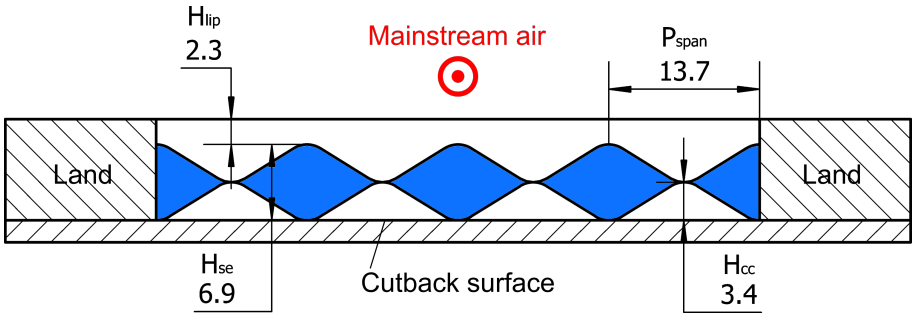


(g) Top plate D, $\theta_{cc} = 120°$

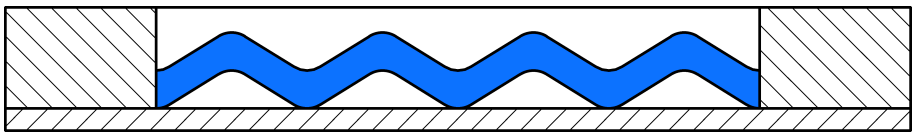


(h) Top plate E, $\theta_{cc} = 120°$

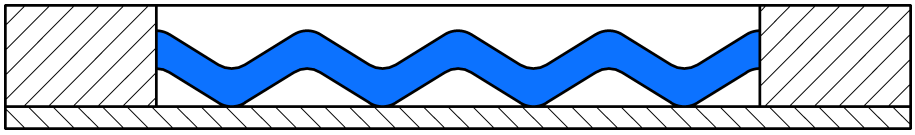
Figure 5.14: Cross corrugated slot plates



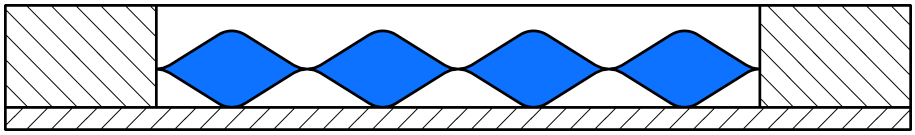
(a) G1 and G5



(b) G2 and G6



(c) G3 and G7



(d) G4 and G8

Figure 5.15: Exit corrugation alignments

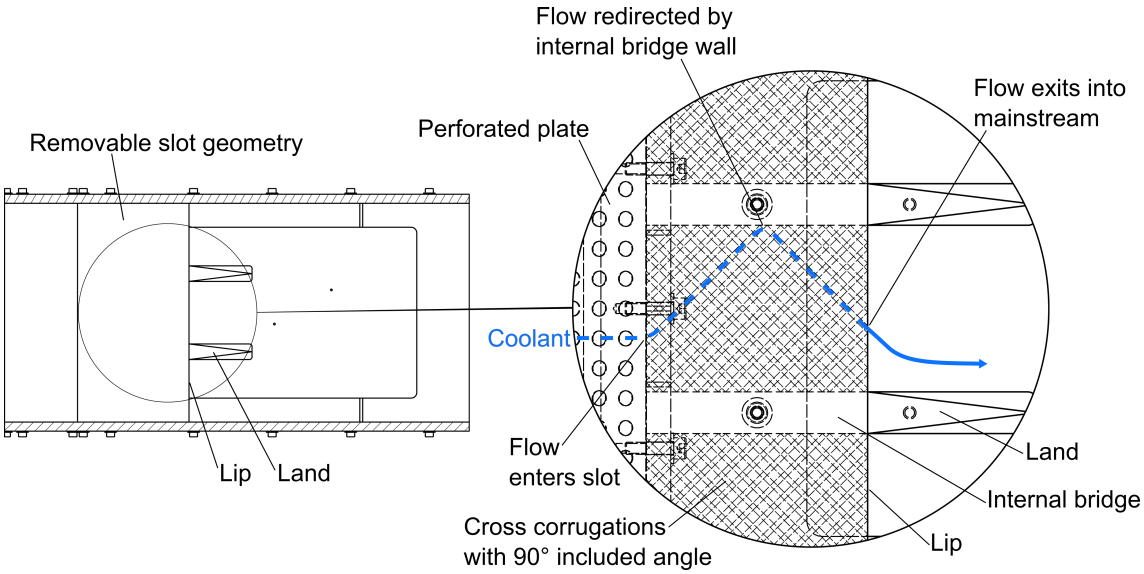


Figure 5.16: X-ray view of coolant flow path through a cross corrugated slot

denoted as G5–8, used an included angle of $120°$ with the same four exit alignments. Table 5.8 also lists the principle dimensions of these geometries. Figure 5.16 illustrates the general coolant flow path through a cross corrugated slot.

Geometry	Plates		H_{se}	A_{se}	H_{lip}	θ_{cc}	P_{span}	H_{cc}
	Bottom	Top	[mm]	[mm^2]	[mm]	[°]	[mm]	[mm]
G0	A	A	4.6	250.8	4.6	—	—	—
G1	B	B	6.9	188.1	2.3	90	13.7	3.4
G2	B	C	6.9	188.1	2.3	90	13.7	3.4
G3	C	B	6.9	188.1	2.3	90	13.7	3.4
G4	C	C	6.9	188.1	2.3	90	13.7	3.4
G5	D	D	6.9	188.1	2.3	120	13.7	3.4
G6	D	E	6.9	188.1	2.3	120	13.7	3.4
G7	E	D	6.9	188.1	2.3	120	13.7	3.4
G8	E	E	6.9	188.1	2.3	120	13.7	3.4

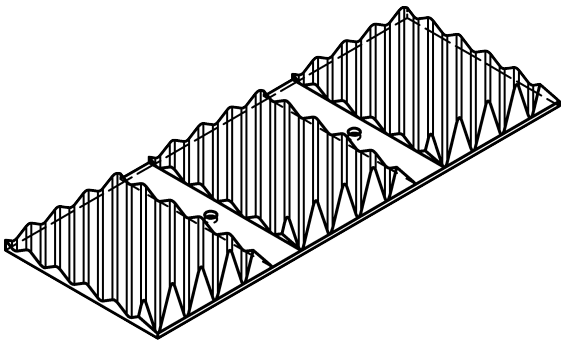
Table 5.8: Cross corrugated plate combinations and dimensions

5.6 Phase 3 geometries

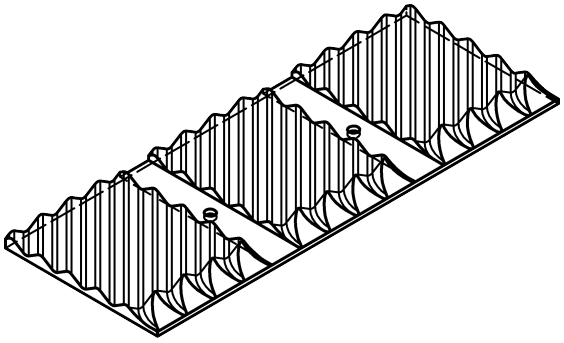
In phase 2 it was observed that the film effectiveness performance of the cross corrugated slot was significantly reduced. The results and discussion thereof are detailed in Chapter 7. In summary, this was in large part due to two factors:

- The non-uniformity of the slot exit profile across the span led to inconsistent spanwise coolant coverage, visible as distinct peaks of high effectiveness with low effectiveness in between and corresponding by and large with the positions of the upper corrugation channels.

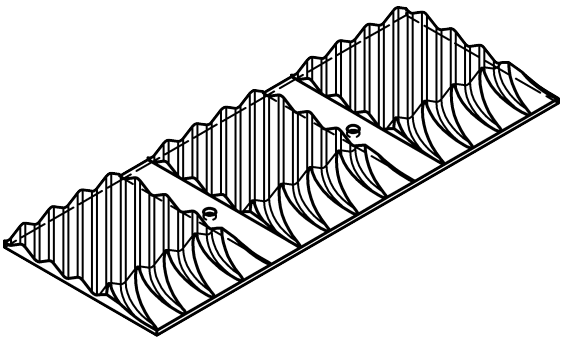
- The angle of the corrugation channels at exit led to the coolant exhausting non-parallel to the mainstream flow, which caused a strong bias of coolant towards one side of the cutback and consequently away from the other side, and also increased the mixing rate with the mainstream resulting in the lack of any potential core region of unity effectiveness as well as a very quick drop off in effectiveness with distance from the slot exit.



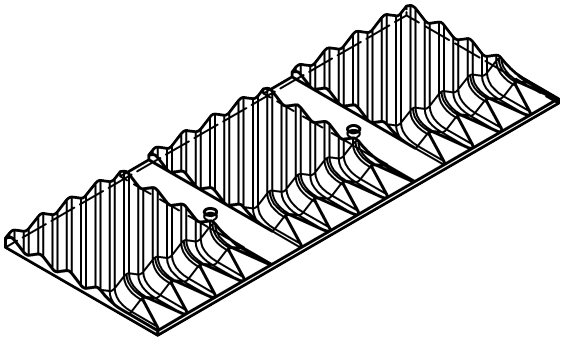
(a) Bottom plate F



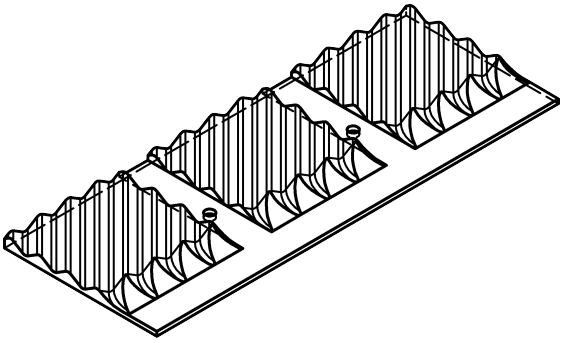
(b) Bottom plate G



(c) Bottom plate H

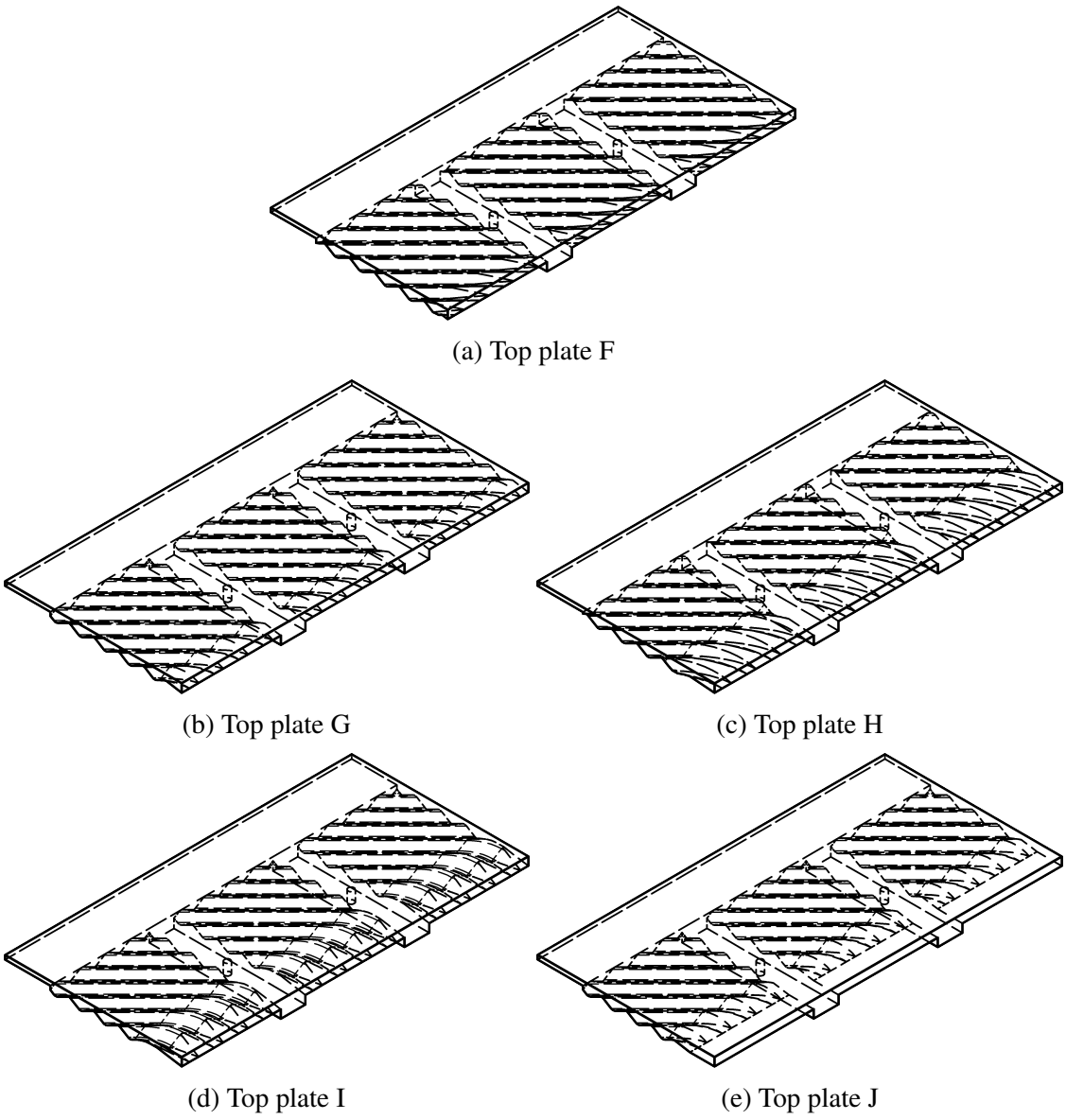


(d) Bottom plate I



(e) Bottom plate J

Figure 5.17: Exit shaped bottom plates



(a) Top plate F

(b) Top plate G

(c) Top plate H

(d) Top plate I

(e) Top plate J

Figure 5.18: Exit shaped top plates

In an effort to negate these factors, two exit shaping design features were considered:

- Flattening and smoothing out the corrugations within the slot towards the exit such that the exit shape would be a plain rectangle identical to the baseline rectangular slot.

- Straightening the corrugations within the slot towards the exit such that the channels and therfore the coolant flow direction would become parallel to the mainstream flow upon exit from the slot.

The objective of the third set of experiments was to measure the effect of this exit shaping on film cooling effectiveness, both on the cutback surface after the slot and on top of the lands. As before, to allow back-to-back comparisons between the geometries, the land shape was kept constant, using the tapered diffuser land used in phase 1.

The exit shaped geometries comprised five pairings of cross corrugated geometries with different types of exit shaping, denoted as G9 to G13. The plates are shown in Figures 5.17 and 5.18 and the pairings are tabulated in Table 5.9 with principle dimensions.

Geometry	Plates		H_{si}	H_{se}	A_{se}	H_{lip}	θ_{cc}	P_{span}	H_{cc}
	Bottom	Top	[mm]	[mm]	[mm^2]	[mm]	[°]	[mm]	[mm]
G9	F	F	6.9	4.6	250.8	4.6	90	13.7	3.4
G10	G	G	6.9	4.6	250.8	4.6	90	13.7	3.4
G11	H	H	6.9	4.6	250.8	4.6	90	13.7	3.4
G12	I	I	6.9	4.6	250.8	4.6	90	13.7	3.4
G13	J	J	6.9	4.6	250.8	4.6	90	13.7	3.4

Table 5.9: Exit shaped plate combinations and dimensions

The cross corrugated geometries G9–13 all used the same spanwise corrugation profile as before with an included angle of $90°$. The exit shaping for each design differed, but all resulted in the same rectangular exit profile identical to the baseline slot in height and width.

The rectangular exit profile was achieved by a “ramp down” section, which included chamfered corrugation ridges and a reduced slot height applied gradually over a specified

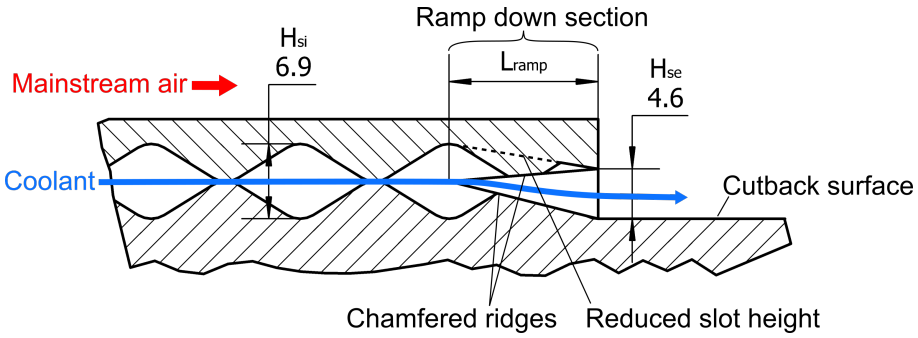
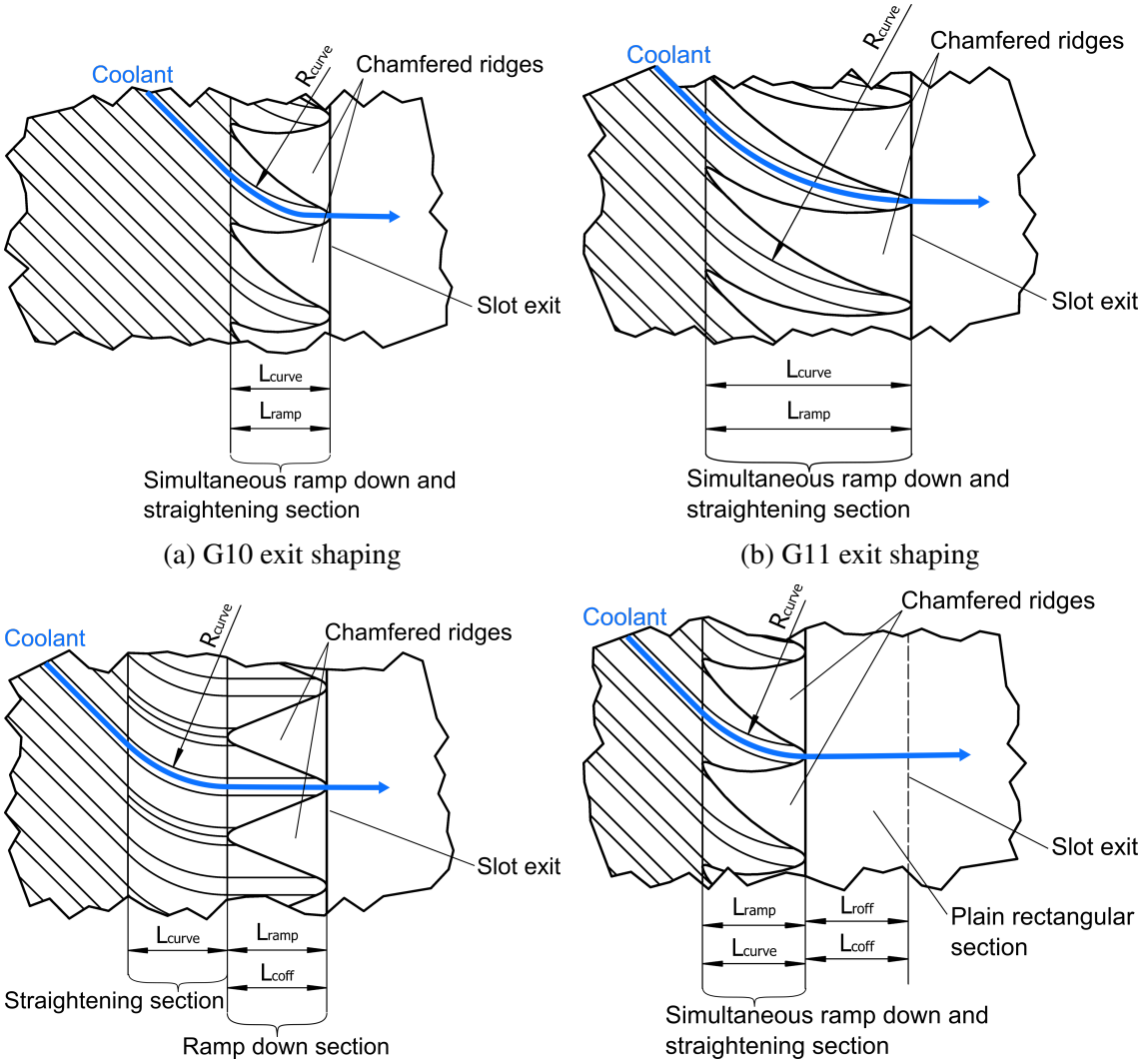


Figure 5.19: Ramp down exit shaping

length. The simplest application of the ramp down was used in G9, shown in Figure 5.19. Upstream of the ramp down section, the slot has internal height H_{si}, which is reduced to the slot exit height, H_{se}. The length of the ramp down section of the slot is defined as the ramp length, L_{ramp}.

In addition to the ramp down, channel straightening was applied to geometries G10–13. The channels which were originally angled at $45°$ to the mainstream flow direction were curved until they were parallel to the mainstream flow. Figure 5.20 shows the dimensions that define the combined channel straightening and ramp down exit shaping as applied to geometries G10–13. The ramp down section has length L_{ramp} and is offset from the slot exit by length L_{roff}. The straightening section has length L_{curve} with a radius of curvature R_{curve} and is offset from the slot exit by length L_{coff}. In the case of G10, shown in 5.20a, both the ramp down section and the straightening section have equal length and no offset from the slot exit, fully overlapping each other. For G11, shown in 5.20b, the length of both has been doubled, again with no offset. For G12, shown in 5.20c, the ramp down section has no offset and the straightening section has an offset equal to the length of the ramp down section, such that the ramp down section immediately follows the straightening section. Finally for G13, shown in 5.20d, both the ramp down section and the straightening section have equal length and offset from the slot exit, resulting in a short length of plain rectangular slot leading up to the slot exit. The exit shaping dimensions are tabulated in Table 5.10. Photographs of the topside of the G13 bottom plate and the underside of the G13 top plate are shown in Figures 5.21a and 5.21b respectively.



(a) G10 exit shaping

(b) G11 exit shaping

(c) G12 exit shaping

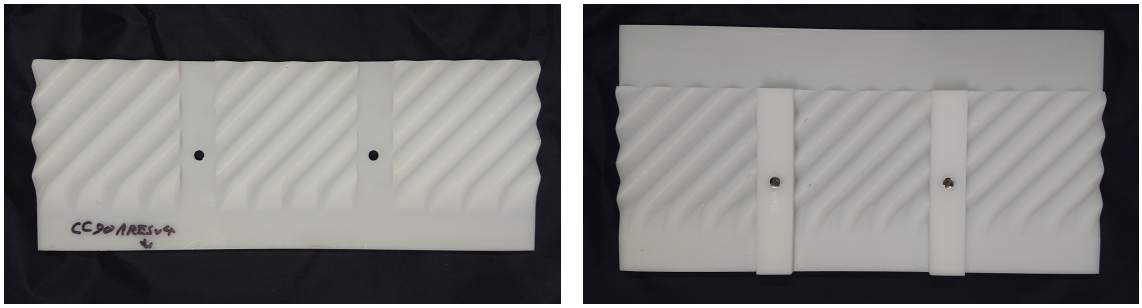
(d) G13 exit shaping

Figure 5.20: Combined channel straightening and ramp down exit shaping

5.7 Coolant feed modifications for carbon dioxide

In order to take effectiveness measurements with a higher coolant-to-mainstream density ratio closer to real engine conditions, it was necessary to switch to using carbon dioxide as the coolant. This would allow an increase in density ratio to 1.52. However, the carbon dioxide was supplied in a $5\,\mathrm{MPa}$ compressed gas cylinder and the expansion of carbon dioxide from this pressure to approximately $500\,\mathrm{kPa}$ through a regulator was similar to a Joule-Thomson expansion and resulted in a significant reduction in coolant gas temperature.

A Joule-Thomson expansion is one where fluid is allowed to flow steadily from a high



(a) Bottom plate J, G13 (b) Top plate J, G13

Figure 5.21: G13 cross corrugated geometry

Geometry	L_{ramp} [mm]	L_{roff} [mm]	L_{curve} [mm]	L_{coff} [mm]	R_{curve} [mm]
G9	13.7	0.0	—	—	—
G10	13.7	0.0	13.7	0.0	19.4
G11	27.4	0.0	27.4	0.0	38.8
G12	13.7	0.0	13.7	13.7	19.4
G13	13.7	13.7	13.7	13.7	19.4

Table 5.10: Exit shaping dimensions

pressure to a low pressure through a valve or porous plug inserted in a pipe. If the pipe is insulated so that heat flow to or from the fluid is negligible and the flow velocity is low such that there is no significant change in kinetic energy, then the steady-flow energy equation implies that the enthalpy of the fluid after the restriction is restored to its initial value before the restriction (Rogers and Mayhew, 1992). For a real gas, this results in a temperature change which is quantified by the Joule-Thomson coefficient.

While the regulators used to expand the nitrogen and carbon dioxide in the current experiment were not insulated and therefore not adiabatic as assumed in a Joule-Thomson expansion, the Joule-Thomson effect still caused the coolant gas to drop in temperature as it passed through the valve. The Joule-Thomson coefficients for nitrogen and carbon dioxide are plotted for $293\,\mathrm{K}$ in Figure 5.22 using data from Lemmon et al. (2017). It can be seen that the Joule-Thomson coefficient when carbon dioxide is expanded is significantly greater than for the expansion of nitrogen for the same drop in pressure.

In phases 1, 2 and 3, nitrogen was used as the coolant gas. This was expanded through the regulator from a maximum bottle pressure of $20\,\mathrm{MPa}$ to approximately $500\,\mathrm{kPa}$ which

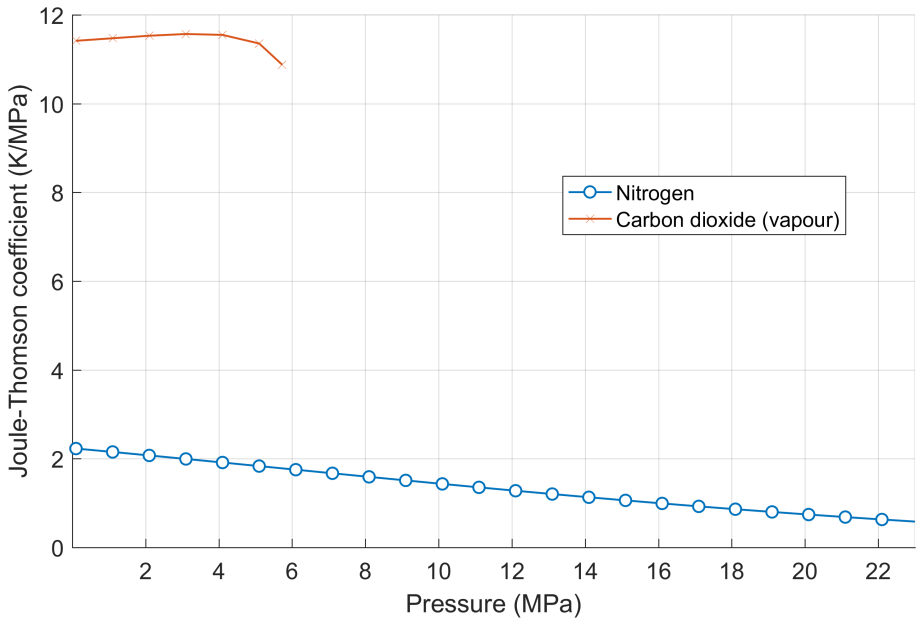


Figure 5.22: Joule-Thomson coefficients for nitrogen and carbon dioxide

was fed to the mass flow controllers. This expansion as an isenthalpic process is illustrated graphically in Appendix A. With an adiabatic valve, this would have resulted in a temperature drop of approximately $30\,\mathrm{K}$. Since the valve was not adiabatic and there was a considerable length of hose leading up to the mass flow controllers and then to test section, the nitrogen was warmed back up to ambient temperature. This was confirmed using temperature measurements taken in the coolant plenum. However, it was observed that if the coolant was allowed to flow continuously at a high mass flow rate, the coolant plenum temperature decreased over time. This was likely due to the coolant feed system gradually being cooled down by the nitrogen and reducing its capacity to warm up the coolant flow back to ambient temperature, evidenced by visible water condensation on the outside of the hoses and even the build up of ice on the nitrogen bottle regulator. Thus it was ensured that the coolant flow was only activated for as long as necessary to achieve a stable mass flow rate and take effectiveness measurements and ample time was allowed in between runs for the coolant feed system to warm back up to ambient temperature.

In phase 4, the coolant was switched to carbon dioxide which was supplied at a lower bottle pressure of $5\,\mathrm{MPa}$. Even so, the Joule-Thomson effect became a much bigger issue. The expansion to $500\,\mathrm{kPa}$ as an isenthalpic process is illustrated graphically in

Appendix A. With an adiabatic valve, this would have resulted in a temperature drop of approximately $75\,\mathrm{K}$. Even more concerning, this would have also brought the coolant past the saturated vapour line into the liquid-vapour mix region resulting in condensation of carbon dioxide within the regulator itself. A BOC model L132 single stage heated regulator for carbon dioxide was installed in order to have the carbon dioxide heated while passing through the regulator, in an effort to deal with these issues. However, the heater power was limited to $150\,\mathrm{W}$ and a flow rate of $30\,\mathrm{l\,min^{-1}}$, insufficient for the flow rates required. Furthermore, the heater was not thermostat controlled, resulting in a temperature increase at the very beginning, reducing with time.

The solution to the issues of phase change and extreme cold was to install an intermediate carbon dioxide reservoir in between the bottle and the mass flow controllers. This reservoir would be slowly filled using the heated bottle regulator up to $700\,\mathrm{kPa}$, allowed to stabilise to ambient temperature, and then used to feed the mass flow controller for the experiments. $700\,\mathrm{kPa}$ was an appropriate intermediate pressure that was low enough such that the expansion of the carbon dioxide through the mass flow controller did not cause a significant reduction in temperature that couldn't then be increased by warming up as the gas passed through the remainder of the coolant system to the test section. The intermediate pressure also had to be sufficiently high, and the pressure vessel sufficiently large, such that it was able to consistently supply the coolant flow at the required flow rates for the duration of the experimental runs without becoming exhausted. The reservoir could then be recharged from the bottle in between runs. An updated schematic of the rig is shown in Figure 5.23.

The intermediate reservoir was constructed from a Victaulic pipe of $304.8\,\mathrm{mm}$ diameter and $3\,\mathrm{m}$ length with blanked ends. On one end, the blank had installed an inlet from the bottle, an outlet to the mass flow controller, a Bourdon pressure gauge and a bimetal thermometer. These fittings are shown in Figure 5.24a and the entire reservoir with nitrogen and carbon dioxide bottles is shown in Figure 5.24b. With this large reservoir, it was possible to supply carbon dioxide to the test section at the required mass flow rates without a significant change in temperature for the duration of each experiment.

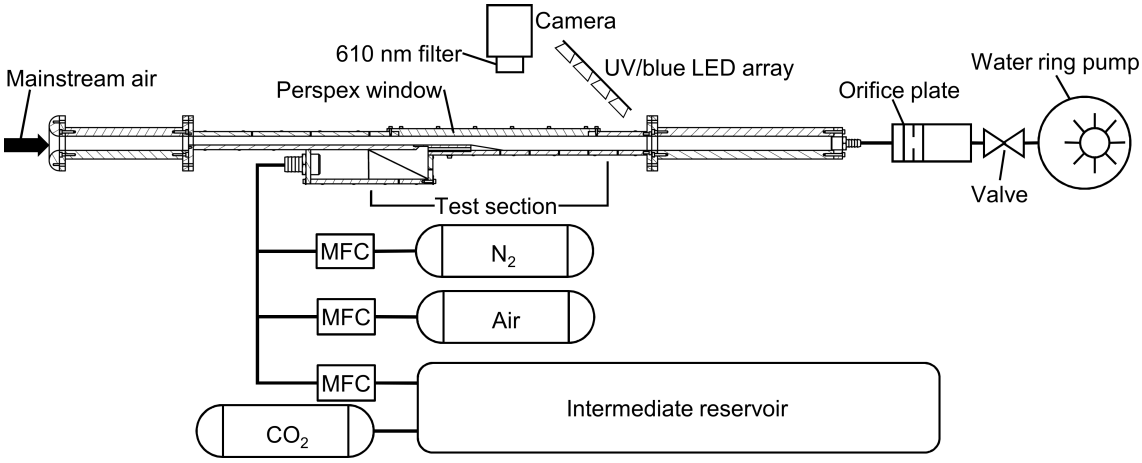
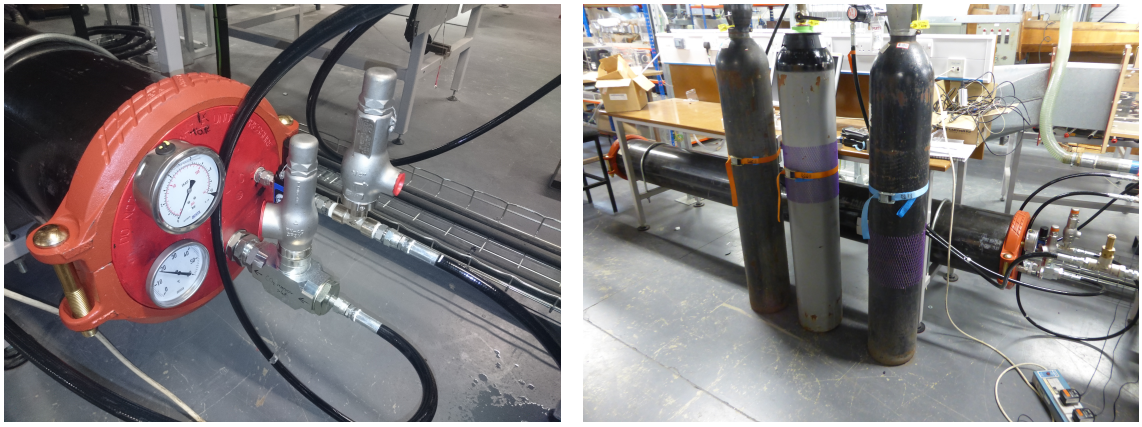


Figure 5.23: Rig schematic with intermediate reservoir



(a) End blank fittings (b) Overview

Figure 5.24: Intermediate reservoir

While the new density ratio of 1.52 still did not gain parity with the real engine conditions, a higher density ratio could not be achieved without using a mixture with a heavier gas such as sulphur hexafluoride. The difficulty in using such gases was deemed impractical for the current study.

5.7.1 Operating conditions

The same range of blowing ratios was tested, so the target mass flows remained the same. However, as the density ratio was increased, the coolant flow velocities were reduced and consequently so were the momentum flux ratios and the coolant Reynolds numbers. The new values are presented in Table 5.11.

M	J	$\dot{m}_c$ [$g\,s^{-1}$]	$\dot{m}_m$ [$g\,s^{-1}$]	$\dot{m}_{tot}$ [$g\,s^{-1}$]	u_c [$m\,s^{-1}$]	u_m [$m\,s^{-1}$]	Re_c
0.6	0.24	4.2	26.8	31.0	3.1	7.8	887
0.8	0.42	5.4	25.6	31.0	3.9	7.4	1131
1.0	0.66	6.5	24.5	31.0	4.7	7.1	1355
1.2	0.95	7.5	23.5	31.0	5.4	6.8	1561
1.4	1.29	8.4	22.6	31.0	6.0	6.6	1751

Table 5.11: Target operating conditions using carbon dioxide coolant

5.8 Phase 4 geometries

The objective of the fourth set of experiments was to measure the effect of density on film cooling effectiveness using the optimised cross corrugated slot geometry G13, both on the cutback surface after the slot and on top of the lands. The baseline plain slot geometry was also tested to compare the two. The baseline geometry is described in Section 5.3 and the optimised cross corrugated slot geometry is described in Section 5.6.

Chapter 6

Effectiveness Measurements — Land Shapes

6.1 Introduction

The objective of the first phase of experiments was to recommend the optimal land shape for trailing edge slot film cooling out of six land shapes similar to modern blade designs. This was accomplished by measuring film effectiveness using each of the land geometries.

The geometries tested are detailed in Section 5.3 and shown in Figure 5.8. This chapter shows the results from phase 1 which are then compared with literature where possible and then back-to-back with each other in order to make recommendations for cooling engineers. These results have been partially published in Wong et al. (2015) and Wong et al. (2016b).

6.2 2D film cooling effectiveness distributions

The PSP technique allows high resolution 2D adiabatic film effectiveness measurements over the cutback surface and top of the lands to be made. The approximate view area and coordinate system is defined in Figure 6.1, where x is the downstream distance

from the slot exit and z is the spanwise displacement from the centreline. These are non-dimensionalised by the slot height of the plain rectangular slot to give x/H and z/H, where $H = H_{\text{slot}} = 4.6\,\text{mm}$. Measurements were taken for $M = 0.6, 0.8, 1.0, 1.2, 1.4$.

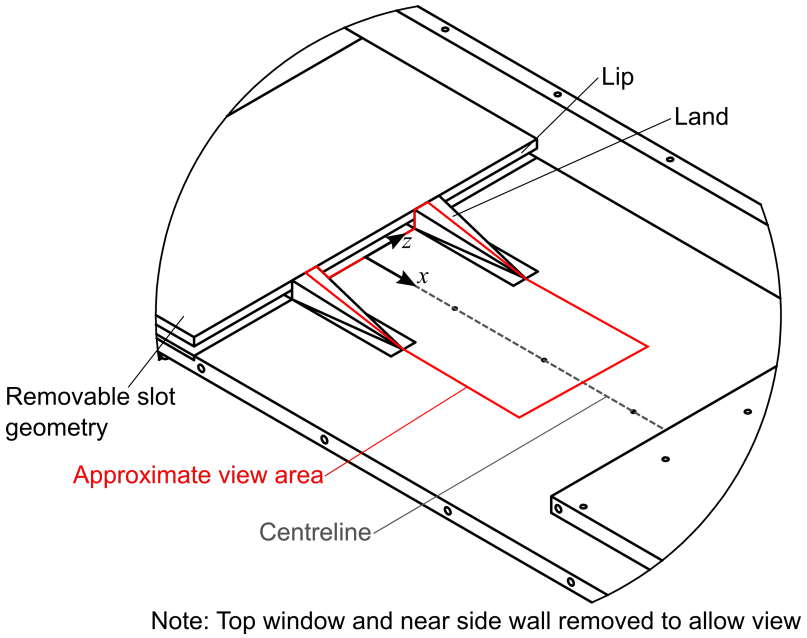
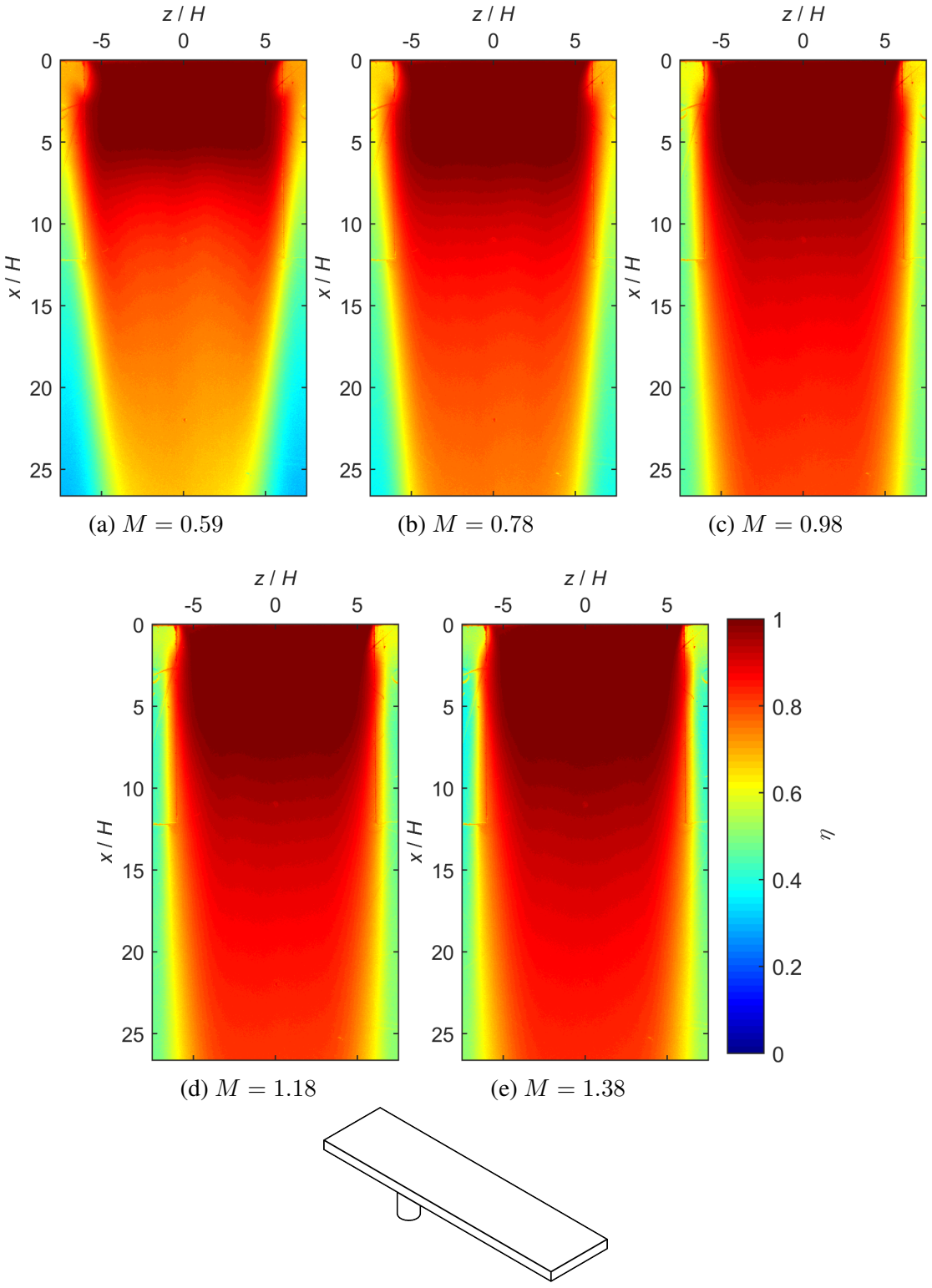


Figure 6.1: Approximate view area and coordinate system

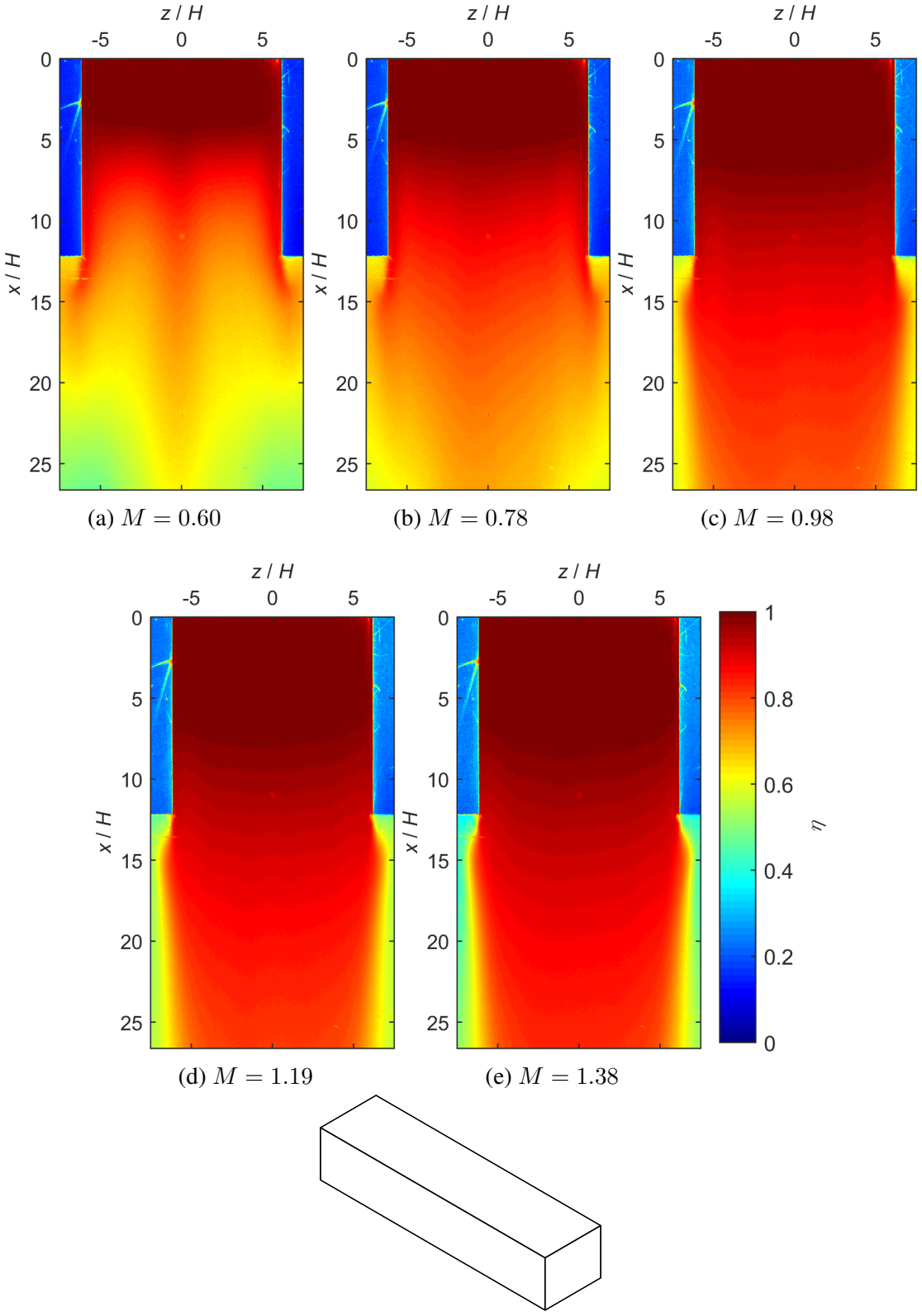
Figures 6.2, 6.3, 6.4, 6.5, 6.6 and 6.7 show all the 2D plots of effectiveness taken in phase 1. All of the figures show a plan view of the cutback region and lands. The slot exit and lip is aligned with the top border of the plots, i.e. where $x/H = 0$. The centreline is at the midpoint between the lands where $z/H = 0$. Blue regions show poor coverage from the nitrogen coolant and correspond to low film cooling effectiveness and red regions correspond to high effectiveness. The lands, where applicable, can be seen as the predominantly blue regions in the top left and top right corners or each plot. Some marks are consistently visible in the same position over the lands for all the geometries. These are due to scratches on the Perspex window, which was replaced for phase 2.



(a) $M = 0.59$ (b) $M = 0.78$ (c) $M = 0.98$

(d) $M = 1.18$ (e) $M = 1.38$

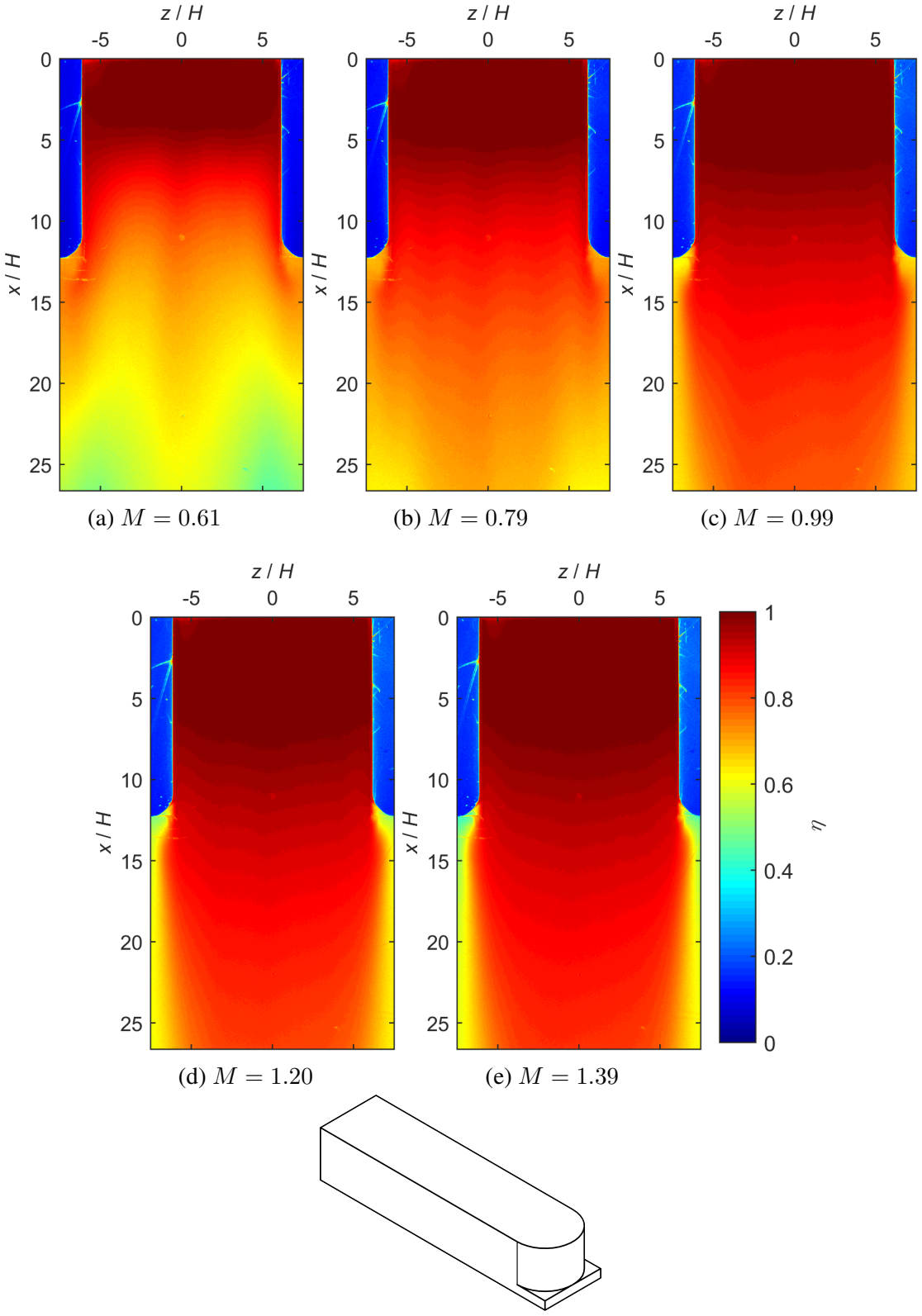
Figure 6.2: 2D η distributions, L1: No lands



(a) $M = 0.60$ (b) $M = 0.78$ (c) $M = 0.98$

(d) $M = 1.19$ (e) $M = 1.38$

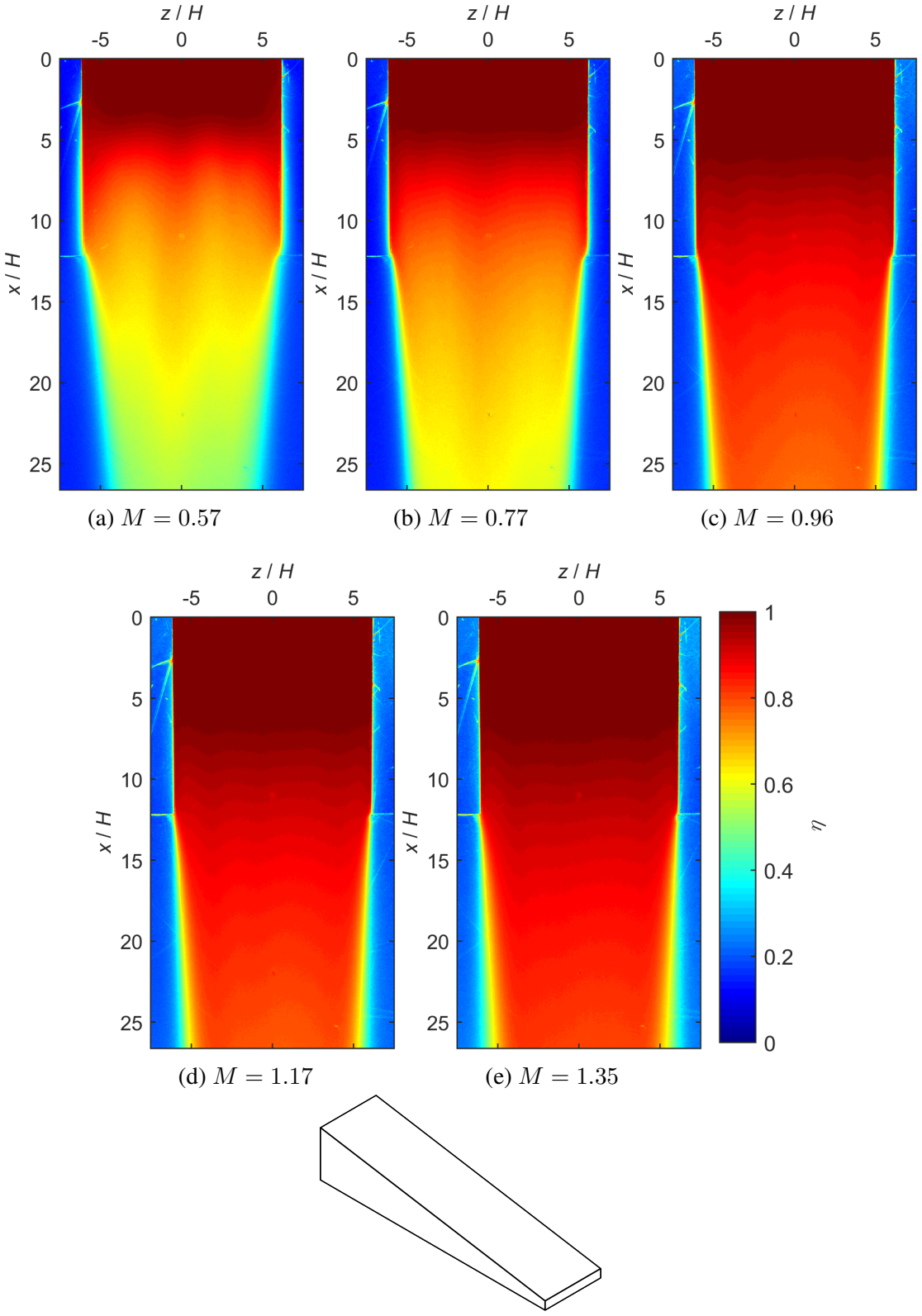
Figure 6.3: 2D η distributions, L2: Block



(a) $M = 0.61$ (b) $M = 0.79$ (c) $M = 0.99$

(d) $M = 1.20$ (e) $M = 1.39$

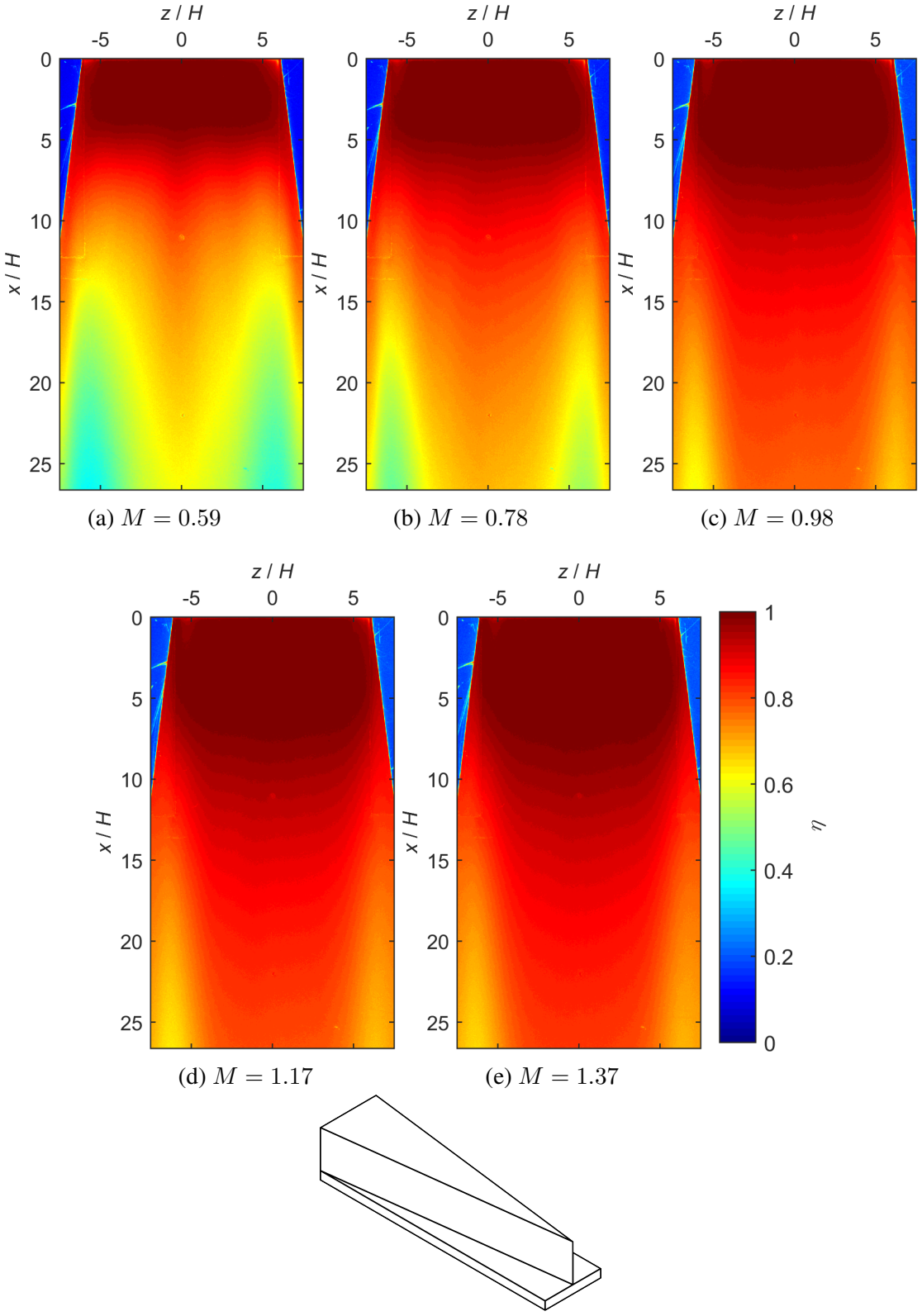
Figure 6.4: 2D η distributions, L3: Rounded



(a) $M = 0.57$ (b) $M = 0.77$ (c) $M = 0.96$

(d) $M = 1.17$ (e) $M = 1.35$

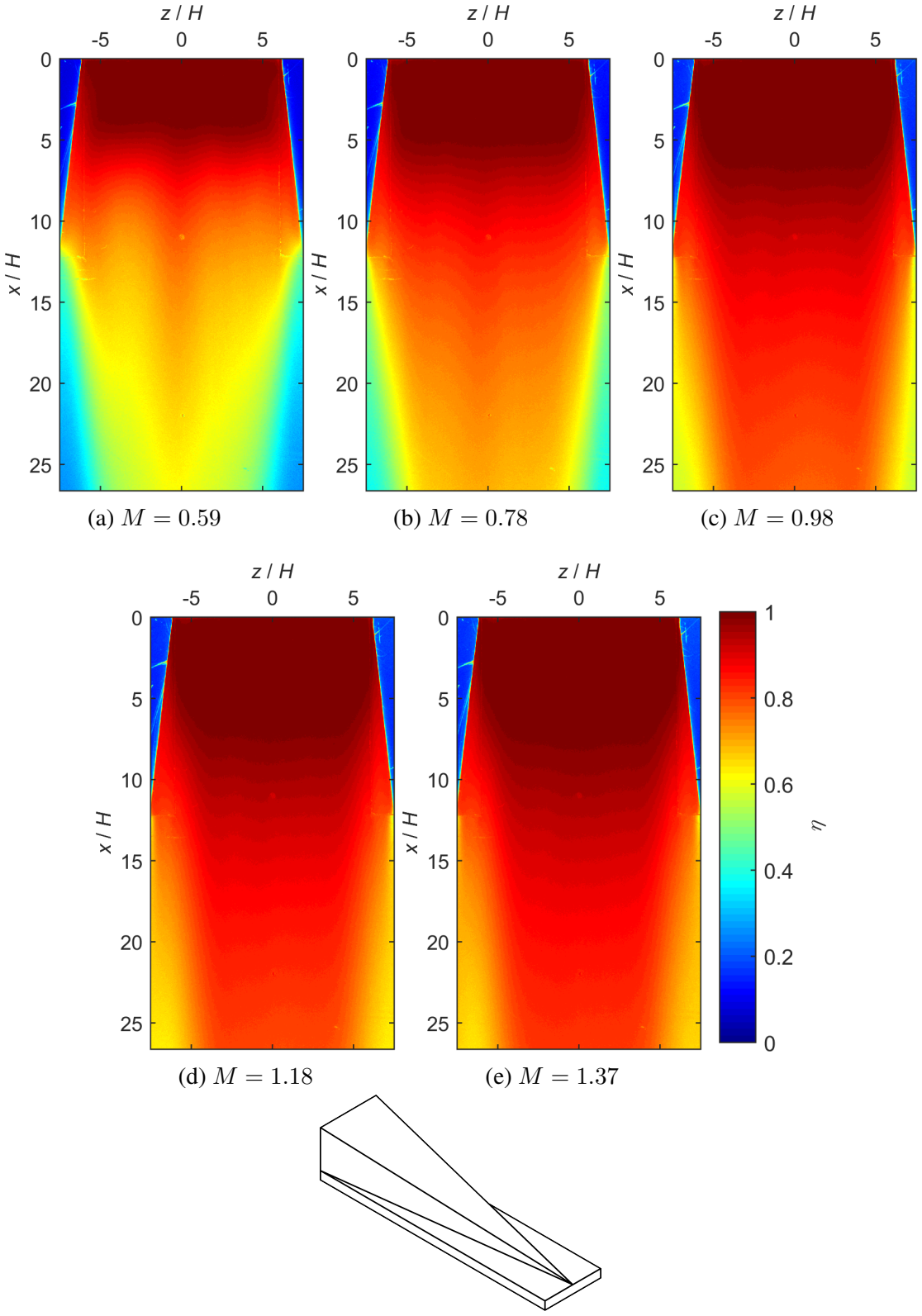
Figure 6.5: 2D η distributions, L4: Tapered



(a) $M = 0.59$ (b) $M = 0.78$ (c) $M = 0.98$

(d) $M = 1.17$ (e) $M = 1.37$

Figure 6.6: 2D η distributions, L5: Diffuser



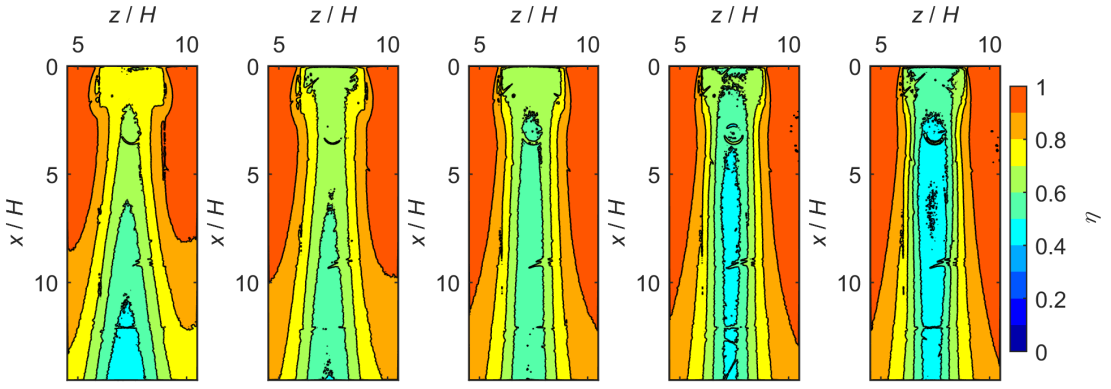
(a) $M = 0.59$ (b) $M = 0.78$ (c) $M = 0.98$

(d) $M = 1.18$ (e) $M = 1.37$

Figure 6.7: 2D η distributions, L6: Tapered diffuser

6.3 Discussion

6.3.1 Land effectiveness

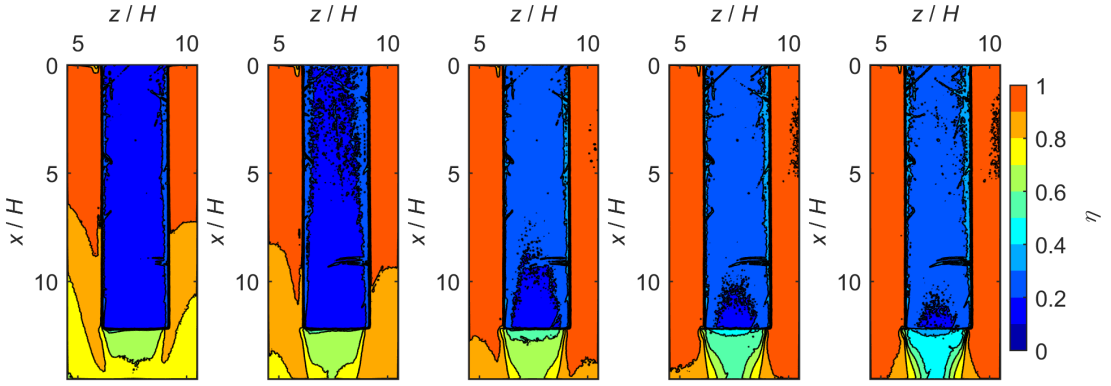


(a) $M = 0.59$ (b) $M = 0.78$ (c) $M = 0.98$ (d) $M = 1.18$ (e) $M = 1.38$

Figure 6.8: 2D land η distributions, L1

Figure 6.8 shows a close-up view of the right hand side land of geometry L1 with no lands. Levels of effectiveness are shown using 10 contour bands at all five blowing ratios. Although there were no lands, the internal bridges still remained, ending abruptly at the slot exit with a square trailing edge of the same width as the lands. It can be seen that the square trailing edge of the bridges left wakes of lower effectiveness behind them, in the gap region where the lands would have bee. The recirculation region created by the sudden end of the internal bridges allowed the coolant flow to enter the gap. However, this also allowed the mainstream flow to enter the gap and resulted in wakes of medium effectiveness extending downstream of the bridges. At $M = 0.6$ the coolant had less momentum leaving the slot and was able to fill in the gap up to an effectiveness of 0.7. However, as blowing ratio was increased, the coolant had greater momentum and was less able to fill the gap and as a result, more mainstream flow was drawn in, creating a more defined wake and reducing the effectiveness to 0.5 at $M = 1.4$.

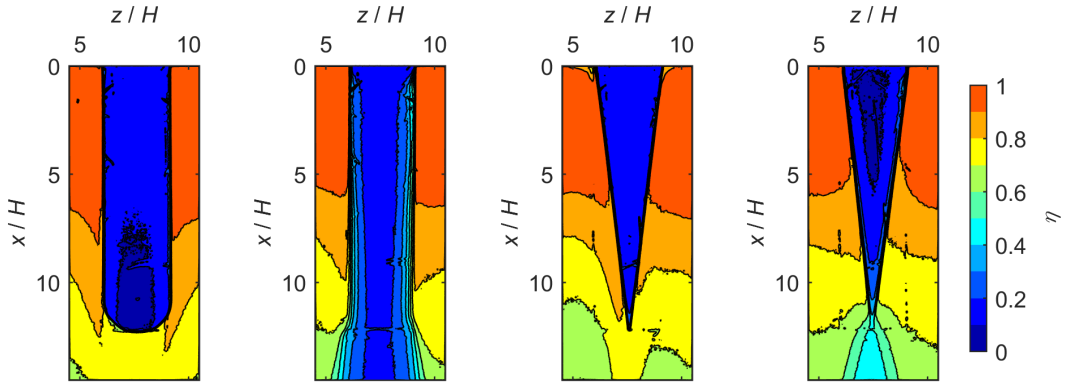
Figure 6.9 shows a close-up view of the right hand side land of geometry L2, the block lands. It can be seen that film cooling effectiveness was very low on top of the lands, not exceeding 0.3 over the majority of its surface. This shows that very little coolant was able to wash over the lands and is common to all the land shapes L2–6. It does appear



(a) $M = 0.60$ (b) $M = 0.78$ (c) $M = 0.98$ (d) $M = 1.19$ (e) $M = 1.38$

Figure 6.9: 2D land η distributions, L2

to show effectiveness increased very slightly with blowing ratio from the 0.1–0.2 band to the 0.2–0.3 band. However, this higher effectiveness band appeared to grow away from the slot exit in tandem with the 0.9–1.0 band on the cutback surface as blowing ratio increased. The low effectiveness also corresponds to low emission intensity and a smaller difference in intensity with the reference image. This makes it more sensitive to other sources of illumination and increases the measurement uncertainty as explained in Section 5.2.8. Therefore, it is possible that this small observed increase in effectiveness on the lands was actually due to the high intensity red light from the cutback surface reflecting on the inside of the window on to the land surface.



(a) L3, $M = 0.61$ (b) L4, $M = 0.57$ (c) L5, $M = 0.59$ (d) L6, $M = 0.59$

Figure 6.10: 2D land η distributions, L3–6, $M \approx 0.6$

Figure 6.10 shows the same view of geometries L3–6 at the lowest blowing ratio of $M = 0.6$. Geometry L3 differs with L2 only in the rounded off downstream end of

the lands. While this did have an effect on the downstream effectiveness after the lands (discussed in Section 6.3.2), this had little consequence on the effectiveness on top of the lands as shown in Figure 6.10a.

Figure 6.10b shows geometry L4 where the lands were tapered down to meet the cutback surface. While the majority of the land surface had low effectiveness as mentioned previously, there was a small increase in effectiveness apparent along the left and right edges of the lands, an effect more apparent at low blowing ratio. Here, the mainstream air appeared to stick to the land surface all the way to the end, encouraging some mixing with the coolant air as it was brought down to the cutback level. This increased the effectiveness slightly on the sides of the lands but reduced the effectiveness on the cutback next to the lands.

The diffuser geometries L5 and L6 are shown in Figures 6.10c and 6.10d respectively. While the coolant did fill in the additional cutback surface left by the narrowing lands, it still did not wash over the top. The same small increase in effectiveness along the edges of the lands as seen for geometry L4 was also apparent in geometry L6, the tapered diffuser land, when compared to its non-tapered counterpart, L5. However, this was to a much smaller extent.

Comparison with literature

Yang and Hu (2011) showed 2D plots of film cooling effectiveness using a "no lands" geometry similar to geometry L1 and a tapered diffuser geometry similar to geometry L6. They used the same $H_{\text{lip}}/H_{\text{slot}} = 1$, but a much smaller $W_{\text{slot}}/H_{\text{slot}} = 2$ compared to the current study's $W_{\text{slot}}/H_{\text{slot}} = 12$. Their report showed a similar result for the "no lands" geometry, with the coolant flow able to spread into the gap region. However, their report for the tapered diffuser geometry showed significantly higher film effectiveness on top of the lands, as much as 0.4 near the lip and 0.7 towards the end. This discrepancy is likely due to the different $W_{\text{slot}}/H_{\text{slot}}$ used in the two studies. Their stereoscopic PIV measurements identified the vortices originating from the corners of the slot channels as

the main factor encouraging coolant flow to wash over the top of the lands, especially when $M < 1.0$. The proximity of the two corners of the slot channels may be a factor in determining how the vortices form and to what extent they encourage flow to wash over the lands, although no 3D or unsteady flow data was taken in the current study to confirm this.

Murata et al. (2012) reported 2D effectiveness measurements taken over the top of the lands for straight and diffuser lands using $W_{\text{slot}}/H_{\text{slot}} = 4.6$. They found very low effectiveness down the length of the lands, not exceeding 0.25 along the centre, with higher effectiveness along the edges. Ling et al. (2015a) used an MRI technique to take 2D effectiveness measurements over the top of the lands for straight and diffuser lands using $W_{\text{slot}}/H_{\text{slot}} = 3$. They also found very low effectiveness on top of the lands for the straight and weakly diffused lands, not exceeding 0.2 along the centre. Both of these reports are in agreement with the current study. However, Ling et al. (2015a) also tested a strongly diffused land with a high diffusion angle and tapering which showed some effectiveness up to 0.4 near the start of the lands. They theorised that this was due to the strong tapering of the land in that case, rather than the diffusion, which caused flow separation at the start of the lands leading to greater coolant mixing and higher effectiveness in that region. This bears some similarity in shape and results to the tapered diffuser geometry used by Yang and Hu (2011) and may also be related to the relatively low $W_{\text{slot}}/H_{\text{slot}}$ used in both studies.

6.3.2 Effectiveness downstream of lands

In Figures 6.2 to 6.7, regions of lower film effectiveness are clearly visible downstream of the lands (bridges in the case of L1) where both mainstream air and coolant was drawn in to the gap to mix, resulting in lower effectiveness levels downstream of the lands in the range 0.1 to 0.7.

The wakes of low effectiveness behind the bridges of geometry L1 described in Section 6.3.1 and visible in Figure 6.2 were very similar to those visible behind the lands of

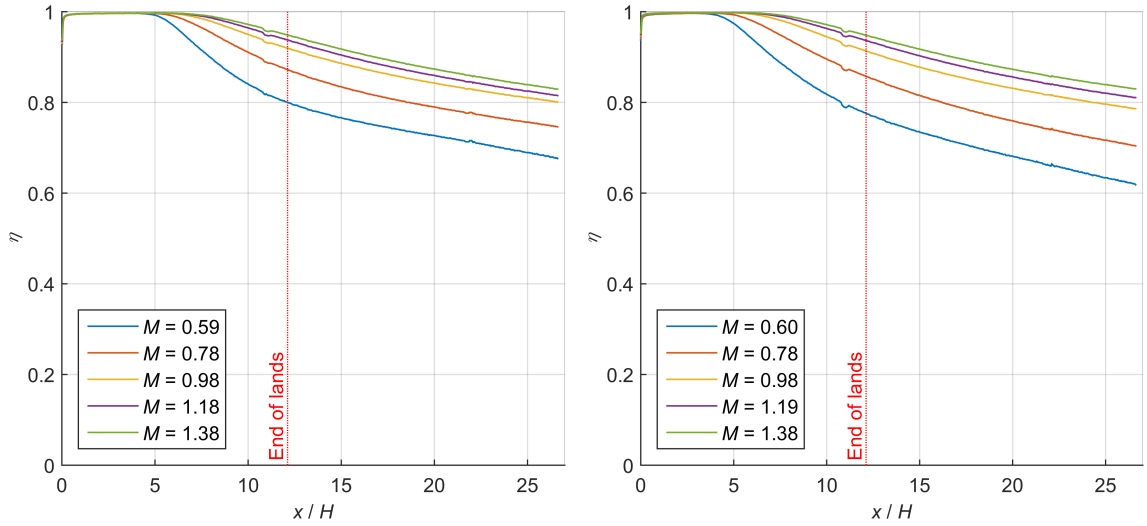
geometry L2 in Figure 6.3. The presence of the block lands served to delay the beginning of the wake by the length of the lands but the wakes remained mostly the same since they both used square shaped blunt trailing edges. The rounding off of these trailing edges in geometry L3 encouraged more coolant to enter the gaps behind the lands, resulting in slightly higher effectiveness in the range 0.5 to 0.7 throughout the wakes showh in Figure 6.4. This was taken further by having sharp pointed trailing edges in geometry L5, producing significantly less pronounced wakes due to the diffuser shape allowing the coolant to more gradually fill in the gaps left by the lands. Effectiveness levels as shown in Figure 6.6 were much higher, in the range 0.6 to 0.9.

For the tapered geometries L4 and L6 (Figures 6.5 and 6.7), the wakes downstream of each land had much lower effectiveness levels down to almost zero and were larger and more pronounced than the corresponding non-tapered equivalents, geometries L2 and L5 respectively (Figures 6.3 and 6.6). This was due to the tapered land surface creating a ramp for the attached mainstream air to follow directly down to the cutback surface without also allowing the coolant to mix after the lands. The non-tapered lands, on the other hand, created a sudden gap which encouraged both the mainstream and coolant flow to mix together in more equal amounts, resulting in higher film effectiveness levels.

6.3.3 Centreline effectiveness

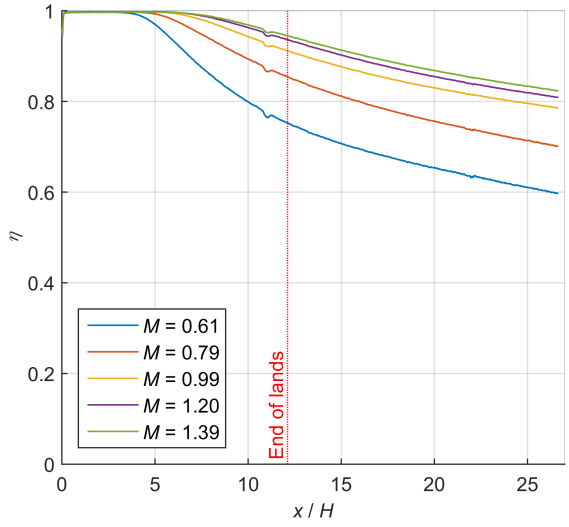
Figure 6.11 shows plots of film cooling effectiveness down the slot centreline for each geometry. This included only a 100 pixel ($8.43\,\mathrm{mm}$) wide strip down the centre of the cutback region extending downstream from the slot. The position of the end of the lands is marked in the plots.

Considering only the centreline effectiveness, all geometries show a similar overall picture, with initial unity effectiveness for some distance, called the potential core length x_p, before decaying. This length is non-dimensionalised by the slot height of the plain rectangular slot to give x_p/H, where $H = H_{\text{slot}} = 4.6\,\mathrm{mm}$. In the current study, x_p/H was determined by plotting the natural logarithm of the centreline effectiveness against

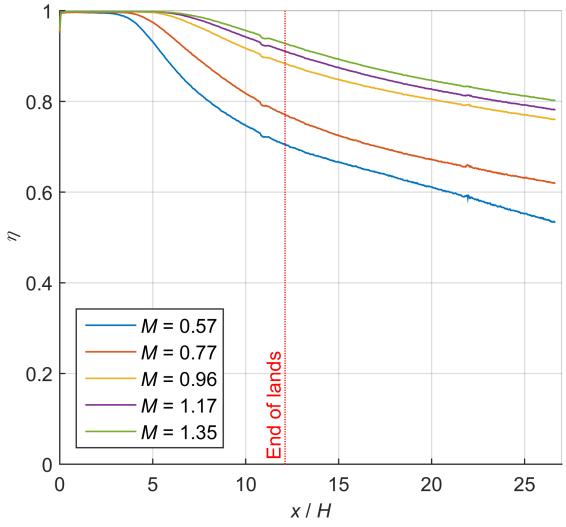


(a) L1

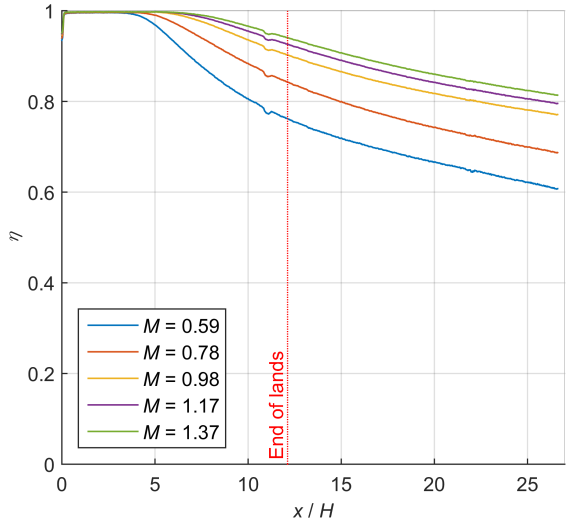
(b) L2



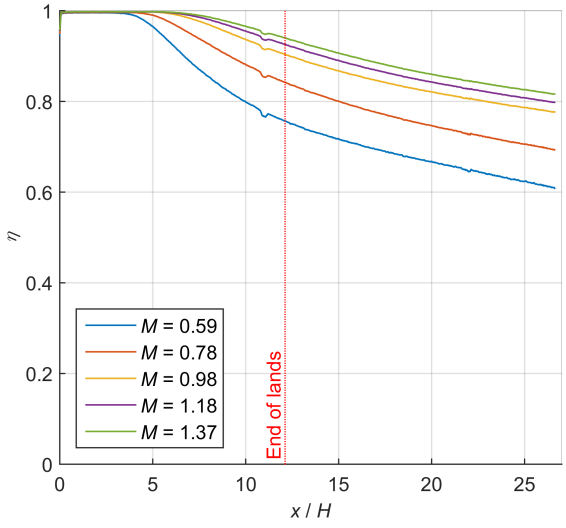
(c) L3



(d) L4



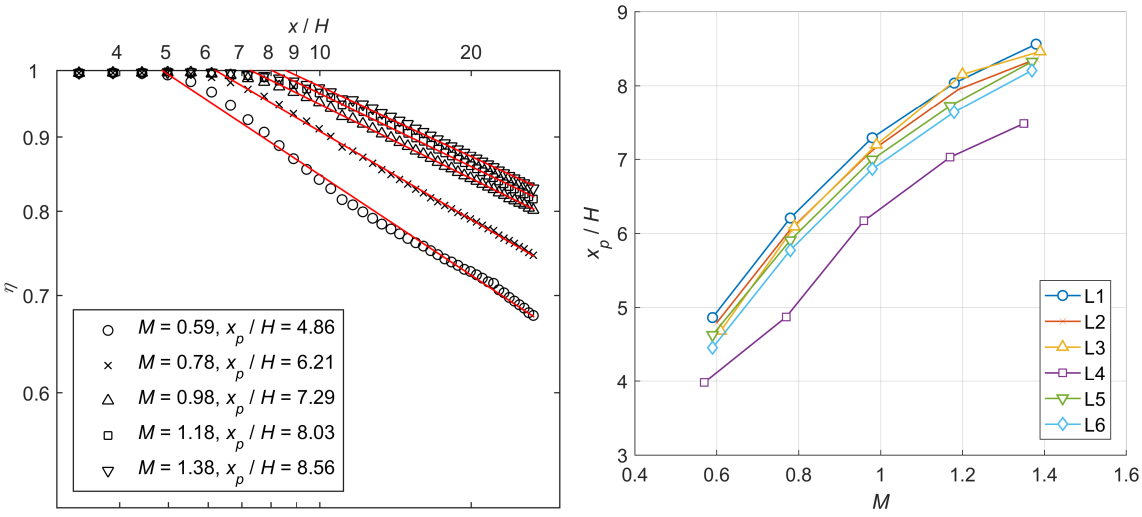
(e) L5



(f) L6

Figure 6.11: Centreline η, all land shapes

the natural logarithm of x/H and taking a straight line extrapolation through the data to the implied end point of unity effectiveness. This process was used by Sturgess (1986) and is illustrated in Figure 6.12a using the block lands as an example. Potential core length increased with blowing ratio for all geometries, as shown in Figure 6.12, to a maximum value of 8.6. The increase in potential core length becomes smaller as blowing ratio increased, suggesting a non-linear relationship between the two. Aside from the tapered case, the shape of the land appeared to have little effect on potential core length.



(a) Determining potential core length for L1

(b) Potential core length at different blowing ratios

Figure 6.12: Potential core length, all land shapes

The rate at which effectiveness decreased was greater for lower blowing ratios. This agrees with the trends shown by Martini et al. (2005a) and Murata et al. (2012) in their film effectiveness studies. Geometry L1 with no lands showed the highest effectiveness, followed by geometries L2, L3, L5 and L6, all with very similar centreline effectiveness for all blowing ratios. Geometry L4 showed the lowest effectiveness, illustrating the previously mentioned issue of the mainstream flow being pulled down by the ramped surface, encroaching into the cutback region before the end of the lands and leaving a large "hot gas" wake behind each land which also affected the central slot region.

Comparison with literature

Sturgess and Pfeifer (1986) found that the potential core length to slot height ratio x_p/H, increased with blowing ratio to a peak value before reducing to a plateau value at very high blowing ratios. x_p/H was also found to increase with a reduction in the MIX_N parameter (where $\text{MIX}_\text{N} = 0$ corresponds to a clean slot with realistically thick lip) and $H_\text{lip}/H_\text{slot}$ for the same blowing ratio. No relationship between the optimum blowing ratio with the largest x_p/H and MIX_N or $H_\text{lip}/H_\text{slot}$ was found. The MIX_N parameter is specific to combustor slot geometries so not all the terms have a direct equivalent in a trailing edge slot. However, the current study can be approximated as a clean slot with an equivalent $\text{MIX}_\text{N} = 0$ and $H_\text{lip}/H_\text{slot} = 1$. Their data for $\text{MIX}_\text{N} = 0.04$ and $H_\text{lip}/H_\text{slot} = 0.4$, the closest available to the current study, is plotted in Figure 6.13, showing a maximum x_p/H of 6.2 for $M = 1.05$. When compared with the Sturgess and Pfeifer (1986) data, x_p/H is greater for all blowing ratios, which may be due to the lower MIX_N. The current study does demonstrate the non-linear relationship between blowing ratio and x_p/H but there is insufficient data for a detailed comparison and the range of blowing ratios in the current study did not show a peak value in x_p/H.

Taslim et al. (1992), using a clean tangential slot with $H_\text{lip}/H_\text{slot} = 1$, $W_\text{slot}/H_\text{slot} = 5$ and $Re_\text{c} = 1400$–12000, reported a linear correlation $x_p/H = 5M$ which is also plotted on Figure 6.13. This is slightly lower than the current study and could be due to the difference in Re_c and $W_\text{slot}/H_\text{slot}$ used. The proximity of the lands in their study may have encouraged mainstream and coolant mixing, resulting in the shorter x_p/H compared to the current study. Predictions of x_p/H based on the correlations of Mukherjee (1976) are also plotted on Figure 6.13. The correlations take Re_c into account but are based on 2D slots without a finite slot width. These agree largely in magnitude with the current study while also being slightly higher than the data of Taslim et al. (1992). This indicates that the $W_\text{slot}/H_\text{slot}$ used in the current study is sufficiently high to nearly approximate a 2D slot along the centreline. However, the correlations of Mukherjee (1976) do predict a linear relationship between x_p/H and blowing ratio which is not apparent in the current

study.

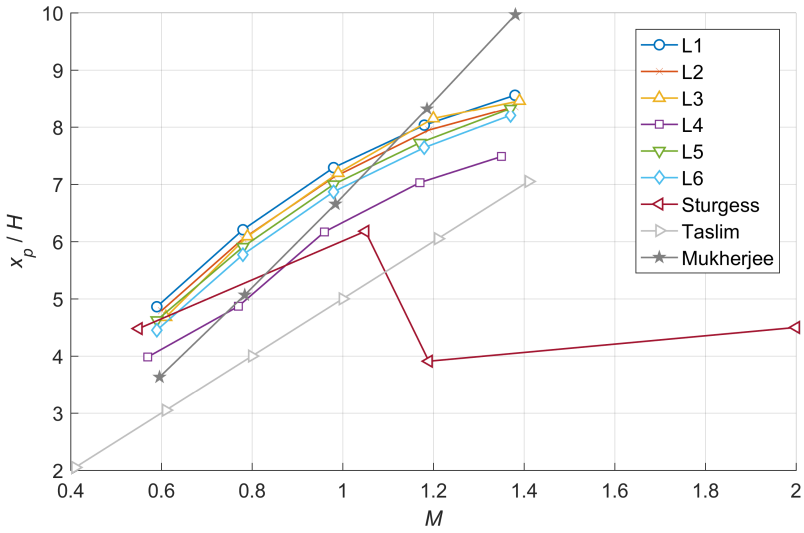


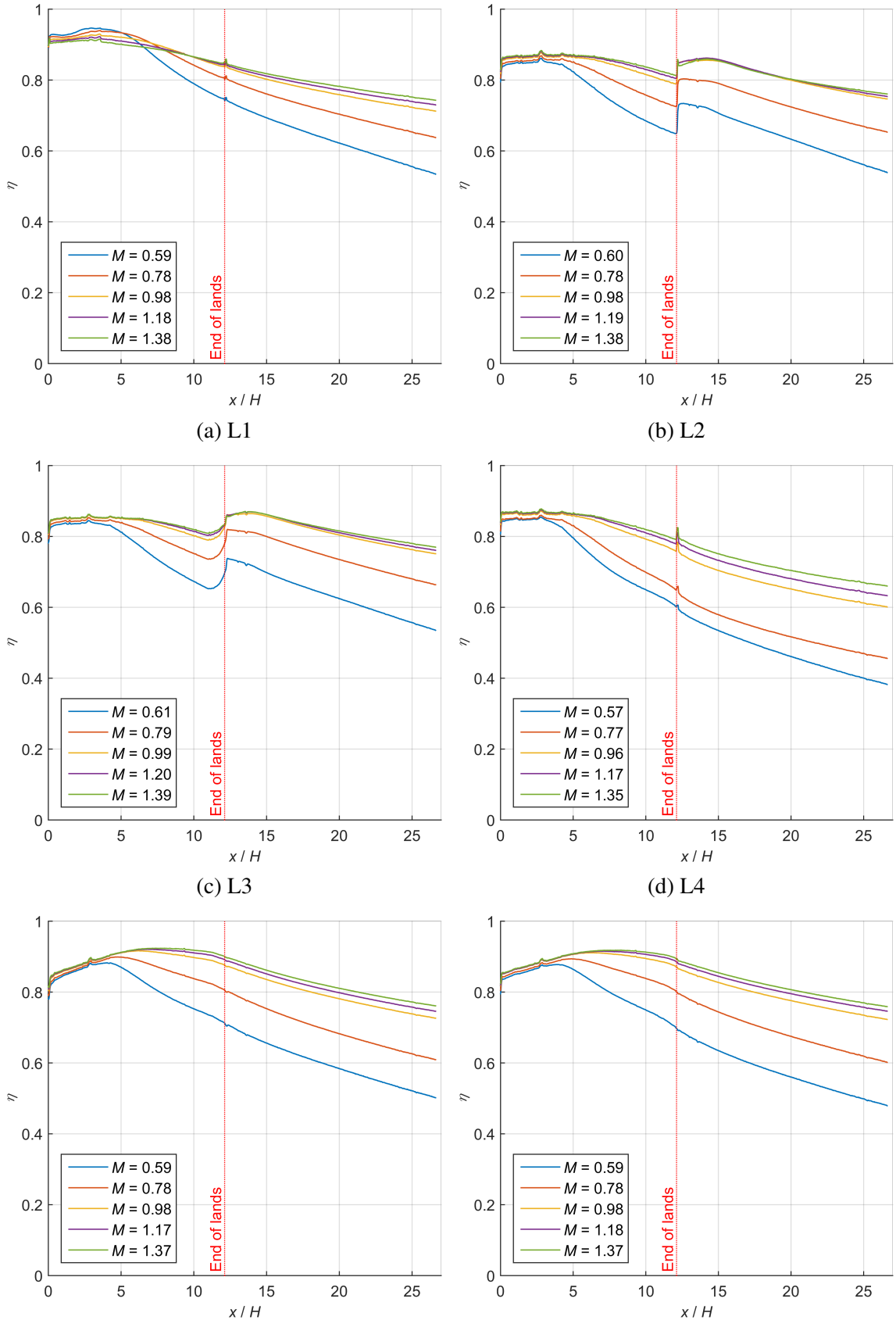
Figure 6.13: Potential core length comparison with literature

6.3.4 Spanwise averaged effectiveness

Figure 6.14 shows plots of spanwise averaged film cooling effectiveness including the lands. The average was taken over the entire region in between the centre-points of the two lands.

Including the lands results in a lower spanwise average for all the geometries, particularly up to the end of the lands. Geometry L1, shown in Figure 6.14a, had a starting effectiveness higher than the others at approximately 0.92. Since it had no lands, it was able to recover some effectiveness due to the coolant being able to spread into the gaps where the lands would be. This effect was more apparent for lower blowing ratio due to the lower coolant exit velocity relative to the mainstream, resulting in higher near-slot effectiveness at low blowing ratios, but this reversed before $x/H = 7.5$. Even with this enhancement however, the effectiveness at the end of the lands still reduced to 0.84 even for $M = 1.4$.

All the other geometries began with an effectiveness of approximately 0.85 since they all start with unity effectiveness across the slot and less than 0.2 on the lands. Geometries L2 and L3, shown in Figures 6.14b and 6.14c respectively, both showed a sudden



(a) L1 (b) L2

(c) L3 (d) L4

(e) L5 (f) L6

Figure 6.14: Spanwise averaged η, all land shapes

increase in effectiveness at the end of the lands due to the coolant spreading into the gap left but this decayed quickly. The rounded geometry had a smoother jump owing to its curvature, but overall was almost identical to the block geometry. After the lands, the effectiveness shown by both geometries was slightly higher than L1, showing that the presence of the lands, while reducing the average effectiveness up to the end of the lands, also slightly delayed mixing with the mainstream by delaying the creation of the wake of low effectiveness.

As in the plots of centreline effectiveness, geometry L4 (Figure 6.14d) showed substantially lower effectiveness, as the mainstream was pulled towards the cutback surface, encouraging earlier mixing with the coolant next to the lands, reducing effectiveness between the lands. Unlike with geometries L2 and L3, the plot does not exhibit a sudden increase in effectiveness because the mainstream air followed the land surface all the way down to the cutback surface which did not allow the coolant to spread into the gap.

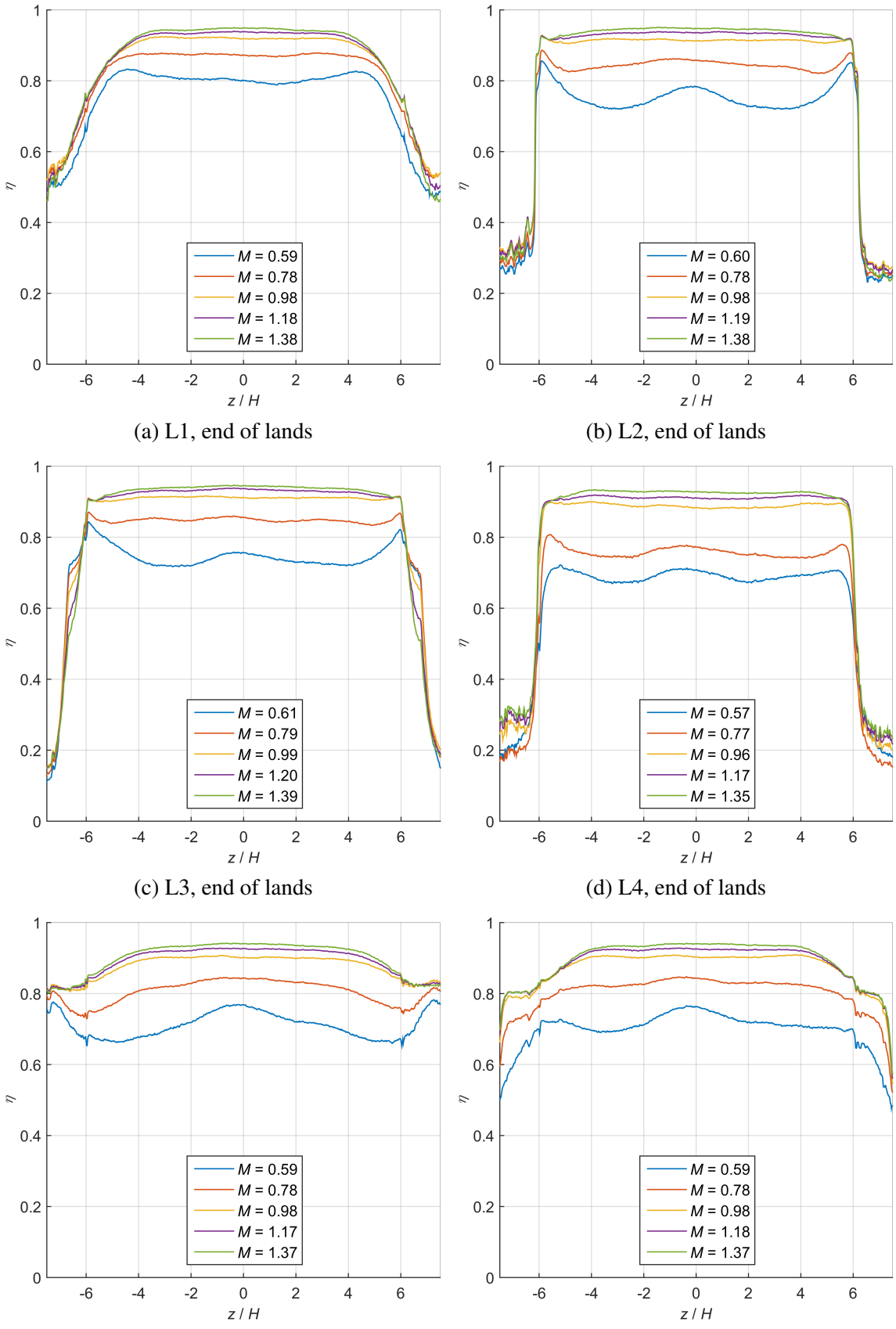
The diffuser geometries L5 and L6 (Figures 6.14e and 6.14f) initially showed a gradual increase in average effectiveness down the length of the lands due to the coolant being allowed to spread over a larger cutback region by the gradually reducing land width, replacing the low effectiveness lands that brought down the average for the other geometries. This resulted in a peak effectiveness of 0.92 at $x/H = 7.5$ for $M = 1.4$ and 0.88 at $x/H = 4.0$ for $M = 0.6$. For $M > 0.8$ the effectiveness from $x/H = 5$ onwards was highest of all the geometries, reaching 0.89 at the end of the lands for $M = 1.4$. However, for $M < 0.8$, the coolant flow was insufficient to fill the entire region, resulting in effectiveness at the end of the lands becoming lower than geometry L1, although still higher than the other geometries. Effectiveness after the lands was slightly lower compared to L2 and L3 since there was no recovery at the end of the lands. The tapered version of the diffuser geometry, L6, showed effectiveness levels almost identical to the non-tapered version L5 up to the end of the lands. At this point however, the wake of low effectiveness became apparent with the tapered version, resulting in slightly lower average effectiveness after the lands.

6.3.5 Spanwise variation of effectiveness at end of lands

Figure 6.15 shows plots of spanwise variation in film cooling effectiveness taken at the end of the lands. This included a 20 pixel ($1.7\,\mathrm{mm}$) wide strip parallel to the slot lip at a distance equal to the length of the lands where $x/H = 12.1$. The spanwise extent starts from the centre of the left hand side land where $z/H = -7.5$ and ends at the centre of the right hand side land where $z/H = 7.5$. $z/H = 0$ marks the centreline of the slot. $z/H = -6$ marks the right side edge of the land hand land, while $z/H = 6$ marks the left side edge of the right hand land. This x/H position is considered to be particularly important as it represents the trailing edge of the blade, where cooling is almost completely reliant on the film effectiveness and large local variations in effectiveness along the trailing edge can lead to high temperature gradients which cause thermal stresses in the blade metal. Since the geometries were symmetrical about the centreline, the resultant spanwise variation in effectiveness was also largely symmetrical about the centreline.

For geometry L1, shown in Figure 6.15a, the wakes of low effectiveness downstream of the internal bridges were visible on the left and right sides. While the effectiveness was quite constant across the middle of the slot, the increased mixing caused by the wakes led to a gradual decline in effectiveness to 0.5 directly behind the lands. This decline was due to the spread of the wake and begins at $z/H = 4$ for $M = 1.4$ and at $z/H = 4.5$ for $M = 0.6$. The overall maximum difference in effectiveness was approximately 0.35 at $M = 0.6$ and 0.45 at $M = 1.4$.

The drop in effectiveness was much greater for geometries L2, L3 and L4. For these geometries, effectiveness at the tip of the lands reduced to between 0.1 and 0.3, a drop of as much as 0.7 at $M = 1.4$. Geometry L2, shown in Figure 6.15b, had a very sharp drop due to the square edged tip keeping effectiveness low all the way to the very end of the land. Geometry L3, shown in Figure 6.15c, had a more gradual drop due to its rounded tip. The minimum effectiveness at the tip of the lands appeared to be largely insensitive to blowing ratio for L2 and L3. Both of these geometries maintained high effectiveness on the cutback in between the lands, right up until the very edge of the



(a) L1, end of lands

(b) L2, end of lands

(c) L3, end of lands

(d) L4, end of lands

(e) L5, end of lands

(f) L6, end of lands

Figure 6.15: Spanwise varation of η, all land shapes

lands. At $M > 0.8$, the effectiveness profile was fairly constant between the lands, but at $M < 0.8$, the highest effectiveness was next to the lands, with a lower peak in the centre and even lower effectiveness either side of the centre. The maximum difference in effectiveness excluding the drop due to the lands was as much as 0.13 between the peak at the land edge and the dips either side of centre for L2 at $M = 0.6$. The overall maximum difference in effectiveness for L2 was approximately 0.6 at $M = 0.6$ and 0.7 at $M = 1.4$. For L3, this was 0.65 at $M = 0.6$ and 0.75 at $M = 1.4$.

Geometry L4, shown in Figure 6.15d, had a reduction in effectiveness that began a small distance before the land edge, at $z/H = 5.5$. Again this was due to the mainstream air being pulled down towards the cutback, resulting in earlier mixing with the coolant such that the mixing already encroaches into the cutback region at this point. Increasing blowing ratio did lead to a slightly higher minimum effectiveness at the tip of the lands, up to 0.3 from 0.2. The overall maximum difference in effectiveness was approximately 0.55 at $M = 0.6$ and 0.65 at $M = 1.4$.

Geometries L5 and L6, shown in Figures 6.15e and 6.15f respectively, displayed significantly higher effectiveness at the tips of the lands, going no lower than 0.75 for L5 and 0.5 for L6. The drop was greater for L6 due to the tapering of the land, bringing the mainstream flow down to the cutback and increasing mixing. With effectiveness in between the lands remaining similar in profile to L2 and L3, this resulted in a considerably more consistent effectiveness level across the span. At low blowing ratios, there still remained a higher concentration of coolant in the centre and next to the lands, resulting in two dips in effectiveness either side of the centre. The overall maximum difference in effectiveness for L5 was approximately 0.1 at $M = 0.6$ and 0.15 at $M = 1.4$. For L6, this was 0.25 at $M = 0.6$ and 0.35 at $M = 1.4$.

6.3.6 Area averaged effectiveness

Figure 6.16 shows a plot of area averaged film cooling effectiveness for all six geometries at their tested blowing ratios. This included the cutback and land top surfaces

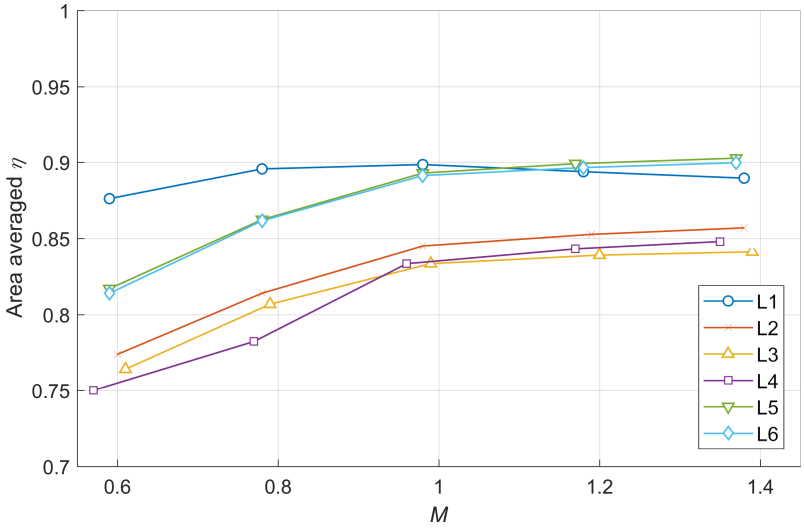


Figure 6.16: Area averaged η, all land shapes

up to the end of the lands where $x/H = 12.1$. It gives an overall picture of the relative performance of each geometry over the region most relevant to trailing edge cooling.

The "no lands" geometry L1 showed an area averaged effectiveness that was fairly constant across the range of blowing ratios tested and higher than all the other geometries for $0.6 < M < 1.0$. This was due to the higher effectiveness in the gap regions where the lands would have been. However, the increase in effectiveness at higher blowing ratios was compensated for by the lower effectiveness in the gap regions due to the more pronounced wake from the internal bridges (See Section 6.3.1), resulting in a slight reduction in area averaged effectiveness.

Geometries L2–4 all performed similarly, with effectiveness increasing with blowing ratio in a similar fashion to the potential core length as shown in Section 6.3.3. However, the performance of geometry L4 was not as severely affected by the tapered design as the potential core length. This was due to the slight increase in effectiveness along the edges of the lands as observed in Section 6.3.1 which compensated for the reduction in effectiveness on the cutback. Since the effectiveness data after the end of the lands was excluded for this plot, the large wakes of low effectiveness created by tapering the lands that caused significantly lower spanwise averaged effectiveness after the lands had no effect.

The diffuser geometries L5 and L6 showed significantly higher area averaged effec-

tiveness across the board compared to L2–4. This was due to the reduced land surface area, reducing the size of the very low effectiveness land top region and replacing it with more cutback surface that the coolant is able to cover. Unlike geometry L1, the gradual reduction of the land allowed the coolant to spread into the extra cutback surface without creating a wake of low effectiveness, resulting in slightly higher area averaged effectiveness at $M > 1.0$ compared to geometry L1. Again, since the data after the end of the lands was excluded for this plot, tapering the land for L6 made little difference to the area averaged effectiveness.

6.4 Summary and conclusions

Detailed distributions of adiabatic film cooling effectiveness have been measured over the cutback and land top surfaces of large scale geometries representing turbine blade trailing edges using the PSP technique. Six different land geometries were tested with blowing ratio ranging from 0.6 to 1.4 with a density ratio of 1. Re_c ranged from 1400 to 2750.

While the simplified nature of the experimental model limits the direct applicability of the measurements to a real blade or vane, the first phase of experiments aimed to compare six land shape designs and show the relative performance of each in terms of effectiveness. The conclusions from these comparisons are as follows:

- Increasing blowing ratio increased the length of the potential core and also reduced the rate at which effectiveness decayed.
- The length of the potential core, x_p was similar in magnitude to 2D correlations from Mukherjee (1976) and mostly insensitive to the land geometry, suggesting a slot width large enough that flow at the centreline was nearly 2D in nature.
- A non-linear relationship was found between blowing ratio and potential core length.

- With all geometries, at all blowing ratios tested, the coolant was largely unable to wash over the top surfaces of the lands resulting in low effectiveness on the land top surface.

- Having no lands at all increased the spanwise averaged effectiveness since the coolant was able to spread into the gap left by the lands.

- Tapering the lands did not significantly encourage coolant flow to wash over the top.

- Tapering the lands pulled the mainstream flow down to the cutback surface, creating a wake of mainstream flow after the land which the coolant flow was unable to penetrate.

- This also encouraged mixing with the flow on the cutback, reducing effectiveness next to the lands.

- The diffuser geometries performed well for $M > 0.8$ as the coolant was able to spread and fill out the increased cutback area.

- These geometries provided higher spanwise averaged effectiveness than all other geometries, including the "no lands" geometry from approximately $x/H = 5$ onwards up until the end of the lands and higher area averaged effectiveness than all other geometries for $M > 1.0$.

- The non-tapered diffuser geometry performed best but the tapered diffuser geometry more closely approximates the land on a real turbine blade with a very small reduction in effectiveness.

- At $M = 0.6$, the coolant was unable to fill the expanding cutback surface and the film decayed faster, resulting in a lower effectiveness than the "no lands" case at the end of the lands, although still better than the other geometries.

In the case of turbine blades and vanes, the end of the lands is also typically at the trailing edge, so the effectiveness after that point is not of great concern (although it may be important in other slot cooling applications, for example, in a combustor liner). The region nearest the trailing edge is generally one of the hottest and most challenging parts to cool, so the effectiveness just before the end of the lands is very important. For this particular application, for $M = 0.8$–1.4, the diffuser lands provided the most favourable effectiveness, especially near the end of the lands, as well as the most consistent spanwise effectiveness at the end of the lands. At $M = 0.6$, no lands is preferable, although if this is not structurally possible, the tapered diffuser land is the next best choice.

As the diffuser geometries performed the best overall and the tapered version more closely approximates a real blade trailing edge, the tapered diffuser geometry L6 was used in all subsequent phases.

Chapter 7

Effectiveness Measurements — Cross Corrugated Slots

7.1 Introduction

The objective of the second phase of experiments was to determine whether or not the novel cross corrugated slot design is suitable for slot film cooling. This was accomplished by measuring film effectiveness using a variety of cross corrugated slot designs.

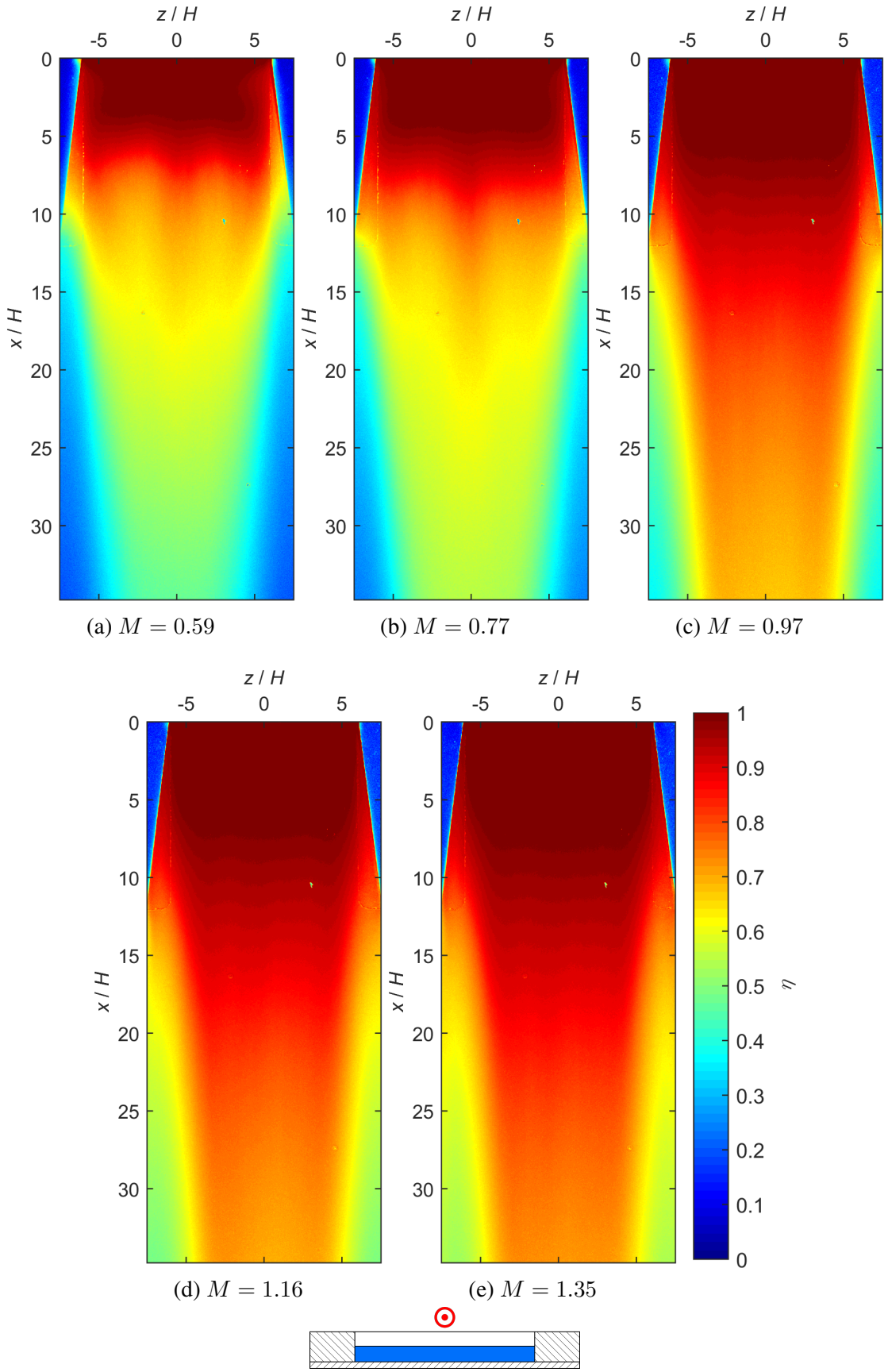
The geometries are detailed in Section 5.5. Eight cross corrugated slot geometries were tested encompassing two included angles of $90°$ and $120°$ with four exit alignments each, shown in Figure 5.15. The tapered diffuser land shape (designated as L6 in Chapter 6) was used in all cases. This chapter shows the results from phase 2 and compares the performance of the various geometries with the baseline plain rectangular slot. These results have been partially published in Wong et al. (2016a).

7.2 2D film cooling effectiveness distributions

The PSP technique allows high resolution 2D adiabatic film effectiveness measurements over the cutback surface and top of the lands to be made. The approximate view area and coordinate system is defined in Figure 6.1, where x is the downstream distance

from the slot exit and z is the spanwise displacement from the centreline. These are non-dimensionalised for all geometries by the slot height of the baseline plain rectangular slot geometry G0 to give x/H and z/H, where $H = H_{\text{slot}} = 4.6\,\text{mm}$. Note that even though the cross corrugated geometries do not have the same exit height as the plain rectangular slot, they were normalised by the same amount to aid back-to-back comparisons. Measurements were taken for $M = 0.6, 0.8, 1.0, 1.2, 1.4$.

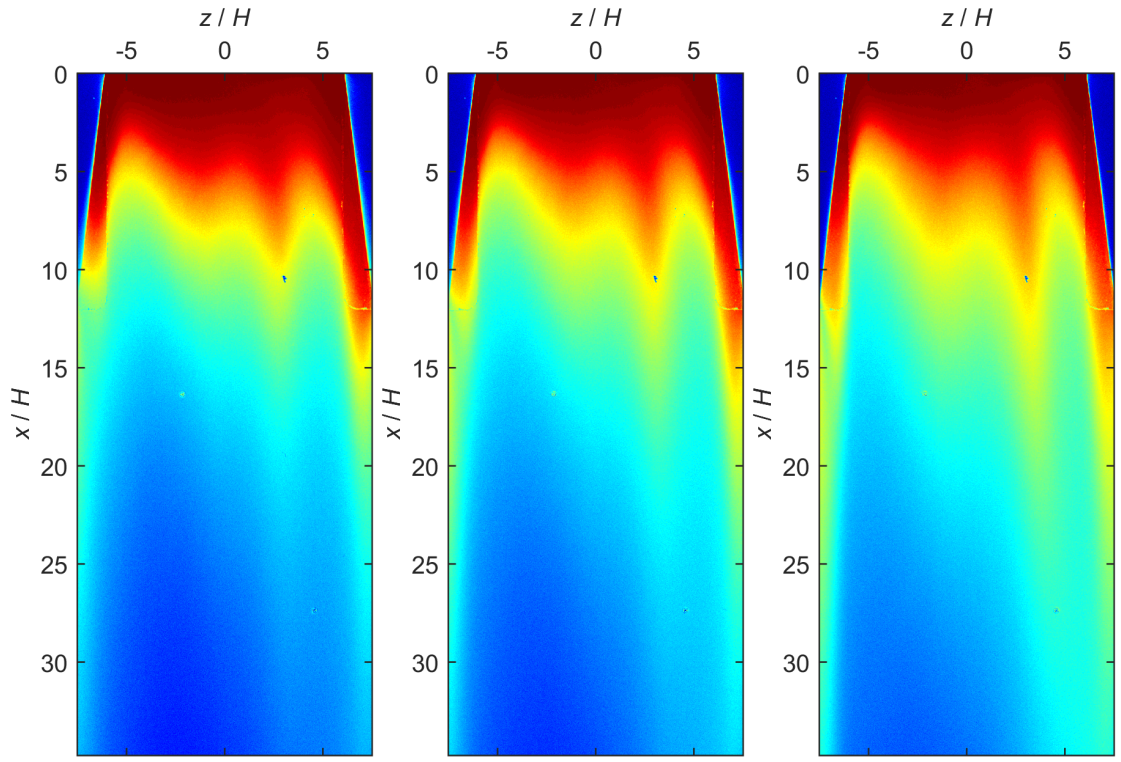
Figures 7.1, 7.2, 7.3, 7.4, 7.5, 7.6, 7.7, 7.8 and 7.9 show all the 2D plots of effectiveness taken in phase 2. All of the figures show a plan view of the cutback region and lands. The slot exit and lip is aligned with the top border of the plots, i.e. where $x/H = 0$. The centreline is at the midpoint between the lands where $z/H = 0$. Blue regions show poor coverage from the nitrogen coolant and correspond to low film cooling effectiveness and red regions correspond to high effectiveness. The lands can be seen as the predominantly blue regions in the top left and top right corners or each plot.



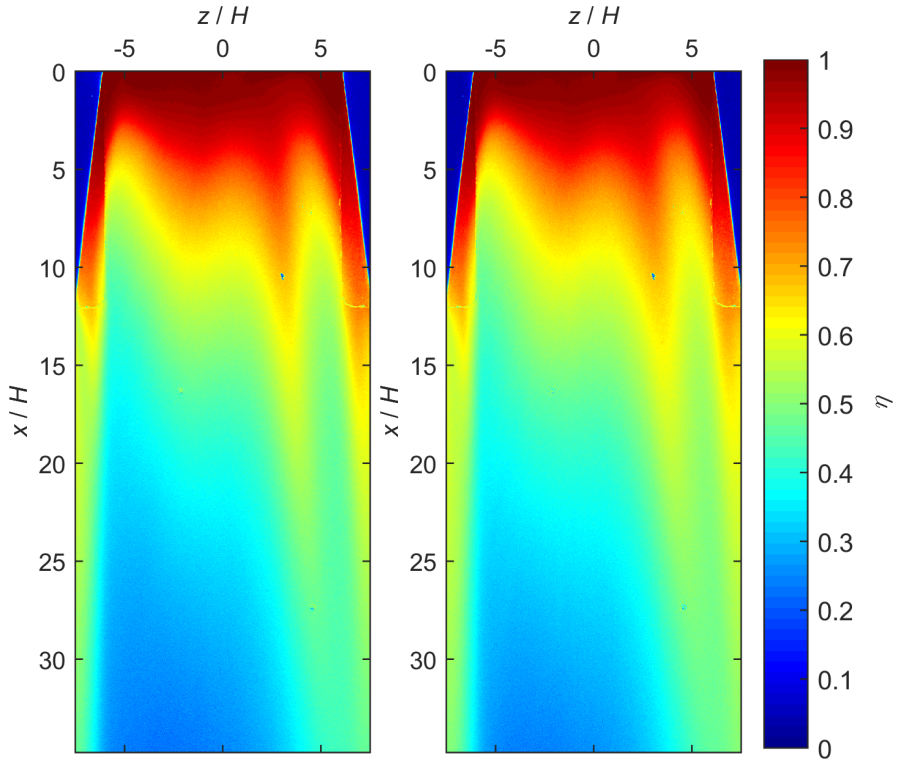
(a) $M = 0.59$ (b) $M = 0.77$ (c) $M = 0.97$

(d) $M = 1.16$ (e) $M = 1.35$

Figure 7.1: 2D η distributions, G0



(a) $M = 0.58$ (b) $M = 0.76$ (c) $M = 0.95$



(d) $M = 1.13$ (e) $M = 1.31$

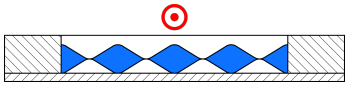
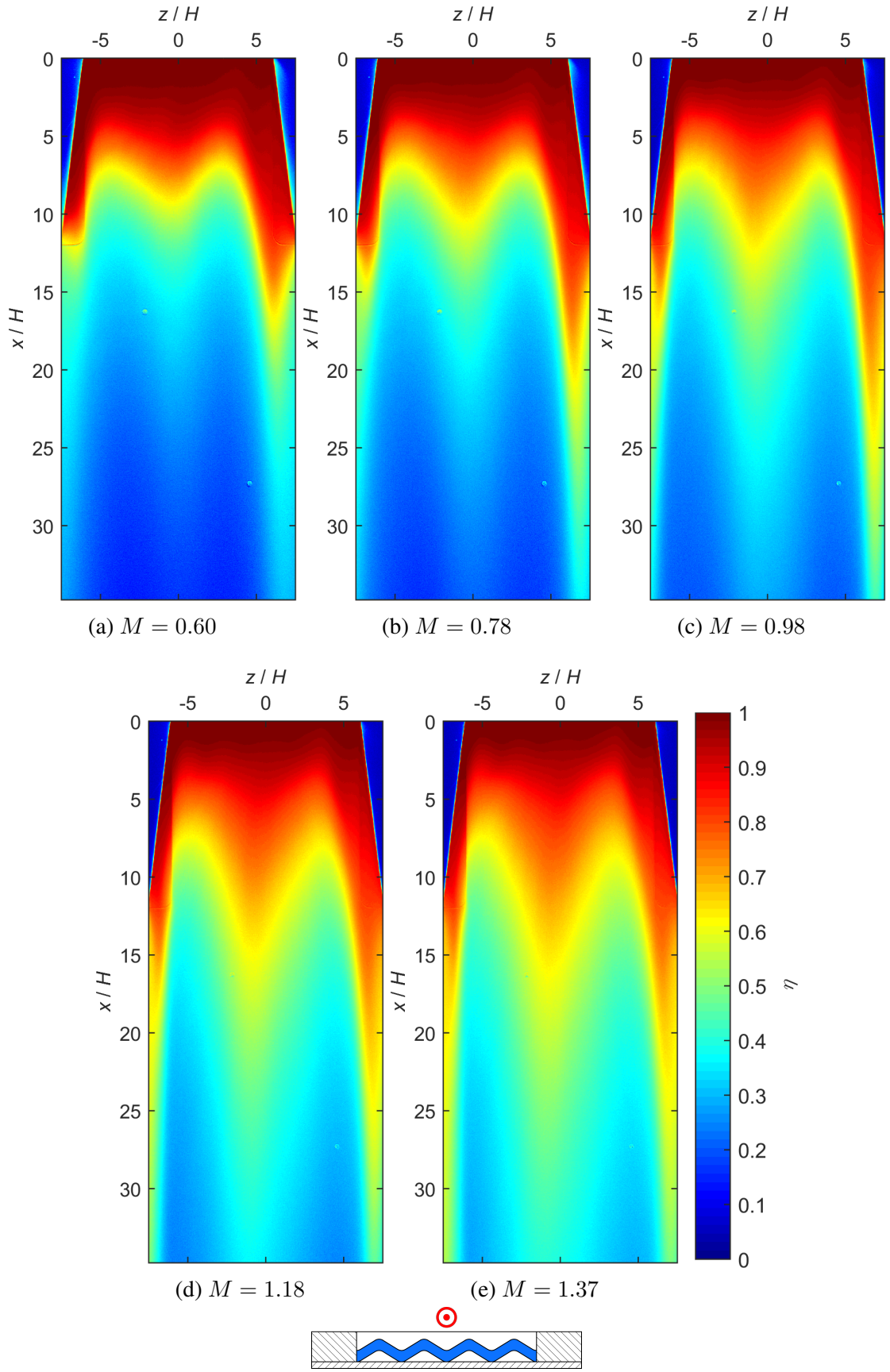


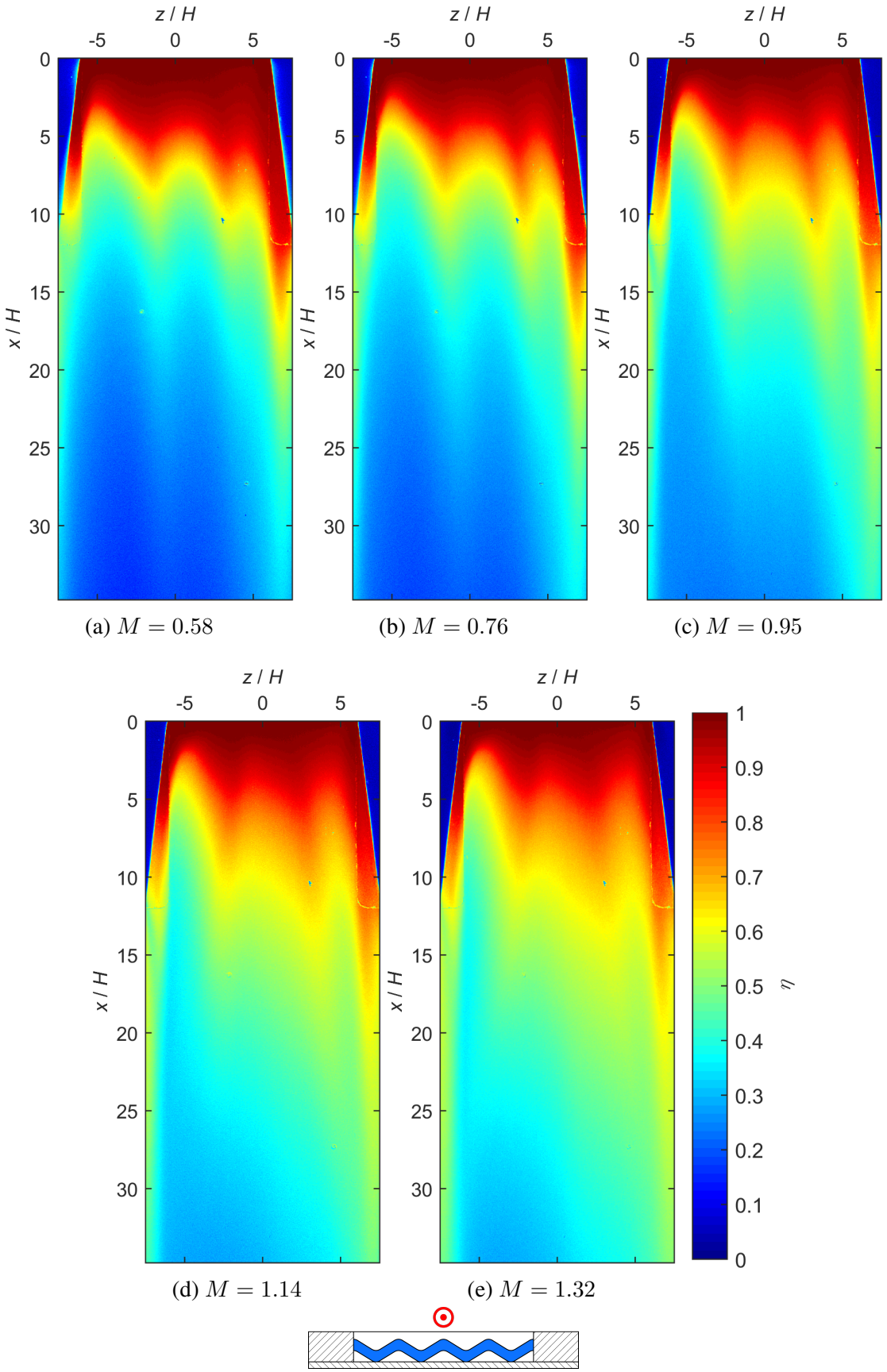
Figure 7.2: 2D η distributions, G1



(a) $M = 0.60$ (b) $M = 0.78$ (c) $M = 0.98$

(d) $M = 1.18$ (e) $M = 1.37$

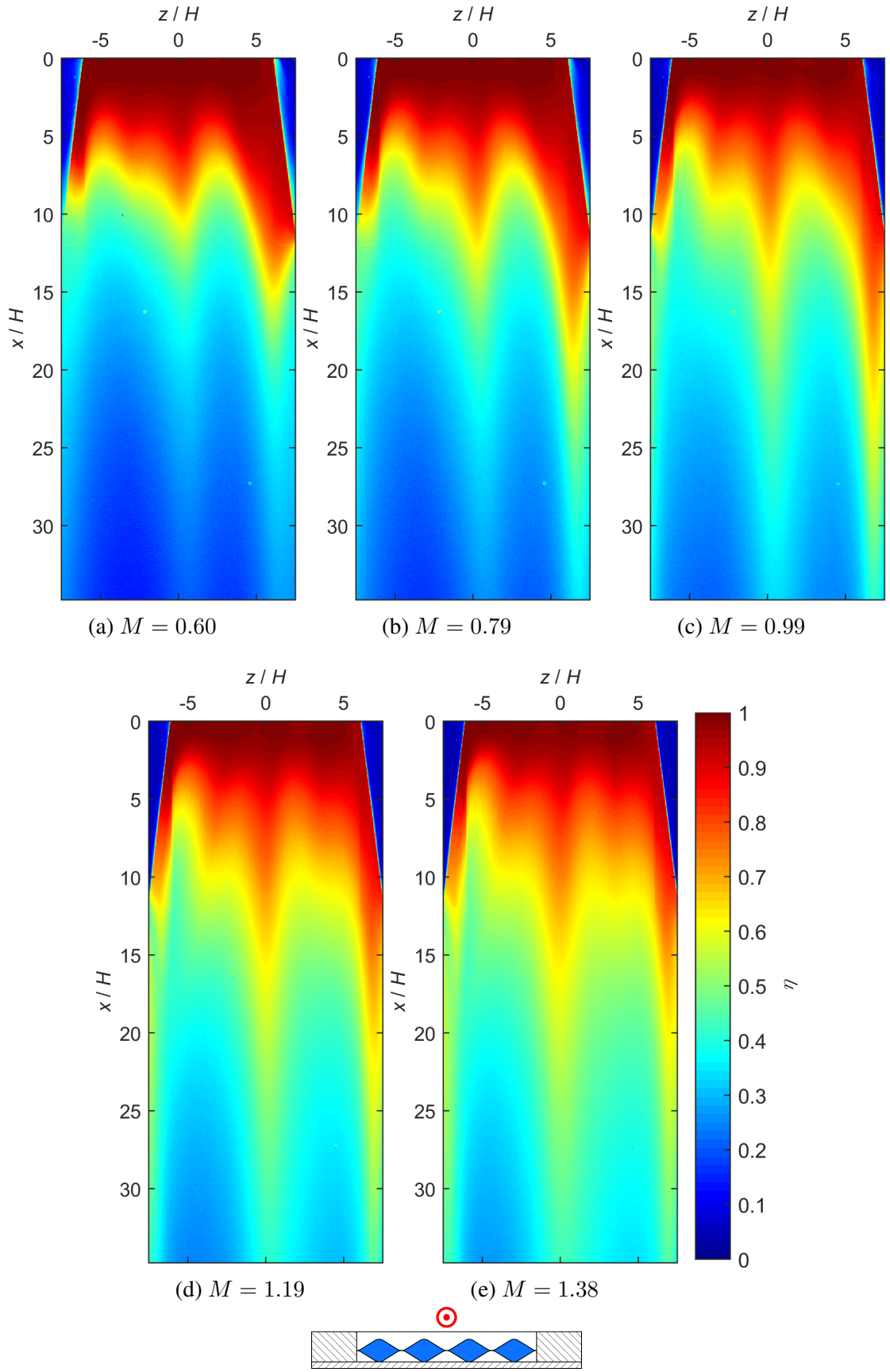
Figure 7.3: 2D η distributions, G2



(a) $M = 0.58$ (b) $M = 0.76$ (c) $M = 0.95$

(d) $M = 1.14$ (e) $M = 1.32$

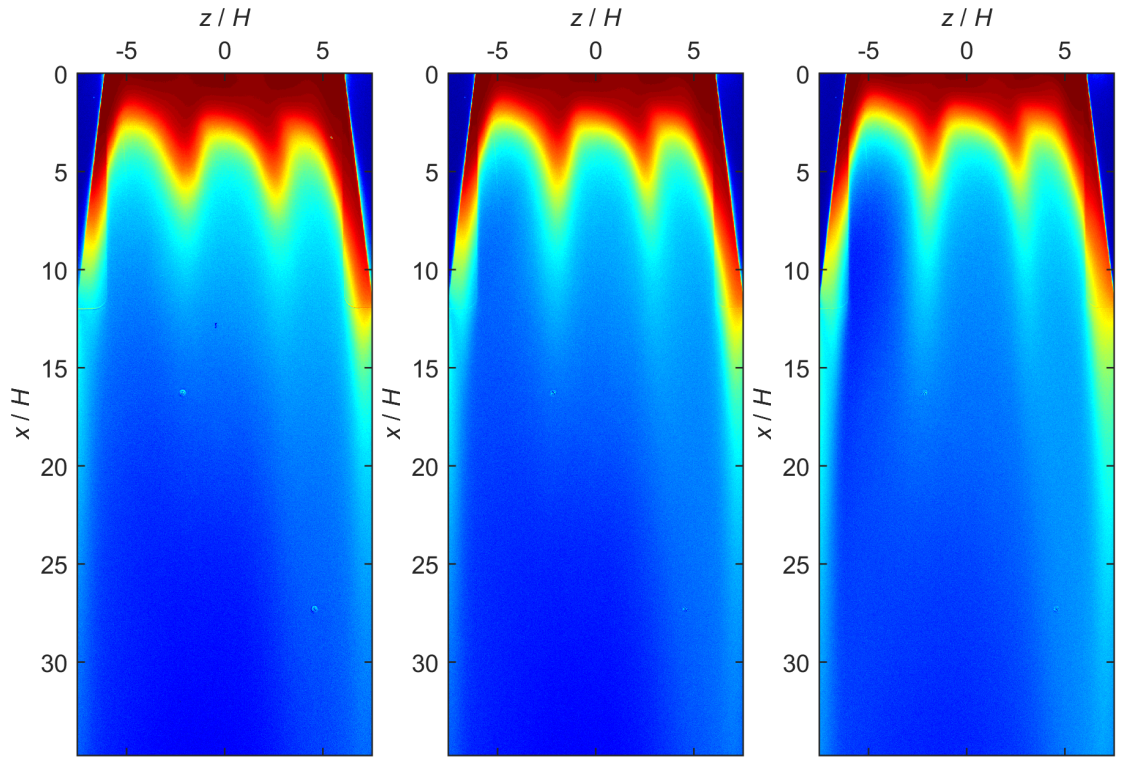
Figure 7.4: 2D η distributions, G3



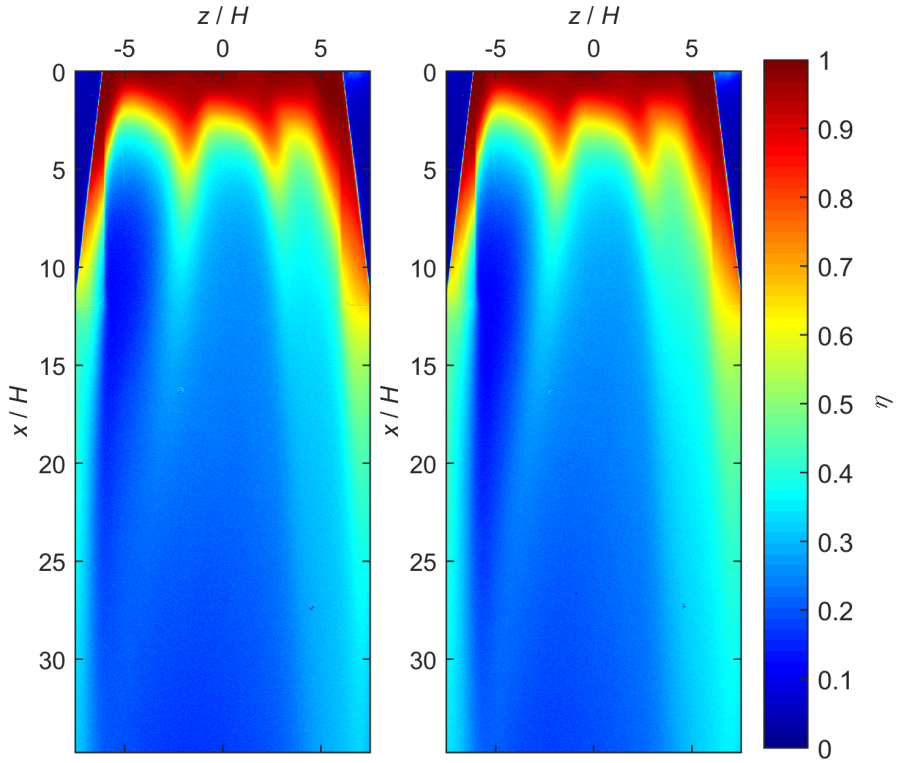
(a) $M = 0.60$ (b) $M = 0.79$ (c) $M = 0.99$

(d) $M = 1.19$ (e) $M = 1.38$

Figure 7.5: 2D η distributions, G4



(a) $M = 0.60$ (b) $M = 0.78$ (c) $M = 0.98$



(d) $M = 1.18$ (e) $M = 1.37$

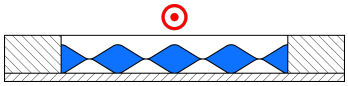
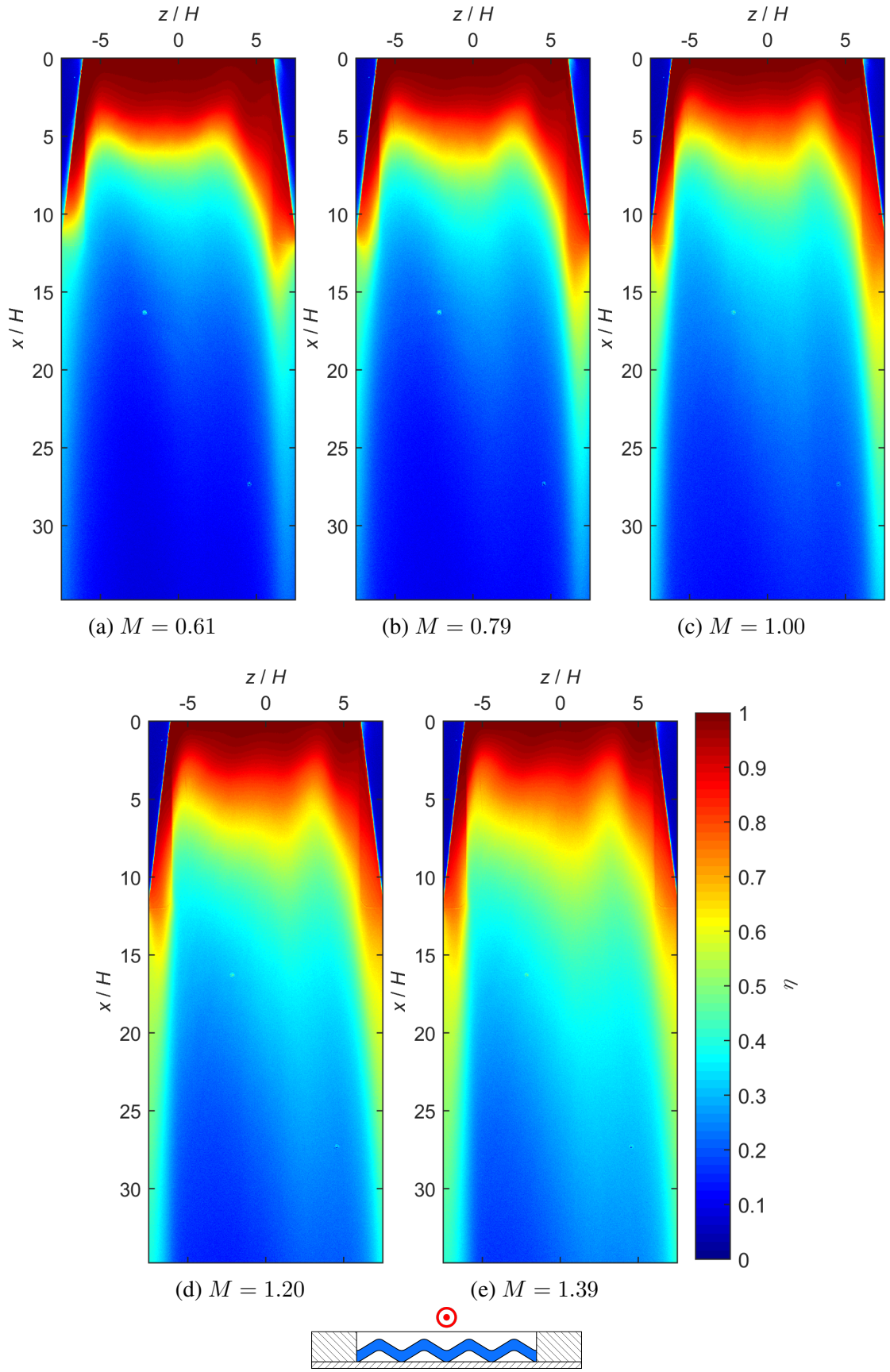


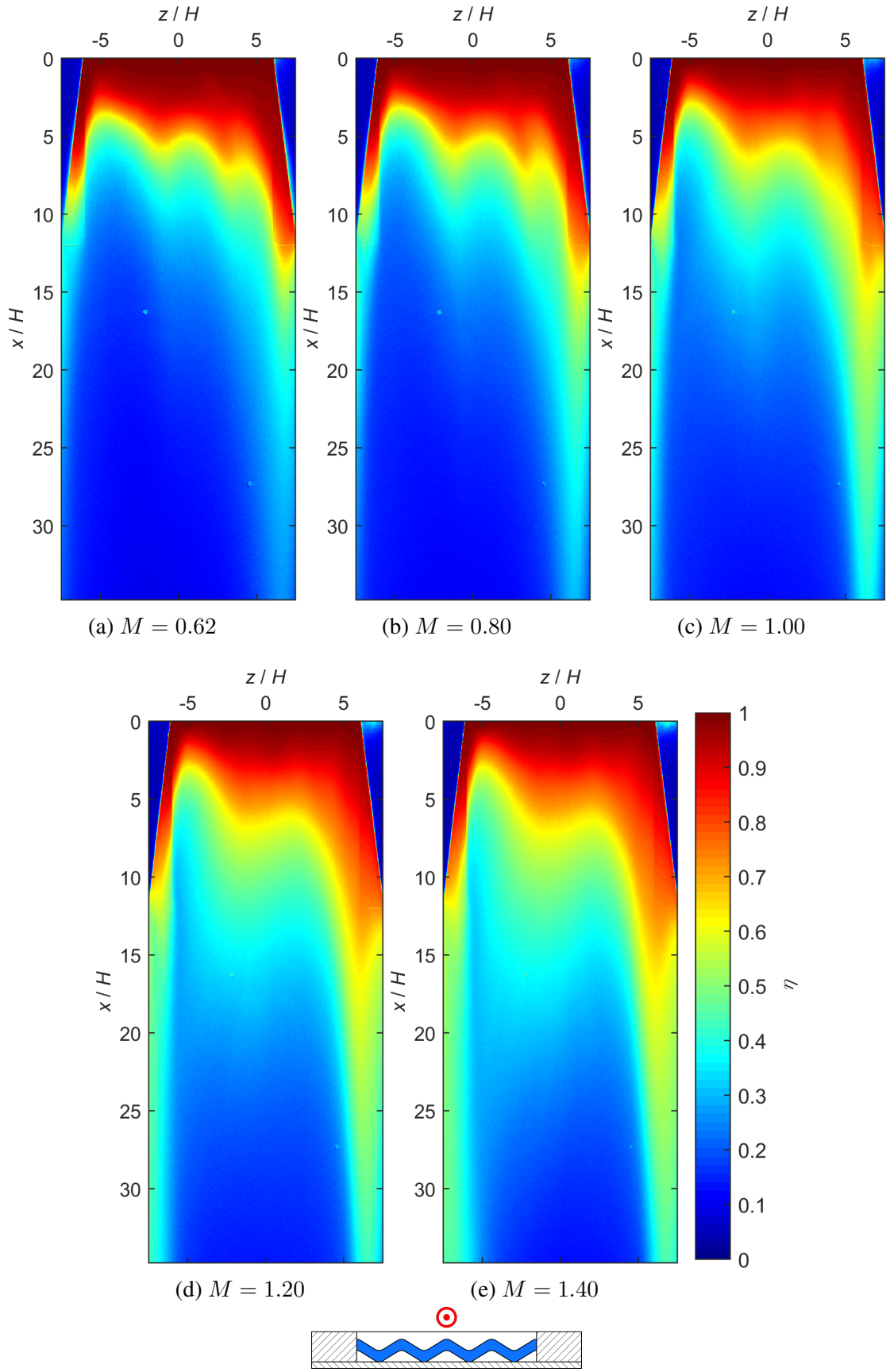
Figure 7.6: 2D η distributions, G5



(a) $M = 0.61$ (b) $M = 0.79$ (c) $M = 1.00$

(d) $M = 1.20$ (e) $M = 1.39$

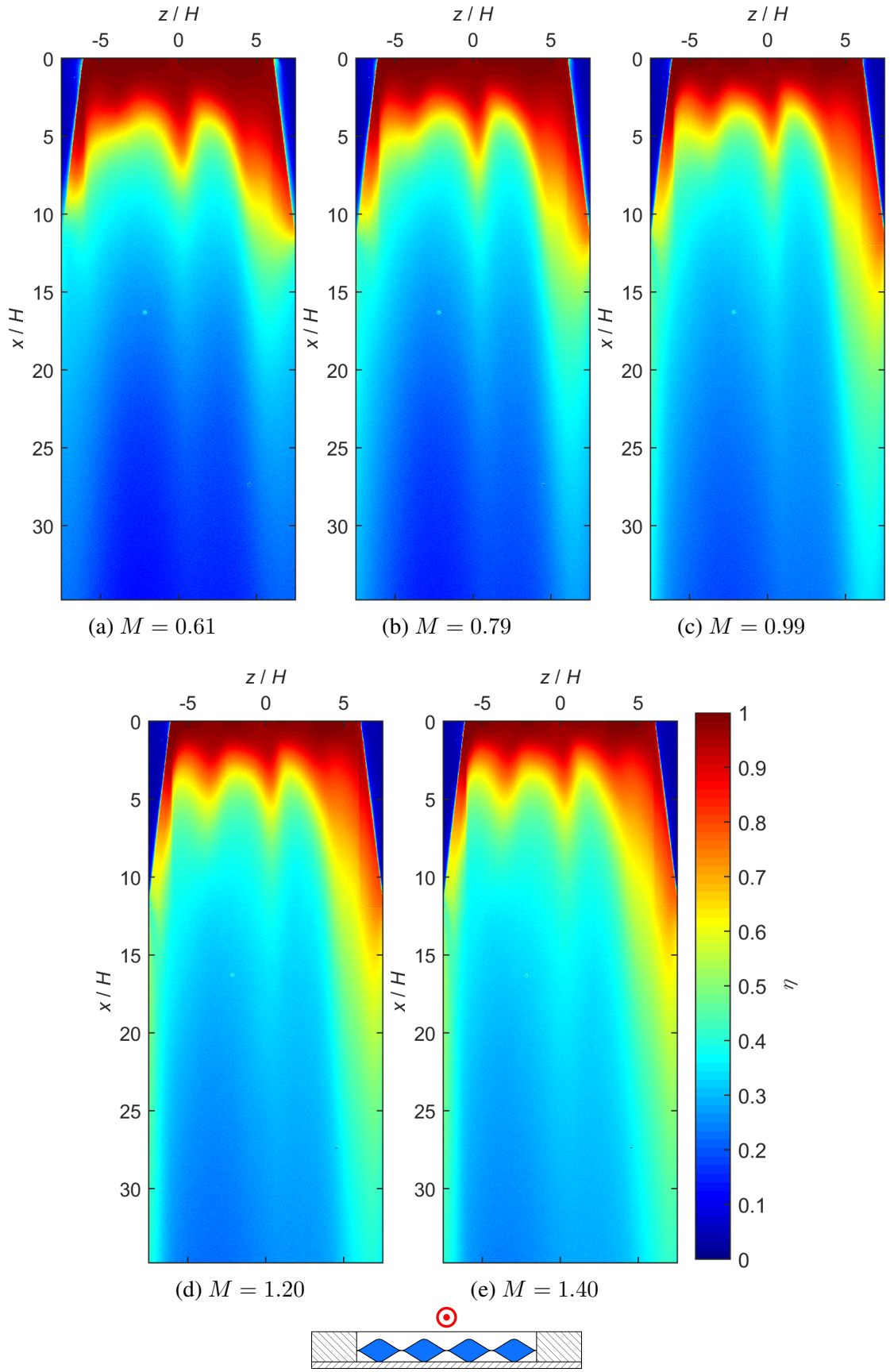
Figure 7.7: 2D η distributions, G6



(a) $M = 0.62$ (b) $M = 0.80$ (c) $M = 1.00$

(d) $M = 1.20$ (e) $M = 1.40$

Figure 7.8: 2D η distributions, G7



(a) $M = 0.61$ (b) $M = 0.79$ (c) $M = 0.99$

(d) $M = 1.20$ (e) $M = 1.40$

Figure 7.9: 2D η distributions, G8

7.3 Discussion

7.3.1 Baseline geometry G0 inconsistency with phase 1

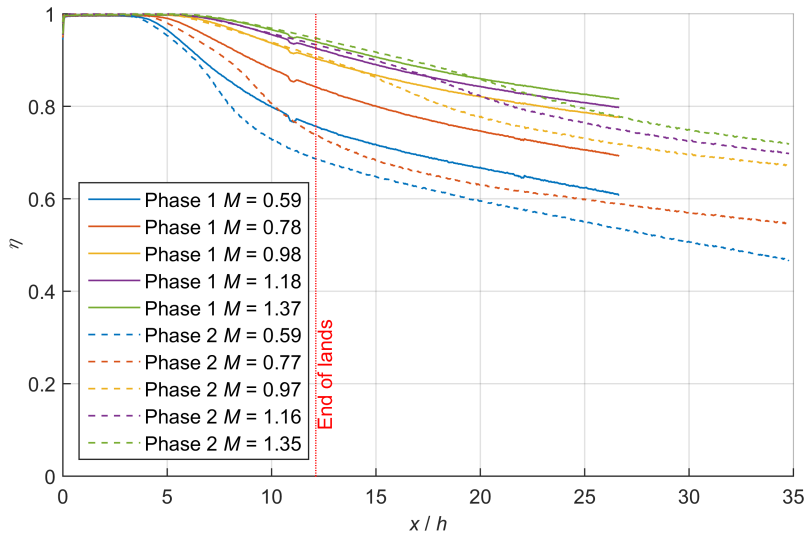


Figure 7.10: Centreline effectiveness comparison between phase 1 and 2

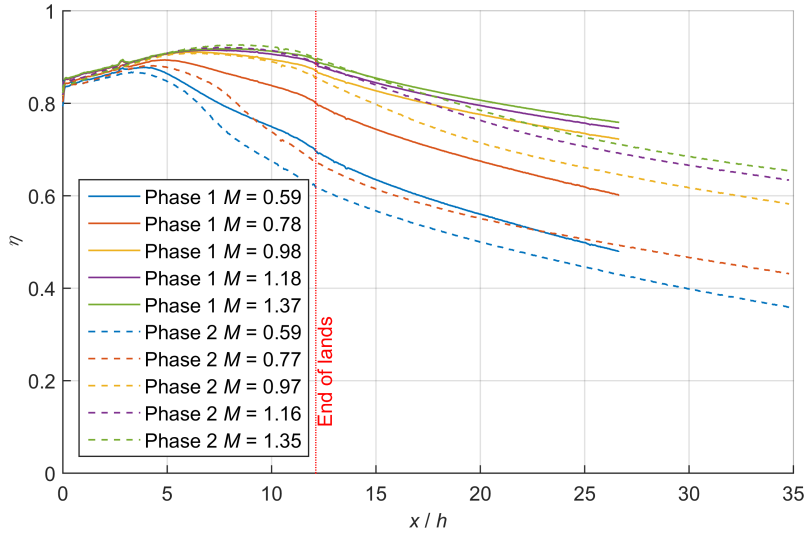


Figure 7.11: Spanwise averaged effectiveness comparison between phase 1 and 2

Figure 7.1 shows effectiveness using the same slot and land configuration as used for geometry L6 in phase 1. While the shape of the effectiveness plot is similar, it can be seen that effectiveness decayed at a faster rate in phase 2. This is illustrated in a centreline effectiveness comparison shown in Figure 7.10 and a spanwise averaged effectiveness comparison shown in Figure 7.11.

At the higher blowing ratios of 1.0 to 1.4, the results from phase 1 and phase 2 were similar up to the end of the lands. Phase 2 centreline effectiveness and spanwise averaged effectiveness was within $0.9\,\%$ and $1.7\,\%$ respectively of phase 1, although this increased after the end of the lands. However, at the lower blowing ratios, there was greater divergence in effectiveness between the two phases. For $M = 0.6$ at the end of the lands, centreline effectiveness was reduced by $9.4\,\%$ and spanwise averaged effectiveness was reduced by $11.2\,\%$. For $M = 0.8$ at the end of the lands, the difference was the greatest. Centreline effectiveness was reduced by $12.4\,\%$ and spanwise averaged effectiveness was reduced by $15.8\,\%$.

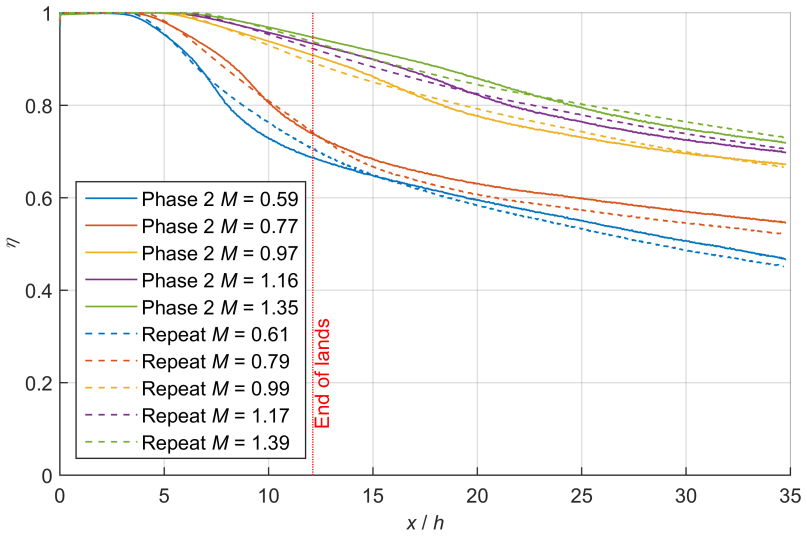


Figure 7.12: Centreline effectiveness comparison between phase 2 and repeat

The phase 2 set-up with the baseline geometry G0 was reassembled and the experiment was repeated under the same conditions. The centreline effectiveness comparison with the first phase 2 attempt is shown in Figure 7.12 and the spanwise averaged effectiveness comparison is shown in Figure 7.13. It can be seen that the repeated experiment is largely in agreement with the first phase 2 attempt, even though the blowing ratios were slightly higher. Centreline effectiveness at the end of the lands was within $3.2\,\%$ and spanwise averaged effectiveness at the same distance was less than $0.8\,\%$.

Since the effectiveness is largely unchanged after repeating the phase 2 test, it is likely that the difference between the phase 1 and phase 2 results is due to one of the changes

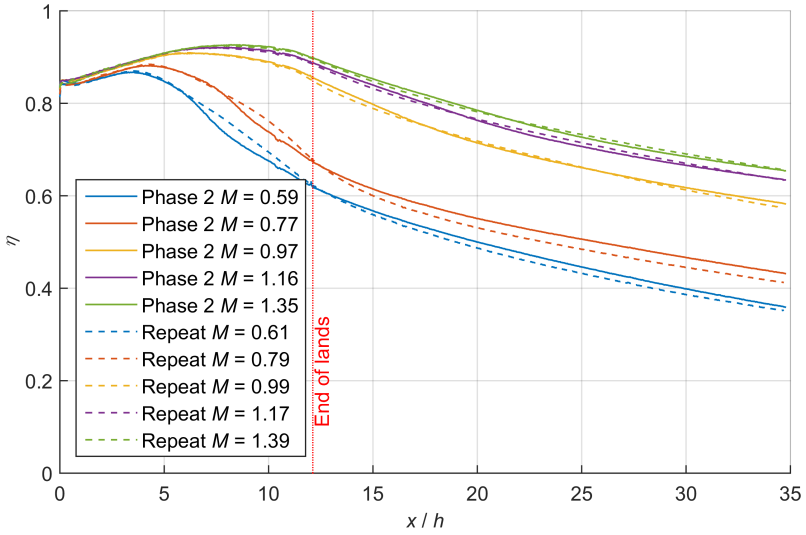


Figure 7.13: Spanwise averaged effectiveness comparison between phase 2 and repeat

in the set-up between the two phases. While this makes it difficult to directly compare the results between phase 1 and the other phases, the repeated phase 2 test shows that the results are still consistent if the set-up is not altered. Therefore, it is still valid to make back-to-back comparisons between the geometries tested within each phase, so long as the baseline is retested with the new set-up, as has been done here.

7.3.2 Cutback effectiveness

G1–4, 90° included angle

The channels of the cross corrugated geometries G1–4 resulted in the majority of the coolant flow exhausting at an angle to the mainstream flow. The lower corrugation channels (nearer to the cutback surface) directed the flow $45°$ towards the left while the upper corrugation channels directed the flow $45°$ towards the right. The resulting coolant coverage in the spanwise direction was very uneven and also asymmetric, with visible peaks and dips in effectiveness shown in Figures 7.2 to 7.5.

Considering first the 2D effectiveness contours of geometry G1 shown in Figure 7.2, four distinct peaks of high effectiveness can be seen extending downstream from the slot exit.

The left-most and right-most peaks appeared to stick to the sides of the lands. This

was likely due to two effects: coolant following the walls of the internal bridges and leaving the slot parallel to the mainstream flow and the coolant from the angled channels impinging on the land wall after leaving the slot. By following the sides of the lands, effectiveness remained high further away from the slot. This effect was so significant that at low blowing ratio, effectiveness near the lands was the same or higher for geometry G1 compared to the baseline geometry G0 shown in Figure 7.1a. What appears to be a line of discontinuity is visible near the lands. This corresponds to the edge of the land insert and is likely due to the land insert surface not being perfectly flush to the cutback surface. The discontinuity was not obvious in Figure 7.1 but combined with the extremely sudden change in effectiveness across the edge caused by the flow pattern from a cross corrugated slot, it became more pronounced in Figures 7.2 to 7.5.

At all blowing ratios shown in Figure 7.2, the central two peaks appeared to be angled slightly to the right and the peak on the left was less pronounced and did not extend as far downstream as the peak on the right. This shows an overall effectiveness bias towards the right and was due to the asymmetric nature of the coolant ejection. Since the lower channels ejected coolant to the left, this created a region of low pressure on the right side of the cutback surface. The upper channels ejected coolant to the right, creating a buffer layer which was drawn downwards onto the surface. However this also created a "gap" region in the upper left which drew up the lower coolant, encouraging mixing with the mainstream flow. This resulted in relatively high effectiveness on the right compared to the left. The rightmost peak also combined with the aforementioned high effectiveness flow following the land, resulting in the largest peak along the right side land. Increasing blowing ratio resulted in the same flow structure, but spread it out further in the downstream direction.

A similar flow structure was evident on geometries G2–4, but with some differences in the strength and position of the peaks and dips in effectiveness. The two strongest peaks remained next to the sides of the lands as in G1, with the right side peak being the largest in all cases. At this included angle, the position of the top plate channels appeared to have the greatest importance. Geometries G1 and G3 shared the same top plate and had a very

similar shape, with two peaks attached to the lands, and two peaks in the middle, although G3 had slightly more defined peaks in the middle (Figure 7.4).

For geometry G2, shown in Figure 7.3, the two central peaks were shifted to the right, resulting in a broad peak slightly left of centre of the slot, and a peak on the right which merged with the peak attached to the land to form a much broader peak. Geometry G4, shown in Figure 7.5, shared the top plate with G2 and had a similar main peak near the centre of the slot, but G4 had a smaller peak visible to the left, distinct from the left-most peak attached to the land. At higher blowing ratio, another smaller peak became visible to the right of the central peak, separating itself from the peak attached to the land. This was likely a result of the exit alignment of G4 creating more defined jets, especially at higher blowing ratio.

G5–8, 120° included angle

Increasing the included angle to 120° forced the coolant flow to exhaust at a steeper angle to the mainstream flow. The lower corrugation channels (nearer to the cutback surface) directed the flow 120° towards the left while the upper corrugation channels directed the flow 120° to the right. This steep angle resulted in a drastic reduction in effectiveness overall.

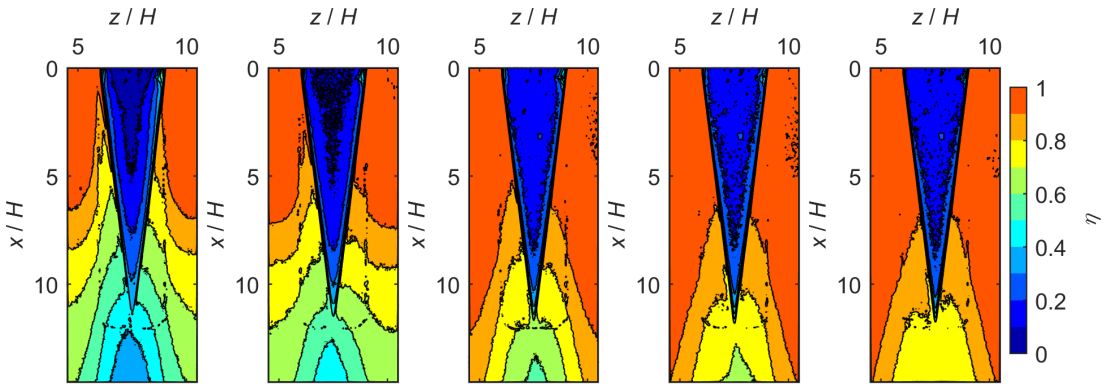
For geometry G5, shown in Figure 7.6, four very distinct peaks in effectiveness could be seen. Similar to G1–4, the left-most and right-most peaks were attached to the sides of the lands and extended further downstream than the central peaks. As before, there was also a very strong bias in effectiveness towards the right due to the asymmetric flow structure described previously.

The peaks in between the lands were much smaller but their positions were still mostly determined by the top plate channels. Geometry G7, shown in Figure 7.8, shared the same top plate with G5 and at low blowing ratio the central peaks were in the same position. However, at this steep angle, the exit alignment had a large effect on the broadness of the peaks. Geometry G5 had very distinct central peaks even at high blowing ratio. G7 on

the other hand had broad peaks at low blowing ratio which become even more spread out as blowing ratio increased. At $M > 1.0$, the right peak had all but merged with the peak attached to the land, forming a very broad peak next to the land.

Geometry G8, shown in Figure 7.9, had the same exit alignment as G4 and similarly displayed a main central peak with an initially small peak to the left at low blowing ratio. At higher blowing ratio, the left peak became more distinct and another peak to the right began to separate from the peak attached to the land. Geometry G6, shown in Figure 7.7, shared the same top plate as G8 but lacked the defined jets created by the exit alignment of G8, resulting in a much broader central peak where the side peaks were no longer visible. Just as in geometry G2, the right peak merged with the peak attached to the land to form a strong and broad peak. At higher blowing ratio, this peak grew closer to the tip of the land and extended further downstream due to the coolant being forced at higher momentum against the side of the land.

7.3.3 Land effectiveness

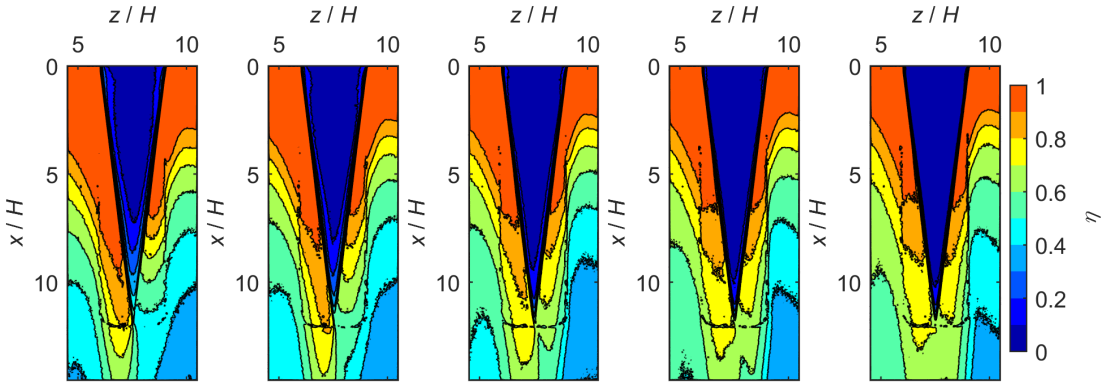


(a) $M = 0.59$ (b) $M = 0.77$ (c) $M = 0.97$ (d) $M = 1.16$ (e) $M = 1.35$

Figure 7.14: 2D land η distributions, G0

Figure 7.14 shows a close-up view of the right hand side land of geometry G0 with effectiveness shown using 10 contour bands at all five blowing ratios. As already described in Section 6.3.1 for land geometry L6, the diffuser shape allowed the coolant to better fill the cutback revealed by the narrowing lands, but there was little evidence of coolant washing over the top of the lands. Due to the tapering, there was some enhancement in

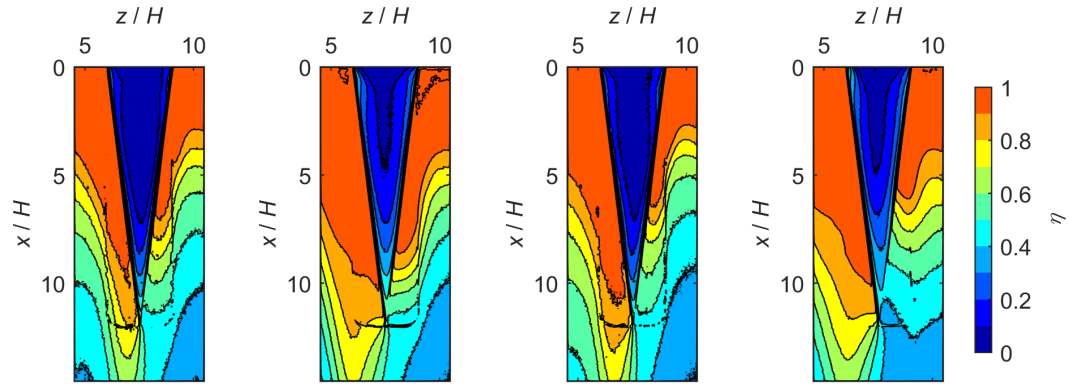
effectiveness along the edges at low blowing ratio, with effectiveness up to 0.3 near the edges.



(a) $M = 0.58$ (b) $M = 0.76$ (c) $M = 0.95$ (d) $M = 1.13$ (e) $M = 1.31$

Figure 7.15: 2D land η distributions, G1

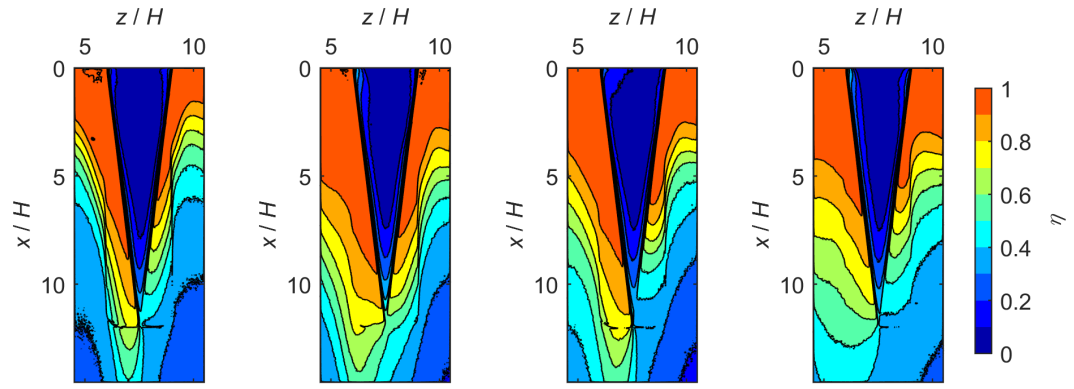
Figure 7.15 shows the view of the right hand side land of geometry G1. It can be seen that effectiveness was still low on top of the lands. As before, the tapering of the land continued to result in a slight enhancement in effectiveness along the left and right edges of the land at low blowing ratio. Increasing the blowing ratio reduced effectiveness on the top of the land, showing that the coolant was more able to wash over the lands when ejected with lower momentum, just as was the case with the baseline geometry G0. This was true for all the cross corrugated geometries G1–8.



(a) G1, $M = 0.58$ (b) G2, $M = 0.60$ (c) G3, $M = 0.58$ (d) G4, $M = 0.60$

Figure 7.16: 2D land η distributions, G0–4, $M \approx 0.6$

Figures 7.16 and 7.17 show land effectiveness for each of the geometries G1–8 at the lowest blowing ratio where the coolant had the greatest influence on effectiveness on top



(a) G5, $M = 0.60$ (b) G6, $M = 0.61$ (c) G7, $M = 0.62$ (d) G8, $M = 0.61$

Figure 7.17: 2D land η distributions, G5–8, $M \approx 0.6$

of the lands. It can be seen that overall, effectiveness was still very low on top of the lands, less than 0.1 over most of the surface for the majority of geometries. This was worse than the baseline geometry, except for G2 and G4 which both showed a very slightly improved effectiveness profile compared to the baseline.

This could have been due to the exit alignment of the top plate which they share as shown in Figure 5.15. However, as mentioned in Section 6.3.1, the measurement uncertainty is significantly higher for low effectiveness measurements and more sensitive to reflections within the test section. Therefore, on the land surface where effectiveness is very low, the small differences in effectiveness found on the surface and between geometries should not be considered absolutely definitive.

Nevertheless, the effectiveness measurements show that even though the cross corrugated channels forced the coolant to exit at an angle that caused impingement against the sides of the lands and higher effectiveness near the lands compared to the baseline geometry, the coolant was still unable to wash over the tops of the lands in any significant amount to increase effectiveness reliably.

7.3.4 Effectiveness downstream of lands

Figure 7.1 shows distinct regions of low effectiveness downstream of the lands as seen in phase 1 for the same baseline geometry, where the mainstream air followed the tapered land surface down to the cutback. In contrast, the angled channels of the cross

corrugated geometries pushed more coolant in the lateral direction. This flow impinged on the sides of the lands and thus, the coolant became more concentrated near the lands, increasing effectiveness there. The coolant flow attached to the sides of the lands then followed the surface downstream, resulting in the regions downstream of the lands having higher effectiveness levels than the central slot region. This effect is visible for all cross corrugated geometries in Figures 7.2 to 7.9.

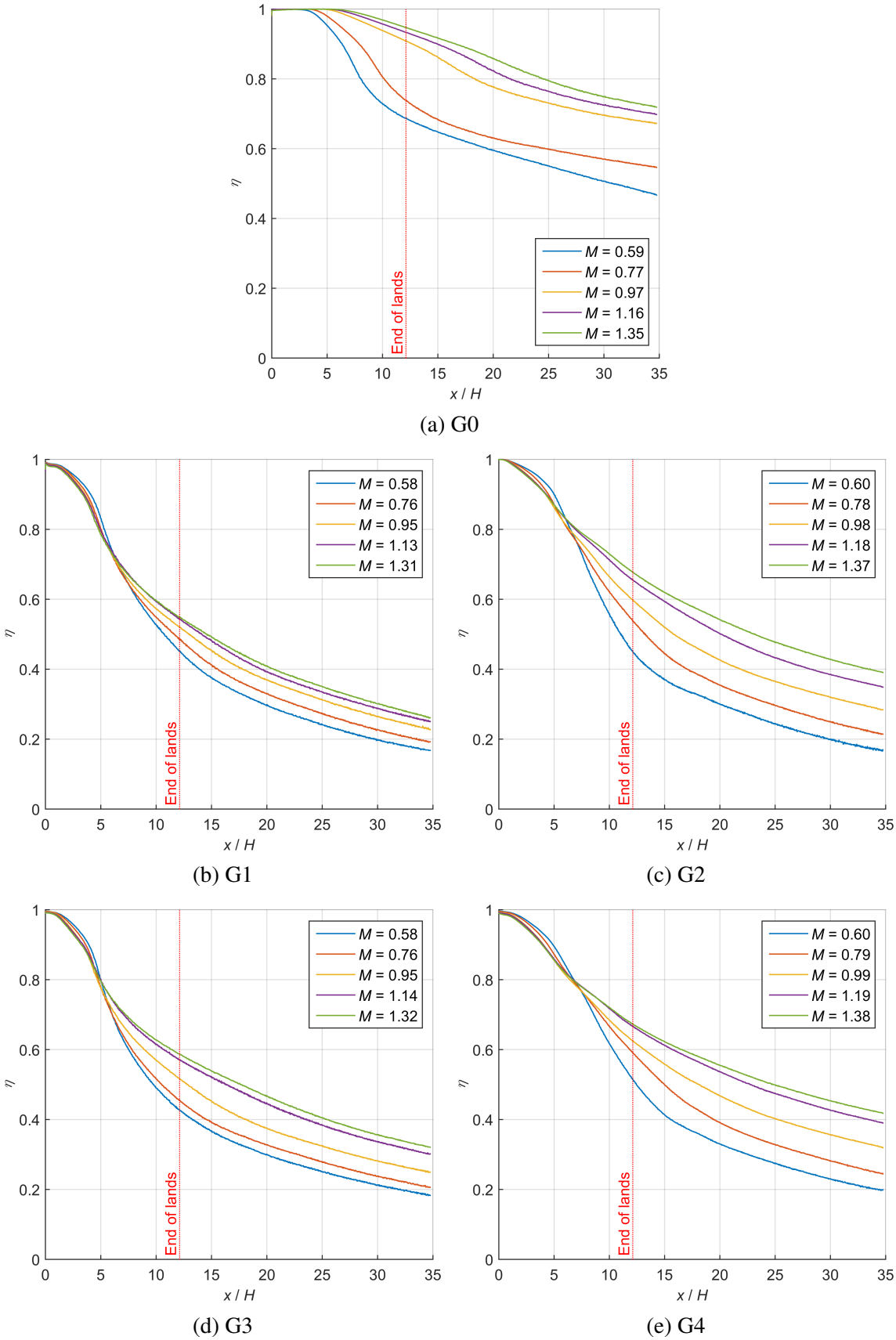
However, since the overall effectiveness levels were much lower for the cross corrugated geometries, this did not necessarily equate to higher effectiveness downstream of the lands compared to the baseline. For geometries G5–8 with an included angle of $120°$, the coolant following the lands mixed abruptly with the mainstream, resulting in a considerably lower effectiveness downstream of the lands.

7.3.5 Centreline effectiveness

Figure 7.18 shows plots of film cooling effectiveness down the slot centreline for geometries G0–4. Figure 7.19 shows the corresponding plots for geometries G5–8. This included only a 100 pixel ($8.43\,\mathrm{mm}$) wide strip down the centre of the cutback region extending downstream from the slot. The position of the end of the lands is marked in the plots.

The potential core in which effectiveness was initially unity for some distance from the slot exit was still apparent for the baseline geometry. However, effectiveness dropped off immediately at the slot exit for the cross corrugated geometries, showing that there was no longer any potential core where the coolant shielded the cutback surface completely from the mainstream gas.

For the baseline geometry G0, after the initial potential core, the rate of decay in effectiveness was higher with lower blowing ratio. However, for the cross corrugated geometries, effectiveness remained slightly higher near the slot exit at lower blowing ratio, before decaying at a faster rate with lower blowing ratio. This resulted in higher effectiveness at low blowing ratio from the slot exit up to a distance of $x/H \approx 6$ for G1–



(a) G0

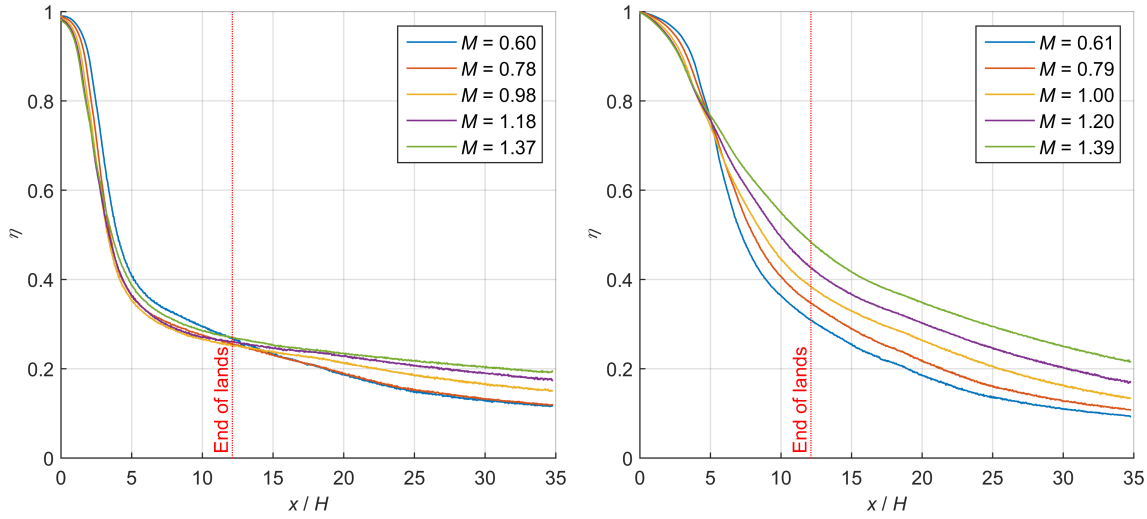
(b) G1

(c) G2

(d) G3

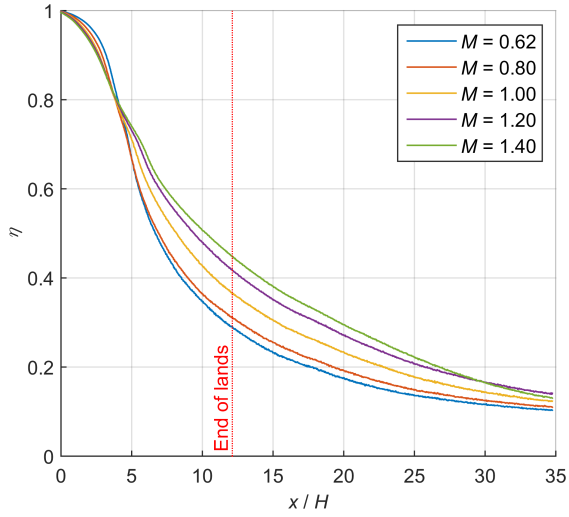
(e) G4

Figure 7.18: Centreline η, slots without exit shaping, G0–4

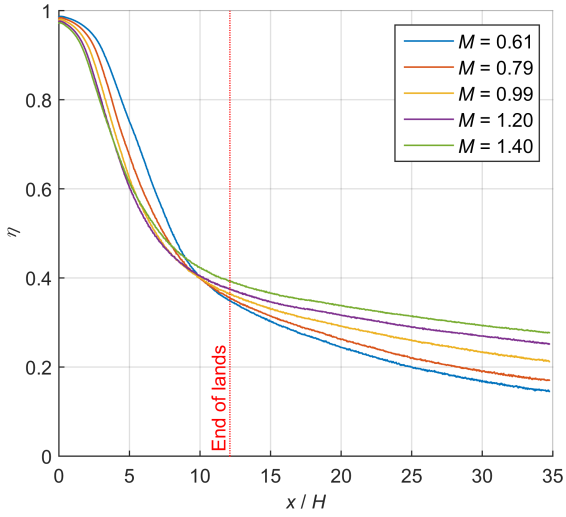


(a) G5

(b) G6



(c) G7



(d) G8

Figure 7.19: Centreline η, slots without exit shaping, G5–8

4. After that point, the lower blowing ratio corresponded to lower effectiveness. This was likely due to the lower velocity jets exiting from the channels at low momentum being able to spread more easily across the slot at first, keeping effectiveness higher initially. However, the lower mass flow of coolant relative to the mainstream eventually dominated as the two flows mixed, resulting in lower effectiveness further away from the slot.

The same effect was observed for G5–8 but the distance at which reversal occurred was less consistent. Geometries G6 and G7 showed higher effectiveness with lower blowing ratio up to $x/H \approx 5$ and $x/H \approx 4$ respectively, whereas geometries G5 and G8 showed the reversal occurring much closer to the end of the lands, at $x/H \approx 13$ and $x/H \approx 10$ respectively.

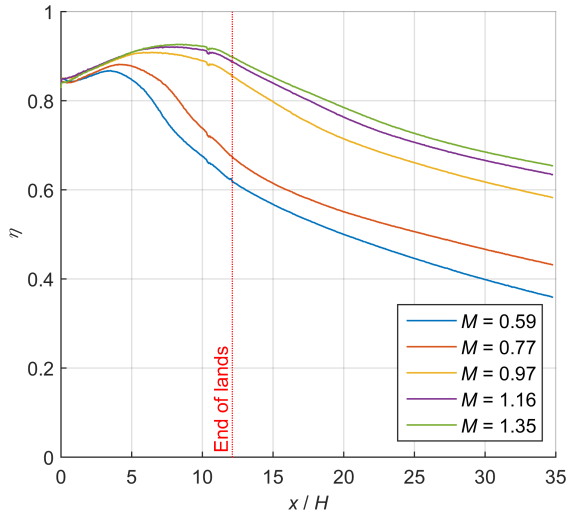
Geometries G2 and G4 showed overall higher centreline effectiveness compared to G1 and G3. However, this was due the slot centreline of G2 and G4 aligning with the strong central peak in effectiveness while the centreline of G1 and G3 so happens to fall in between two peaks in effectiveness. Similarly, the centrelines of geometries G6 and G8 fall roughly on top of the central peak in effectiveness while the centrelines of G5 and G7 fall in between the peaks.

7.3.6 Spanwise averaged effectiveness

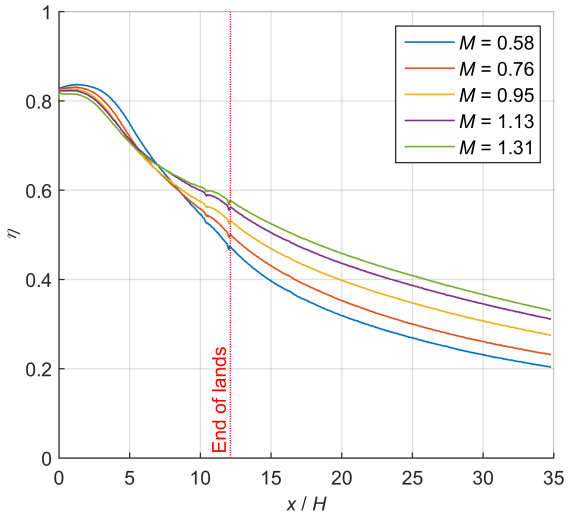
Figures 7.20 and 7.21 show plots of spanwise averaged film cooling effectiveness including the lands. The average was taken over the entire region in between the centrepoints of the two lands.

Due to the inclusion of the diffuser shaped lands which were mostly uncooled with very low effectiveness on top, the starting effectiveness was reduced to 0.81 to 0.84 with some recovery in effectiveness as the lands reduced in width up to the tip and the coolant was allowed to spread out. However, this recovery effect was not sufficient to increase spanwise effectiveness by more than 0.04 for the cross corrugated geometries.

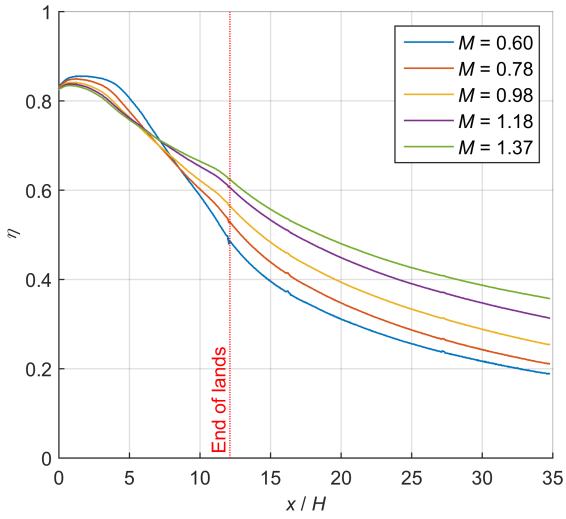
The spanwise averaged effectiveness profiles for geometries G1–4 were fairly similar despite the different exit alignments. Effectiveness decayed faster than G0 as was the



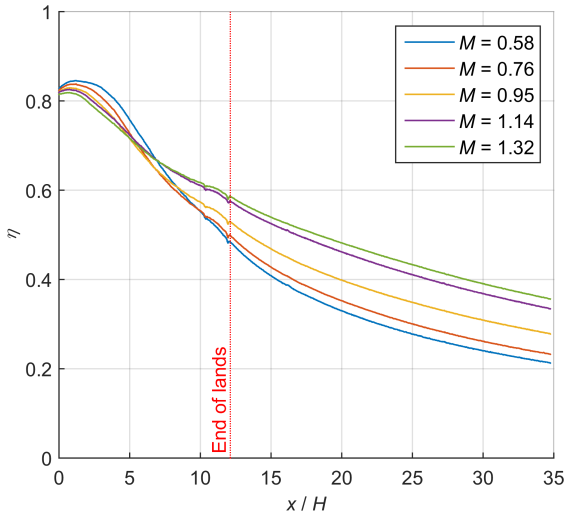
(a) G0



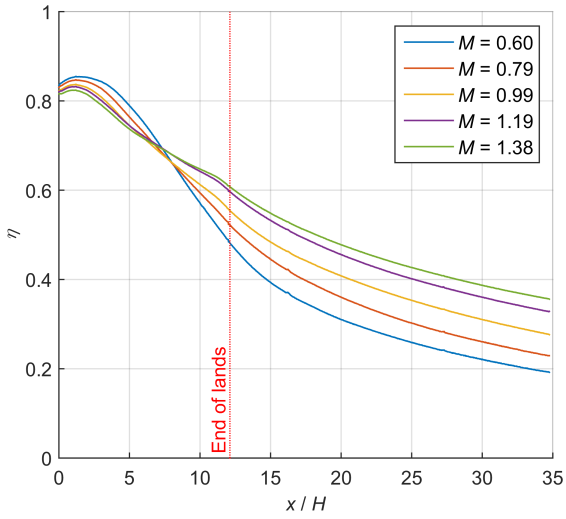
(b) G1



(c) G2

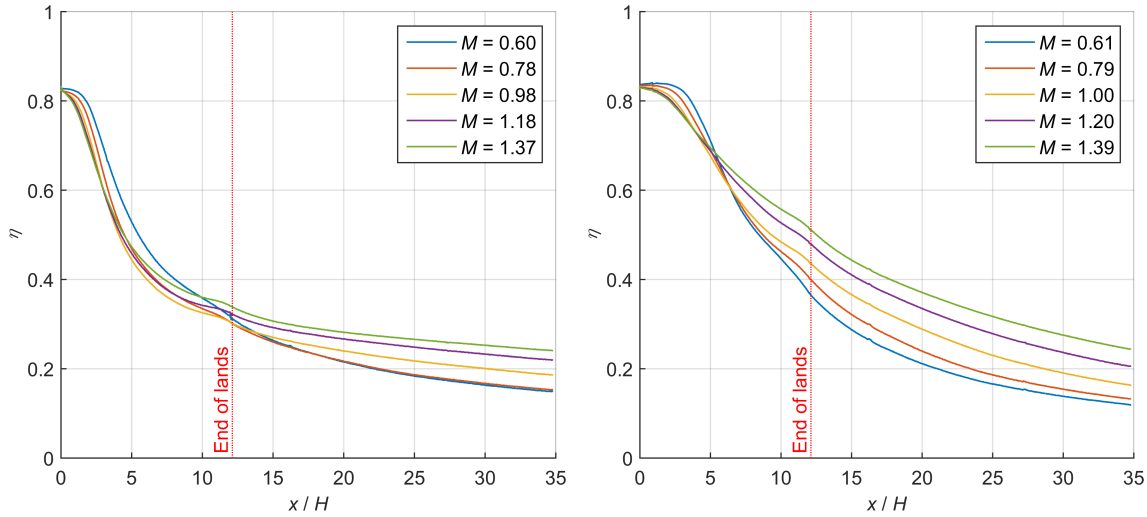


(d) G3



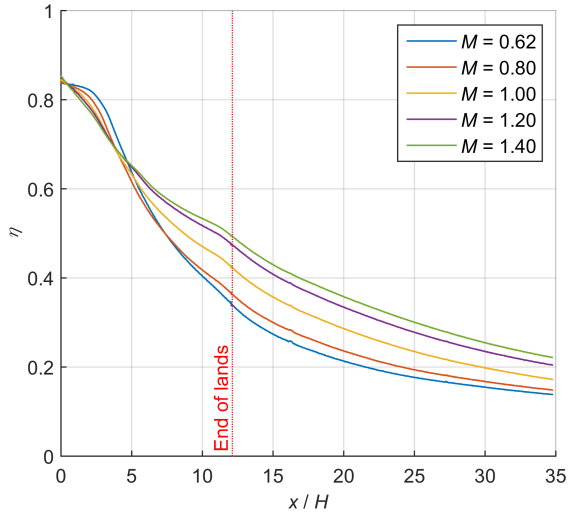
(e) G4

Figure 7.20: Spanwise averaged η, slots without exit shaping, G0–4

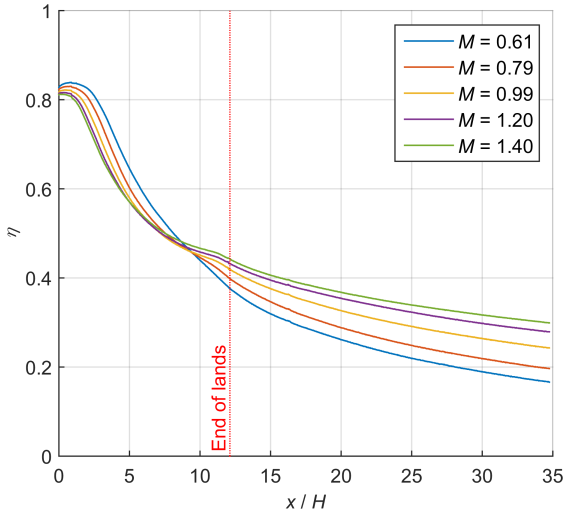


(a) G5

(b) G6



(c) G7



(d) G8

Figure 7.21: Spanwise averaged η, slots without exit shaping, G5–8

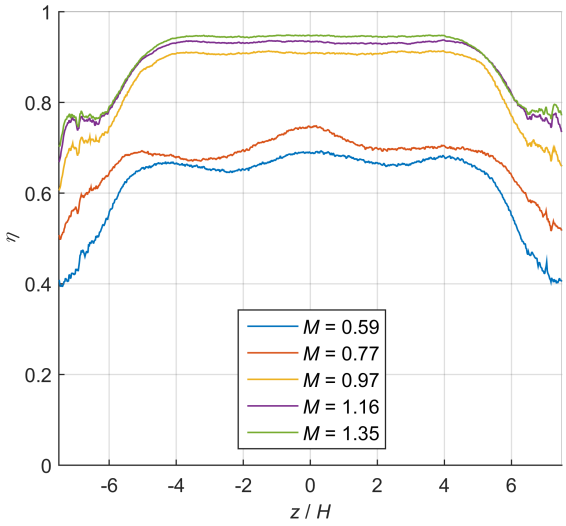
case in the previous centreline effectiveness plots. However, taking an average across the slot reduced the influence of local peaks in effectiveness, showing that changing the exit alignment did not have a large effect on the overall effectiveness levels, only the distribution of coolant in the spanwise direction.

As described in Section 7.3.5, lower blowing ratio actually increased average effectiveness near to the slot exit. This reversed at a distance of $x/H \approx 7$. Effectiveness at the end of the lands was reduced by $31\,\%$ to $36\,\%$ at high blowing ratio compared to the baseline G0 and by $21\,\%$ to $24\,\%$ at low blowing ratio.

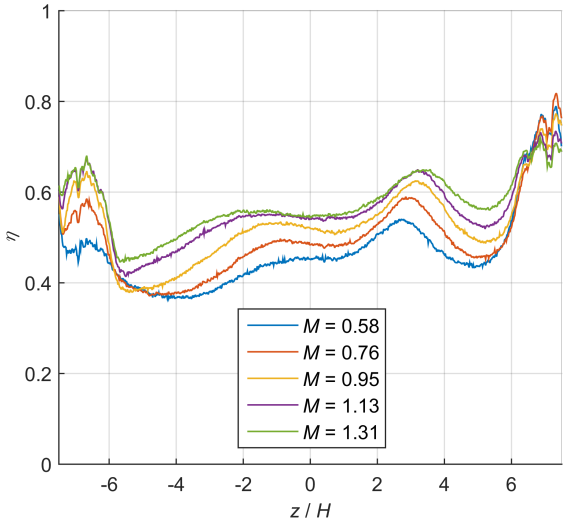
Spanwise averaged effectiveness for geometries G5–8 decayed even faster compared to G1–4. At the higher included angle, exit alignment had a greater effect on effectiveness. Similar to G1–4, lower M gives higher effectiveness near the slot exit and this reverses quickly for G6 and G7 at $x/H \approx 5$ but appears to persist further for G8 up to $x/H \approx 9$ and G5 up to $x/H \approx 10$. Effectiveness at the end of the lands was the lowest for G5, with a reduction of $62\,\%$ at high blowing ratio compared to the baseline and $50\,\%$ at low blowing ratio. G6–8 reduced effectiveness by $43\,\%$ to $51\,\%$ at high blowing ratio and $39\,\%$ to $41\,\%$ at high blowing ratio.

7.3.7 Spanwise variation of effectiveness at end of lands

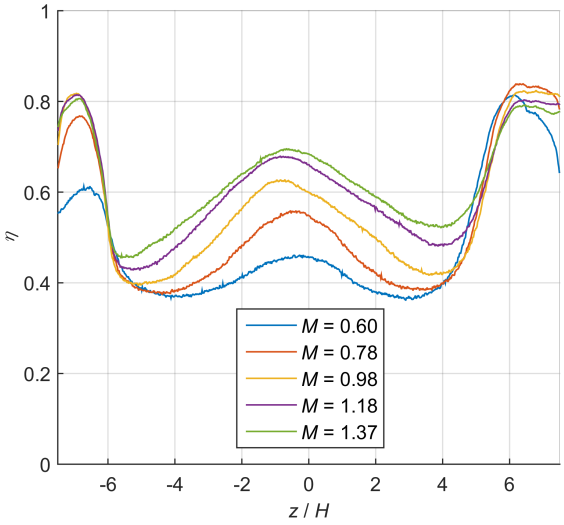
Figures 7.22 and 7.23 show plots of spanwise variation in film cooling effectiveness taken at the end of the lands. This included a 20 pixel ($1.7\,\mathrm{mm}$) wide strip parallel to the slot lip at a distance equal to the length of the lands where $x/H = 12.1$. The spanwise extent starts from the centre of the left hand side land where $z/H = -7.5$ and ends at the centre of the right hand side land where $z/H = 7.5$. $z/H = 0$ marks the centreline of the slot. $z/H = -6$ marks the right side edge of the land hand land, while $z/H = 6$ marks the left side edge of the right hand land. This x/H position is considered to be particularly important as it represents the trailing edge of the blade, where cooling is almost completely reliant on the film effectiveness and large local variations in effectiveness along the trailing edge can lead to high temperature gradients which cause thermal stresses in



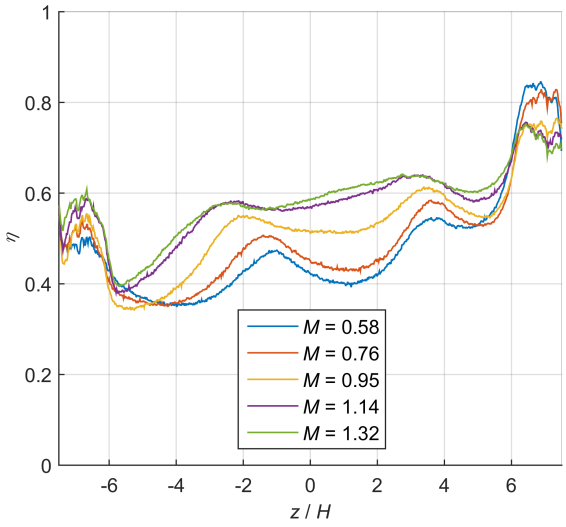
(a) G0, end of lands



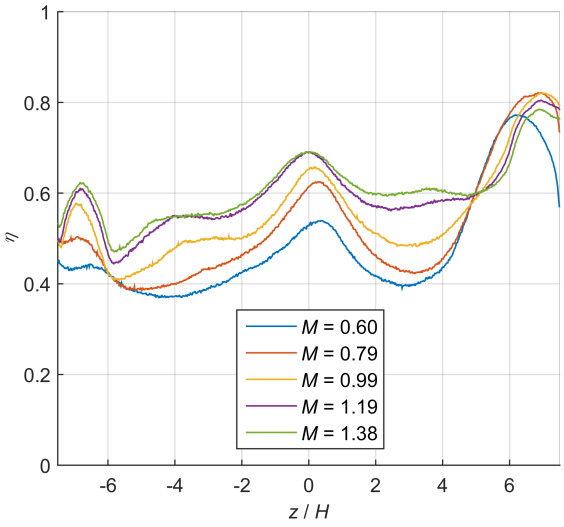
(b) G1, end of lands



(c) G2, end of lands

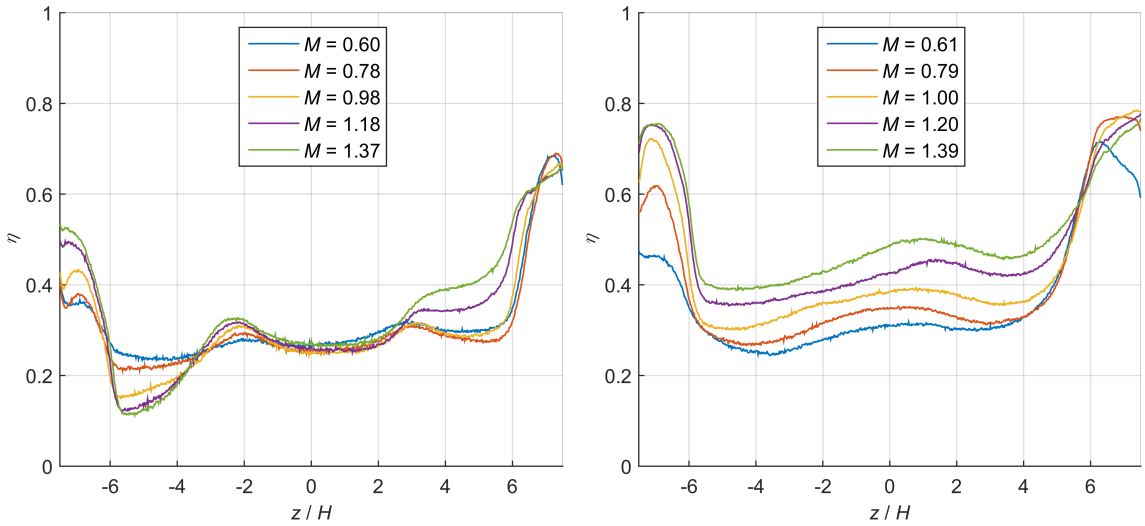


(d) G3, end of lands



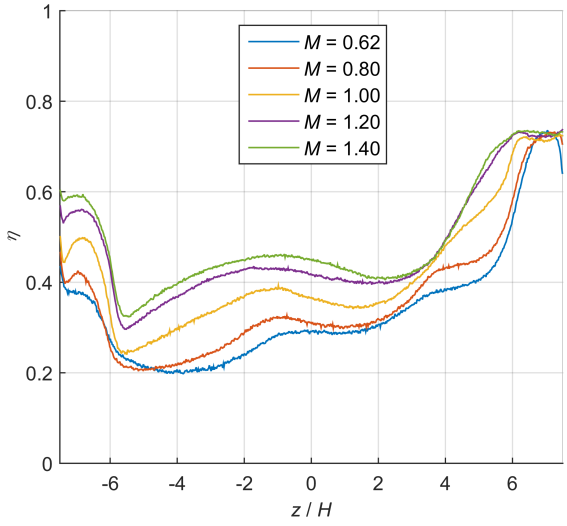
(e) G4, end of lands

Figure 7.22: Spanwise variation of η, slots without exit shaping, G0–4

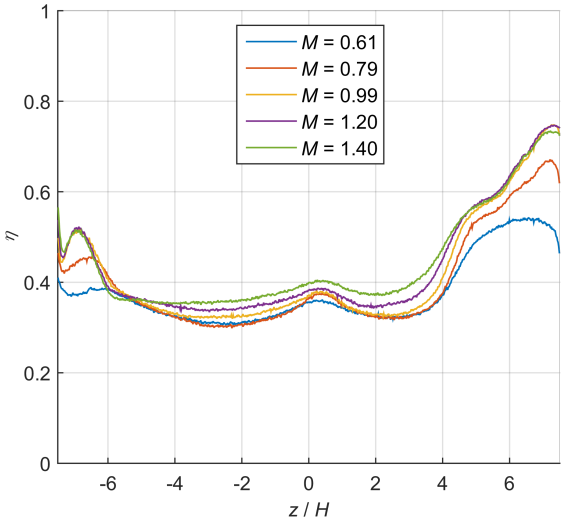


(a) G5, end of lands

(b) G6, end of lands



(c) G7, end of lands



(d) G8, end of lands

Figure 7.23: Spanwise varation of η, slots without exit shaping, G5–8

the blade metal that can affect blade life.

The uneven coverage of coolant across the cutback shown in the 2D effectiveness distributions is still visible in the spanwise variation plots at the end of the lands in Figures 7.22 and 7.23 even though the unevenness of the flow was allowed to mix out over the space between the slot exit and the end of the lands. For all the cross corrugated geometries, peaks of high effectiveness are still visible but are less pronounced than immediately after exit from the slot due to this mixing. This was more apparent with the geometries G5–8 which used a steeper included angle of $120°$, forcing quicker mixing and the corresponding drop in spanwise averaged effectiveness with distance from the slot exit. The result was a flatter, more even spanwise effectiveness profile between the lands compared to geometries G1–4, albeit with considerably lower effectiveness across the span as well.

There remained a significant bias towards the right due to the upper corrugation channels directing coolant towards the right. Geometries G1 and G3, sharing the same top plate, displayed the same two peaks downstream of the slot while geometries G2 and G4, sharing a different top plate, displayed the large central peak with G4 also showing smaller peaks to the sides. This confirmed the top plate as the dominating factor for the effectiveness distribution across the span. However, regardless of exit alignment, all cross corrugated geometries had significantly lower effectiveness downstream of the slot at all blowing ratios. Even the peaks in effectiveness did not come close to matching the baseline levels.

Effectiveness at the tips of the lands was increased due to the concentration of coolant directed along or towards the lands by the corrugation channels. In some cases, this increased effectiveness near the tips of the lands to above the baseline levels, especially near the right side land where the majority of coolant was focused. There, effectiveness reached as high as 0.8 and appeared to be less sensitive to blowing ratio.

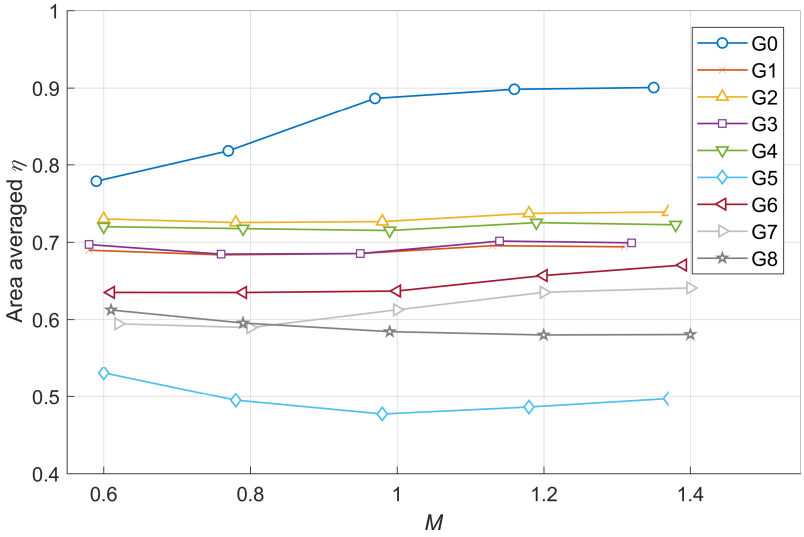


Figure 7.24: Area averaged η, slots without exit shaping, G0–8

7.3.8 Area averaged effectiveness

Figure 7.24 shows a plot of area averaged film cooling effectiveness for all nine geometries at their tested blowing ratios. This included the cutback and land top surfaces up to the end of the lands where $x/H = 12.1$. It gives an overall picture of the relative performance of each geometry over the region most relevant to trailing edge cooling.

It is immediately apparent that all the cross corrugated geometries G1–8 performed poorly overall compared to the baseline geometry G0 across all blowing ratios where $0.6 < M < 1.4$. The highest area averaged effectiveness achieved by any of the cross corrugated geometries was only 0.74 by G2 at the highest blowing ratio. Whereas the lowest area averaged effectiveness achieved by the baseline geometry was 0.78 at the lowest blowing ratio.

Geometries G1–4 all used an included angle of $90°$ with different exit alignments. While there were significant differences in the 2D effectiveness contours shown in Section 7.2 caused by the different exit alignments, Figure 7.24 shows a relatively small difference in area averaged effectiveness across these geometries, showing that the exit alignment had little effect on the overall effectiveness levels, only the distribution of coolant in the spanwise direction. There was also very little change in effectiveness with blowing ratio. In Sections 7.3.5 and 7.3.6 it was observed that for low blowing ratios, effectiveness was

higher near to the slot exit before dropping off quickly with distance. Whereas for high blowing ratios, effectiveness was lower near the slot exit before dropping off less quickly with distance. The higher effectiveness near to the slot exit compensated for the quicker drop in effectiveness for the low blowing ratios up until the end of the lands, resulting in a fairly constant area averaged effectiveness even as blowing ratio increased. Past the lands, as the mainstream and coolant streams became more mixed, the relative mass flow rates of the two streams became the dominant effect and effectiveness increased with blowing ratio. This would have resulted in a lower area averaged effectiveness at low blowing ratio if the surface downstream had been included in the region of interest for the area averaged effectiveness calculation.

With a the steeper included angle of $120°$, cooling performance was further reduced. Geometries G5–8 show significantly reduced effectiveness across all blowing ratios due to the rapid decrease in effectiveness with distance from the slot exit. There was also a marked change in effectiveness between the different exit alignments used with G5 showing the lowest effectiveness and G6 showing the highest. As discussed in Section 7.3.2, this was likely due to the exit alignment affecting the spread of the coolant in the spanwise direction. The exit alignment used in G5, shown in Figure 5.15a, resulted in more distinct jets of coolant leaving the slot as visible in Figure 7.6, leading to low effectiveness in between the jets, reducing the average effectiveness. Whereas the exit alignment used in G6, shown in Figure 5.15b, encouraged a more even "sheet" of coolant leaving the slot as visible in Figure 7.7, leading to slightly increased average effectiveness. Area averaged effectiveness did change with blowing ratio, largely dependent on the position of the point at which the relative mass flow rates of the two streams became the dominant effect on effectiveness rather than the momentum of the coolant leaving the slot. Geometries G6 and G7 had a more spread out slot exit flow and show a slight upward trend in effectiveness with blowing ratio whereas G5 and G8 had more distinct jets of slot exit flow and show a slight downward trend in effectiveness with blowing ratio, although in the case of G5, this is only the case initially, with a slight increase in effectiveness with blowing ratio for $1.0 < M < 1.4$.

7.4 Summary and conclusions

Detailed distributions of adiabatic film cooling effectiveness have been measured over the cutback and land top surfaces of large scale geometries representing turbine blade trailing edges using the PSP technique. One baseline rectangular slot geometry and eight different cross corrugated slot geometries were tested with blowing ratio ranging from 0.6 to 1.4 and a density ratio of 1. The cross corrugated geometries used four different exit alignments each at two included angles of $90°$ and $120°$. The tapered diffuser land shape was used in all cases.

While the simplified nature of the experimental model limits the direct applicability of the measurements to a real blade or vane, the second phase of experiments aimed to compare nine slot designs and show the relative performance of each in terms of effectiveness. The conclusions from these comparisons are as follows:

- The effectiveness on the cutback surface was found to be significantly reduced when using cross corrugated slots compared to the baseline rectangular slot.
- Effectiveness began to fall immediately on slot exit, with the potential core of unity effectiveness no longer apparent.
- Effectiveness was very uneven in the spanwise direction and asymmetric in shape.
- The unevenness in the spanwise direction was still very apparent at the end of the lands, although to a lesser extent.
- The side that the upper channels of the cross corrugation were angled towards dictated a bias in coolant flow in that direction. In this case, the upper channels directed flow towards the right, leading to higher effectiveness on the right.
- Exit alignment was found to affect the position and intensity of the peaks in effectiveness.
- Each upper channel had a corresponding peak of high effectiveness extending downstream of the exit.

- The alignments shown in Figures 5.15a and 5.15d generated distinct jets of coolant resulting in more intense and distinct peaks in effectiveness.
- The alignments shown in Figures 5.15b and 5.15c generated a more even "sheet" of coolant resulting in a more even spanwise effectiveness profile.
- The cross corrugated channels forced the coolant to impinge against the sides of the lands, resulting in higher effectiveness near the lands.
- While there was some evidence of a small amount of coolant washing over the tops of the lands and increasing effectiveness on top of the lands, this was not in any significant amount to increase effectiveness reliably.
- Due to the concentration of coolant near the lands, effectiveness downstream of the lands was higher than the central slot region. However, the effectiveness level downstream of the lands was still lower than the baseline.
- The tendency of lower momentum jets to spread out more evenly on exit from the slot resulted in higher effectiveness at lower blowing ratio near to the slot exit.
- Further away from the slot exit, as the mainstream and coolant streams mixed out and the relative mass flow rates became the dominating factor, effectiveness was reduced for lower blowing ratio, similar to the baseline.
- With a $90°$ included angle, the area averaged effectiveness was not greatly affected by blowing ratio due to the higher effectiveness near the slot compensating for lower effectiveness far from the slot.
- With a $90°$ included angle, the area averaged effectiveness was not greatly affected by exit alignment.
- Increasing the included angle to $120°$ exacerbated all of the aforementioned effects, with further reduced effectiveness, greater bias towards one side and more distinct peaks of effectiveness with regions of low effectiveness between them.

- With a 120° included angle, the area averaged effectiveness was significantly affected by exit alignment and also by blowing ratio to a lesser extent.

The second phase of experiments has shown that if cross corrugated internal slot geometries are used in a trailing edge cooling design for purposes of pressure loss and mass flow control through the slot, there will be a significant penalty in virtually all aspects of film cooling performance. In order to achieve acceptable cutback effectiveness at least on par with the rectangular slot, it is necessary to incorporate exit shaping into the cross corrugated slot design. This has been explored further in the third phase of experiments.

Chapter 8

Effectiveness Measurements — Exit Shaping

8.1 Introduction

In Chapter 7 it was observed that the poor film effectiveness performance of the cross corrugated slot was in large part due to two factors:

- The non-uniformity of the slot exit profile across the span led to inconsistent spanwise coolant coverage, visible as distinct peaks of high effectiveness with low effectiveness in between and corresponding by and large with the positions of the upper corrugation channels.
- The angle of the corrugation channels at exit led to the coolant exhausting non-parallel to the mainstream flow, which caused a strong bias of coolant towards one side of the cutback and consequently away from the other side, and also increased the mixing rate with the mainstream resulting in the lack of any potential core region of unity effectiveness as well as a very quick drop off in effectiveness with distance from the slot exit.

In an effort to negate these factors, two exit shaping design features were considered:

- Flattening and smoothing out the corrugations within the slot towards the exit such that the exit shape would be a plain rectangle identical to the baseline rectangular slot.

- Straightening the corrugations within the slot towards the exit such that the channels and therfore the coolant flow direction would become parallel to the mainstream flow upon exit from the slot.

The objective of the third phase of experiments was to attempt to optimise the novel cross corrugated slot geometry for improved film effectiveness on the cutback surface by using a combination of these exit shaping design features. This was accomplished by measuring film effectiveness using a variety of cross corrugated slot with exit shaping designs.

The geometries are detailed in Section 5.6. Five cross corrugated slot geometries with an included angle of $90°$ and exit shaping were tested. The tapered diffuser land shape (designated as L6 in Chapter 6) was used in all cases. This chapter shows the results from phase 3 and compares the performance of the various geometries with the designs from phase 2 and the baseline plain rectangular slot. These results have been partially published in Wong et al. (2016a) and Wong et al. (2017).

8.2 2D film cooling effectiveness distributions

The PSP technique allows high resolution 2D adiabatic film effectiveness measurements over the cutback surface and top of the lands to be made. The approximate view area and coordinate system is defined in Figure 6.1, where x is the downstream distance from the slot exit and z is the spanwise displacement from the centreline. These are non-dimensionalised for all geometries by the slot height of the baseline plain rectangular slot geometry G0 to give x/H and z/H, where $H = 4.6\,\mathrm{mm}$. In phase 3, the cross corrugated geometries have the same exit height as the plain rectangular slot. Measurements were taken for $M = 0.6, 0.8, 1.0, 1.2, 1.4$.

Figures 8.1, 8.2, 8.3, 8.4 and 8.5 show all the 2D plots of effectiveness taken in phase 3. All of the figures show a plan view of the cutback region and lands. The slot exit and lip is aligned with the top border of the plots, i.e. where $x/H = 0$. The centreline is at the midpoint between the lands where $z/H = 0$. Blue regions show poor coverage from the nitrogen coolant and correspond to low film cooling effectiveness and red regions correspond to high effectiveness. The lands can be seen as the predominantly blue regions in the top left and top right corners or each plot.

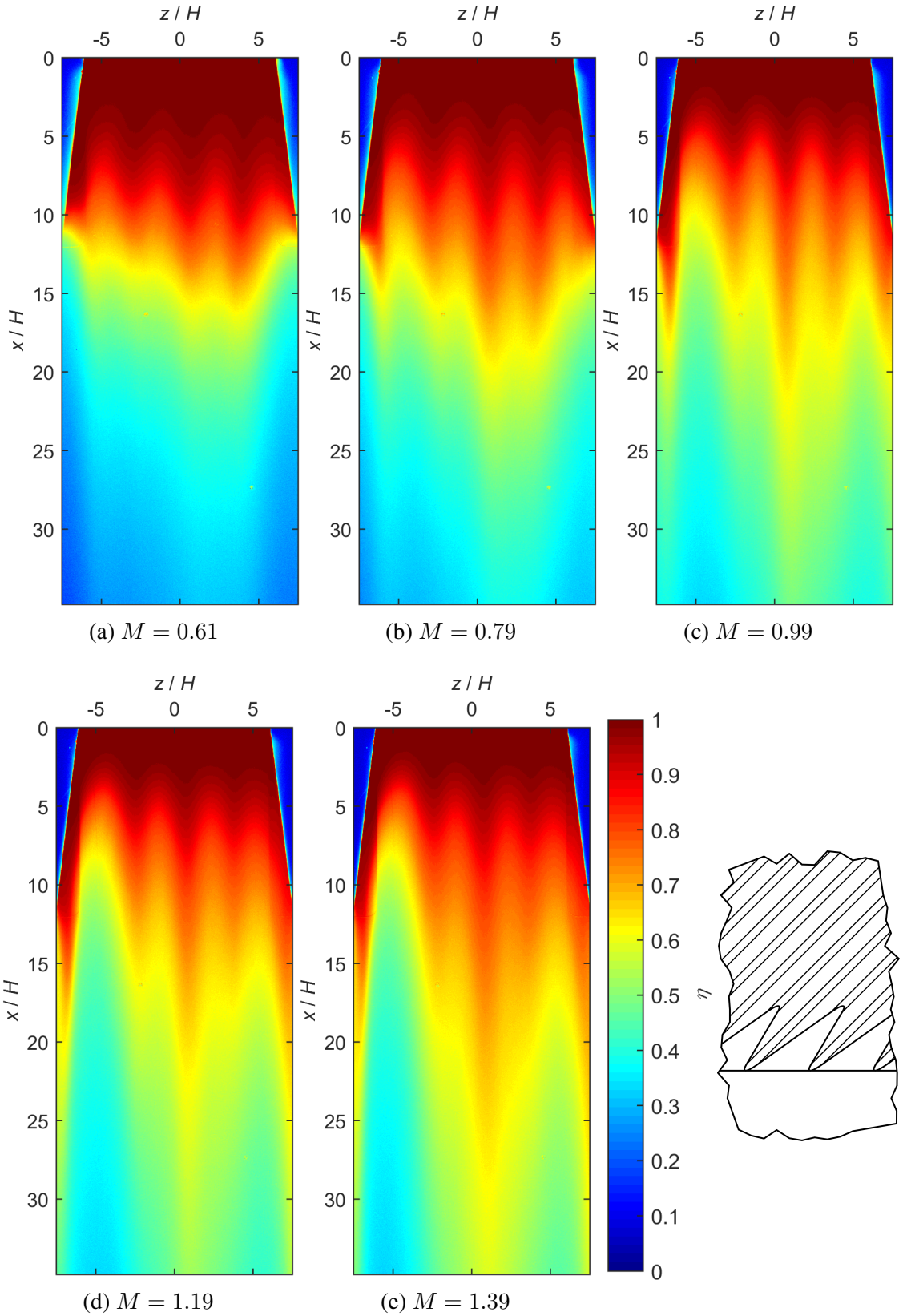
8.3 Discussion

8.3.1 Cutback effectiveness

Addition of ramp down section

The "ramp down" section described in Section 5.6 modified the slot exit profile such that it was identical to the baseline rectangular slot. Geometry G9 included only this ramp down section, without any additional coolant flow straightening section. The upper corrugation channels were still directed at an angle of $45°$ from the mainstream towards the right, while the lower corrugations channels were directed at an angle of $45°$ from the mainstream towards the left. This resulted in a considerably more consistent spanwise distribution of effectiveness. Figure 8.1 shows that, although distinct peaks of high effectiveness corresponding to the channels were still visible and there was still a bias towards the right side of the slot, these flow features were far less pronounced than for G1–4.

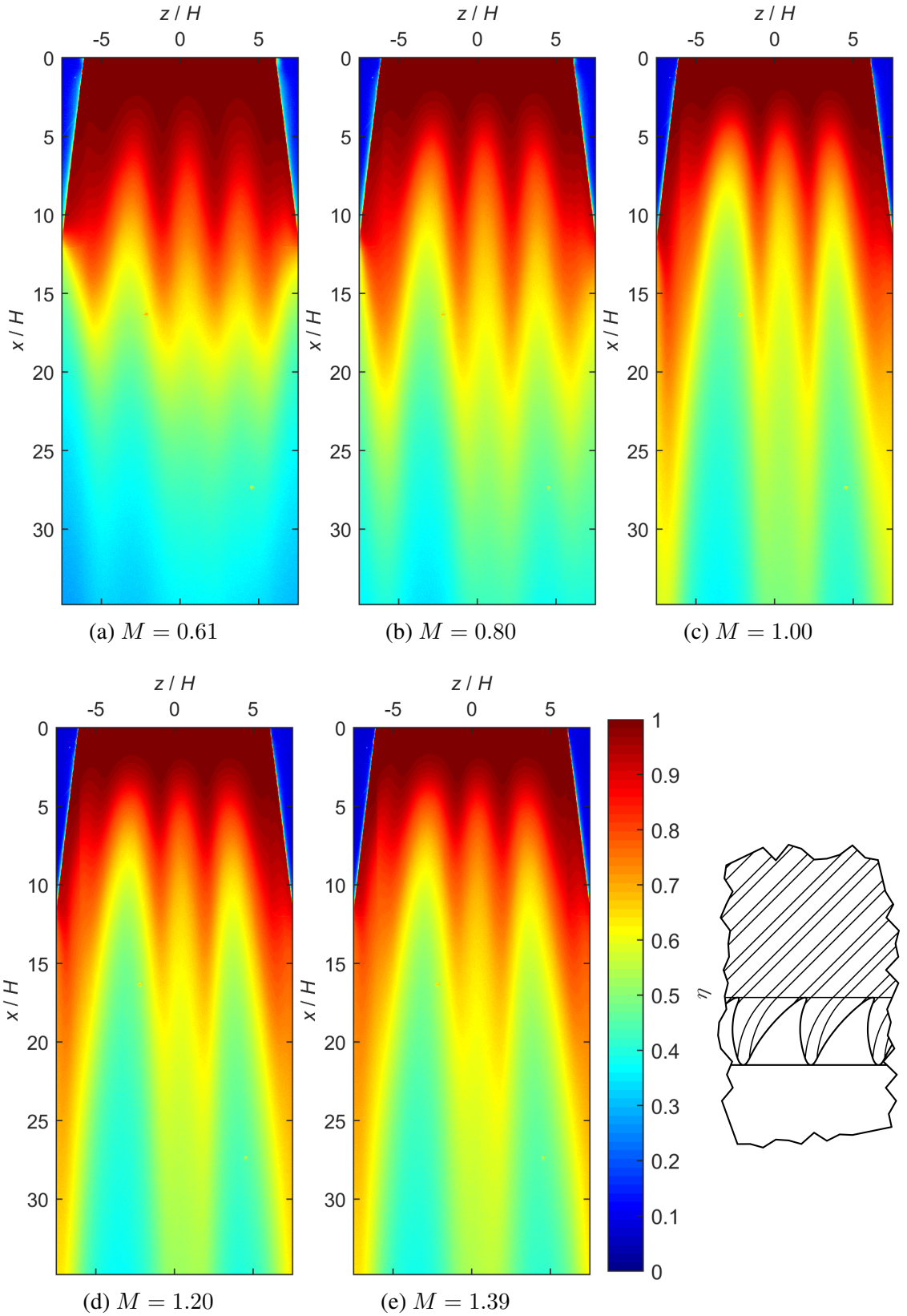
Figures 8.1a and 8.1b show the effectiveness patterns at the lower blowing ratios, $M = 0.6$ and $M = 0.8$ respectively, to be much more similar to the baseline case shown in Figures 7.1a and 7.1b. The spanwise coverage was more even and the peaks of high effectiveness less obvious. In contrast, at higher blowing ratios where $M > 0.8$, Figures 8.1c to 8.1e show much more distinct peaks of effectiveness and a greater concentration of coolant near the lands as was the case with the cross corrugated slots without exit shaping in Chapter 7. This indicated that the exit shaping combined with low flow mo-



(a) $M = 0.61$ (b) $M = 0.79$ (c) $M = 0.99$

(d) $M = 1.19$ (e) $M = 1.39$

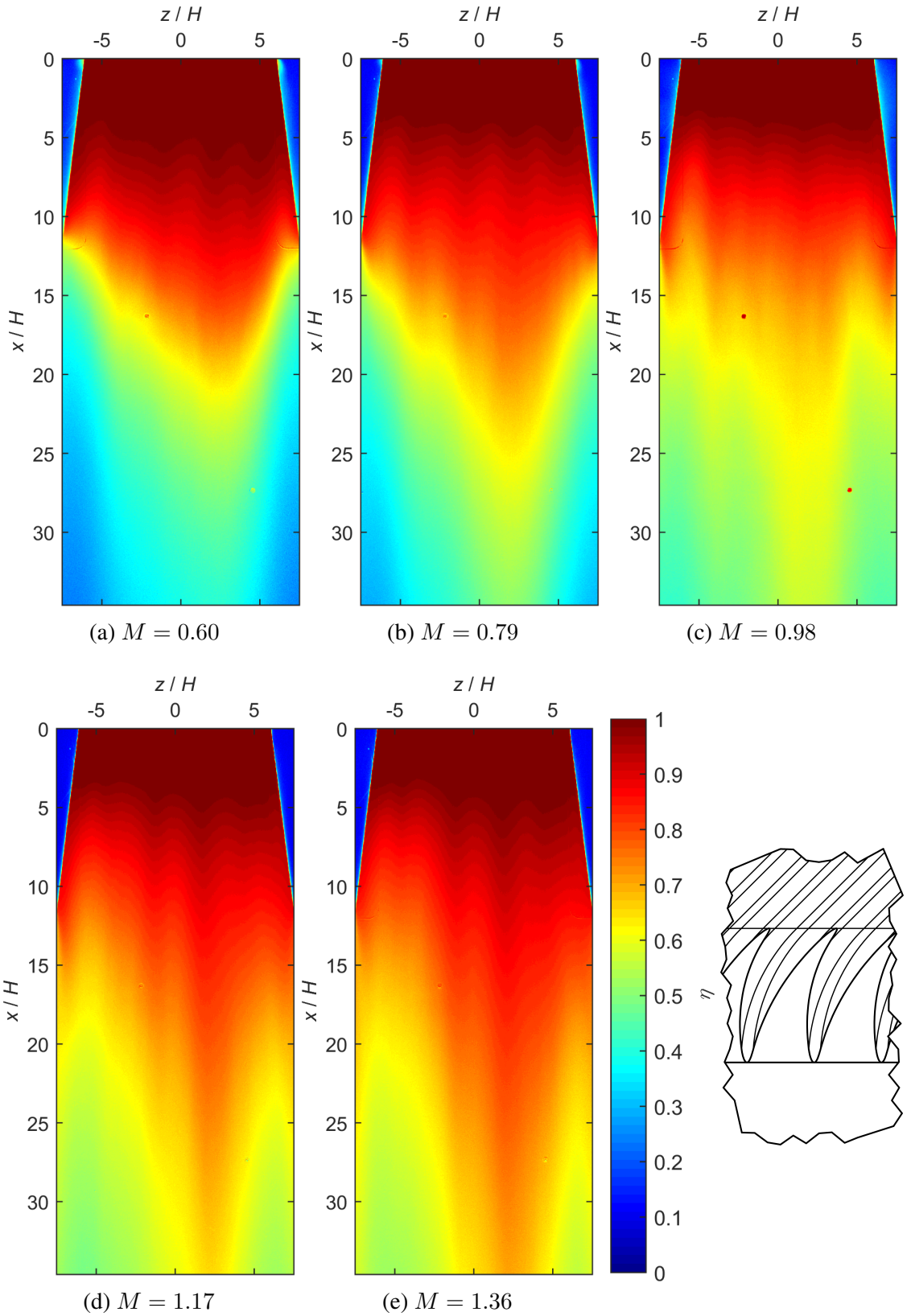
Figure 8.1: 2D η distributions, G9



(a) $M = 0.61$ (b) $M = 0.80$ (c) $M = 1.00$

(d) $M = 1.20$ (e) $M = 1.39$

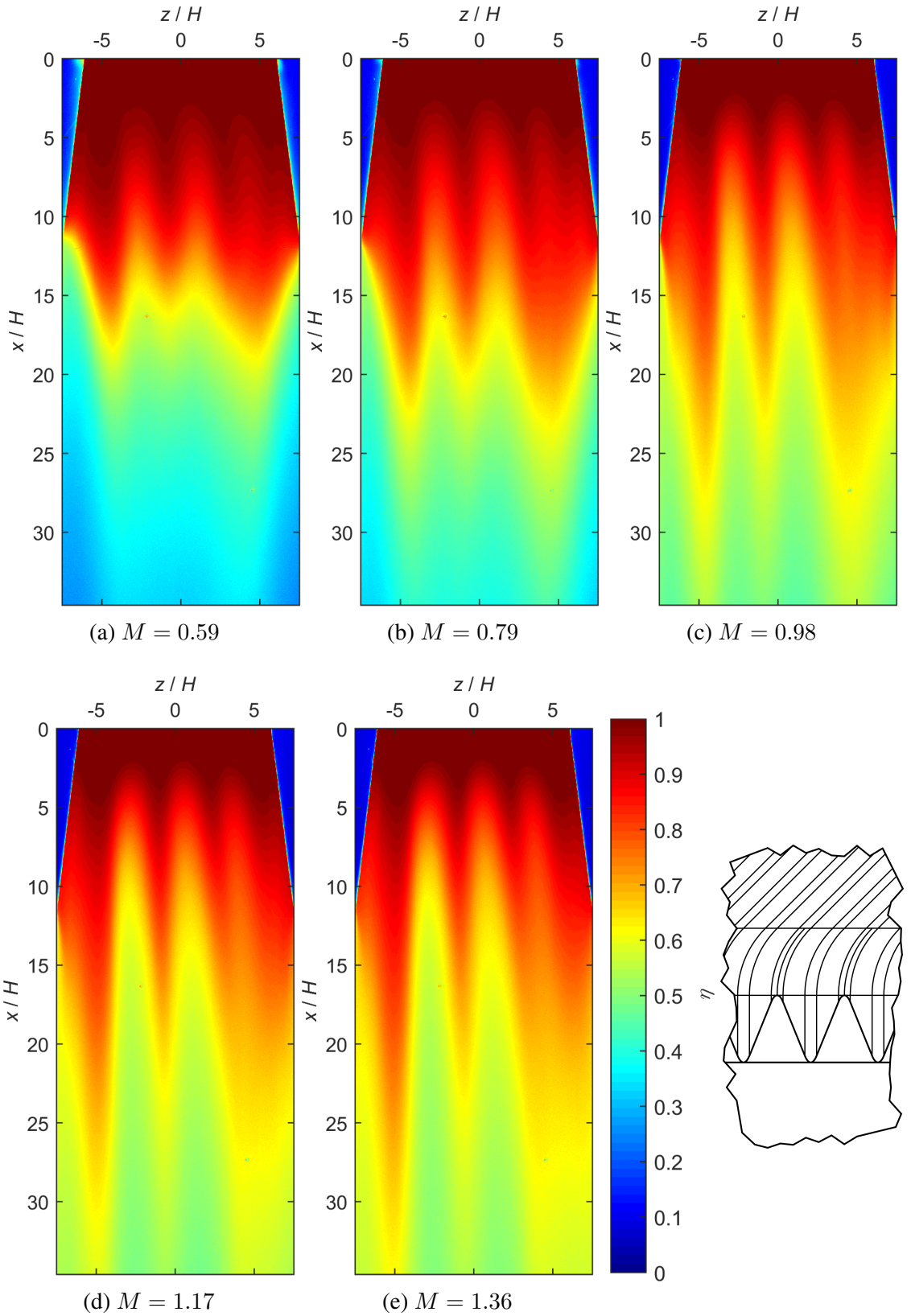
Figure 8.2: 2D η distributions, G10



(a) $M = 0.60$ (b) $M = 0.79$ (c) $M = 1.17$

(d) $M = 1.17$ (e) $M = 1.36$

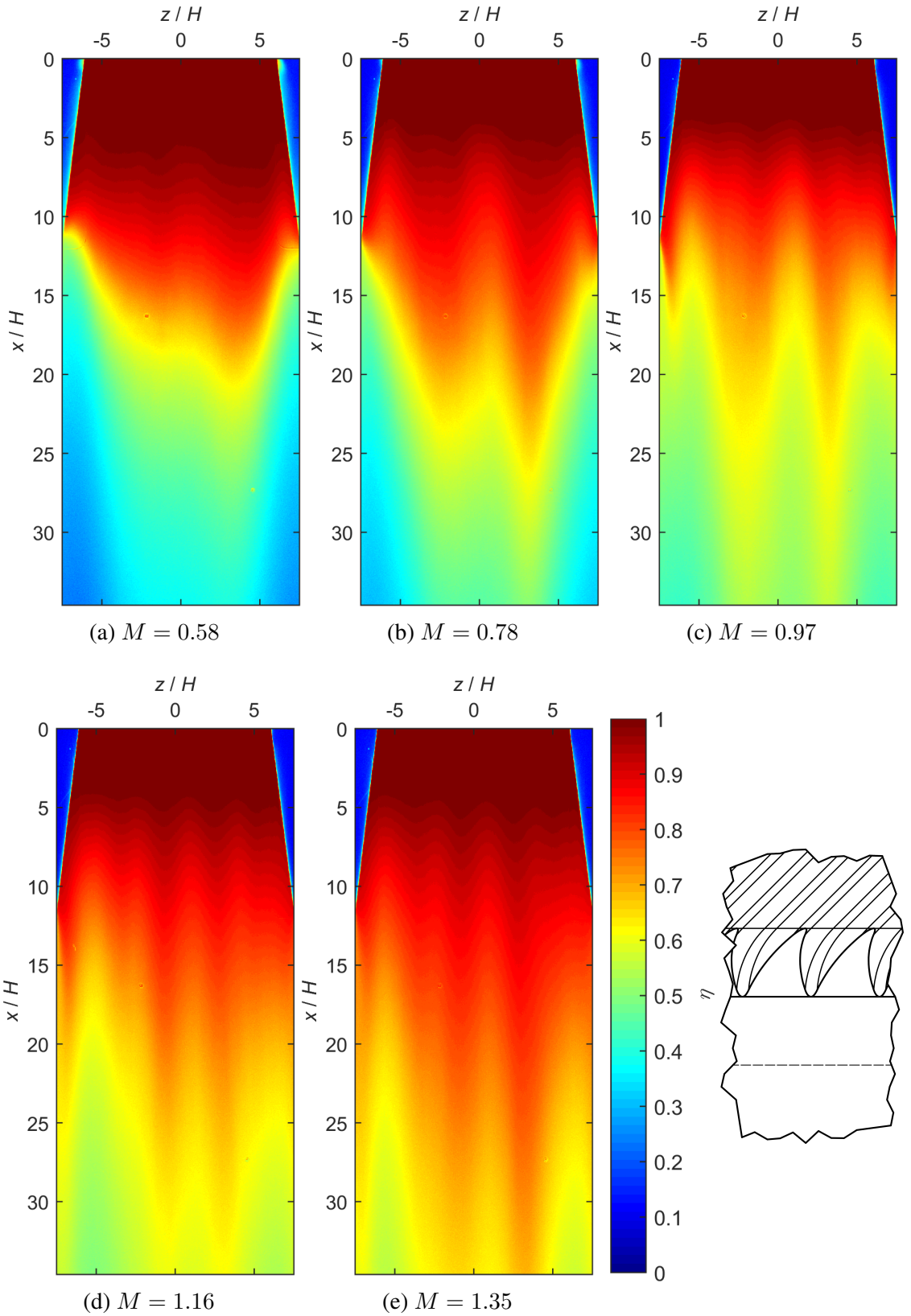
Figure 8.3: 2D η distributions, G11



(a) $M = 0.59$ (b) $M = 0.79$ (c) $M = 0.98$

(d) $M = 1.17$ (e) $M = 1.36$

Figure 8.4: 2D η distributions, G12



(a) $M = 0.58$ (b) $M = 0.78$ (c) $M = 0.97$

(d) $M = 1.16$ (e) $M = 1.35$

Figure 8.5: 2D η distributions, G13

mentum at low blowing ratios allowed the coolant to spread out more evenly along the spanwise length of the slot before exiting. However, at high blowing ratios, with high flow momentum, the coolant streams following each corrugation channel maintained more of their structure and direction before exiting the slot. Thus, the high effectiveness peaks remained distinct, with impingement on the sides of the lands and a bias to the right, although the peaks did reach much further away from the slot exit than in the previous cases.

Further addition of straightening section

The straightening section described in Section 5.6 further modified the internal cross corrugated slot geometry near the exit such that the corrugation channels were curved to become parallel to the mainstream flow before the slot exit. Geometries G10–13 included this straightening section in addition to the ramp down section with variations in the precise length and position of the exit shaping sections.

In geometry G10, the straightening section was positioned fully overlapping the ramp down section, with the same length as in G9. The straightening of the coolant flow resulted in the flow leaving the slot nearly parallel to the mainstream flow. However, since the exit shaping was applied very close to the slot exit, the flows from individual channels were not given sufficient space and time to spread out in the spanwise direction. This resulted in four distinct jets of coolant exiting the slot, visible as the four high effectiveness peaks in 8.2, each corresponding directly in pitch and position to the flow from one of the channels. Since they exited parallel to the mainstream, they were able to extend far downstream of the slot exit, maintaining a high level of effectiveness for longer and dissipating much later compared to the geometries without flow straightening. Similar to those geometries, the left-most and right-most peaks appeared to attach to the sides of the lands. This phenomenon became more evident at higher blowing ratio. For $M > 1.0$, the left-most and right-most peaks very clearly diverged from the centre towards the lands and extended much further downstream compared to the central peaks. This was likely

due to the combination of coolant impinging on and attaching to the sides of the lands and coolant following the walls of the internal bridges and leaving the slot parallel to the mainstream flow with less spanwise momentum and greater streamwise momentum, reducing mixing with the mainstream. Due to the substantially parallel coolant ejection, the bias towards the right was less obvious, especially at higher blowing ratios.

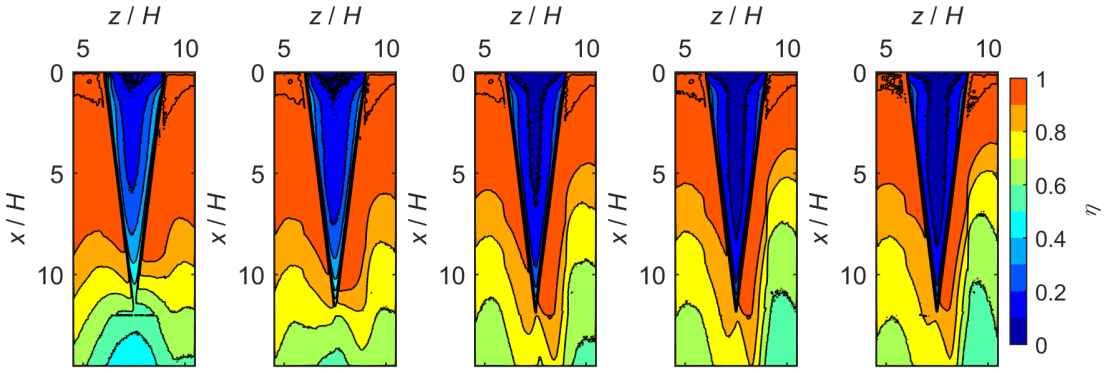
Geometry G11 extended the straightening and ramp down lengths by a factor of two, resulting in a more gradual transition from the corrugated channels to the rectangular exit. This provided extra space for the individual channel flows to spread out more evenly across the slot resulting in a marked improvement in terms of achieving a more consistent spanwise effectiveness profile across the slot as shown in Figure 8.3. Since the coolant still exited the slot parallel to the mainstream, effectiveness remained high far downstream of the slot exit. However, a slight right-side bias was still visible, indicating that some spanwise momentum still remained.

In contrast, geometry G12 showed an effectiveness distribution very similar to G10, with distinct high effectiveness peaks extending far downstream visible in Figure 8.4. This design placed the straightening section before the ramp down section which was immediately before the exit. As before, the straightening section provided higher effectiveness further downstream. However, having the ramp down section being so short in length and immediately before the exit meant that the coolant jets were not able to spread out in the spanwise direction, leading to the distinct peaks of high effectiveness with low effectiveness in between them and an overall uneven spanwise coverage similar to G10. The bias towards the right appeared to be more pronounced though, with the third peak from the left almost combining with the right-most peak next to the land.

Geometry G13 added an offset for the ramp down section such that the last section of the slot immediately before the exit had a constant plain rectangular profile 3 slot heights long. This effectively acted as a short settling section, allowing the coolant to spread out and fill the slot in the spanwise direction without the entrainment of mainstream gas that occurs after exit. The resulting effectiveness pattern shown in Figure 8.5 was considerably more even in the spanwise direction while maintaining high effectiveness far downstream

of the exit due to the straightening section. The right-side bias was still present similar to G11.

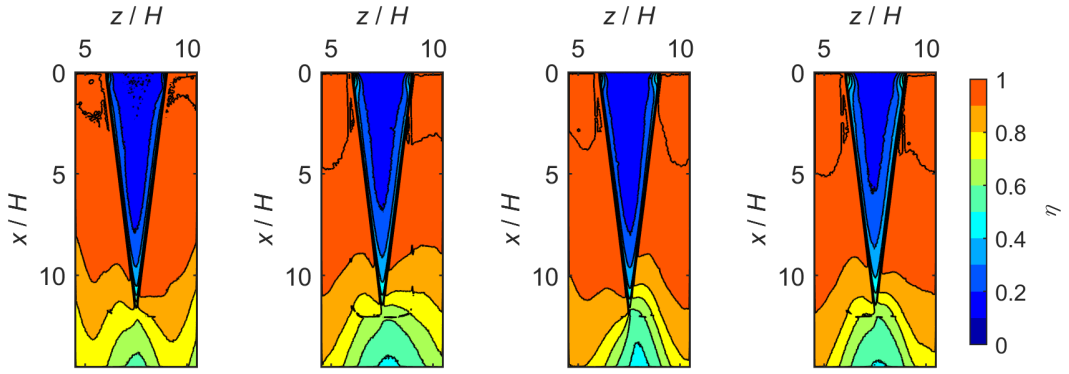
8.3.2 Land effectiveness



(a) $M = 0.61$ (b) $M = 0.79$ (c) $M = 0.99$ (d) $M = 1.19$ (e) $M = 1.39$

Figure 8.6: 2D land η distributions, G9

Figure 8.6 shows a close-up view of the right hand side land of geometry G9 with effectiveness shown using 10 contour bands at all five blowing ratios. When compared with the baseline geometry G0 seen in Figure 7.14, the effectiveness levels over the top of the lands were similarly low, mostly under 0.2. As before, there was some enhancement of effectiveness along the edges of the lands due to the tapering but only at low blowing ratio.



(a) G10, $M = 0.61$ (b) G11, $M = 0.60$ (c) G12, $M = 0.59$ (d) G13, $M = 0.58$

Figure 8.7: 2D land η distributions, G10–13, $M \approx 0.6$

Figure 8.7 shows land effectiveness for each of the geometries G10–13 at the lowest blowing ratio where the coolant had the greatest influence on effectiveness on top of the

lands. Very little change in effectiveness on top of the lands can be seen between the geometries. Effectiveness along the edges was slightly higher, but as with the baseline geometry G0 and geometry G9, not significantly so.

This shows that the addition of exit shaping to the cross corrugated slots had no substantial effect on effectiveness on top of the lands when compared with the baseline rectangular slot or the cross corrugated geometries without exit shaping.

8.3.3 Effectiveness downstream of lands

In Section 7.3.4 it was noted that the channels of the cross corrugated slot geometries pushed much of the coolant towards the sides of the lands, increasing effectiveness near the lands and resulting in higher effectiveness directly downstream of the lands than in between them. This was the reverse of the baseline rectangular slot geometry, where the highest effectiveness was always down the middle of the slot and the lowest effectiveness directly behind the lands. However, since the coolant coverage was reduced so much across the board, effectiveness was still lower downstream of the lands when using cross corrugated slots.

The addition of the ramp down section in geometry G9 improved coolant uniformity significantly. At low blowing ratio, for $M = 0.6$ and $M = 0.8$ (Figures 8.1a and 8.1b respectively), the coolant coverage was similar to the baseline geometry G0 shown in Figures 7.1a and 7.1b with lower effectiveness directly downstream of the lands than in between them. However, at higher blowing ratios where $M > 0.8$, the coolant coverage was more similar to the cross corrugated geometries without exit shaping. The coolant impinged on and followed the sides of the lands to create regions of higher effectiveness directly downstream of the lands, with reduced effectiveness across the centre.

Further modifying the exit of the cross corrugated geometry to add flow straightening in geometry G10 resulted in the coolant flow leaving the slot closer to parallel with the mainstream flow. Nevertheless, the coolant still had a strong tendency to attach to the sides of the lands. At the lowest blowing ratio shown in Figures 8.2a, effectiveness was

not particularly enhanced directly downstream of the lands. However, at higher blowing ratios where $M > 0.8$, the coolant was most heavily concentrated near the lands, resulting in much higher effectiveness downstream of the lands compared to the centre, as high as 0.7 even at a distance of $x/H = 25$. This was considerably higher than the baseline case or any of the previous cross corrugated cases.

In contrast, by using geometry G11, effectiveness far downstream of the lands was reduced compared to the central region for all blowing ratios. This would appear to indicate that the coolant flow at exit had less spanwise momentum, resulting in less coolant being directed against the sides of the lands and the absence of the highest effectiveness peak attached to the lands that was a common characteristic of all previous cross corrugated geometries.

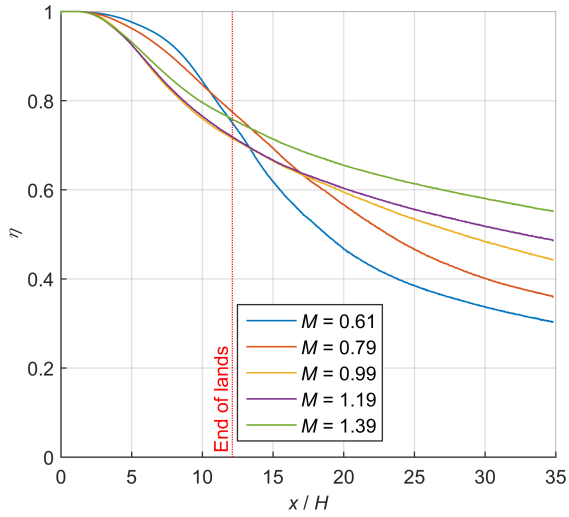
Geometry G12 showed an effectiveness profile more similar to G10. As blowing ratio was increased, the peaks in effectiveness near the lands became more distinct and extended further downstream. However, the left-most peak appeared to detach from the land side, resulting in the largest peak appearing slightly to the right of the land centreline rather than directly downstream of the land as was the case with G10.

Geometry G13 performed similarly to G11. The coolant flow did not exhibit such a strong tendency to concentrate near and attach to the sides of the lands. While there was still high effectiveness near the lands and downstream of them for $M > 0.8$, there was also high effectiveness across the central region.

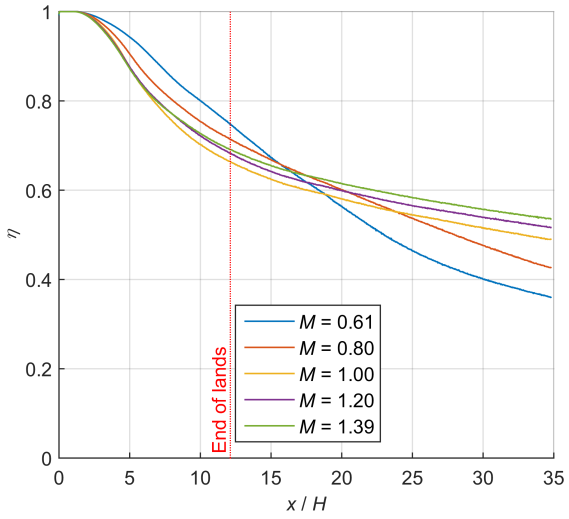
8.3.4 Centreline effectiveness

Figure 8.8 shows plots of film cooling effectiveness down the slot centreline for geometries G9–13. This included only a 100 pixel ($8.43\,\mathrm{mm}$) wide strip down the centre of the cutback region extending downstream from the slot. The position of the end of the lands is marked in the plots.

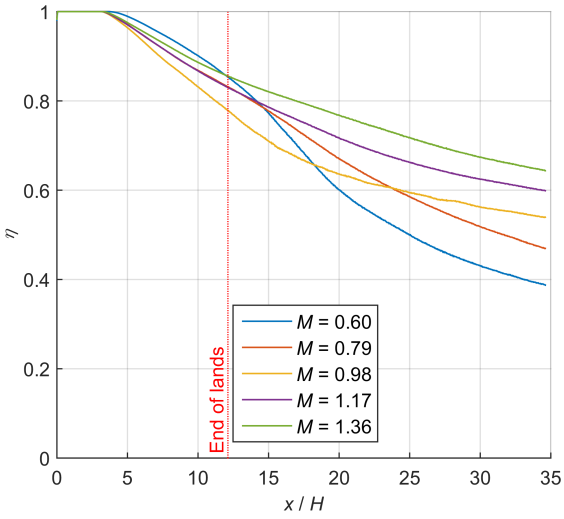
In Section 7.3.5, it was found that the potential core, in which effectiveness was initially unity for some distance from the slot, was completely absent for the cross corrugated



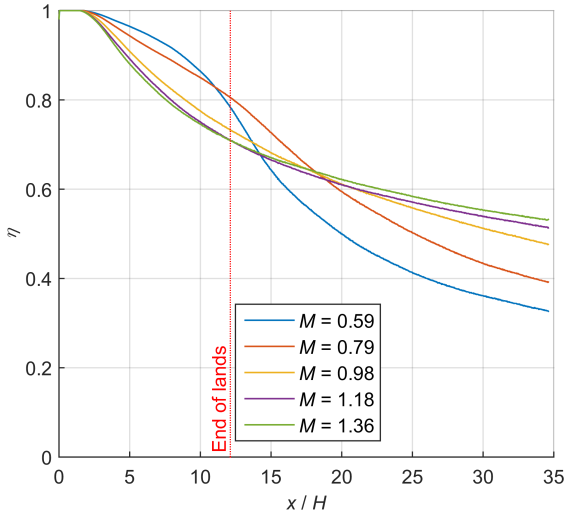
(a) G9



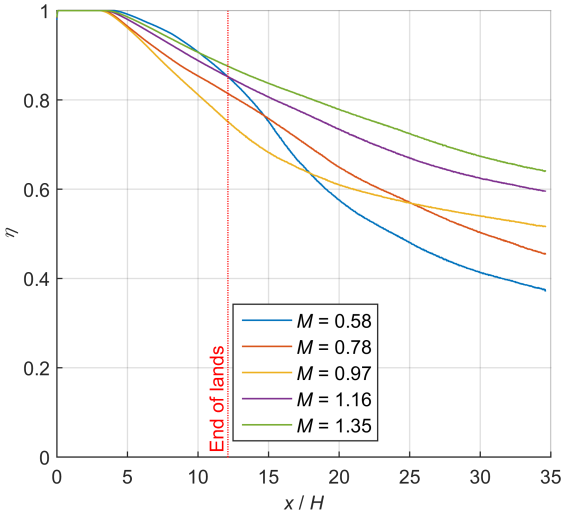
(b) G10



(c) G11



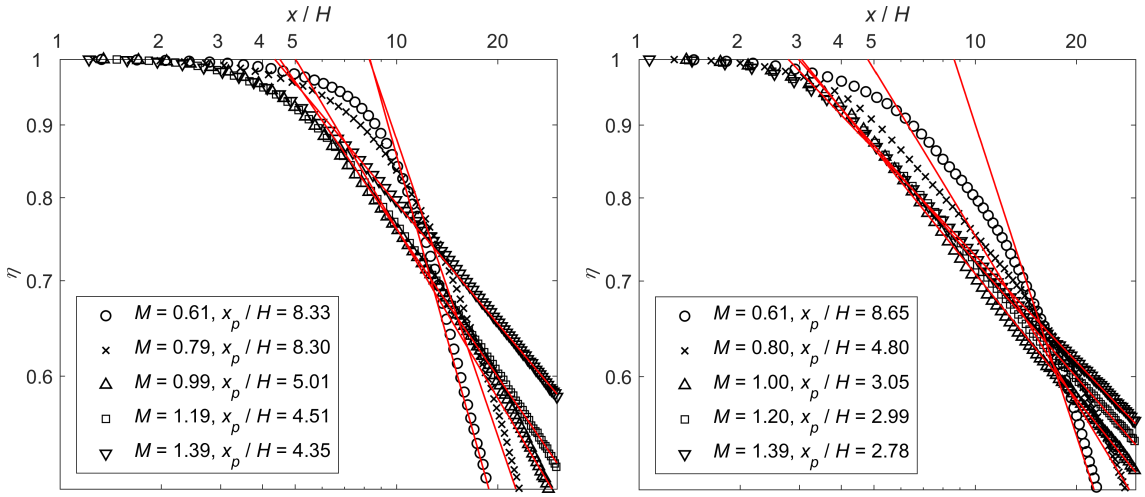
(d) G12



(e) G13

Figure 8.8: Centreline η, slots with exit shaping, G9–13

geometries. As soon as the coolant gas left the slot, the uneven spanwise distribution with distinct jets and gaps led to immediate entrainment of the mainstream gas and thus an immediate drop in effectiveness. By using exit shaping, there was a much more consistent "sheet" of coolant across the span of the slot, shielding the cutback surface completely from the mainstream gas for some distance before mixing. Consequently, the potential core became apparent again.

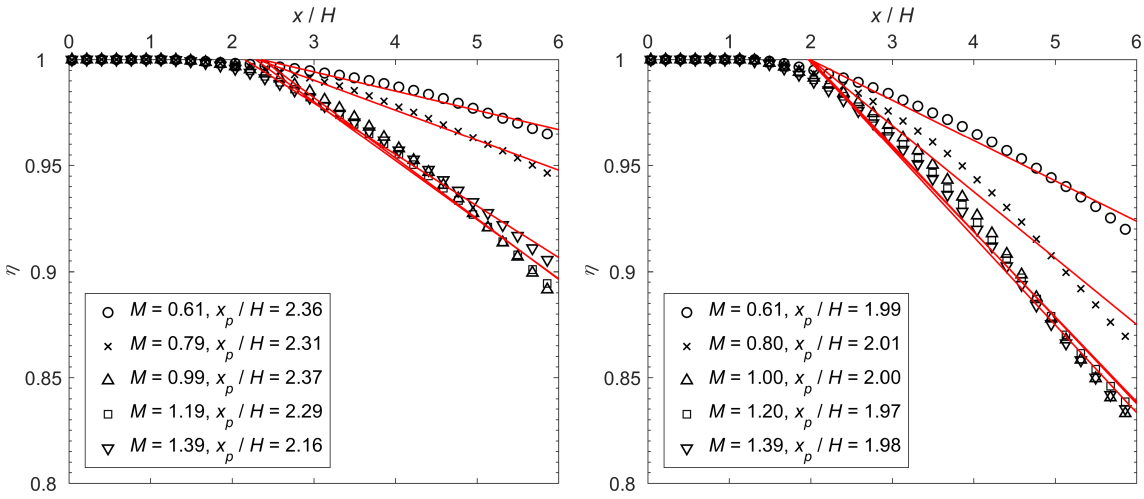


(a) G9 (b) G10

Figure 8.9: Determining potential core length with cross corrugated slot using logarithmic plot

However, attempting to use the same method to determine the potential core length as in Section 6.3.3 did not provide a reasonable estimation of potential core length. This is shown in Figure 8.9 using geometries G9 and G10 as examples. It can be seen that, particularly at low blowing ratio, taking a straight line extrapolation through the far downstream data where effectiveness was below about 0.8 on a logarithmic plot implied an end point of unity effectiveness that was quite a long distance from the slot exit. However, the data points where effectiveness was above about 0.8 did not fall on this line.

In order to determine a more reasonable estimate of the potential core length for the exit shaped cross corrugated geometries, the data points where $x/H > 6$ were filtered out and a straight line extrapolation was taken using the remaining points on a plot of centreline effectiveness against x/H. Two examples of this are shown in Figure 8.10 using the same geometries G9 and G10. This was found to more closely estimate the



(a) G9 (b) G10

Figure 8.10: Determining potential core length with cross corrugated slot using filtered data

implied end point of unity effectiveness.

Figure 8.11 shows a plot of potential core length for geometries G9–13 with G0 for comparison. It can be seen that while there was a potential core for geometries G9, G10 and G12, it was very short at only 2 slot heights long and remained the same length at all blowing ratios. On the other hand, geometries G11 and G13 had a potential core as long as the baseline G0 at the lowest blowing ratio of $M = 0.6$. However, potential core length decreased slightly with increased blowing ratio for G11 and G13, in contrast with the baseline rectangular slot geometry which showed greatly increased potential core length with blowing ratio. For $M > 1.0$, G13 showed a small recovery in potential core length but not up to the same length as $M = 0.6$.

The longest potential core at the lowest blowing ratio was likely due to the lower momentum coolant flow being able to spread out more evenly as it passed through the exit shaping sections, resulting in a more consistent sheet of coolant on the cutback immediately after exit. Whereas at higher blowing ratios, the higher momentum of the coolant flow resulted in less spanwise consistency and earlier entrainment of the mainstream flow between the jets of coolant.

This effect was still apparent after the potential core region, with effectiveness reducing less quickly with distance at low blowing ratio compared to high blowing ratio.

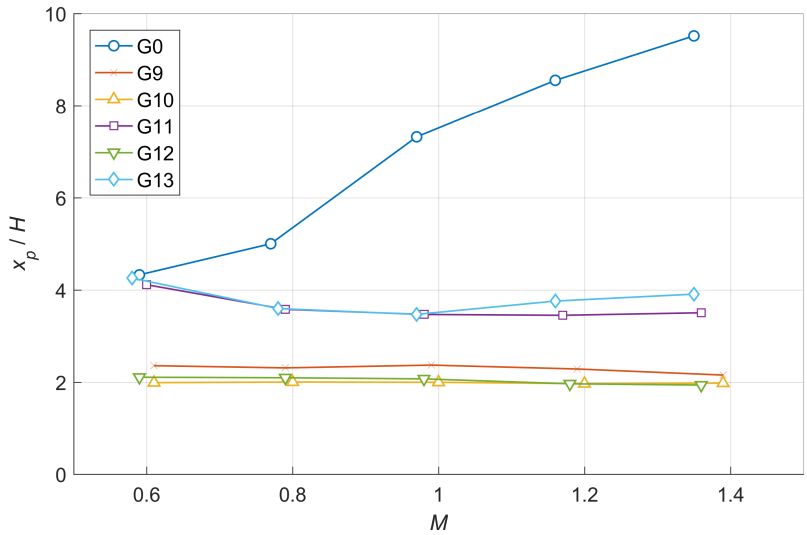


Figure 8.11: Potential core length, cross corrugated geometries with exit shaping

Further away from the slot, as the spanwise flow inconsistencies tended to mix out, this effect became less important than the mass flow ratio between the coolant and mainstream, resulting in the high blowing ratios with greater coolant to mainstream mass flow ratios maintaining higher effectiveness far from the slot exit compared to the low blowing ratios. This reversal was similar to the cross corrugated geometries without exit shaping (geometries G1–8) discussed in Section 7.3.5 and show in Figures 7.18b to 7.18e and Figure 7.19. However, with exit shaping this occurred later, at a distance of at least $x/H \approx 10$ with G13 and as far as $x/H \approx 15$ for G10, compared to $x/H \approx 6$ with G1–4. This allowed a significant benefit to effectiveness near the slot exit at low blowing ratios. The result was that, compared with the cross corrugated geometries without exit shaping, centreline effectiveness was higher at all blowing ratios both near to and far from the slot exit.

Compared with the baseline rectangular slot (geometry G0) shown in Figure 7.18a, centreline effectiveness was lower at all blowing ratios far from the slot exit and lower for $M > 0.8$ near to the slot exit. However, for $M < 0.8$, effectiveness near the slot exit was higher than the baseline case. Geometries G11 and G13 showed the greatest near slot effectiveness improvement at $M = 0.6$, with effectiveness at the end of the lands of over 0.85 while G0 had an effectiveness of less than 0.7 at the same distance and blowing ratio. This was despite geometries G11 and G13 having a shorter potential core than G0.

8.3.5 Spanwise averaged effectiveness

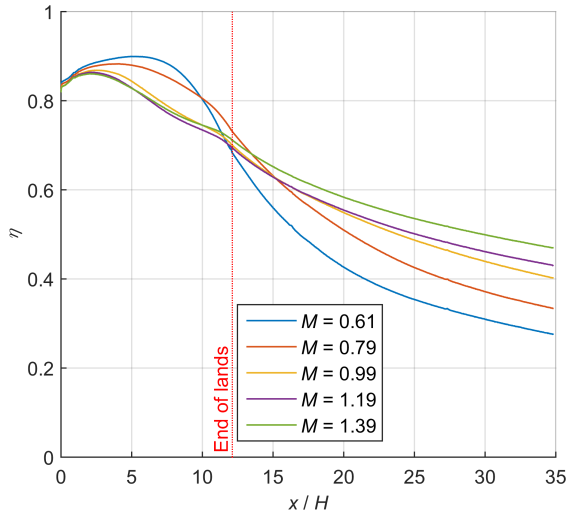
Figure 8.12 shows plots of spanwise averaged film cooling effectiveness including the lands. The average was taken over the entire region in between the centre-points of the two lands.

Due to the inclusion of the diffuser shaped lands which were mostly uncooled with very low effectiveness on top, the starting effectiveness was reduced to about 0.82 to 0.84, a similar level as the baseline geometry G0 shown in Figure 7.20a. The starting effectiveness appears to be slightly higher for $M = 0.6$ compared ot the higher blowing ratios by about 0.02 due to the slightly increased effectiveness on top of the lands. However taking into account the uncertainty in that region, this difference is not very significant.

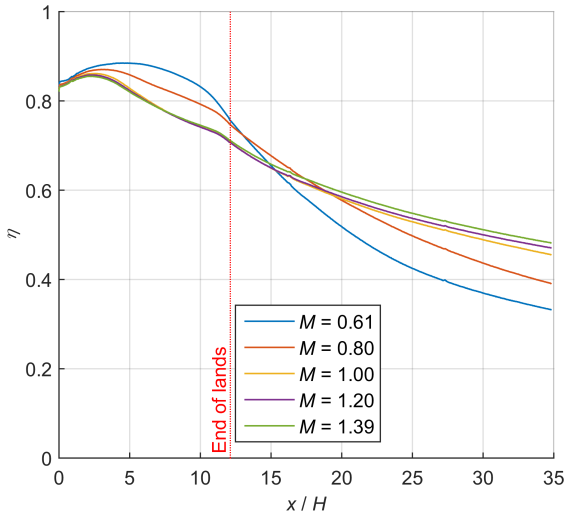
As the lands reduced in width up to the tip and the coolant was allowed to spread out, effectiveness was able to recover somewhat. At low blowing ratios where $M < 0.8$, this recovery effect was substantial, increasing spanwise effectiveness as much as 0.08 for $M = 0.6$ using geometry G13, considerably greater than the 0.03 using G0 as well as all of cross corrugated geometries without exit shaping, G1–8 (Section 7.3.6). This was apparent for all of the geometries with exit shaping, G9–13 and was due to the cross corrugated geometries directing some coolant flow towards the sides of the lands, resulting in higher effectiveness near the lands. Whereas the baseline geometry typically had low effectiveness near the lands since the coolant flow separated slightly from the lands upon exit from the slot. This benefit had less significance far downstream from the slot exit, where the cross corrugated geometries had lower effectiveness across the board.

Owing to the recovery effect, peak effectiveness was much higher for G9–13 compared to G0. Figure 8.13 shows a plot of peak spanwise averaged effectiveness for geometries G9–13 as well as the baseline geometry G0.

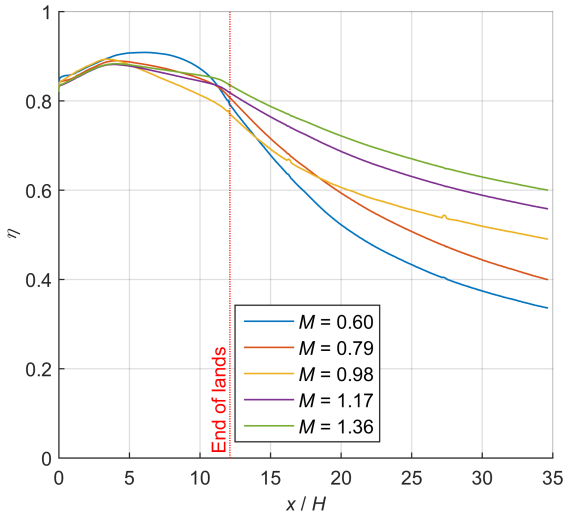
It can be seen that due to the recovery effect geometries G9–13 performed better than G0 for $M = 0.6$. However, at mid to high blowing ratios where $M > 0.8$, the recovery effect was no longer sufficient, exhibiting reduced spanwise averaged effectiveness across G9–13 compared to the baseline G0 although still far higher than geometries G1–8. Peak



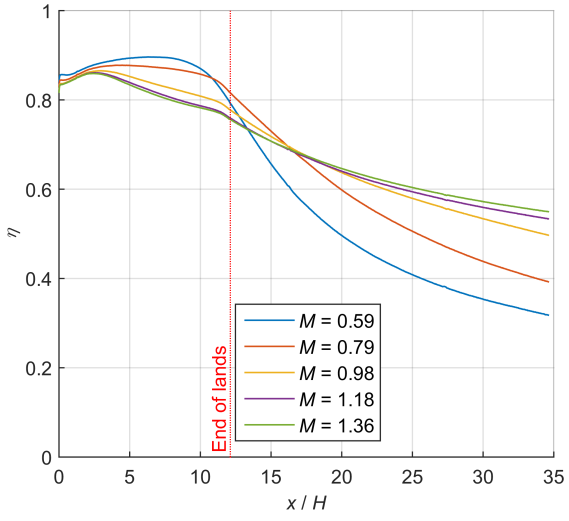
(a) G9



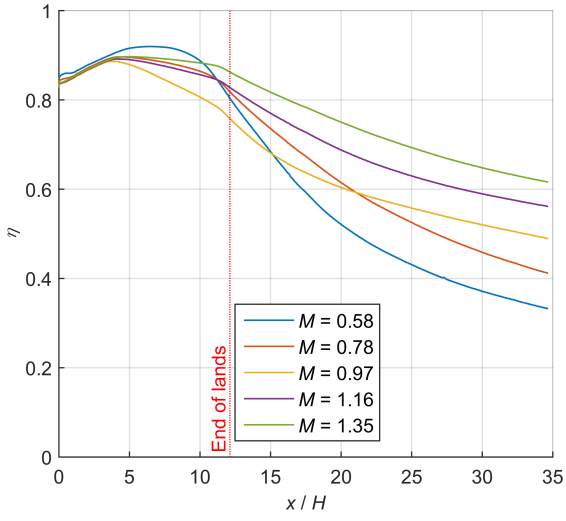
(b) G10



(c) G11



(d) G12



(e) G13

Figure 8.12: Spanwise averaged η, slots with exit shaping, G9–13

effectiveness for G9–13 of 0.88 to 0.92 was achieved at the lowest blowing of $M = 0.6$ compared to 0.93 at the highest blowing ratio of $M = 1.4$ for G0.

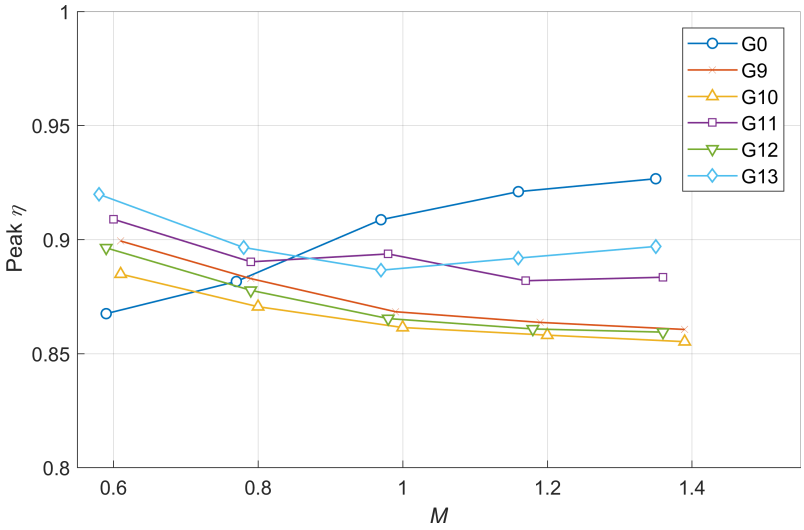
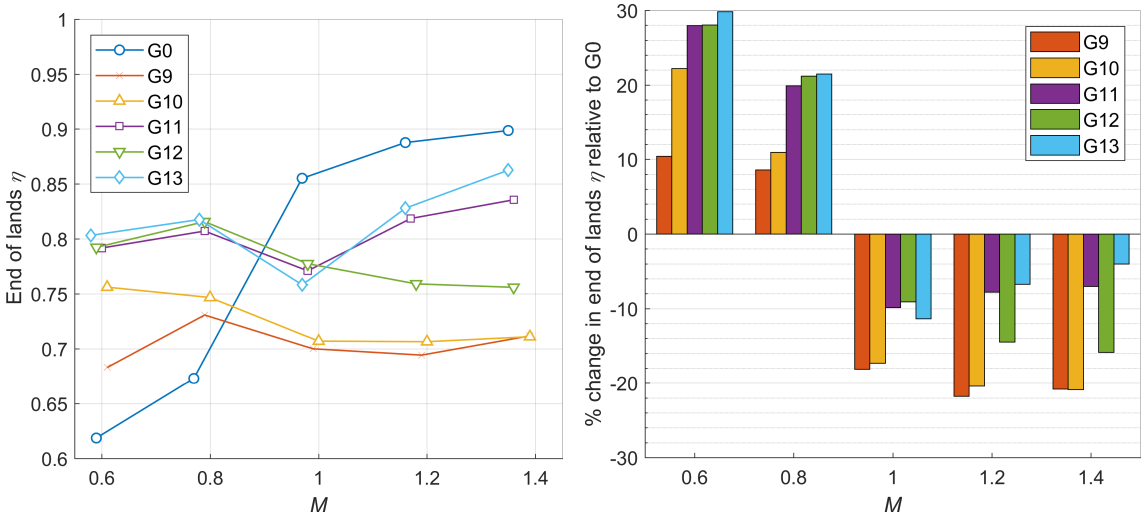


Figure 8.13: Peak η, slots with exit shaping, G0 and G9–13

Similar to geometries G1–8 in Section 7.3.6, geometries G9–13 started with the highest effectiveness at the lowest blowing ratio near the slot exit, until a certain point where the trend reversed to get highest effectiveness at the highest blowing ratio. For G1–4 this point occurred quite consistently at $x/H \approx 6$ but for G9–13 this was delayed to at least $x/H \approx 10$. Geometry G10 actually showed the highest effectiveness at $M = 0.6$ all the way until $x/H \approx 13$. Owing to this, effectiveness at the end of the lands was increased significantly with exit shaping.

Figure 8.14a shows a plot of spanwise averaged effectiveness at the end of the lands where $x/H = 12.1$ for all five geometries along with the baseline geometry at their tested blowing ratios. For blowing ratios of $M = 0.8$ and below, the cross corrugated geometries with exit shaping performed significantly better. However, for blowing ratios of $M = 1.0$ and above, they performed worse. Amongst the cross corrugated geometries, G13 fared the best at most blowing ratios. Figure 8.14b shows the same data represented as a percentage change relative to the baseline geometry G0. At the lowest blowing ratio of $M = 0.6$, G9–13 performed $10\,\%$ to $30\,\%$ better than the baseline but at the highest blowing ratio of $M = 1.4$, it performed $4\,\%$ to $21\,\%$ worse.



(a) Absolute value

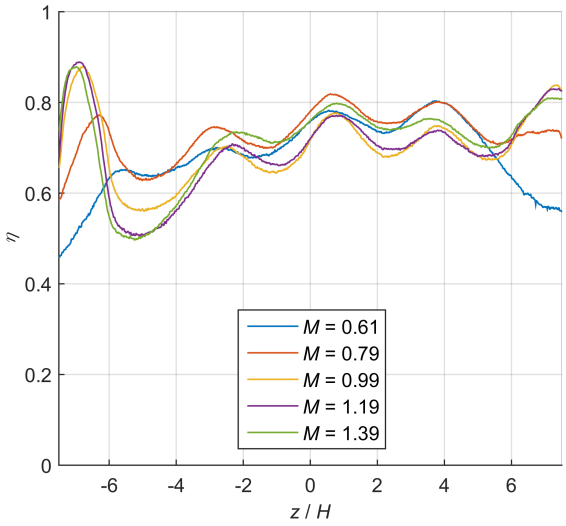
(b) Percentage change relative to G0

Figure 8.14: End of lands η, slots with exit shaping, G0 and G9–13

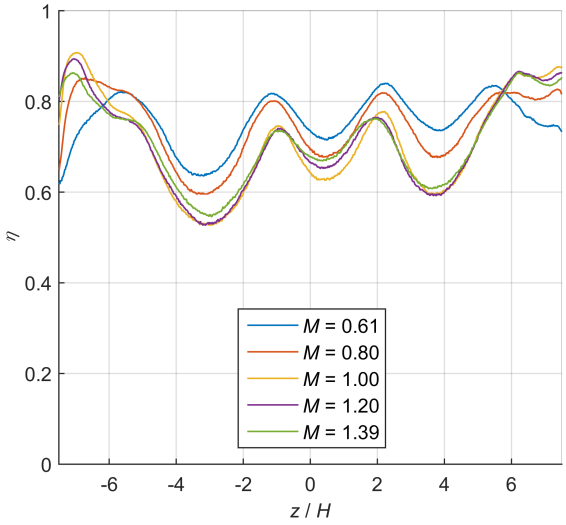
8.3.6 Spanwise variation of effectiveness at end of lands

Figure 8.15 shows plots of spanwise variation in film cooling effectiveness taken at the end of the lands. This included a 20 pixel ($1.7\,\mathrm{mm}$) wide strip parallel to the slot lip at a distance equal to the length of the lands where $x/H = 12.1$. The spanwise extent starts from the centre of the left hand side land where $z/H = -7.5$ and ends at the centre of the right hand side land where $z/H = 7.5$. $z/H = 0$ marks the centreline of the slot. $z/H = -6$ marks the right side edge of the land hand land, while $z/H = 6$ marks the left side edge of the right hand land. This x/H position is considered to be particularly important as it represents the trailing edge of the blade, where cooling is almost completely reliant on the film effectiveness and large local variations in effectiveness along the trailing edge can lead to high temperature gradients which cause thermal stresses in the blade metal that can affect blade life.

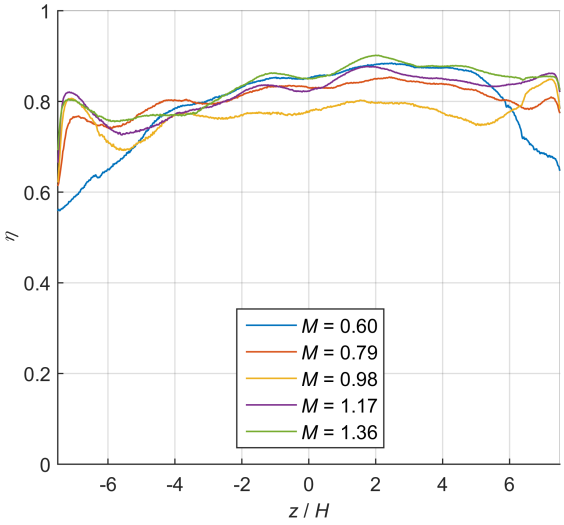
In Section 8.3.5 it was mentioned that at low blowing ratio, geometries G9–13 displayed a greater recovery in spanwise averaged effectiveness a short distance from the slot exit compared to the baseline geometry G0, in large part due to the higher effectiveness near the lands using the cross corrugated slot. This effect can be seen by comparing the spanwise variation plots for G0 in Figure 7.22a with those for G9–13 in Figure 8.15. For G0, effectiveness was significantly lower near the lands whereas for G9–13, effec-



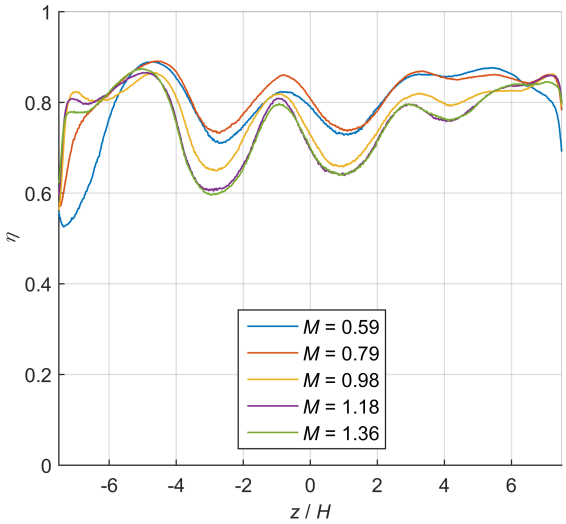
(a) G9, end of lands



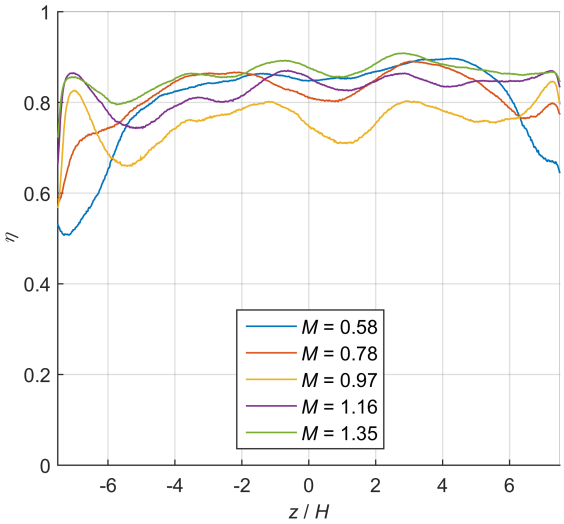
(b) G10, end of lands



(c) G11, end of lands



(d) G12, end of lands



(e) G13, end of lands

Figure 8.15: Spanwise varation of η, slots with exit shaping, G9–13

tiveness did not drop as much near the lands and in some cases was actually higher near the lands.

In between the lands, effectiveness was much higher compared to G1–8 shown in Figures 7.22 and 7.23, particularly at low blowing ratio. While effectiveness generally increased with blowing ratio at the end of the lands for geometries G0–8, effectiveness was roughly consistent regardless of blowing ratio for geometries G9–13. This was because the end of the lands was close to the point at which the near slot effects that increased effectiveness at low blowing ratio were outweighed by the bulk mixing effects that increased effectiveness with blowing ratio, as discussed in Section 8.3.5.

In terms of spanwise consistency, geometries G9, G10 and G12 were somewhat lacking. Figures 8.15a, 8.15b and 8.15d show quite clearly the presence of the peaks of effectiveness caused by the cross corrugated slot, the magnitudes of which were an approximately 0.2 difference between the peaks and troughs. Evidently, the spanwise inconsistencies described in Section 8.3.1 were not able to mix out by this point. However, Figures 8.15c and 8.15e display a much more consistent effectiveness in between the lands for geometries G11 and G13. Excluding the larger changes in effectiveness near the lands, the effectiveness did not change by more than 0.1 across the span for any blowing ratio. Even near the lands, for $1.0 < M < 1.4$, the effectiveness remained at roughly the same level. For $M < 0.8$, the effectiveness did drop near the lands, but still to a lesser extent than with geometry G0. Overall, the exit shaping allowed for a fairly consistent level of effectiveness at about 0.8 with less sensitivity to blowing ratio.

8.3.7 Area averaged effectiveness

Figure 8.16 shows a plot of area averaged film cooling effectiveness for all five geometries along with the baseline geometry at their tested blowing ratios. This included the cutback and land top surfaces up to the end of the lands where $x/H = 12.1$. It gives an overall picture of the relative performance of each geometry over the region most relevant to trailing edge cooling.

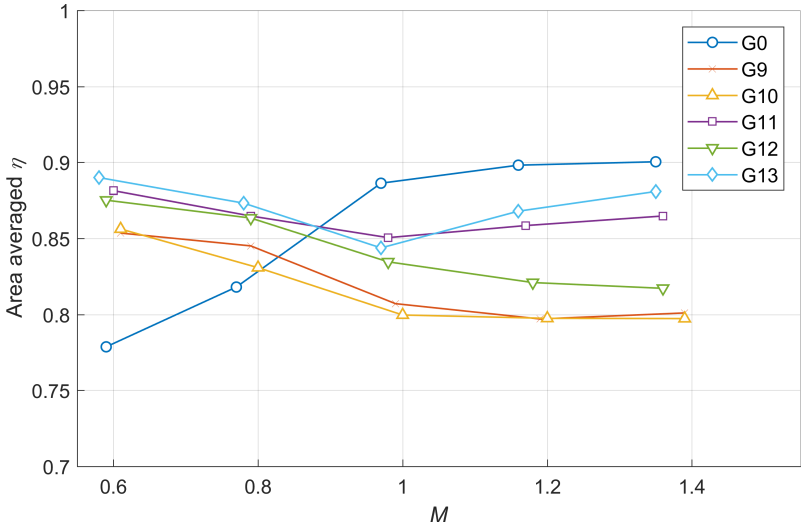


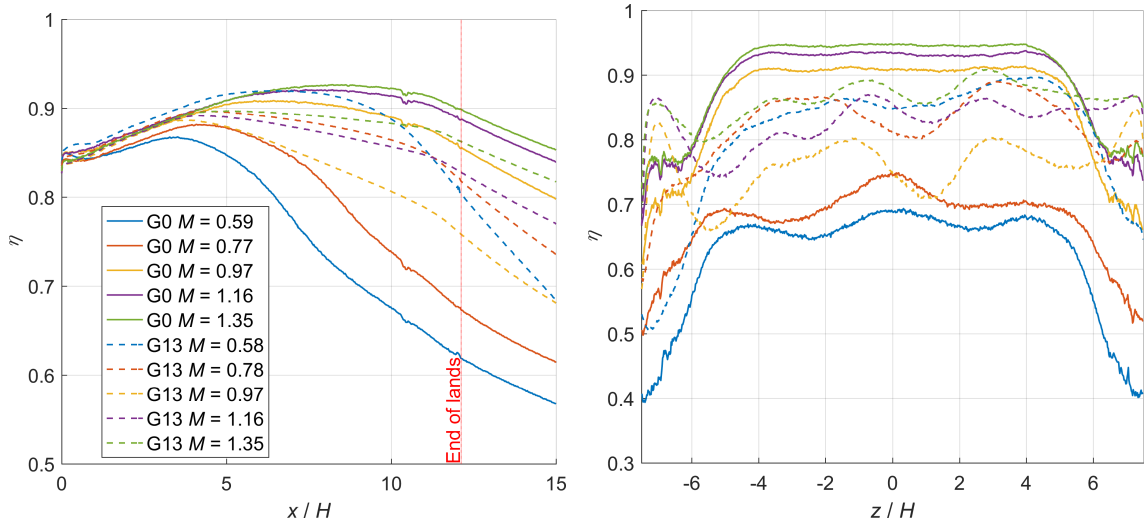
Figure 8.16: Area averaged η, slots with exit shaping, G0 and G9–13

Unlike the cross corrugated geometries without exit shaping shown in Section 7.3.8, performance was comparable to the baseline geometry, actually exceeding it for $M < 0.8$ with effectiveness as high as 0.89. Performance for $M > 1.0$ was not as high as the baseline but remained relatively high with the lowest average effectiveness at approximately 0.80.

Like the cross corrugated geometries without exit shaping, performance was relatively insensitive to blowing ratio, with average effectiveness not varying by more than 0.05 for each geometry. G13 showed a dip in effectiveness at $M = 1.0$ but this was recovered at higher blowing ratio. G9, G10 and G12 showed a downwards trend in average effectiveness with increasing blowing ratio. These were also the geometries with the most inconsistencies in spanwise effectiveness profile as described in Section 8.3.1 and visible as distinct streaks in high and low effectiveness in Figures 8.1, 8.2 and 8.4. It is likely that increasing the blowing ratio caused the these jets of coolant leaving the slot to spread out less in the spanwise direction, leaving large gaps in between them which encouraged the entrainment of mainstream gas and reduced the average effectiveness. For geometries G11 and G13, the coolant flow leaving the slot was sufficiently even in the spanwise direction that it maintained spanwise consistency even at higher blowing ratios.

8.3.8 Most optimised geometry

Based on area averaged effectiveness, geometry G13 performed the best out of the cross corrugated geometries tested at all blowing ratios except $M = 1.0$ where G11 performed slightly better. G13 also had the highest end of lands effectiveness relative to the baseline at all blowing ratios, again with the exception of $M = 1.0$ where G11 and G12 performed slightly better. The spanwise variation in effectiveness at the end of the lands was relatively low, with a fairly flat profile in between the lands even though there was a drop in effectiveness near the tips of the lands at low blowing ratio.



(a) Spanwise averaged η (b) Spanwise variation at end of lands

Figure 8.17: Comparison of η between G0 and G13

Figure 8.17a shows a direct comparison of spanwise averaged effectiveness between G0 and G13 focusing on the region up to the end of the lands. Peak effectiveness of 0.92 was achieved at $M = 0.6$ at a distance of $x/H = 6.67$, compared to the peak effectiveness of 0.93 achieved by G0 at $M = 1.4$ at a distance of $x/H = 8.59$. At $M = 1.4$, effectiveness at the end of the lands where $x/H = 12.1$ was reduced by $4.0\,\%$. However, at $M = 0.8$, effectiveness at the same distance was increased by $21.5\,\%$ while at $M = 0.6$, effectiveness was increased by $29.8\,\%$.

Figure 8.17b shows a direct comparison of spanwise effectiveness profiles at the end of the lands. G13 displayed fairly consistent effectiveness across the span and was relatively

insensitive to blowing ratio compared to G0. Effectiveness near the tips of the lands was higher at all blowing ratios, in particular for $M > 1.0$ where it remained at roughly the same level as the middle of the slot. For $M < 0.8$, effectiveness did drop near the lands, but still remained higher than G0.

8.4 Summary and conclusions

Detailed distributions of adiabatic film cooling effectiveness have been measured over the cutback and land top surfaces of large scale geometries representing turbine blade trailing edges using the PSP technique. Five different cross corrugated slot geometries with exit shaping were tested with blowing ratio ranging from 0.6 to 1.4 and a density ratio of 1. The cross corrugated geometries all used an included angle of $90°$ and tapered diffuser lands.

While the simplified nature of the experimental model limits the direct applicability of the measurements to a real blade or vane, the third phase of experiments aimed to improve to improve film cooling performance of the cross corrugated geometries in Chapter 7 by testing various exit shaping strategies and comparing them relative to each other and to the baseline slot. The conclusions from these comparisons are as follows:

- The use of a "ramp down" exit shaping section to morph the slot exit profile into simple rectangle increased cooling performance significantly compared to the cross corrugated slots without exit shaping.
- At blowing ratios below 0.8, near slot effectiveness was improved significantly and was comparable to the baseline rectangular slot.
- Far from the slot and at higher blowing ratios above 0.8, effectiveness was inferior to the baseline.
- Spanwise consistency was improved greatly compared to the geometries without exit shaping but still not as consistent as the baseline.

- Overall effectiveness was reduced as blowing ratio was increased, although it was not as sensitive to blowing ratio as the baseline.
- Effectiveness near the lands was increased, as with the cross corrugated geometries without exit shaping, but without sacrificing effectiveness in between the lands to such a great extent.
- On top of the lands, effectiveness was slightly improved along the edges at low blowing ratios, but not to a significant degree.
- The addition of a flow straightening section to turn the channels from $45°$ to the mainstream to parallel to the mainstream increased effectiveness far downstream of the slot.
- However, the resulting spanwise effectiveness profile was more uneven.
- Placing the straightening section immediately on top of the ramp down section did not significantly increase overall effectiveness.
- Placing the straightening section immediately before the ramp down section increased overall effectiveness significantly but still remained uneven in spanwise consistency.
- Extending the length of the ramp down and straightening sections, thereby allowing for a more gradual transition to the rectangular exit profile, resulted in a much more even spanwise profile, as well as greatly increased effectiveness at blowing ratios above 1.0.
- Offsetting the ramp down and straightening sections from the slot exit to leave a short settling section with a plain rectangular profile just before the exit also resulted in a much more even spanwise profile, as well as even greater increase in effectiveness at blowing ratios above 1.0.

The third phase of experiments has shown that the film cooling performance of cross corrugated slots can be improved significantly with the use of exit shaping, to the point where at low blowing ratios, film cooling performance can be superior to a simple rectangular slot.

The final design G13 (shown in Figure 5.20d) was found to be the best cross corrugated design overall and superior to the baseline rectangular slot up to a blowing ratio of 0.8. Spanwise averaged effectiveness at the end of the lands was increased by $29.8\,\%$ at a blowing ratio of 0.6 and $21.5\,\%$ at a blowing ratio of 0.8. Spanwise averaged effectiveness at the end of the lands was reduced by $4.0\,\%$ at a blowing ratio of 1.4. The spanwise effectiveness profile at the end of the lands was found to be more even and relatively insensitive to blowing ratio compared to the baseline geometry.

Chapter 9

Effectiveness Measurements — Density Ratio Effects

9.1 Introduction

In Chapter 8 it was shown that the most optimised cross corrugated slot design, geometry G13, was able to provide film cooling performance on par with and in some aspects better than the baseline rectangular slot geometry at lower blowing ratios.

However, the use of nitrogen as the coolant in these experiments meant that it was not possible to simultaneously match both the blowing ratio and the momentum flux ratio. The density ratio between nitrogen and air is effectively 1, while the coolant to mainstream density ratio in the engine is closer to 2. Thus, the tested momentum flux ratios in the experiments were approximately double that of the real engine. Momentum flux ratio is the principle parameter that affects the penetration of coolant exhausted from a film hole into the mainstream. For tangential injection, penetration of coolant into the mainstream is not expected to be as significant a factor. However, in order to confirm the conclusions of Chapter 8 at a more engine representative momentum flux ratio, it was deemed useful to test using a higher density ratio if possible.

The objective of the fourth phase of experiments was to determine the effects of using a higher density ratio on film cooling performance of the optimised cross corrugated

slot design. This was accomplished by measuring film effectiveness again using the most optimised geometry from Chapter 8 as well as the baseline rectangular slot. However, instead of nitrogen, carbon dioxide was used as the coolant gas. With air as the mainstream, this allowed a density ratio of 1.52. For each given blowing ratio, Table 9.1 shows the momentum flux ratios using nitrogen coolant, carbon dioxide coolant and how it would be in a real engine (where the density ratio is approximately 2). A higher density ratio that matches that of a real engine could not be achieved without using a mixture with a heavier gas like sulphur hexafluoride which was deemed impractical for the current study.

M	J_{N_2}	J_{CO_2}	J_{engine}
0.6	0.37	0.24	0.18
0.8	0.66	0.42	0.32
1.0	1.03	0.66	0.50
1.2	1.49	0.95	0.72
1.4	2.02	1.29	0.98

Table 9.1: Comparison of momentum flux ratio using nitrogen and carbon dioxide coolant compared to a real engine

This chapter shows the results from phase 4 and discusses how an increased density ratio affected the film cooling effectiveness using the cross corrugated geometry and the plain rectangular slot and whether this altered the relative performance between the two.

9.2 2D film cooling effectiveness distributions

The PSP technique allows high resolution 2D adiabatic film effectiveness measurements over the cutback surface and top of the lands to be made. The approximate view area and coordinate system is defined in Figure 6.1, where x is the downstream distance from the slot exit and z is the spanwise displacement from the centreline. These are non-dimensionalised for all geometries by the slot height of the baseline plain rectangular slot geometry G0 to give x/H and z/H, where $H = 4.6\,\text{mm}$. In phase 4, the cross corrugated geometry G13 had the same exit height as the plain rectangular slot. Measurements were

taken for $M = 0.6, 0.8, 1.0, 1.2, 1.4$.

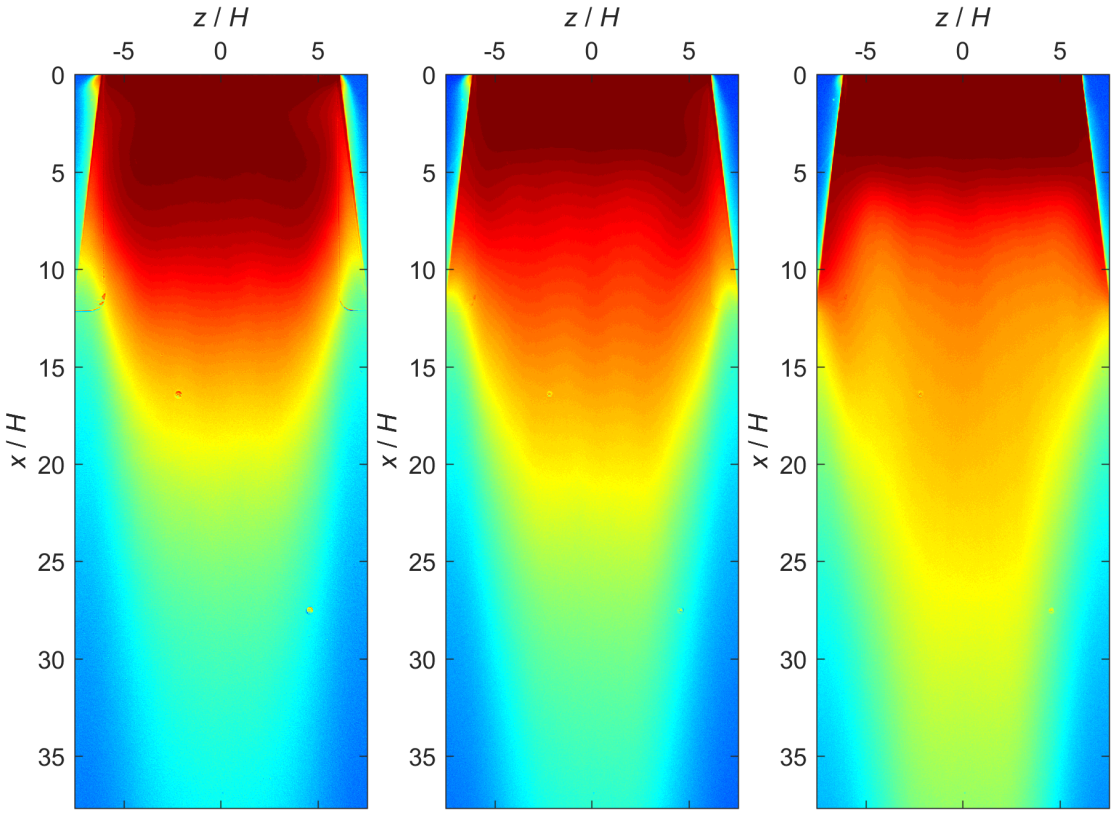
Figures 9.1 and 9.2 show the 2D plots of effectiveness taken in phase 4. All of the figures show a plan view of the cutback region and lands. The slot exit and lip is aligned with the top border of the plots, i.e. where $x/H = 0$. The centreline is at the midpoint between the lands where $z/H = 0$. Blue regions show poor coverage from the carbon dioxide coolant and correspond to low film cooling effectiveness and red regions correspond to high effectiveness. The lands can be seen as the predominantly blue regions in the top left and top right corners or each plot.

9.3 Discussion

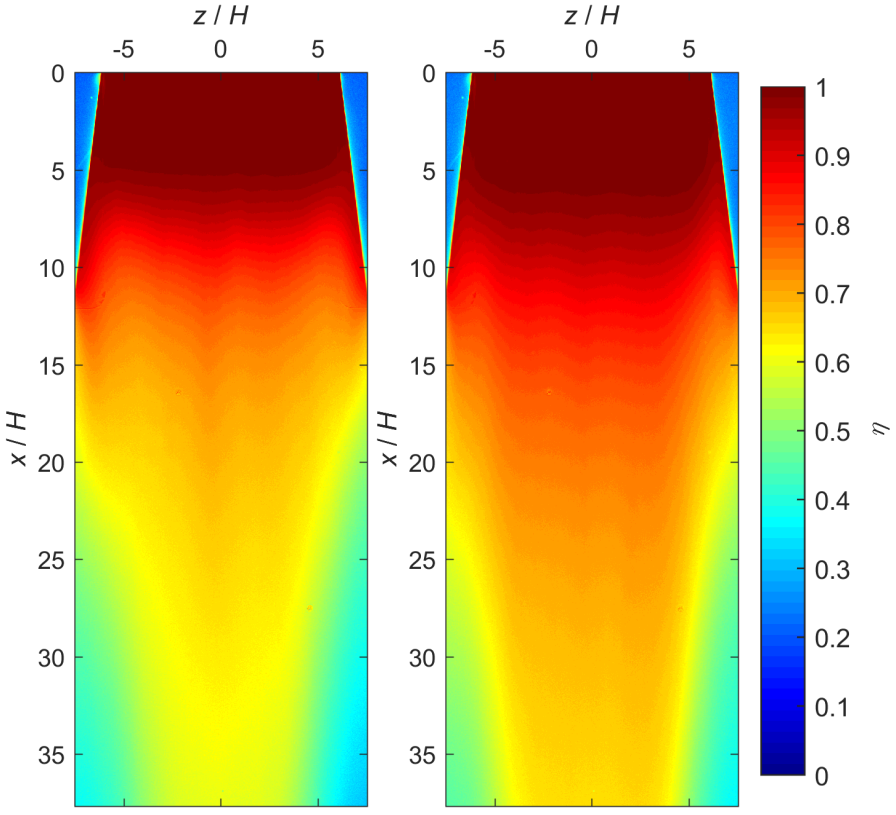
9.3.1 Cutback effectiveness

The baseline rectangular slot G0 shown in Figure 9.1 displays a similar mixing pattern to what was seen in phase 2 using nitrogen coolant, shown in Figure 7.1. Effectiveness was greater near the centreline and fairly even across the span of the slot, reducing near the lands. The potential core region, where effectiveness was essentially unity near the slot, was clearly visible and bore a similar size and shape at the lowest blowing ratio of $M = 0.6$. However, as blowing ratio increased, the potential core length did not appear to increase significantly when using carbon dioxide as the coolant. Outside of the potential core region, effectiveness also reduced significantly more quickly with distance from the slot exit, such that using carbon dioxide at $M = 1.4$ resulted in a similar effectiveness plot as using nitrogen at $M = 1.0$. However, for $M = 1.0$, effectiveness near the lands did appear to be slightly increased when using carbon dioxide.

The optimised cross corrugated slot geometry G13, shown in Figure 9.2, also shows a similar mixing pattern to the nitrogen coolant counterpart shown in Figure 8.5. The streaks of high effectiveness and the right-side bias were still apparent when using carbon dioxide as the coolant. As in the previous phase, the potential core region was insensitive to blowing ratio, remaining roughly the same size regardless of blowing ratio.

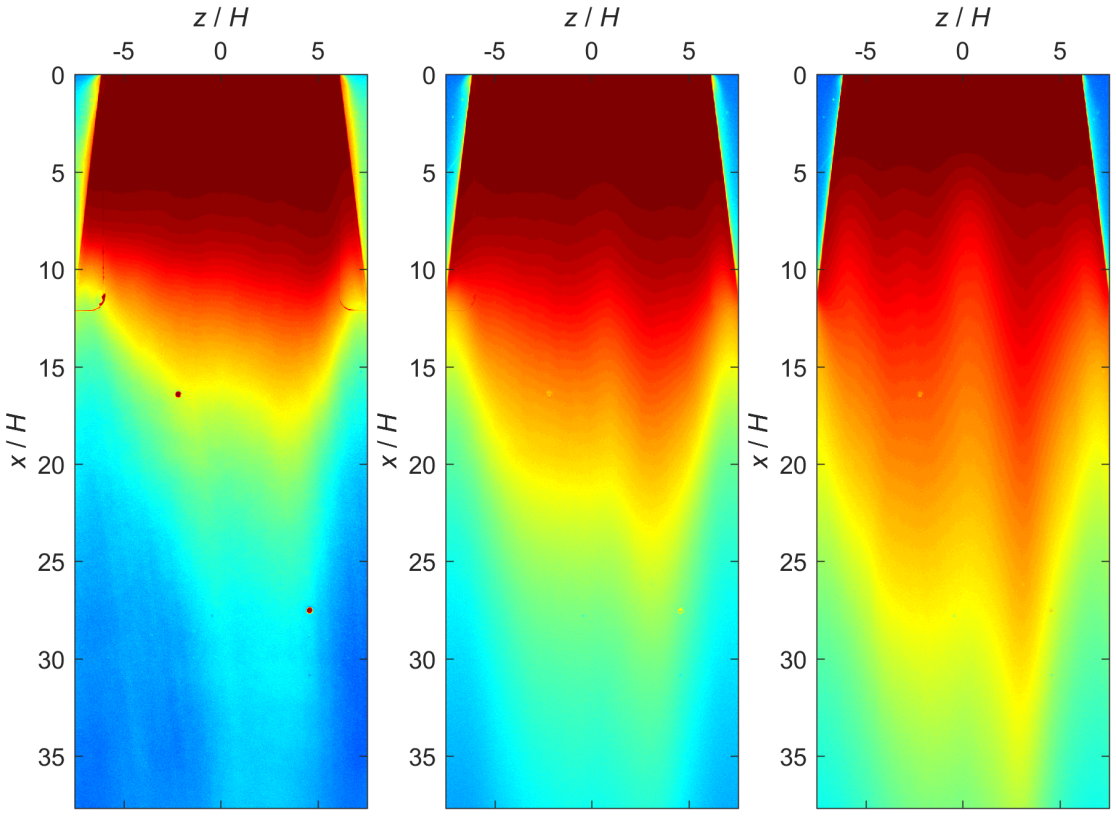


(a) $M = 0.58$ (b) $M = 0.79$ (c) $M = 0.97$

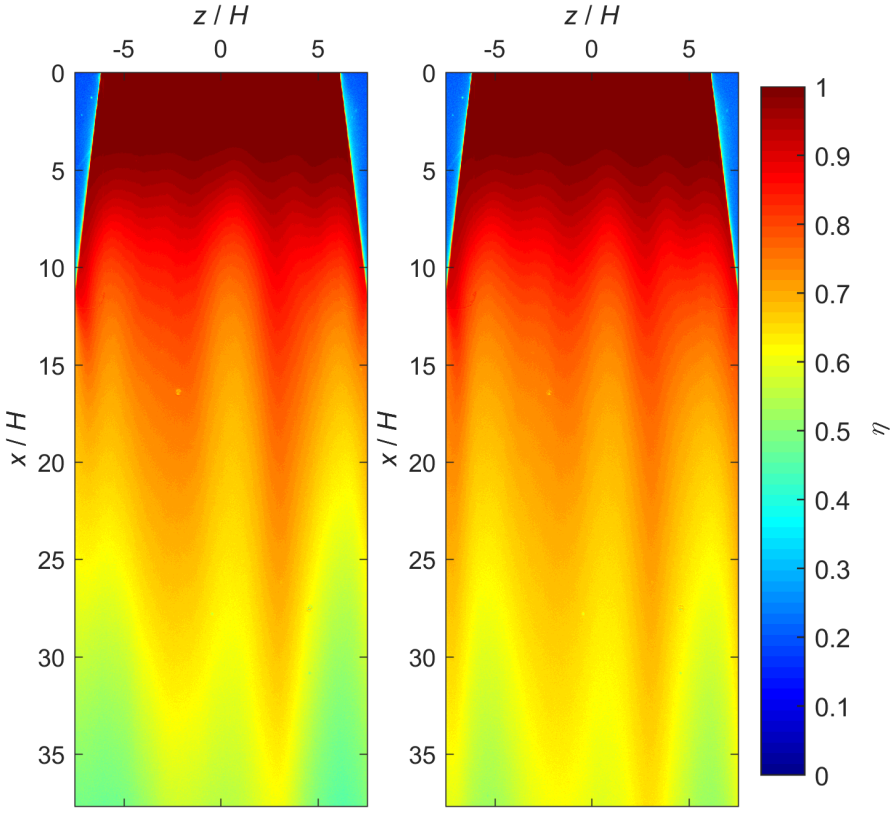


(d) $M = 1.15$ (e) $M = 1.33$

Figure 9.1: 2D η distributions using carbon dioxide coolant, G0



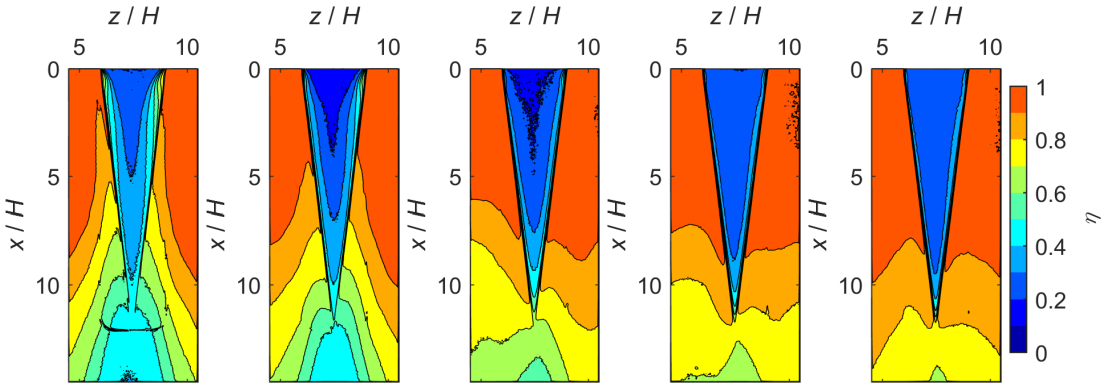
(a) $M = 0.59$ (b) $M = 0.77$ (c) $M = 0.97$



(d) $M = 1.15$ (e) $M = 1.33$

Figure 9.2: 2D η distributions using carbon dioxide coolant, G13

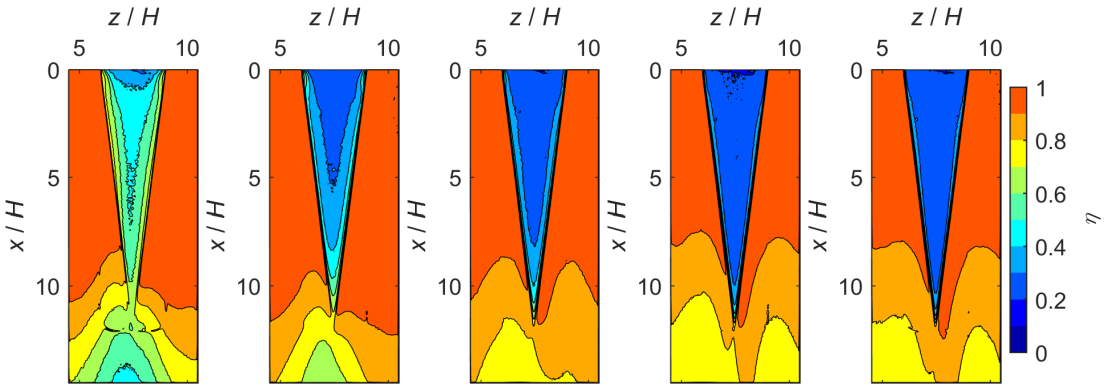
9.3.2 Land effectiveness



(a) $M = 0.58$ (b) $M = 0.79$ (c) $M = 0.97$ (d) $M = 1.15$ (e) $M = 1.33$

Figure 9.3: 2D land η distributions using carbon dioxide coolant, G0

Figure 9.3 shows a close-up view of the right hand side land of geometry G0 with effectiveness shown using 10 contour bands at all five blowing ratios. Compared with Figure 7.14 which shows the same geometry using nitrogen coolant, it can be seen that effectiveness is higher by as much as 0.2 on top the lands at low blowing ratio. At higher blowing ratios, the change in effectiveness was not as significant. It is apparent that when ejected at the same low mass flow ratio, the denser carbon dioxide coolant had reduced momentum and was more able to wash over the edges of the tapered lands, resulting in higher effectiveness at low blowing ratio. Effectiveness next to the lands was unchanged, although at high blowing ratio, effectiveness further away from the lands was reduced.



(a) $M = 0.59$ (b) $M = 0.77$ (c) $M = 0.97$ (d) $M = 1.15$ (e) $M = 1.33$

Figure 9.4: 2D land η distributions using carbon dioxide coolant, G13

Figure 9.4 shows the same view of geometry G13 using identically spaced effective-

ness contours. It is immediately apparent that effectiveness on top of the lands was significantly increased for low blowing ratio. In Section 8.3.2, it was noted that the cross corrugated geometries did not appear to significantly affect the effectiveness on top of the lands when compared with the baseline rectangular slot. However, comparing Figure 9.4a with Figure 8.7d which shows the same geometry using nitrogen coolant at $M = 0.6$, effectiveness is higher by as much as 0.4. It appears that using the denser, lower momentum carbon dioxide coolant combined with the angled corrugation channels imparting spanwise momentum to the flow resulted in a significant amount of coolant washing over the edges of the tapered lands, increasing effectiveness on top. This effect reduced very quickly with increased blowing ratio, showing very little difference for $M > 0.8$.

This shows that only at very low blowing ratio and momentum flux ratio does the cross corrugated slots with exit shaping have a substantial effect on effectiveness on top of the lands when compared with the baselines rectangular slot.

9.3.3 Effectiveness downstream of lands

In Section 7.3.4, the regions downstream of the lands had the lowest effectiveness when using the baseline rectangular geometry G0. This was due to the mainstream air following down the tapered land surface to the cutback. With a change of coolant to carbon dioxide, there was increased coolant flow over the tops of the lands and next to the lands, and this was visible in the higher effectiveness on top of and next to the lands. However, this was not enough to stop the mainstream flow from following the tapered surface and causing the same expanding region of low effectiveness downstream of the lands.

Using carbon dioxide coolant, geometry G13 also performed similarly compared to using nitrogen in Section 8.3.3. At low blowing ratio, effectiveness was significantly augmented on top of the lands and next to the lands, but not significantly so downstream of the lands. However, at higher blowing ratios, there was considerably higher effectiveness downstream of the lands, although the central region still had the largest high effectiveness

streak.

9.3.4 Centreline effectiveness

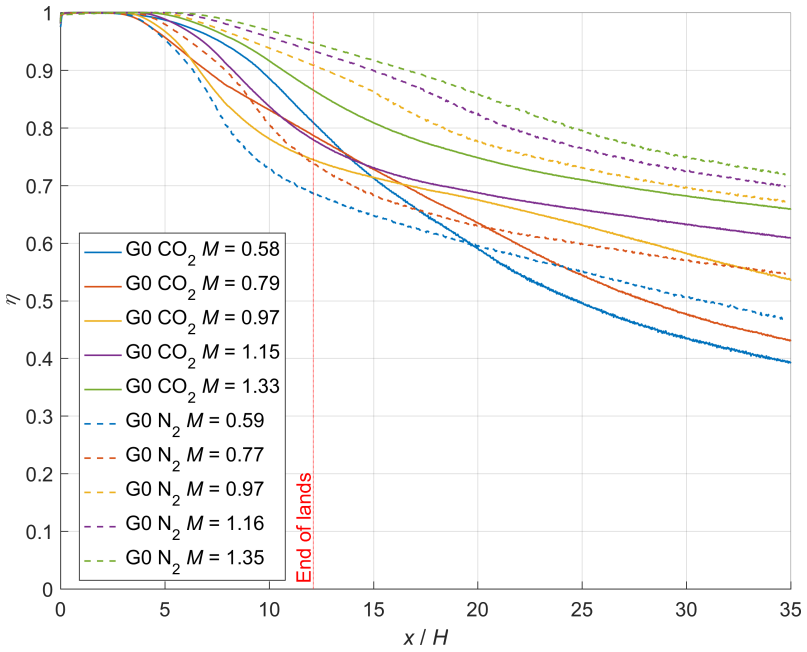


Figure 9.5: Centreline η using carbon dioxide coolant, G0

Figure 9.5 shows a plot of film cooling effectiveness along the slot centreline for geometry G0 using carbon dioxide coolant along with the data for the same geometry using nitrogen coolant taken in phase 2 for comparison. This included only a 100 pixel ($8.43\,\mathrm{mm}$) wide strip down the centre of the cutback region extending downstream from the slot. The position of the end of the lands is marked in the plots.

It can be seen that when using carbon dioxide coolant, the effectiveness no longer consistently increased with blowing ratio for any given distance from the slot exit, as it did when using nitrogen coolant. Instead, there are two regions with different features. In the near slot region, where $x/H < 15$, effectiveness was high at the lowest blowing ratio of $M = 0.6$ and decreased with increasing blowing ratio to a minimum when $M = 1.0$. Increasing the blowing ratio further then resulted in effectiveness increasing again to its highest at $M = 1.4$. In the region far from the slot, where $x/H < 15$, effectiveness increased monotonically with blowing ratio, as expected.

This peculiarity in the near slot region has been observed by Holloway et al. (2002a) and Martini et al. (2005a) in experimental measurements using carbon dioxide coolant and reproduced in numerical simulations in Holloway et al. (2002b). Their explanation was that at low blowing ratios, the coolant side vortices being shed from the lip were dominant, while at high blowing ratios, the mainstream side vortices were dominant. At intermediate blowing ratios, the vortices from both sides were of similar strength and shed in an alternating manner, resulting in increased mixing between the flows and a dip in effectiveness at $M = 1.0$.

Far from the slot, the flows had mixed out sufficiently such that the interactions between the vortices were no longer the dominating factor causing reduced effectiveness. Instead, the bulk coolant concentration became the dominating factor. Increasing blowing ratio increased the mass flow ratio between coolant and mainstream and consequently resulted in monotonically increasing effectiveness with blowing ratio.

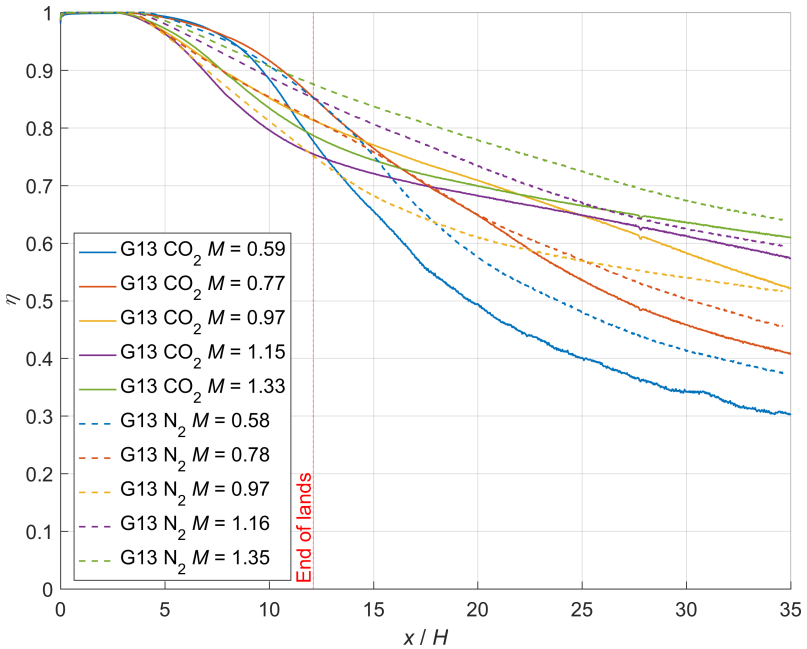


Figure 9.6: Centreline η using carbon dioxide coolant, G13

Figure 9.6 shows the same plot for geometry G13 using carbon dioxide alongside the data for the same geometry using nitrogen coolant taken in phase 3 for comparison.

In Section 8.3.4, it was noted that near the slot exit, effectiveness was improved the most compared to G0 at $M = 0.6$. However, using carbon dioxide coolant, the effective-

ness near the slot exit was most improved at $M = 0.8$, reducing to the lowest point at $M = 1.2$ before increasing again slightly at $M = 1.4$. This sudden drop in effectiveness at high blowing ratio can be explained by referring to Figure 9.2, where it can be seen that there was a gap of reduced effectiveness between two large streaks of high effectiveness caused by the corrugation channels. This gap appears to have changed position slightly with blowing ratio such that at $M = 1.2$, and to a lesser extent at $M = 1.4$, it coincided with the centreline of the slot, thus causing the drastic reduction in effectiveness seen in Figure 9.6.

As before, further away from the slot, the coolant and mainstream flows were sufficiently mixed out such that effectiveness monotonically increased with blowing ratio.

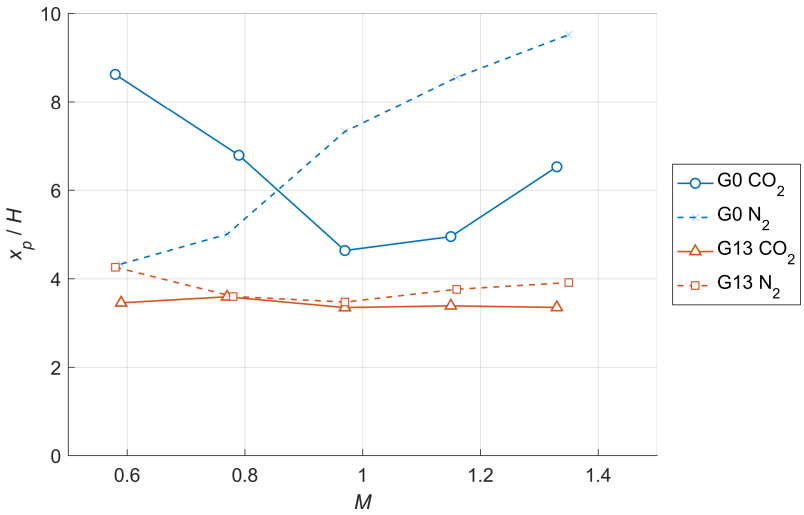


Figure 9.7: Potential core length of G0 and G13 using carbon dioxide coolant

The potential core length for geometry G0 was determined using the same method as in Section 6.3.3 while the potential core length for geometry G13 was determined using the modified method in Section 8.3.4. Figure 9.7 shows a plot of potential core length for both geometries G0 and G13 alongside the corresponding data from phases 2 and 3 for comparison.

At the lowest blowing ratio of $M = 0.6$, the potential core length using geometry G0 was twice as long using carbon dioxide coolant compared to using nitrogen coolant. This then reduced to a minimum at $M = 1.0$ before increasing again with blowing ratio up to $M = 1.4$. As explained above, this could have been caused by the vortices alternating

between the coolant and mainstream sides, increasing the mixing between the flows and reducing effectiveness. If instead of blowing ratio, the potential core length is plotted against momentum flux ratio as shown in Figure 9.8, the two curves for geometry G0 appear to be more closely aligned, suggesting that the change in potential core length is more affected by momentum flux ratio than blowing ratio. It is possible that at even lower blowing ratios than $M = 0.6$ using nitrogen as the coolant, a similar increase in potential core length may be observed.

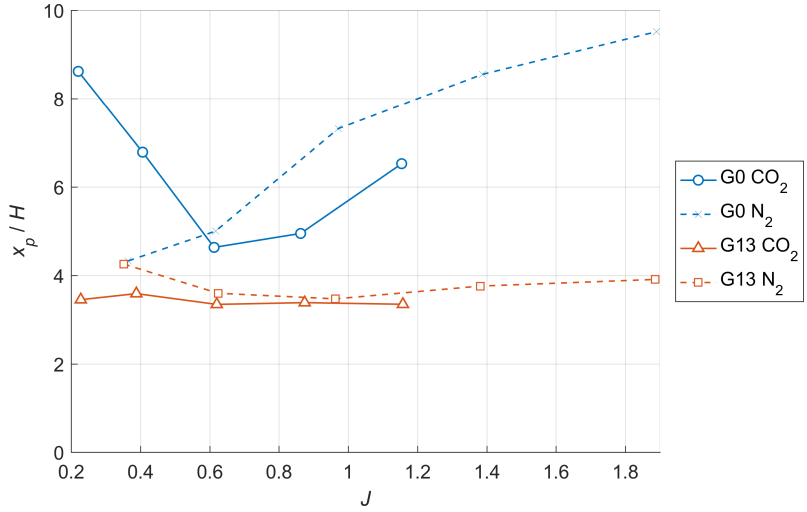


Figure 9.8: Potential core length against momentum flux ratio, G0 and G13

The potential core length using geometry G13 was relatively insensitive to blowing ratio or momentum flux ratio, largely in agreement with the data from phase 3. This suggests that it is also insensitive to density ratio.

9.3.5 Spanwise averaged effectiveness

Figure 9.9 shows a plot of spanwise averaged film cooling effectiveness for geometry G0 using carbon dioxide coolant. The average was taken over the entire region between the centre-points of the two lands. It is plotted with the data for the same geometry using nitrogen coolant taken in phase 2 for comparison.

As with the centreline plots, there are two regions visible separated by a slot exit distance of approximately $x/H = 13$. In the near slot region, where $x/H < 13$, effectiveness was lowest for an intermediate blowing ratio of $M = 1.0$. Whereas in the region

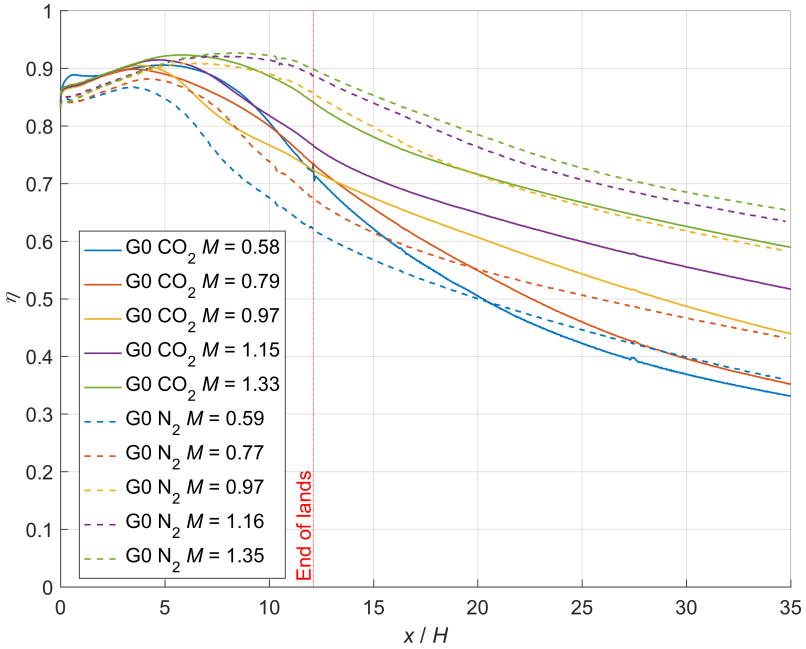


Figure 9.9: Spanwise averaged η using carbon dioxide coolant, G0

far from the slot, where $x/H < 13$, effectiveness increased monotonically with blowing ratio.

Due to the inclusion of the diffuser shaped lands, the potential core was no longer apparent, with a lower effectiveness at the slot exit, increasing slightly as the lands reduced in width with distance from the slot exit. The starting effectiveness was higher using carbon dioxide coolant by about 0.02 due to the slightly increased effectiveness on top of the lands as noted in Section 9.3.2. At the lowest blowing ratio of $M = 0.6$, this was increased further by another 0.02 due to the lower momentum flow washing over the lands. Compared to the phase 2 data with nitrogen coolant, the spanwise averaged effectiveness in the near slot region was higher when $M < 0.8$, a minimum at $M = 1.0$ and then increased at the higher blowing ratios. This was consistent with the variation in potential core lengths shown in Figure 9.7.

Far from the slot, this effectiveness became linked to blowing ratio, just as with the centreline plots in Figure 9.5.

Figure 9.10 shows the same plot for geometry G13 using carbon dioxide alongside the data for the same geometry using nitrogen coolant taken in phase 3 for comparison.

Similar to geometry G0, the use of carbon dioxide coolant increased effectiveness in

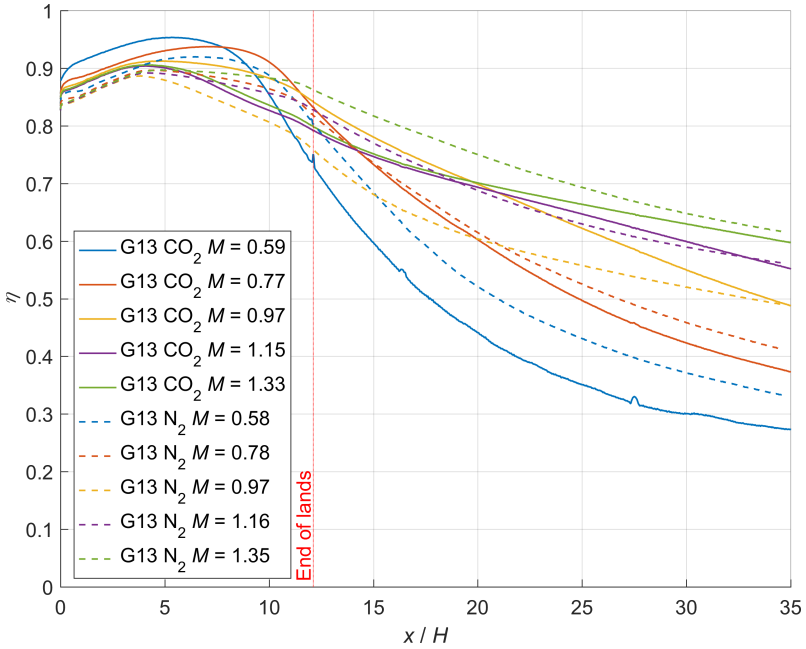
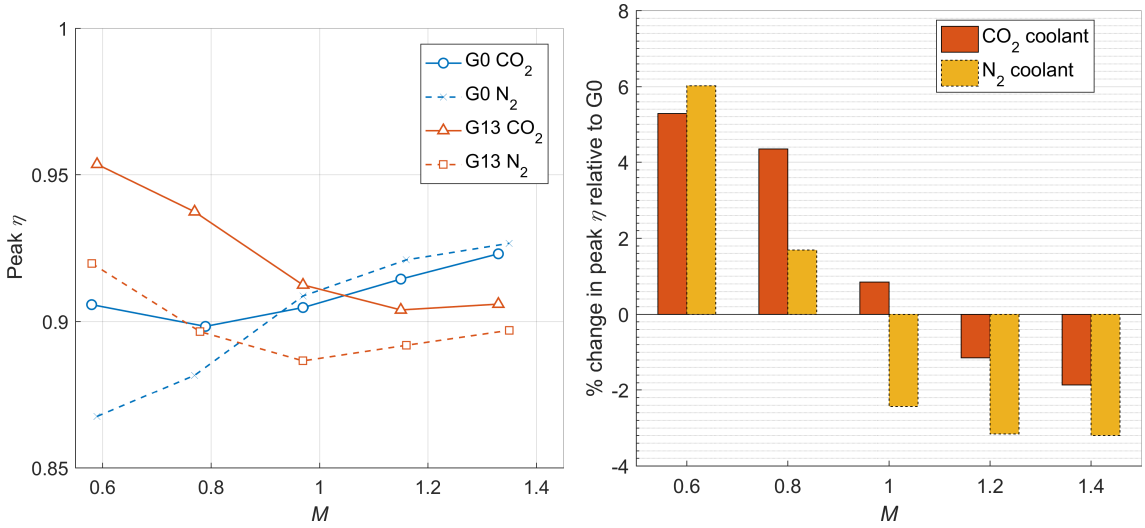


Figure 9.10: Spanwise averaged η using carbon dioxide coolant, G13

the near slot region due to the higher effectiveness on top of the lands noted in Section 9.3.2. At intermediate to high blowing ratios, this enhanced effectiveness by about 0.02. At the lowest blowing ratio, where the change in effectiveness was the greatest, this enhanced effectiveness by almost 0.05. Nevertheless, compared to geometry G0, the change in coolant density did not cause as large a difference in effectiveness in this near slot region. This was consistent with the potential core length being insensitive to blowing ratio, as shown in Figure 9.7.

Figure 9.11a shows a plot of peak spanwise averaged effectiveness for both geometries G0 and G13 using carbon dioxide coolant alongside the corresponding data using nitrogen coolant from phases 2 and 3.

Geometry G0 had similar peak effectiveness for $M > 0.8$. However, for $M < 0.8$, peak effectiveness was considerably higher when using carbon dioxide coolant. At $M = 0.6$, peak effectiveness was 0.91 compared to 0.87 using nitrogen coolant. This was due to the combined factors of increased land effectiveness and potential core length, both of which were most significant at low blowing ratios (See sections 9.3.2 and 9.3.4). At higher blowing ratios, the potential core length was shorter, reducing effectiveness. However, this was balanced by the increased land effectiveness, resulting in little change in the



(a) Absolute value

(b) Percentage change relative to G0

Figure 9.11: Peak η, G0 and G13 using carbon dioxide coolant

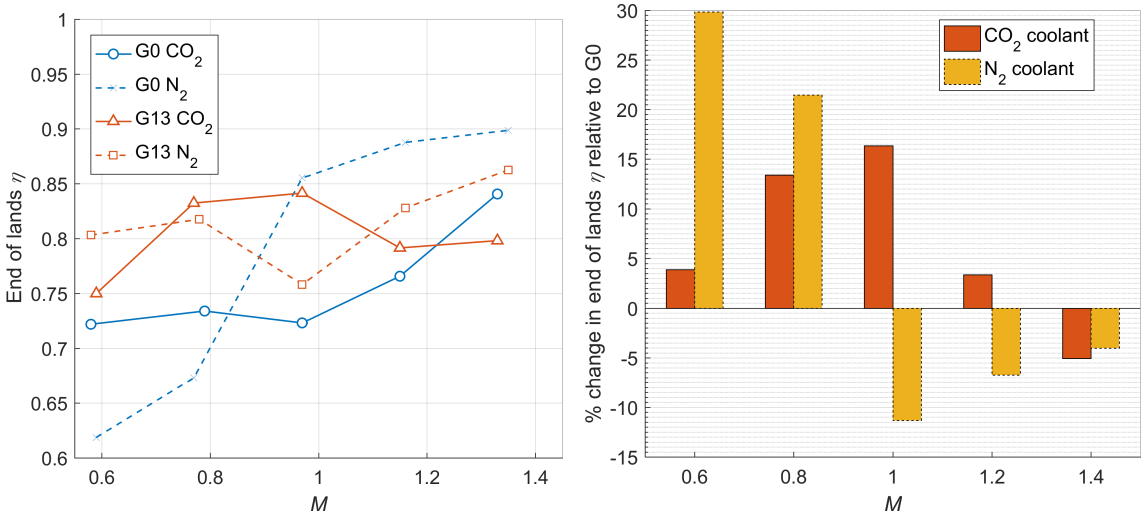
peak effectiveness.

Geometry G13 showed increased peak effectiveness when using carbon dioxide coolant across all blowing ratios, with the greatest increase in peak effectiveness at low blowing ratios. Since the potential core length was insensitive to coolant density or blowing ratio, this was likely due to the increased effectiveness on top of the lands. This is consistent with Section 9.3.2 which showed the greatest enhancement of effectiveness at low blowing ratios.

Figure 9.11b compares the baseline geometry G0 with the optimised cross corrugated geometry G13 using carbon dioxide coolant and nitrogen coolant. G13 was shown to perform better than G0 in terms of peak effectiveness up to $M = 1.0$. This was a a significant difference with using nitrogen coolant where it only performed better up to $M = 0.8$. For $M > 1.0$, peak effectiveness using geometry G13 remained lower than G0 but to a lesser extent.

Figure 9.12a shows a plot of spanwise averaged effectiveness at the end of the lands for both geometries G0 and G13 using carbon dioxide coolant alongside the corresponding data using nitrogen coolant from phases 2 and 3.

At the end of the lands, the enhancement of effectiveness on top of the lands was no longer of great significance. Therefore, the potential core length became the dominating



(a) Absolute value

(b) Percentage change relative to G0

Figure 9.12: End of lands η, G0 and G13 using carbon dioxide coolant

factor for geometry G0. As was the case in Figure 9.7, low blowing ratios showed significantly increased end of lands effectiveness while intermediate to high blowing ratios showed significantly reduced end of lands effectiveness relative to the phase 2 data. The largest increase in end of lands effectiveness was at $M = 0.6$ by $17\,\%$ while the largest reduction in end of lands effectiveness was at $M = 1.0$ by $15\,\%$. Nevertheless, in absolute terms, there was only a slight dip in effectiveness at $M = 1.0$. This dip was caused by the interaction of the vortices described in Section 9.3.4 but was much less distinct since at this distance from the slot exit, the vortices have become less of the dominating factor and bulk mixing has become more important.

For geometry G13, since land effectiveness was no longer a significant factor and potential core length was insensitive to blowing ratio and density ratio, the changes in end of lands effectiveness were not as large, varying by $2\,\%$ to $7\,\%$ for most blowing ratios. However, at $M = 1.0$, there is a more significant increase in end of lands effectiveness of $11\,\%$.

Figure 9.12b compares the baseline geometry G0 with the optimised cross corrugated geometry G13 using carbon dioxide coolant and nitrogen coolant. G13 performed better than G0 in terms of end of lands film cooling effectiveness up to $M = 1.2$, another significant difference with using nitrogen coolant where it only performed better up to

$M = 0.8$. However, the performance boost was considerably smaller using carbon dioxide at low blowing ratios. About 26 percentage points lower at $M = 0.6$ and about 8 percentage points lower at $M = 0.8$.

9.3.6 Spanwise variation of effectiveness at end of lands

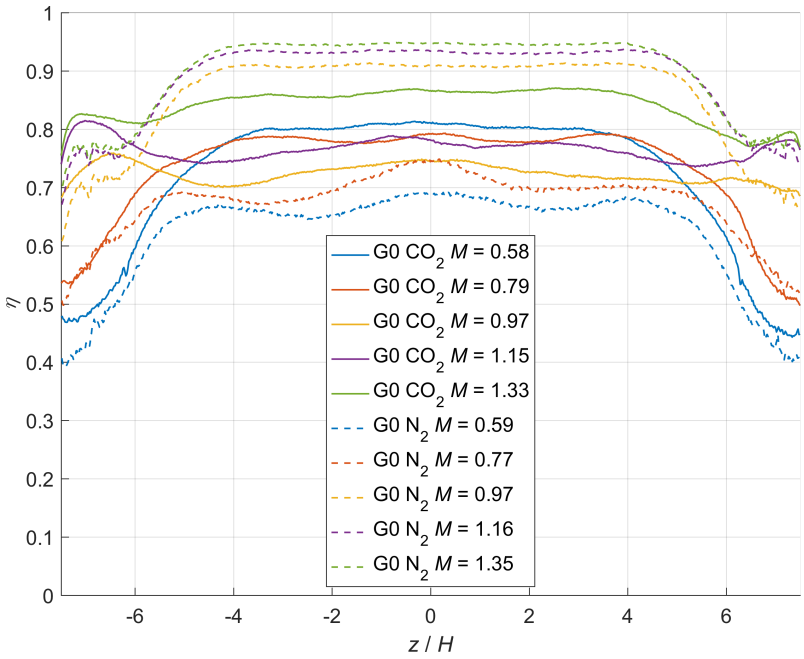


Figure 9.13: Spanwise varation of η using carbon dioxide coolant, G0

Figure 9.13 shows a plot of spanwise variation in film cooling effectiveness taken at the end of the lands for geometry G0 using carbon dioxide coolant. This included a 20 pixel ($1.7\,\mathrm{mm}$) wide strip parallel to the slot lip at a distance equal to the length of the lands where $x/H = 12.1$. The spanwise extent starts from the centre of the left hand side land where $z/H = -7.5$ and ends at the centre of the right hand side land where $z/H = 7.5$. $z/H = 0$ marks the centreline of the slot. $z/H = -6$ marks the right side edge of the land hand land, while $z/H = 6$ marks the left side edge of the right hand land. This x/H position is considered to be particularly important as it represents the trailing edge of the blade, where cooling is almost completely reliant on the film effectiveness and large local variations in effectiveness along the trailing edge can lead to high temperature gradients which cause thermal stresses in the blade metal that can affect blade life. The

data for the same geometry using nitrogen coolant taken in phase 2 has also been included for comparison.

As mentioned in Section 9.3.5, at this distance from the slot, the land width was reduced to zero and the increased effectiveness on top of the lands did not translate into significantly increased effectiveness at the tips of the lands. The greatest change in effectiveness was across the width of the slot which was caused by the difference in potential core length. Spanwise consistency in between the lands remained fairly flat.

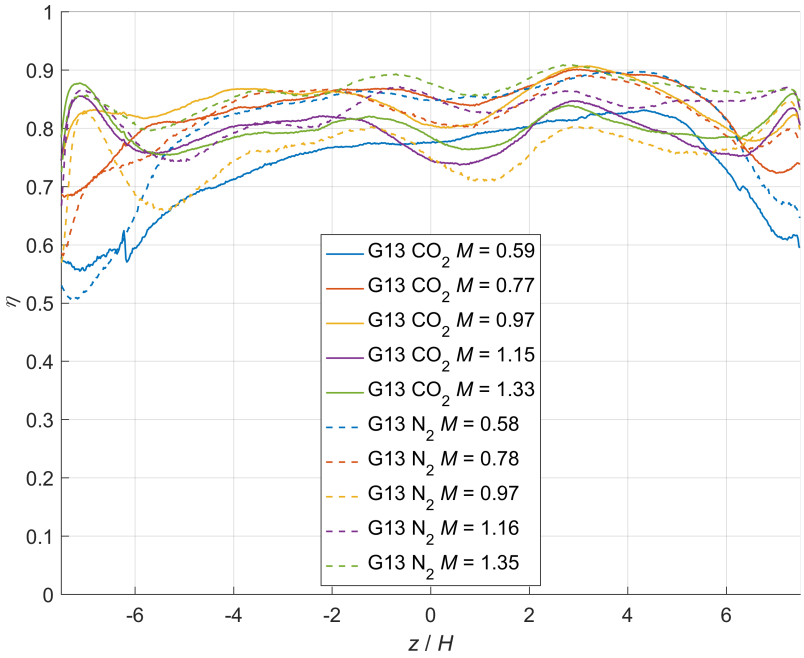
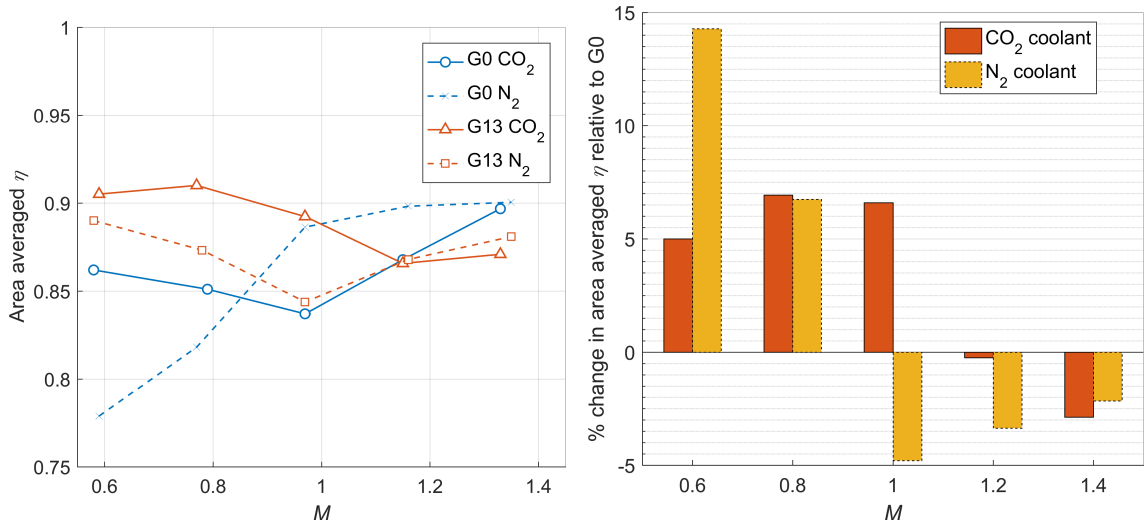


Figure 9.14: Spanwise varation of η using carbon dioxide coolant, G13

Figure 9.14 shows the same spanwise variation in effectiveness plot for geometry G13 using carbon dioxide alongside the data for the same geometry using nitrogen coolant taken in phase 3 for comparison.

Similarly, the change in effectiveness appeared to be greatest in between the lands, with the effectiveness at the tip of the lands not significantly affected. At most blowing ratios, the change in effectiveness across the span and spanwise consistency was not altered a great amount. However, at $M = 1.0$, effectiveness in between the lands was significantly increased and also significantly more consistent.

9.3.7 Area averaged effectiveness



(a) Absolute value

(b) Percentage change relative to G0

Figure 9.15: Area averaged η, G0 and G13 using carbon dioxide coolant

Figure 9.15a shows a plot of area averaged film cooling effectiveness for both geometries G0 and G13 using carbon dioxide coolant. This included the cutback and land top surfaces up to the end of the lands where $x/H = 12.1$. It gives an overall picture of the relative performance over the region most relevant to trailing edge cooling. The data for the same geometry using nitrogen coolant taken in phases 2 and 3 were included for comparison.

For geometry G0, area averaged effectiveness was increased for $M < 0.8$ when using carbon dioxide coolant compared to using nitrogen coolant. For $M > 0.8$, this was reversed, and effectiveness was reduced using carbon dioxide coolant. This trend is consistent with the effects of land top effectiveness and potential core length discussed in Sections 9.3.2 and 9.3.4. In absolute terms, effectiveness was lowest at $M = 1.0$, also consistent with the observations regarding potential core length. However, the difference in effectiveness between different blowing ratios was considerably less than in phase 2. Using nitrogen as the coolant, area averaged effectiveness differed by as much as 0.12 whereas when carbon dioxide was used, effectiveness differed by a maximum of only 0.06. The overall effect is a more consistent area averaged cooling performance across

the blowing ratios, even though locally the effectiveness may differ significantly.

In the case of geometry G13, area averaged effectiveness was increase for $M < 1.0$ when using carbon dioxide coolant. This was largely due to the increase in effectiveness on the lands at lower blowing ratios, with little effect at higher blowing ratios. In absolute terms, effectiveness was highest at $M = 0.8$ and lowest at $M = 1.2$. However, the range in effectiveness was only 0.04, comparable to the range using nitrogen coolant of 0.05.

Figure 9.15b compares the baseline geometry G0 with the optimised cross corrugated geometry G13 using carbon dioxide coolant and nitrogen coolant. G13 performed better than G0 in terms of area averaged film cooling effectiveness up to $M = 1.0$, again differing with using nitrogen coolant where it only performed better up to $M = 0.8$. The performance boost was smaller by about 9 percentage points using carbon dioxide at $M = 0.6$. At $M = 0.8$ there was little difference between the two coolants. At $M = 1.0$ the performance boost using carbon dioxide was about $7\,\%$ better compared to using nitrogen where it was about $5\,\%$ worse.

9.4 Summary and conclusions

Detailed distributions of adiabatic film cooling effectiveness have been measured over the cutback and land top surfaces of large scale geometries representing turbine blade trailing edges using the PSP technique. The baseline rectangular geometry and optimised cross corrugated slot geometry chosen in Chapter 8 were tested with blowing ratio ranging from 0.6 to 1.4 and a coolant to mainstream density ratio of 1.52. The geometries all used tapered diffuser lands and the cross corrugated geometry used an included angle of $90°$.

While the simplified nature of the experimental model limits the direct applicability of the measurements to a real blade or vane, the fourth phase of experiments aimed to improve the representativeness of the model by using a density ratio much closer to the real engine, allowing blowing ratio and momentum flux ratio to be matched more closely. The effect of increasing density ratio on the cooling performance of both geometries has been observed. The conclusions from these observations are as follows:

- On top of the lands, increasing density ratio greatly increased effectiveness at low blowing ratios. This was due to the lower momentum flux ratio allowing the coolant to wash over the lands. This effect was exacerbated using the cross corrugated slot geometry.

- Potential core length was significantly altered for the baseline rectangular slot using a high density ratio. Instead of a monotonic increase with blowing ratio, a minimum point was found at the intermediate blowing ratio of 1 caused by the interaction of the vortices shedding from both sides of the slot lip.

- Potential core length for the cross corrugated geometry was relatively insensitive to blowing ratio and density ratio.

- Increased land effectiveness at low blowing ratios resulted in increased peak spanwise averaged effectiveness for both geometries.

- At the end of the lands, the increased land effectiveness no longer had a significant effect. Instead, potential core length was the dominating factor, resulting in an increase in end of lands effectiveness at low blowing ratios for the baseline geometry. The cross corrugated geometry was less affected due to its fairly constant potential core length.

- The aforementioned factors resulted in an overall increase in effectiveness for both geometries at low blowing ratios when density ratio was increased.

- In terms of peak effectiveness, the optimised cross corrugated geometry performed better than the baseline geometry up to a blowing ratio of 1.0.

- In terms of end of lands effectiveness, the optimised cross corrugated geometry performed better than the baseline geometry up to a blowing ratio of 1.2.

- In terms of spanwise consistency at the end of lands, the optimised cross corrugated geometry was on par with the baseline geometry, with less sensitivity to blowing ratio.

- In terms of area averaged effectiveness, the optimised cross corrugated geometry performed better than the baseline geometry up to a blowing ratio of 1.0.

The fourth phase of experiments has shown that density ratio has a material effect on film cooling performance and attempts should always be made to match density ratio with the engine as closely as possible. Since the density ratio of 1.52 used still does not match the real engine density ratio of approximately 1.9, it would be highly beneficial for further work to be undertaken to assess effectiveness at higher density ratios. This might be accomplished by either using a heavier coolant gas, using a lighter mainstream gas, cooling the coolant stream or heating the mainstream.

Nevertheless, even at a higher density ratio, the final optimised cross corrugated design G13 (shown in Figure 5.20d) was found to be superior to the baseline rectangular up to a blowing ratio of 1.0 with an optimal operating range of 0.8 to 1.0. Spanwise averaged effectiveness at the end of the lands was increased by $13.4\,\%$ at a blowing ratio of 0.8, $16.3\,\%$ at a blowing ratio of 1.0 and $5.4\,\%$ at a blowing ratio of 1.2. Area averaged effectiveness was increased by $6.9\,\%$ at a blowing ratio of 0.8 and $6.6\,\%$ at a blowing ratio of 1.0. The spanwise effectiveness profile at the end of the lands was found to be more even and relatively insensitive to blowing ratio compared to the baseline geometry.

Chapter 10

Pressure Loss Measurements

10.1 Introduction

One of the key benefits of the cross corrugated slot design mentioned in Section 3.3.1 was the high pressure losses through the slot caused by the corrugation channels. This would aid in reducing the excessive coolant flow that tends to leave the slot when used for cooling the HP turbine blade trailing edge. By changing the included angle, corrugation pitch, corrugation height and other geometric parameters, it would also be possible for the cooling designer to tune the pressure losses as needed.

While the main body of work in this thesis was focussed on improving film cooling effectiveness rather than testing a wide range of geometric parameters, pressure loss measurements were taken for all of the geometries tested in phases 2 to 3. This encompassed the baseline rectangular slot and all of the cross corrugated slot geometries. Amongst these were two included angles, four exit alignments and five exit shaping modifications.

This chapter collects the pressure loss results for all geometries and discusses how the variations in included angle, exit alignment and exit shaping affected the hydraulic performance of the slots.

10.2 Pressure loss characteristics

The pressure loss through a duct can be expressed as Fanning friction factors, defined as:

$$f = \frac{D_{\mathrm{h}} \Delta p}{2 \rho \bar{u}^2 L} \tag{10.1}$$

Where D_{h} is the hydraulic diameter of the duct, Δp is the pressure loss through the duct, $\bar{u}$ is the bulk flow velocity through the duct and L is the length of the duct. Using continuity and substituting in quantities relevant to a slot geometry, Equation 10.1 can be rewritten as:

$$f = \frac{D_{\mathrm{h,se}} \Delta p_{\mathrm{slot}} \rho_{\mathrm{c}} A_{\mathrm{se}}^2}{2 \dot{m}_{\mathrm{c}}^2 L_{\mathrm{slot}}} \tag{10.2}$$

$$\text{Where the slot exit hydraulic diameter } D_{\mathrm{h,se}} = \frac{4 A_{\mathrm{se}}}{P_{\mathrm{se}}} \tag{10.3}$$

Δp_{slot} is the pressure loss through the slot, ρ_{c} is the coolant density, A_{se} is the slot exit area, $\dot{m}_{\mathrm{c}}$ is the coolant mass flow rate, L_{slot} is the slot length and P_{se} is the slot exit perimeter.

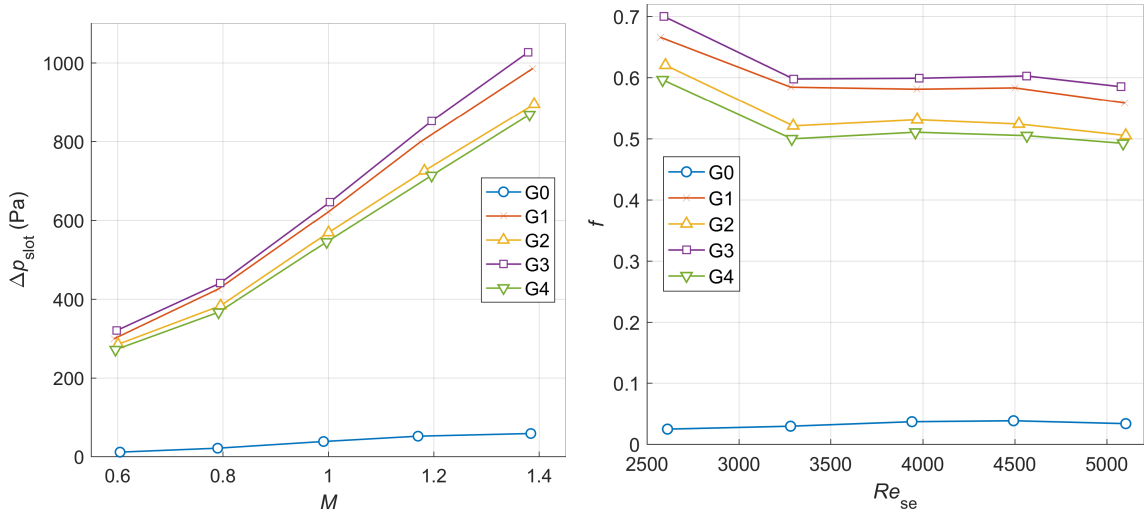
The Reynolds number Re_{se} can also be defined based on the slot exit dimensions:

$$Re_{\mathrm{se}} = \frac{\rho_{\mathrm{c}} \bar{u}_{\mathrm{se}} D_{\mathrm{h,se}}}{\mu_{\mathrm{c}}} \tag{10.4}$$

Using continuity, Equation 10.4 becomes:

$$Re_{\mathrm{se}} = \frac{\dot{m}_{\mathrm{c}} D_{\mathrm{h,se}}}{A_{\mathrm{se}} \mu_{\mathrm{c}}} \tag{10.5}$$

Note that in calculations using Equations 10.2, 10.3 and 10.5, $D_{\mathrm{h,se}}$, L_{slot} and P_{se} were entered in m and A_{se} was entered in m^2.



(a) Pressure loss against blowing ratio

(b) Fanning friction factor against slot exit Reynolds number

Figure 10.1: Pressure losses with included angle of $90°$, G0–4

10.3 Cross corrugated slots with 90° included angle

Figure 10.1a shows plots of pressure loss against blowing ratio for geometries G0–4. This compares the baseline rectangular slot with the cross corrugated slots with an included angle of $90°$ and no exit shaping. The pressure losses are considerably higher with cross corrugated slots compared to the baseline, increasing with blowing ratio as expected.

Figure 10.1b shows the Fanning friction factor against slot exit Reynolds number calculated using Equations 10.2, 10.3 and 10.5. The Fanning friction factor for the baseline rectangular slot was fairly constant, irrespective of Re_{se}. This demonstrates that the flow was fully turbulent within the tested range of operating conditions. In contrast, the cross corrugated geometries G1–4 only displayed an independence to Re_{se} for $Re_{se} > 3300$. This shows that at the lower mass flow rate, the flow was still transitioning from laminar to fully turbulent. Lau et al. (1989) measured the friction factor of a trailing edge cooling design with pin-fin arrays to be in the range 0.2 to 0.4. The cross corrugated slots with an included angle of $90°$ displayed a friction factor approximately $2\times$ greater, showing that the cross corrugated geometry is capable of significantly greater flow restriction, albeit at the expense of film effectiveness performance without exit shaping.

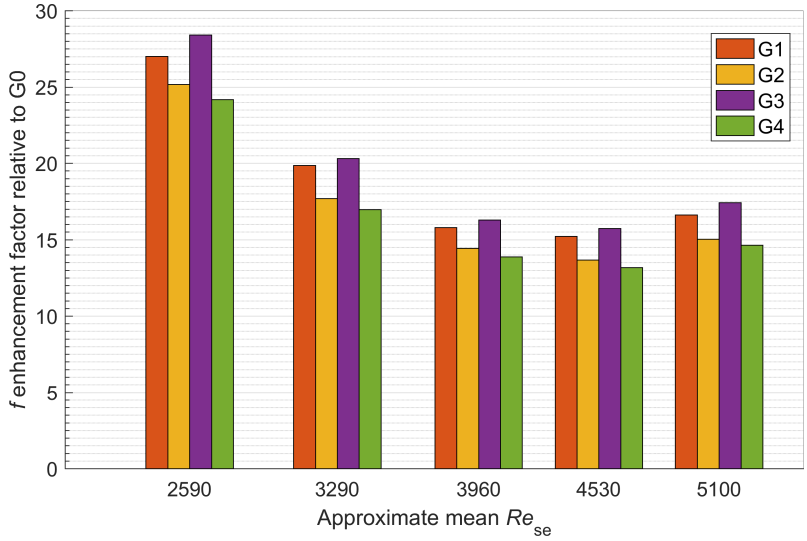
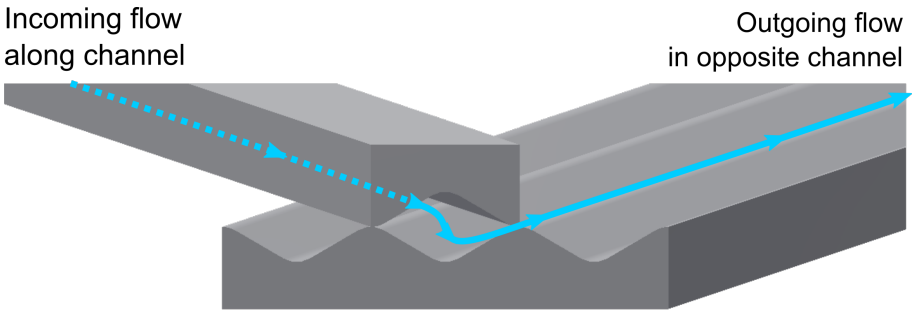


Figure 10.2: Enhancement in Fanning friction factor relative to G0, G1–4

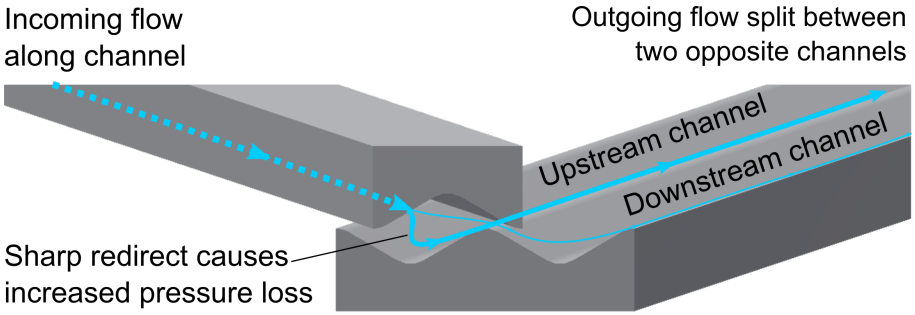
Figure 10.2 shows the enhancement factor of Fanning friction factor for geometries G1–4 relative to the baseline G0. For fully turbulent flow, the enhancement factor was in the neighbourhood of $15\times$, increasing to $25\times$ in the transition zone.

Amongst the cross corrugated geometries, there was a consistent ranking in terms of Fanning friction factor across the tested range, although the differences between them were relatively small. Since all geometric parameters were identical between these geometries, the influencing factor was presumed to be the alignment of the corrugation channels. Internally, the bridge walls caused the flow to be redirected from the corrugation channels of one side to the other. The manner in which the flow was redirected affected the pressure loss associated with the turning of the flow.

In the set of geometries G1–4, the side wall alignments and presumed flow structures are shown in Figure 10.3. Geometries G1 and G4 both had an anti phase alignment such that the ridges of the corrugation channels on both sides coincided at the bridge wall. This would encourage the flow from one channel to be reflected directly into the opposing channel as illustrated in Figure 10.3a. Geometries G2 and G3 both had a $90°$ out of phase alignment such that the ridges were offset from each other slightly. This would encourage the flow to split between two channels in the opposing wall as illustrated in Figure 10.3b. Due to the gap leading to the downstream channel being more restricted, more of the flow



(a) Anti phase alignment, G1 and G4

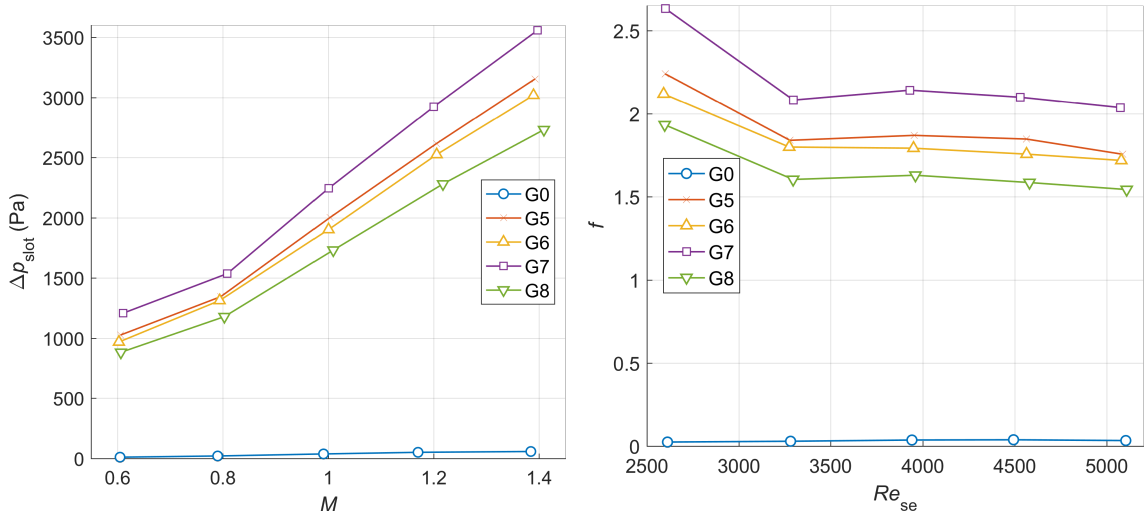


(b) 90° out of phase alignment, G2 and G3

Figure 10.3: Bridge wall flow reflection

would be forced to redirect into the upstream channel, increasing pressure loss due to this sharp redirection.

Based on the presumed flow structures, it was expected that geometries G2 and G3 would display a greater pressure loss. However, this prediction was not borne out by the pressure loss measurements which consistently showed geometry G3 displaying the highest friction factor, followed by G1, then G2 and finally G4. No other factors were identified that could explain this observed ranking in pressure loss. Further work is necessary to investigate the cause of this phenomenon. This should include a pressure survey across the slot inlet and slot exit to explore whether local pressure fluctuations caused by the complex flow structures entering and leaving the cross corrugated slots might be affecting the results.



(a) Pressure loss against blowing ratio

(b) Fanning friction factor against slot exit Reynolds number

Figure 10.4: Pressure losses with included angle of 120°, G0, G5–8

10.4 Cross corrugated slots with 120° included angle

Figure 10.4a shows plots of pressure loss against blowing ratio for geometries G0 and G5–8. This compares the baseline rectangular slot with the cross corrugated slots with an included angle of 120° and no exit shaping. The pressure losses are even higher with these cross corrugated slots compared to the baseline and approximately three-fold compared to geometries G1–4.

Figure 10.4b shows the Fanning friction factor against slot exit Reynolds number. Similar to their 90° included angle counterparts, geometries G5–8 were in the transition zone for $Re_{se} < 3300$ and fully turbulent for $Re_{se} > 3300$. Compared to the pin-fin array in Lau et al. (1989), the cross corrugated slots with an included angle of 120° displayed a friction factor approximately 7× greater.

Figure 10.5 shows the enhancement factor of Fanning friction factor for geometries G5–8 relative to the baseline G0. For fully turbulent flow, the enhancement factor was on average about 50×, increasing to 90× in the transition zone.

As with geometries G1–4, there was a consistent ranking in terms of Fanning friction factor across the tested range. The exit alignment and bridge wall alignments were identical between geometries G5–8 and their 90° included angle counterparts, with the principle

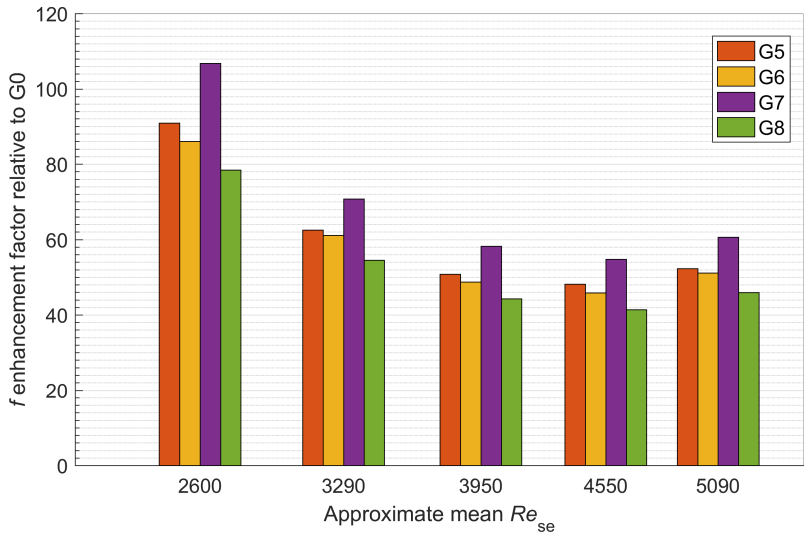
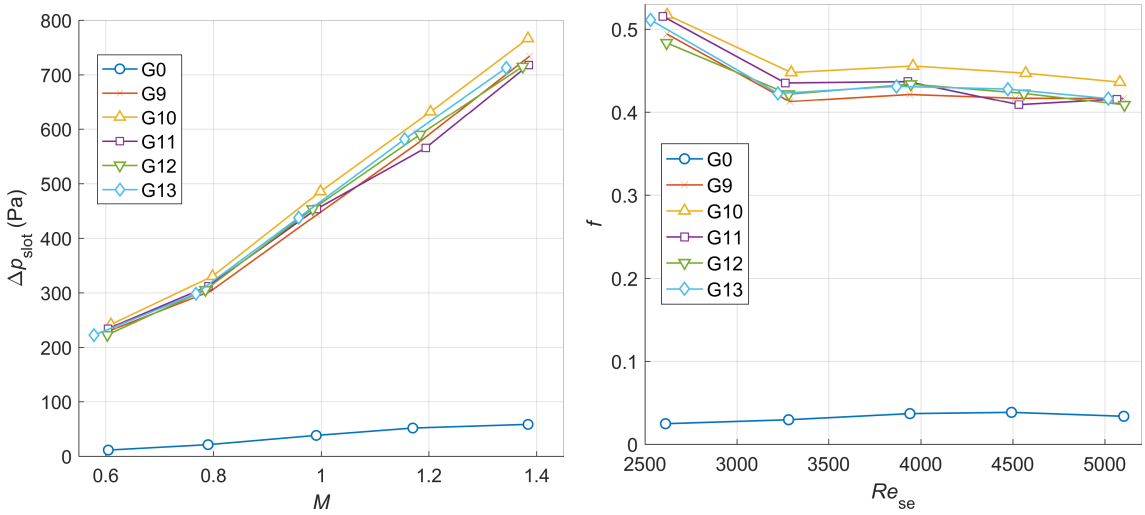


Figure 10.5: Enhancement in Fanning friction factor relative to G0, G5–8

difference being the steeper included angle and therefore double the number of flow reflections. The ranking was the same as well, with geometry G7 displaying the highest friction factor, followed by G5, then G6 and finally G8. The explanation for this ranking is evidently common between both sets of cross corrugated slots. However, further work will be necessary to identify the cause.

10.5 Cross corrugated slots with exit shaping



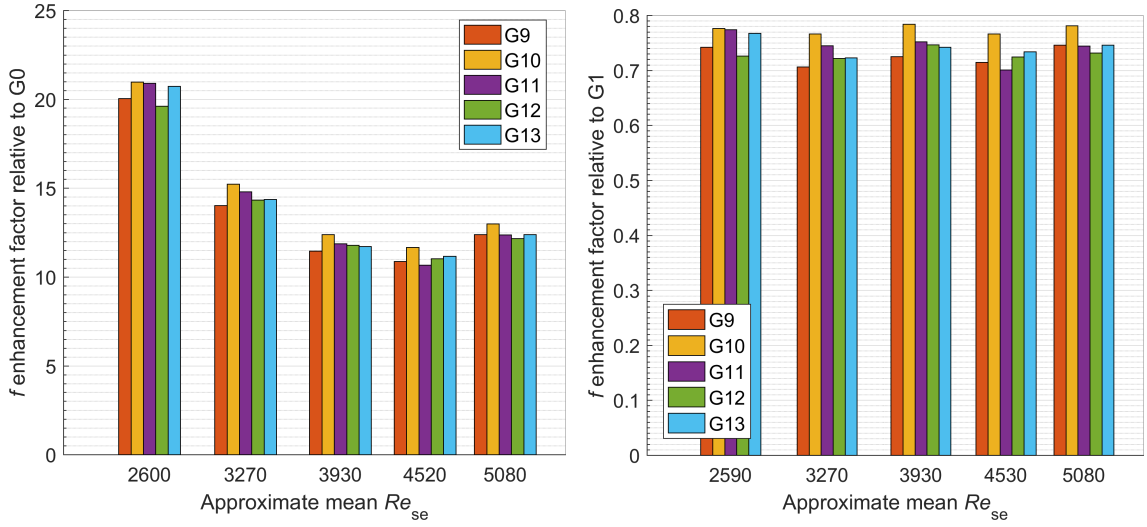
(a) Pressure loss against blowing ratio

(b) Fanning friction factor against slot exit Reynolds number

Figure 10.6: Pressure losses with exit shaping, G0, G9–13

Figure 10.6a shows plots of pressure loss against blowing ratio for geometries G0 and G9–13. This compares the baseline rectangular slot with the cross corrugated slots with an included angle of $90°$ and with exit shaping. The pressure losses were slightly lower than G1–4 but still considerably higher than the baseline.

Figure 10.6b shows the Fanning friction factor against slot exit Reynolds number. As with all the other cross corrugated geometries, geometries G9–13 were in the transition zone for $Re_{se} < 3300$ and fully turbulent for $Re_{se} > 3300$. Compared to the pin-fin array in Lau et al. (1989), the cross corrugated slots with an included angle of $90°$ and exit shaping displayed a friction factor approximately $1.5\times$ greater. This demonstrates that cross corrugated slots can restrict coolant flow better than a pin-fin array whilst simultaneously achieving film cooling performance on par with the ideal plain rectangular slot.



(a) Relative to G0 (b) Relative to G1

Figure 10.7: Enhancement in Fanning friction factor, G9–13

Figure 10.7a shows the enhancement factor of Fanning friction factor for geometries G9–13 relative to the baseline G0. For fully turbulent flow, the enhancement factor was approximately $12\times$, increasing to $20\times$ in the transition zone. Figure 10.7b compares the friction factor with geometry G1. All of the exit shaped geometries showed consistently less pressure loss than geometry G1 even though they shared the same included angle. The Fanning friction factor was reduced by the roughly the same factor across all tested Re_{se}. This was due to the addition of the exit shaping sections which reduced the length

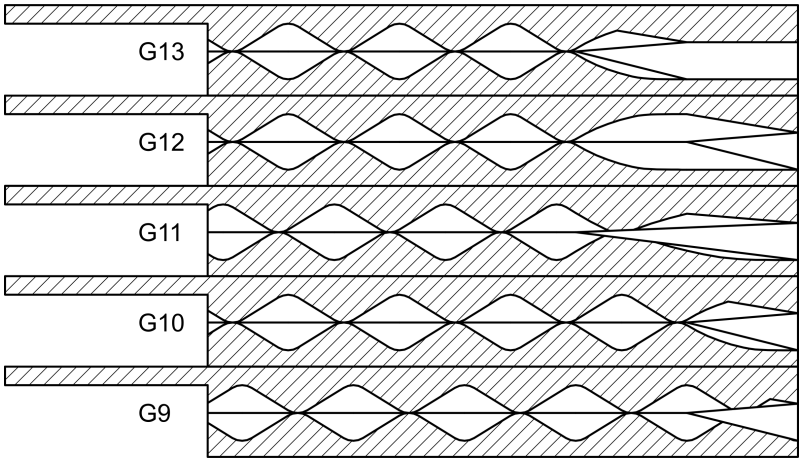


Figure 10.8: Bridge wall alignment, G9–11

of the cross corrugated sections, thereby reducing pressure loss.

Amongst the exit shaped geometries, there was no significant variation in friction factor between them for any given Re_{se}. Figure 10.8 shows the side wall alignments for geometries G9–11 stacked on top of each other. It can be seen that they all shared the same anti phase alignment at the side wall. There were differences in the number of side wall reflections due to variations in the length of the exit shaping section for each geometry, but this still did not cause a significant change in Fanning friction factor between them.

10.6 Summary and conclusions

Pressure loss measurements have been taken for a large scale model of the turbine blade trailing edge using a baseline rectangular slot as well as a variety of cross corrugated slots encompassing two included angles of $90°$ and $120°$, four different corrugation alignments each, and five exit shaped geometries with an included angle of $90°$.

While the simplified nature of the experimental model limits the direct applicability of the measurements to a real blade or vane, this series of pressure measurements aimed to quantify the effects of various included angles, alignments and exit shaping strategies on the hydraulic performance of the cross corrugated slot relative to the baseline rectangular slot. A parallel coordinates plot summarising all of the friction factor measurements is shown in Figure 10.9.

The conclusions from these measurements are as follows:

- Within the range of coolant flow rates measured, the Fanning friction factor for the baseline rectangular slot was insensitive to slot exit Reynolds number. This indicated that the flow through the slot was fully turbulent.
- The flow within the cross corrugated slots was fully turbulent for Reynolds number of greater than 3300.
- Using an included angle of $90°$, the Fanning friction factor was enhanced relative to the baseline by a factor of $15\times$ for fully turbulent flow and $25\times$ for transitional flow. Relative to a pin-fin array it was enhanced by $2\times$.
- Using an included angle of $120°$, the Fanning friction factor was enhanced relative to the baseline by a factor of $50\times$ for fully turbulent flow and $90\times$ for transitional flow. Relative to a pin-fin array it was enhanced by $7\times$.
- Using an included angle of $90°$ and exit shaping, the Fanning friction factor was enhanced relative to the baseline by a factor of $12\times$ for fully turbulent flow and $20\times$ for transitional flow. Relative to a pin-fin array it was enhanced by $1.5\times$.
- Changing the corrugation channel alignment did affect the pressure loss to some extent. The was not entirely due to the alignment at the internal bridge side walls of the slot. Further work is necessary to identify the cause of this discrepancy.
- While exit shaping did reduce pressure loss by virtue of reducing the length of the cross corrugated section with the slot, there was no significant change in pressure loss between different exit shaping strategies.

The pressure loss measurements have shown that the use of cross corrugated slots can drastically increase the friction factor relative to the baseline rectangular slot and a pin-fin array. This can also be varied to a huge degree by changing the included angle or other geometric parameters without resorting to changing slot height.

This could be greatly beneficial for trailing edge cooling design since it can significantly reduce coolant mass flow through the trailing edge slot without requiring the use of impractically thin slots or flow restrictors within the feed passages. Along with exit shaping, it can also provide film cooling performance on par with the idealised slot cooling geometry represented by the baseline rectangular slot.

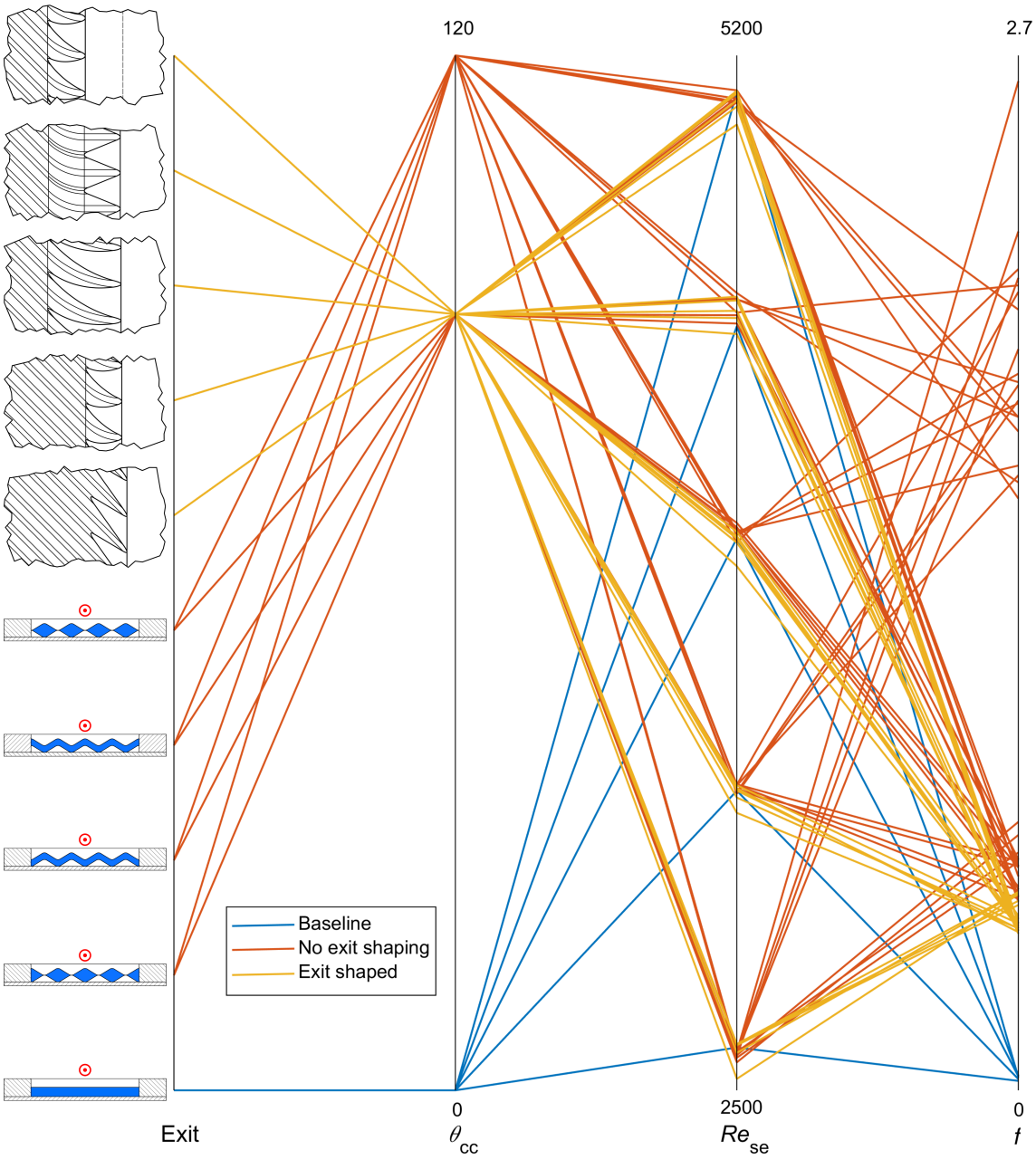


Figure 10.9: Parallel coordinates summary of all friction factor results

Chapter 11

Numerical Analysis

11.1 Introduction

The adiabatic film cooling effectiveness measurements taken in Chapters 6 to 9 have demonstrated that the flow downstream of the cross corrugated slots was highly complex and the effects of large flow structures were visible on the cutback surface. However, experimental methods using pressure sensitive paint were only capable of providing 2D data on the surfaces of the cutback and lands. As such, it was only possible to infer the 3D flow structures based on the 2D results. Therefore, it was deemed useful to use numerical methods to simulate the experiments in order to gain some understanding of the 3D flow structures.

Furthermore, with such a large number of parameters within the definition of the cross corrugated slot geometry that may be adjusted to finely tune performance, it would be infeasible to conduct experiments spanning the entire design space and allow for optimisation of the design to a specific purpose. Thus, it would be useful to investigate whether or not current numerical methods for modelling trailing edge cooling are able to accurately model the flow and predict the film cooling performance.

This chapter covers the numerical methods and computational domain used as well as the analysis and comparison of the results against experimental data.

11.2 Numerical methods

The computational fluid dynamics (CFD) simulation software used in the study was ANSYS Fluent versions 17.1 and 17.2. Computational domain meshes were generated using ANSYS ICEM CFD version 17.1. ANSYS Workbench 17.1 was also used for CFD case and work-flow management. Computations were carried out on local machines at the Osney Thermo-Fluids Laboratory as well as on the University of Oxford Advanced Research Computing (ARC) facility (Richards, 2015).

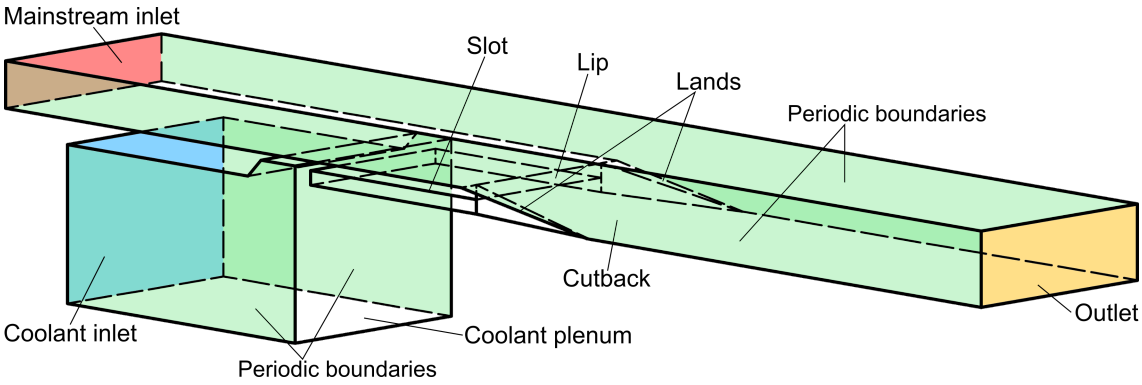
11.2.1 Computational domain

Due to constraints on the available time and resources for simulations, only two geometries were simulated:

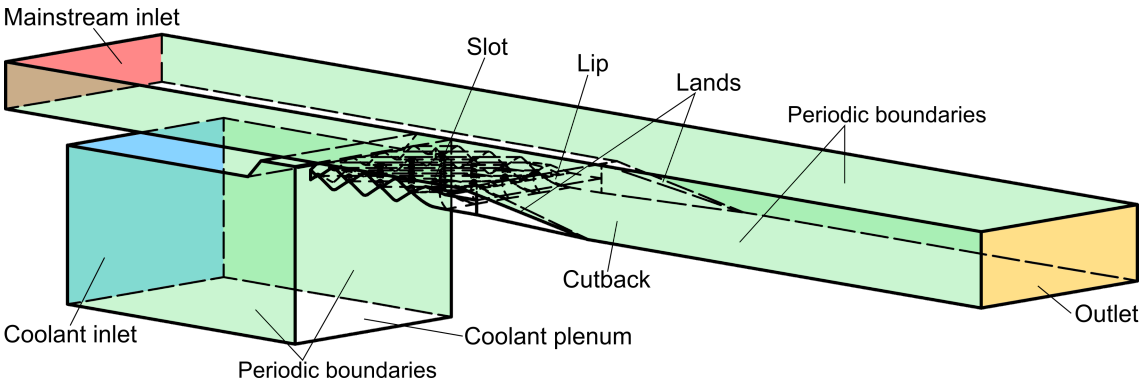
- G0: the baseline rectangular slot.
- G13: the most optimised cross corrugated slot with an included angle of $90°$ and exit shaping which incorporated a simultaneous ramp down and straightening section followed by a plain rectangular settling section.

Rather than simulating the entire test section, the coolant plenum was simplified and the spanwise extent was cut to include only the central slot and half of the lands on either side. These boundaries were then treated as periodic. The two computational domains are shown in Figure 11.1.

Both geometries were generated as unstructured tetrahedral meshes. The mesh for geometry G0 contained around 16 million elements and geometry G13 contained around 21 million elements. 10 prism layers were used on all the walls where the boundary layer was important achieving a $y^+ < 1$ throughout. A high mesh density zone was set around the slot exit region extending to one slot height upstream of the lip, one slot height above the lip and five slot heights downstream of the lip. This high density zone was also extended to about one slot height around the lands. A midspan section view of the mesh



(a) Baseline rectangular slot geometry G0



(b) Cross corrugated slot geometry G13

Figure 11.1: Computational domains

for G0 is shown in Figure 11.2 along with zoomed views of the high density zones at midspan and at the lands.

11.2.2 Simulation settings

Simulations were conducting using the Reynolds-averaged Navier-Stokes (RANS) equations closed for solving using the SST $k-\omega$ turbulence model. This turbulence model was developed to combine the best elements of the $k-\epsilon$ and $k-\omega$ models by using the $k-\omega$ formulation in the sub- and log-layer and switching to $k-\epsilon$ in the wake region of the boundary layer and in free shear layers (Menter, 1994). Since the flow speed was very low, the flow was considered incompressible. In accordance with the mass transfer analogy used for the experiments, the energy equations were turned off and the species transport model for an inert mixture were used.

Initially each simulation was run in steady-state to convergence. However, based on

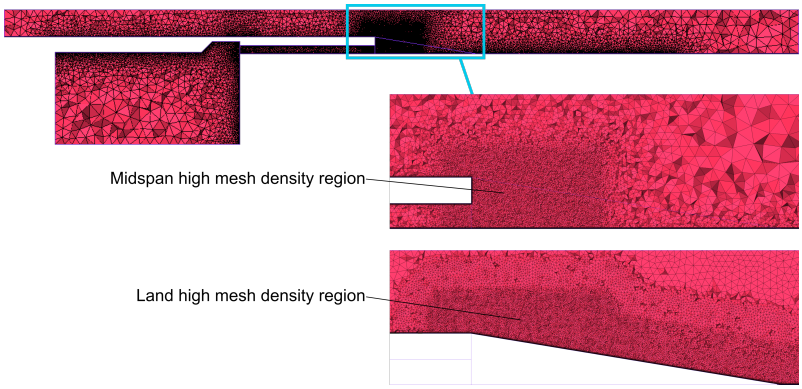
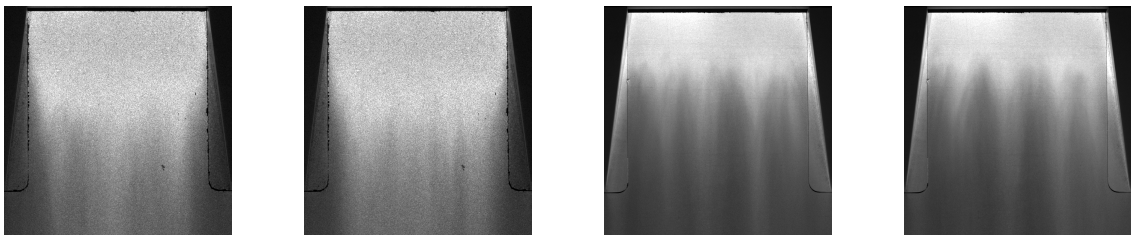


Figure 11.2: Mesh detail



(a) G0 frame 1 (b) G0 frame 2 (c) G13 frame 1 (d) G13 frame 2

Figure 11.3: Pressure losses with included angle of 120°, G0, G5–8

previous studies of trailing edge cooling geometries (Holloway et al., 2002a,b, Ravelli and Barigozzi, 2013, 2014), it was known that steady RANS simulations on this geometry would vastly over-predict effectiveness on the cutback and it would be necessary to also run unsteady RANS simulations of each case in order to approach similarity with the experimental data. The unsteadiness was also visible during the experiments, as can be seen in the example single frame cuts in Figure 11.3.

However, running unsteady RANS was considerably more expensive in computing time and resources. Due to these constraints, only two operating conditions were simulated:

- G0 using carbon dioxide coolant at a blowing ratio of 0.8
- G13 using carbon dioxide coolant at a blowing ratio of 0.8

These were chosen to represent the best cross corrugated slot design as selected by the experimental campaign as well as the baseline rectangular slot geometry for comparison. The blowing ratio of 0.8 was chosen as an operating point that was likely to be chosen by a

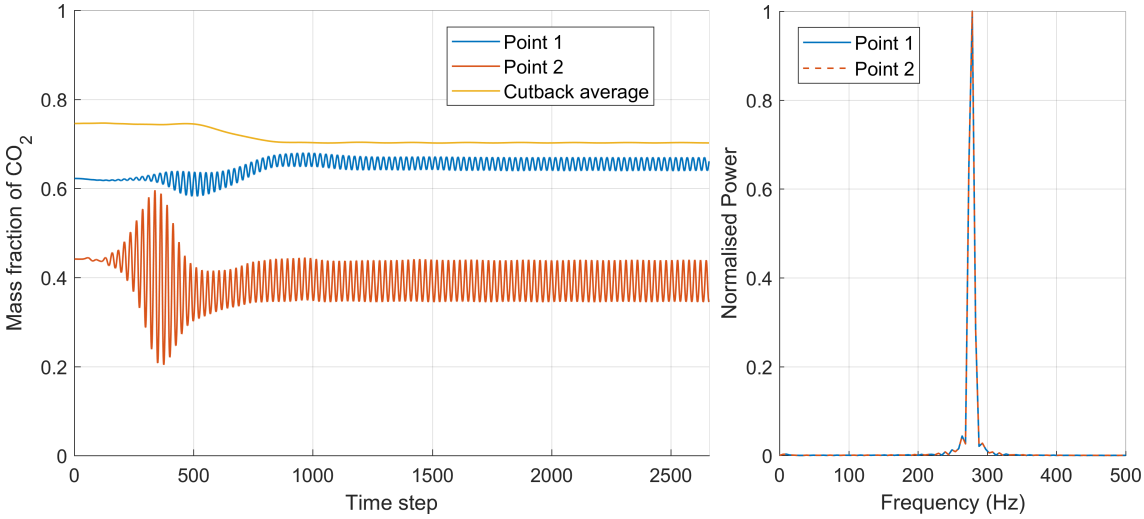
cooling designer for the lower mass flow rate but sufficient cooling performance. Carbon dioxide was used as the coolant to more closely represent the engine density ratio.

The mainstream and coolant inlets were initially set using the mass flow rate boundary condition with the outlet set as a static pressure boundary condition. These were set at the measured rig conditions for each operating condition. Once convergence was achieved, inlet total pressure profile was fixed and the mainstream inlet boundary condition was replaced with a total pressure boundary condition. This was in order to aid stability when conducting the unsteady RANS simulations.

The time step for unsteady RANS was chosen based on a Strouhal number *St* of 0.2 which was shown by Holloway et al. (2002b) to be representative of the shedding from the lip. Using $St = 0.2$, the expected shedding frequency was calculated to be no more than $350\,\mathrm{Hz}$, which is equivalent to an oscillation period of $0.003\,\mathrm{s}$. Therefore, in order to resolve the oscillations confidently, the time step was set at $0.000\,15\,\mathrm{s}$, 1/20th of the oscillation period. Stability would be presumed when the flow appeared to reach a consistent oscillation pattern. To that end, two monitoring points were placed at the $(x/H, y/H, z/H)$ positions (Defined in Figure 6.1) $(1, 1.5, 0)$ and $(12.1, 1.5, 0)$ which is in line with the end of the lands. The carbon dioxide mass fraction was then monitored at these two point as well as averaged over the cutback surface. Figure 11.4a shows the monitor output for the case of G0. The dominant frequency was shown to be $278\,\mathrm{Hz}$ which implies $St = 0.22$, not dissimilar to what was expected.

11.3 Results

Figure 11.5 shows contours of carbon dioxide mass fraction on a surface perpendicular to the cutback surface and intersecting the slot centreline. The flow is moving from left to right, with the mainstream on the top and the coolant on the bottom exiting the slot. In the instantaneous snapshot of the flow using the baseline rectangular slot geometry G0 (Figure 11.5a), vortex shedding from the slot lip can be clearly seen. These vortices are rotating in a clockwise direction, indicating that the vortices shedding from the main-



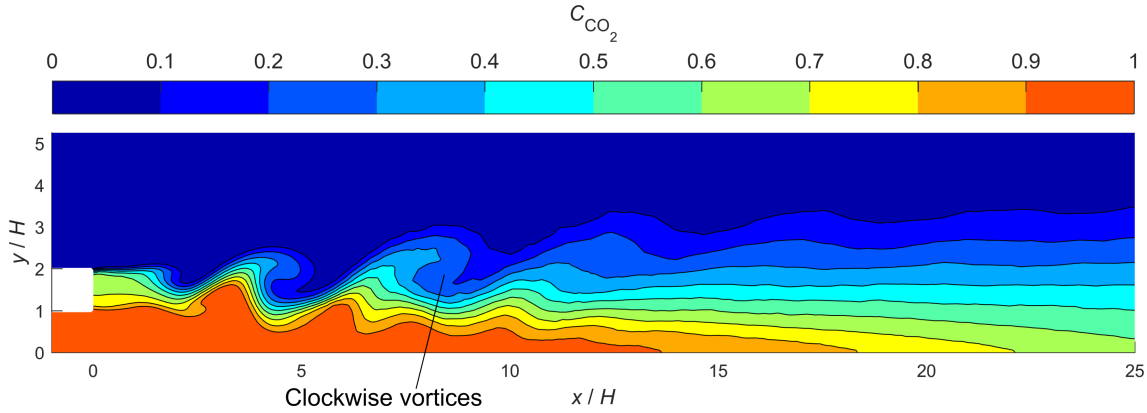
(a) Mass fraction against time step number (b) Frequency spectrum analysis

Figure 11.4: Unsteady simulation monitoring data for G0

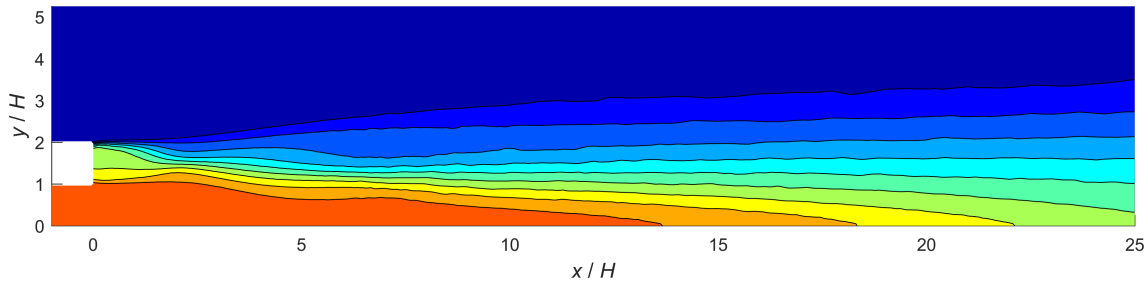
stream side of the lip are dominating. This leads to earlier entrainment of the mainstream flow and reduced time averaged film cooling effectiveness as seen in Figure 11.5b. This is in agreement with Holloway et al. (2002b) and Ravelli and Barigozzi (2014).

These vortices are no longer visible when the cross corrugated slot geometry G13 is used. Instead, there are two visible jets of high coolant concentration that appear to move in a direction non-parallel to the mainstream flow. This is evidence of the flow leaving the slot at an angle due to the inclination of the corrugation channels noted in Chapter 7. In the frequency spectrum analysis shown in Figure 11.6b, it can be seen that instead of a single large peak corresponding to vortex shedding from the slot lip, there are many smaller peaks at low frequency. Together with the monitoring data in Figure 11.6a displaying no obvious periodic pattern in the flow, this suggests a very chaotic flow structure indeed. In the time averaged flow shown in Figure 11.5d, this structure is elongated but still present, suggesting that the jets do not remain at a constant angle and position with time and may be fluttering in the $x - z$ plane.

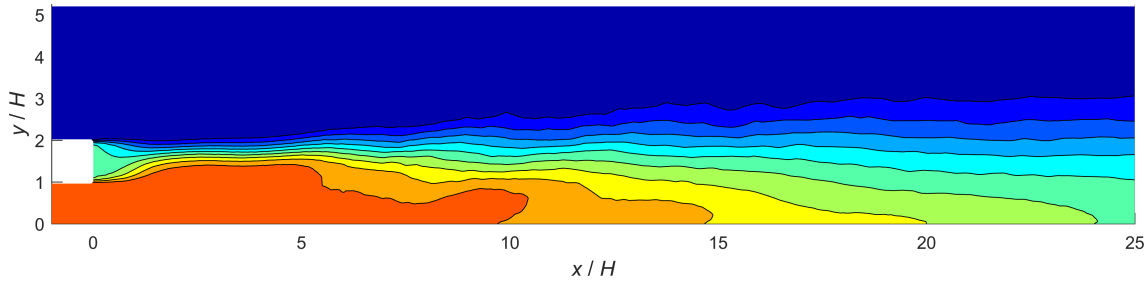
Figure 11.7a shows a 2D plot of effectiveness on the cutback and on top of the lands using G0. The plan view is the same as that used in the presentation of the experimental results. Compared to the experimental results shown in Figure 9.1b, the flow patterns share some similarities, although the effectiveness levels differ. On top of the lands, the



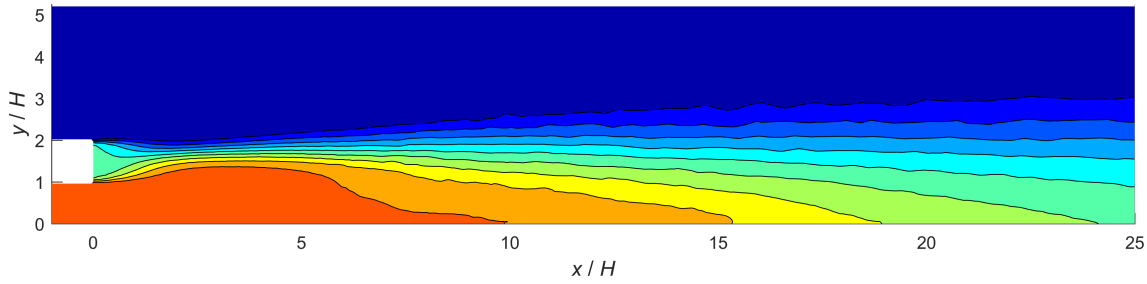
(a) Baseline slot G0 instantaneous



(b) Baseline slot G0 time averaged

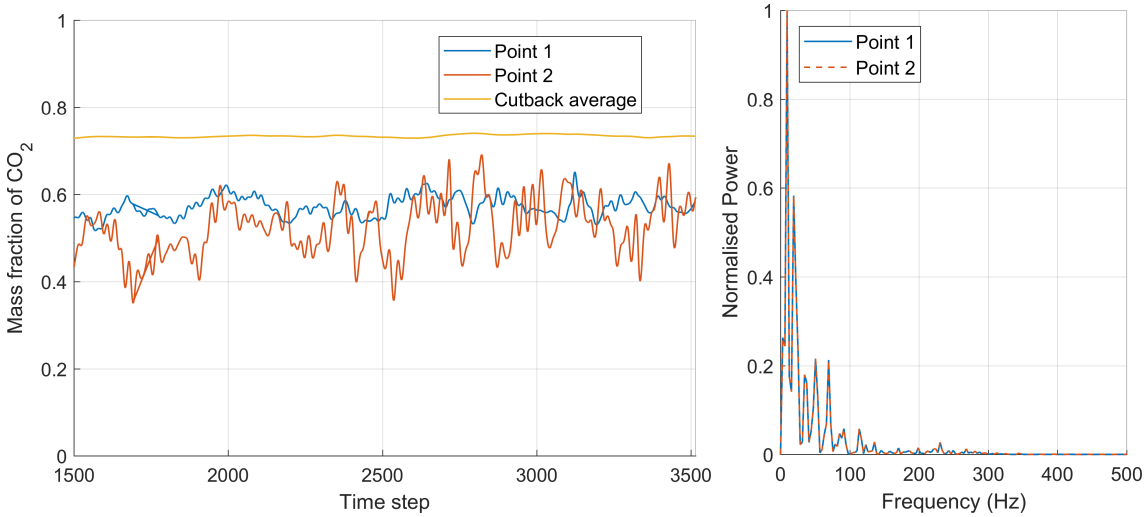


(c) Cross corrugated slot G13 instantaneous



(d) Cross corrugated slot G13 time averaged

Figure 11.5: Flow visualisation on midslot plane

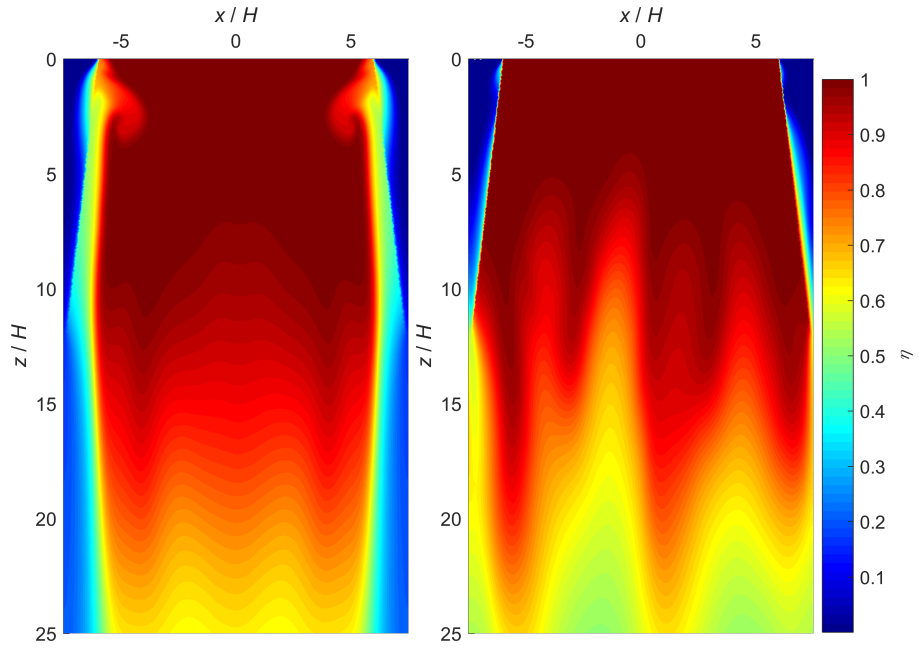


(a) Mass fraction against time step number (b) Frequency spectrum analysis

Figure 11.6: Unsteady simulation monitoring data for G13

enhancement in cooling on the edges was apparent in both CFD and experiments, but was lower in the CFD. In the CFD, the coolant flow detached from the walls of the lands almost immediately, resulting in a region of low effectiveness in the corners and very low effectiveness next to and downstream of the lands. In the experiments, this detachment occurred later, almost at the tips of the lands, although the wake of low effectiveness behind the lands was also present. In between the lands, the effectiveness was higher for considerably further compared to the experiments.

Figure 11.7b showing the cross corrugated geometry G13 paints a very different picture to the experimentally acquired contours shown in Figure 9.2b. The CFD predicted almost zero effectiveness on top of the lands near the slot exit but increasing with distance. The coolant appeared to remain attached to the sides of the lands, washing up over the top towards the tips and resulting in high effectiveness downstream as well. In the experiment, the coolant also remained attached but also washed over the lands near the slot exit. Downstream of the lands, the coolant appears to have mixed out quickly compared to the CFD. In between the lands, the simulation predicted very uneven effectiveness across the span, with five distinct peaks of high effectiveness which were much more similar to the flow pattern displayed by geometry G12 shown in Figure 8.4b. Evidently, the CFD has not correctly simulated the mixing of the flow within the settling section portion of the



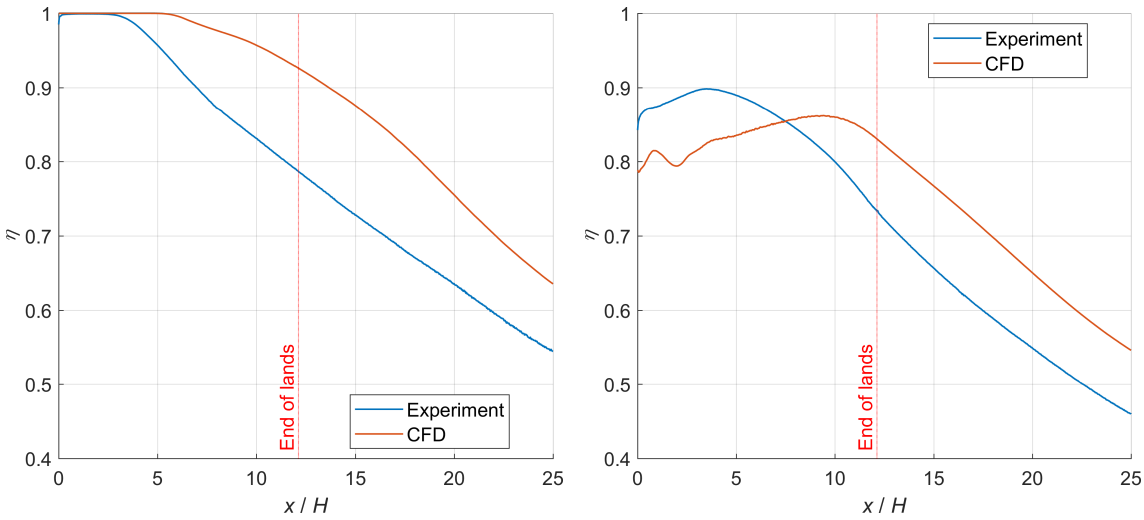
(a) Baseline slot G0 (b) Cross corrugated slot G13

Figure 11.7: Effectiveness on cutback and lands

exit shaped slot, resulting in less even spanwise coverage upon exit

Figure 11.8a shows how the potential core extended considerably further in the CFD, resulting in over-predicting effectiveness levels by about 0.1 throughout. In Figure 11.8b the effects of the lower land effectiveness and early detachment from the land walls can be seen in the lower starting spanwise averaged effectiveness value and less recovery of effectiveness as the land width reduced with distance from the slot exit. Peak effectiveness was under-predicted by 0.04. Further away, the effectiveness in between the lands dominated and the CFD again over-predicted effectiveness, with the end of lands effectiveness over-predicted by 0.1. Due to the under-prediction of spanwise averaged effectiveness near the slot, area averaged effectiveness was under-predicted by 0.02.

Figure 11.9a shows a surprising level of agreement between the CFD and the experiment when considering centreline effectiveness. Both appeared to have a similar potential core length and effectiveness then degraded at a similar rate with distance from the slot exit, although the CFD still over-predicted effectiveness slightly. The unevenness in the curve for the CFD was due to the peaks of effectiveness having a spanwise component that crossed the centreline. In terms of spanwise averaged effectiveness, the CFD again



(a) Centreline η (b) Spanwise averaged η

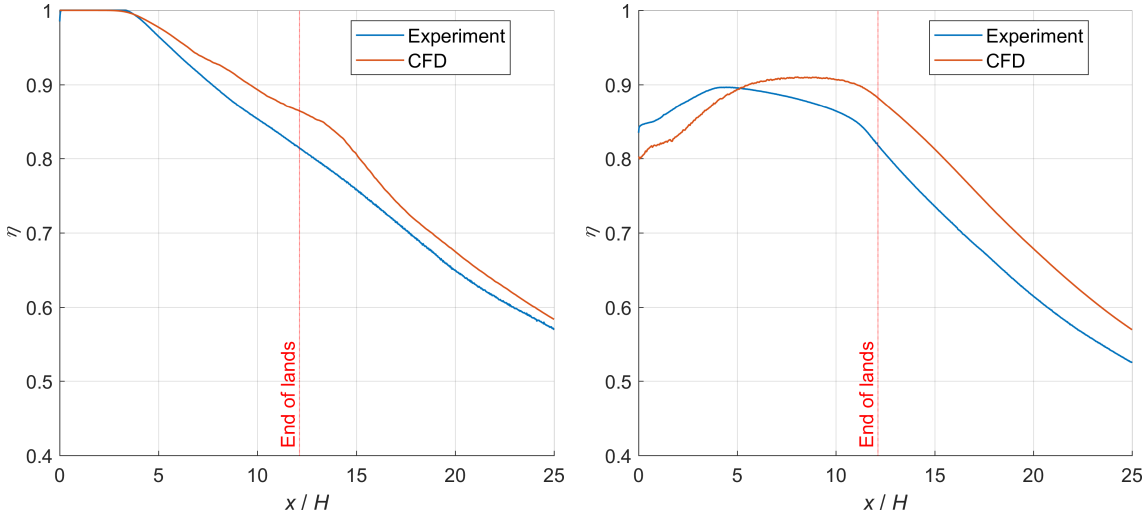
Figure 11.8: Comparison of η between experiment and CFD, G0

under-predicted effectiveness near the slot due to under-predicting effectiveness on top of the lands. With distance, this then became an over-prediction by about 0.04 to 0.07. Peak effectiveness was over-predicted by 0.01 while end of lands effectiveness was over-predicted by 0.06. Due to the under-prediction of effectiveness on the lands, area averaged effectiveness was under-predicted only slightly by 0.01.

11.4 Summary and conclusions

An attempt has been made to numerically model the cross corrugated slot geometry and simulate the complex flow out of the slot. Only two geometries, the baseline rectangular slot and the most optimised cross corrugated slot with exit shaping were modelled, and simulated at the blowing ratio of 0.8 using carbon dioxide as the coolant. The conclusions are as follows:

- The flow structures from the cross corrugated slot are highly complex with many low frequency unsteady effects completely suppressing the vortex shedding from the slot lip.
- CFD was unable to correctly simulate the spreading of the flow in the settling section of the exit shaped slot, resulting in poor spanwise consistency predicted in the



(a) Centreline η (b) Spanwise averaged η

Figure 11.9: Comparison of η between experiment and CFD, G13

film.

- CFD consistently under-predicted effectiveness on top of the lands, resulting in under-predicting spanwise averaged effectiveness near the slot.
- Farther from the slot, CFD consistently over-predicted effectiveness, although to a lesser extent with the cross corrugated geometry.

This short study has shown that using unsteady RANS simulations was not able to fully model the flow from the cross corrugated slot and just as with the baseline slot geometry, it tends to over-predict effectiveness. However, it was able to identify some flow features and predict averaged effectiveness better with the cross corrugated slot than with the baseline slot. Further work is necessary to improve the simulation quality so that it may be used to model the cross corrugated geometry using a broad range of geometric parameters and arrive at a fully optimised design.

Chapter 12

Conclusions

A novel cooling design for the high pressure turbine blade or vane trailing edges has been conceived and introduced in this study. The principle advantage of this geometry is the ability to control pressure loss and therefore flow rate through a trailing edge slot without having to either reduce the slot thickness — which would be detrimental to the structural robustness of the blade — or add a flow restrictor in the feed passage — which would increase the risk of blockage and limit flow to the tip. The cross corrugated pattern also potentially allows the ceramic core used to cast the blade to be strengthened, improving manufacturing yield. Furthermore, the geometry can be modified in a multitude of ways to tailor the pressure loss and flow rate specifically to the requirements of the cooling designer.

However, the principle disadvantage of this geometry has been identified as poor film cooling performance on the cutback after the coolant exits from the slot. This has been investigated experimentally using the pressure sensitive paint technique to measure adiabatic film cooling effectiveness. It was found that:

- Effectiveness on the cutback surface was drastically reduced at all blowing ratios. The potential core of unity effectiveness that is a highly beneficial aspect of slot cooling was completely absent. Effectiveness fell immediately from slot exit.

- The effectiveness profile was extremely uneven in the spanwise direction and asym-

metric in shape. This was affected by the orientation of the channels and the alignment between the channels, with the upper channels being the deciding factor for which side the coolant was biased towards.

- The coolant was forced to impinge on the sides of the lands, resulting in higher effectiveness near the lands. However, this did not translate into higher effectiveness on top of the lands and soon dissipated further downstream.

- Near to the slot, reducing blowing ratio increased effectiveness while far from the slot, increasing blowing ratio increased effectiveness.

- Increasing the included angle exacerbated all the aforementioned effects, resulting in even worse film cooling performance.

With such a significant penalty to virtually all aspects of cooling performance, it was absolutely necessary to figure out a way to improve the quality of the film leaving the cross corrugated slot. To that end, various exit shaping strategies were trialled and the findings were:

- A combination of reshaping the exit into a rectangle, straightening the channels to become parallel to the mainstream flow and including a rectangular settling section just before the exit led to the creation of an optimised cross corrugated slot geometry that displayed excellent film cooling performance.

- Spanwise consistency was greatly improved, mostly due to more coolant being pushed towards the lands, compensating for the low effectiveness near to and on the lands as well as downstream of them that was an issue with the baseline slot.

- Cooling performance was also relatively insensitive to blowing ratio, which improves the predictability of the cooling ability of the blade under non-ideal conditions.

- Spanwise averaged effectiveness at the end of the lands — corresponding to the trailing edge of the blade — was increased relative to the baseline by $20\,\%$ to $30\,\%$

up to a blowing ratio of 0.8. At high blowing ratios it was only reduced slightly by $4\,\%$ relative to the baseline.

- Under higher coolant-to-mainstream density ratios, the performance of the cross corrugated slot was shown to be better than the baseline for a wider range of blowing ratios. Spanwise average effectiveness at the end of the lands was $13\,\%$ to $16\,\%$ better than the baseline, up to a blowing ratio of 1.0, while area averaged effectiveness was increased by about $7\,\%$. The spanwise consistency remained more even and relatively insensitive to blowing ratio compared to the baseline.

Pressure loss measurements were also taken for all of the geometries tested, and it was confirmed that the pressure losses through the cross corrugated slot were enhanced considerably:

- Changing the included angle had the greatest effect on pressure losses. With an included angle of $90°$, the Fanning friction factor was enhanced by a factor of 15 to 25 times. With an included angle of $120°$, this was increased to 50 to 90 times.

- Changing the corrugation channel alignment had a lesser, but still significant effect on pressure losses, while adding exit shaping reduced pressure losses relative to the non-exit shaped counterparts by a factor of 0.7.

- The flow through the cross corrugated was fully turbulent for most of the test range, but for Reynolds numbers of less than 3300, the flow was transitional, increasing the Fanning friction factor at low flow rates.

A short CFD study using unsteady RANS was conducted to attempt to model the cross corrugated slot flow. This proved to be difficult and the simulations tended to over-predict effectiveness on the cutback surface and incorrectly predict the spanwise consistency of the film. However, the amount of over-prediction was less than for the baseline slot.

In conclusion, the cross corrugated slot geometry has been proven to be a viable candidate for inclusion in the cooling design of a turbine blade or vane trailing edge, provided

exit shaping is used to bring film cooling performance up to requirements. The design is versatile and can be used to achieve very high pressure losses through the slot without sacrificing film cooling performance, as required by the designer.

12.1 Suggestions for further work

While the issue with film cooling has effectively been solved, more work could be done to better understand and characterise the complex flow features of the cross corrugated geometry and potentially find other uses for the design. Some suggestions for further work are:

- While many studies have been conducting to measure internal heat transfer in cross corrugated heat exchanger geometries, they have generally not considered geometries of this scale and under these operating conditions. Internal heat transfer measurements could be taken using the thermochromic liquid crystal technique to understand the ability of the slot to cool the blade internally.

- Only two included angles were considered in this study. The higher included angle of $120°$ caused such a reduction in film cooling performance and such an increase in pressure loss that it is unlikely to be a used in a cooling design. It would be beneficial to trial a lower range of included angles, in smaller increments so as to gain more of an understanding in how this would affect both film cooling performance and pressure losses. For example from $30°$ to $90°$ in increments of $10°$.

- In this study, corrugation alignment was identified as a factor affecting pressure losses, but the precise mechanism by which it does this is not fully understood. Further experiments focused on measuring pressure losses more accurately using a traverse and a four-hole probe would characterise the inlet and outlet flows and help improve understanding.

- Density ratio was shown to affect film cooling performance. Further work could be undertaken to assess effectiveness at even higher density ratios. This might be

accomplished by either using a heavier coolant gas, using a lighter mainstream gas, cooling the coolant stream or heating the mainstream.

- The CFD simulations included in this study were limited due to a lack of time and resources. However, it showed some promise in simulating the complex flow from the cross corrugated slots. The model could be further validated and improved by investigated more blowing ratios and geometries as well as using supplementary numerical methods such as scale adaptive simulation or detached eddy simulation.

- The large scale flat plate model used in the current study was only an approximation of the blade trailing edge. The next step would be to test the recommended geometries in more engine representative conditions, for example in a high speed blow down facility that is able to match Mach number to the engine. Such an experimental facility has already been constructed in the Osney Thermo-Fluids Laboratory based on the methods and lesson learned from this study (Gurram et al., 2016) and could be used to progress the technology readiness level of the cross corrugated slot concept.

- Uneven effectiveness distribution on the cutback surface and especially along the trailing edge is known to be detrimental for the blade life due to the thermal gradients and therefore thermal stresses generated. It would be useful to link the effectiveness distributions measured with what is considered an acceptable level of temperature variation in a real engine, taking into account lateral conduction within the substrate.

- Unsteady effects of the cross corrugated slot on the film effectiveness could be measured experimentally using fast response PSP. Understanding of the 3D flow structures within and downstream of the cross corrugated slot could be improved experimentally using particle image velocimetry.

Bibliography

S. Acharya, F. Zhou, J. Lagrone, G. Mahmood, and R. S. Bunker. Latticework (vortex) cooling effectiveness: Part 2 — rotating channel experiments. *ASME Conference Proceedings*, 2004(41685):833–843, January 1, 2004 2004. doi: 10.1115/GT2004-53983. URL http://dx.doi.org/10.1115/GT2004-53983.

J. C. Adams. *Advanced Heat Transfer Surfaces for Gas Turbine Heat Exchangers*. PhD thesis, 2004. DPhil Thesis, University of Oxford, Oxford, United Kingdom.

J. Ahn, H.-K. Moon, M. T. Schobeiri, and J.-C. Han. Film cooling effectiveness on the leading edge region of a rotating turbine blade with two rows of film cooling holes using pressure sensitive paint. *Journal of Heat Transfer*, 128(9):879–888, April 22 2006. doi: 10.1115/1.2241945.

M. Annerfeldt, A. Shukin, and S. Shukin. Blade or vane for a rotary machine, 2005.

P. Bonnet. *Applications of Liquid Crystals in Aerodynamic Testing*. PhD thesis, 1989. DPhil Thesis, University of Oxford, Oxford, United Kingdom.

R. S. Bunker. Latticework (vortex) cooling effectiveness: Part 1 — stationary channel experiments. *ASME Conference Proceedings*, 2004(41685):909–918, January 1, 2004 2004. doi: 10.1115/GT2004-54157. URL http://dx.doi.org/10.1115/GT2004-54157.

R. S. Bunker. *Innovative Gas Turbine Cooling Techniques*, volume 22 of *Thermal Engineering in Power Systems*, pages 199–229. WIT, Southampton, 1st edition, 2008. ISBN 9781845640620.

G. Caciolli, B. Facchini, A. Picchi, and L. Tarchi. Comparison between psp and tlc steady state techniques for adiabatic effectiveness measurement on a multiperforated plate. *Experimental Thermal and Fluid Science*, 48(0):122–133, 7 2013. doi: http://dx.doi.org/10.1016/j.expthermflusci.2013.02.015.

M. Cakan and M. Taslim. Experimental and numerical study of mass/heat transfer on an airfoil trailing-edge slots and lands. In *ASME Turbo Expo 2006: Power for Land, Sea, and Air*, pages 957–967. American Society of Mechanical Engineers, 2006.

M. Ciofalo, J. Stasiek, and M. W. Collins. Investigation of flow and heat transfer in corrugated passages-ii. numerical simulations. *International Journal of Heat and Mass Transfer*, 39(1):165–192, 1 1996. doi: 10.1016/S0017-9310(96)85014-9.

N. A. Cumpsty. *Jet propulsion: a simple guide to the aerodynamics and thermodynamic design and performance of jet engines*, volume 2. Cambridge Univ Pr, 2003.

J. D. Denton. Loss mechanisms in turbomachines. *Journal of Turbomachinery*, 115(4): 621–656, 1993.

S. V. Ekkad and J. C. Han. A transient liquid crystal thermography technique for gas turbine heat transfer measurements. *Measurement Science and Technology*, 11(7):957, 2000. URL `http://stacks.iop.org/0957-0233/11/i=7/a=312`.

S. V. Ekkad, D. Zapata, and J. C. Han. Heat transfer coefficients over a flat surface with air and co[sub 2] injection through compound angle holes using a transient liquid crystal image method. *Journal of Turbomachinery*, 119(3):580–586, July 1997 1997a. doi: 10.1115/1.2841161. URL `http://dx.doi.org/10.1115/1.2841161`.

S. V. Ekkad, D. Zapata, and J. C. Han. Film effectiveness over a flat surface with air and co[sub 2] injection through compound angle holes using a transient liquid crystal image method. *Journal of Turbomachinery*, 119(3):587–593, July 1997 1997b. doi: 10.1115/1.2841162. URL `http://dx.doi.org/10.1115/1.2841162`.

W. W. Focke and P. G. Knibbe. Flow visualization in parallel-plate ducts with corrugated walls. *Journal of Fluid Mechanics*, 165(1):73–77, 1986. doi: 10.1017/S0022112086003002.

W. W. Focke, J. Zachariades, and I. Olivier. The effect of the corrugation inclination angle on the thermohydraulic performance of plate heat exchangers. *International Journal of Heat and Mass Transfer*, 28(8):1469–1479, 8 1985. doi: 10.1016/0017-9310(85)90249-2.

G. Gaiser and V. Kottke. Flow phenomena and local heat and mass transfer in corrugated passages. *Chemical Engineering and Technology*, 12(1):400–405, 1989. URL `http://dx.doi.org/10.1002/ceat.270120157`. M3: 10.1002/ceat.270120157.

D. R. H. Gillespie and P. T. Ireland. Lattice cooling baseline heat transfer end of testing report. Technical Report OUEL 2140/97, University of Oxford, 1997.

R. J. Goldstein. Film cooling. *Advances in heat transfer*, 7(1):321–379, 1971.

R. J. Goldstein, G. Shavit, and T. S. Chen. Film-cooling effectiveness with injection through a porous section. *Journal of Heat Transfer*, 87(3):353–359, August 1965 1965. doi: 10.1115/1.3689114. URL `http://dx.doi.org/10.1115/1.3689114`.

R. J. Goldstein, E. R. G. Eckert, and J. W. Ramsey. Film cooling with injection through holes: Adiabatic wall temperatures downstream of a circular hole. *Journal of Engineering for Power*, 90(4):384–393, October 1968 1968. doi: 10.1115/1.3609223. URL `http://dx.doi.org/10.1115/1.3609223`.

V. A. Goreloff, M. M. Goychenberg, and V. A. Malkoff. The investigation of heat transfer in cooled blades of gas turbines. In *26th Joint Propulsion Conference*, Joint Propulsion Conferences, Orlando, FL, 16/07 1990. American Institute of Aeronautics and Astronautics. doi: 10.2514/6.1990-2144. URL `http://dx.doi.org/10.2514/6.1990-2144`. AIAA-90-2144.

N. Gurram, P. T. Ireland, T. H. Wong, and K. P. Self. Study of film cooling in the trailing edge region of a turbine rotor blade in high speed flow using pressure sensitive paint. In *ASME Turbo Expo 2016*, Seoul, South Korea, 2016. ASME. GT2016-57356.

J.-C. Han and A. Rallabandi. Turbine blade film cooling using psp technique. *Frontiers in Heat and Mass Transfer (FHMT)*, 1(1):013001, 2010.

J. P. Hartnett, R. C. Birkebak, and E. R. G. Eckert. Velocity distributions, temperature distributions, effectiveness and heat transfer for air injected through a tangential slot into a turbulent boundary layer. *Journal of Heat Transfer*, 83(3):293–305, August 1961 1961. doi: 10.1115/1.3682263. URL `http://dx.doi.org/10.1115/1.3682263`.

A. A. Hauser, T. T. Eckert, and J. D. McDonel. Cooling slot for aerofoil blade, 1974.

D. S. Holloway, J. H. Leylek, and F. A. Buck. Pressure-side bleed film cooling: Part i — steady framework for experimental and computational results. *ASME Conference Proceedings*, 2002(36088):835–843, January 1, 2002 2002a. doi: 10.1115/GT2002-30471. URL `http://dx.doi.org/10.1115/GT2002-30471`.

D. S. Holloway, J. H. Leylek, and F. A. Buck. Pressure-side bleed film cooling: Part ii — unsteady framework for experimental and computational results. *ASME Conference Proceedings*, 2002(36088):845–853, January 1, 2002 2002b. doi: 10.1115/GT2002-30472. URL `http://dx.doi.org/10.1115/GT2002-30472`.

J. H. Horlock. The basic thermodynamics of turbine cooling. *Journal of Turbomachinery*, 123(3):583–592, 2001.

A. M. Howatson, P. G. Lund, and J. D. Todd. *Engineering tables and data*. Chapman & Hall, London, 2nd edition, 1991. ISBN 0412389703.

Innovative Scientific Solutions Inc. Unifib pressure sensitive paint, 2016. `http://www.psp-tsp.com/index.php?id=115`; accessed 31/08/2013.

P. T. Ireland and T. V. Jones. The response time of a surface thermometer employing encapsulated thermochromic liquid crystals. *Journal of Physics E: Scientific Instruments*, 20(10):1195–1199, 1987. URL `http://stacks.iop.org/0022-3735/20/i=10/a=008`.

P. T. Ireland and T. V. Jones. Liquid crystal measurements of heat transfer and surface shear stress. *Measurement Science and Technology*, 11(7):969, 2000. URL `http://stacks.iop.org/0957-0233/11/i=7/a=313`.

P. T. Ireland, A. J. Neely, D. R. H. Gillespie, and A. J. Robertson. Turbulent heat transfer measurements using liquid crystals. *International Journal of Heat and Fluid Flow*, 20 (4):355–367, 8 1999. doi: 10.1016/S0142-727X(99)00030-2.

ISO. *ISO 5167-1:2003 Measurement of fluid flow by means of pressure differential devices inserted in circular cross-section conduits running full – Part 1: General principles and requirements*. International Organization for Standardization, Geneva, 2003a. `http://www.iso.org/iso/catalogue_detail?csnumber=28064`; accessed 08/12/2016.

ISO. *ISO 5167-2:2003 Measurement of fluid flow by means of pressure differential devices inserted in circular cross-section conduits running full – Part 2: Orifice plates*. International Organization for Standardization, Geneva, 2003b. `http://www.iso.org/iso/catalogue_detail?csnumber=30190`; accessed 08/12/2016.

T. V. Jones. Theory for the use of foreign gas in simulating film cooling. *International Journal of Heat and Fluid Flow*, 20(3):349–354, 6 1999. doi: http://dx.doi.org/10.1016/S0142-727X(99)00017-X.

S. C. Kacker and J. H. Whitelaw. The dependence of the impervious wall effectiveness of a two-dimensional wall-jet on the thickness of the upper lip boundary layer. *International Journal of Heat and Mass Transfer*, 10(11):1623–1624, 11 1967. doi: http://dx.doi.org/10.1016/0017-9310(67)90014-2.

W. M. W. Kays. *Convective heat and mass transfer*. Boston : McGraw-Hill Higher Education, Boston, 4th ed. / w.m. kays, m.e. crawford, bernhard weigand. edition, 2005. ID: oxfaleph015969483.

K. Kusterer, D. Bohn, T. Sugimoto, and R. Tanaka. Double-jet ejection of cooling air for improved film-cooling. *ASME Conference Proceedings*, 2006(4238X):677–687, January 1, 2006 2006. doi: 10.1115/GT2006-90854. URL http://dx.doi.org/10.1115/GT2006-90854.

P. W. Kwan. *Flow Management in Heat Exchanger Installations for Intercooled Turbofan Engines*. PhD thesis, 2011. DPhil Thesis, University of Oxford, Oxford, United Kingdom.

S. C. Lau, J. C. Han, and T. Batten. Heat transfer, pressure drop, and mass flow rate in pin fin channels with long and short trailing edge ejection holes. *Journal of Turbomachinery*, 111(2):116–123, 04/01 1989. URL http://dx.doi.org/10.1115/1.3262245. 10.1115/1.3262245.

E. W. Lemmon, M. O. McLinden, and D. G. Friend. *Thermophysical Properties of Fluid Systems*. NIST Chemistry WebBook, NIST Standard Reference Database Number 69. National Institute of Standards and Technology, Gaithersburg MD, 2017. doi: 10.18434/T4D303. accessed 17/01/2017.

S.-J. Li, A. P. Rallabandi, and J.-C. Han. Influence of unsteady wake with trailing edge coolant ejection on turbine blade film cooling. *Journal of Turbomachinery*, 134(6): 061026–061026, September 4 2012. doi: 10.1115/1.4004883.

G. P. Liang. Airfoil pedestaled trailing edge region cooling configuration, 1983.

P. M. Ligrani, J. M. Wigle, S. Ciriello, and S. M. Jackson. Film-cooling from holes with compound angle orientations: Part 1—results downstream of two staggered rows of holes with 3d spanwise spacing. *Journal of Heat Transfer*, 116(2):341–352, May

1994 1994. doi: 10.1115/1.2911406. URL http://dx.doi.org/10.1115/1.2911406.

J. Ling, R. Rossi, and J. K. Eaton. Near wall modeling for trailing edge slot film cooling. *Journal of Fluids Engineering*, 137(2):021103–021103, September 26 2014. doi: 10.1115/1.4028498.

J. Ling, C. J. Elkins, and J. K. Eaton. The effect of land taper angle on trailing edge slot film cooling. *Journal of Turbomachinery*, 137(7):071003–071003, July 1 2015a. doi: 10.1115/1.4029174.

J. Ling, C. J. Elkins, and J. K. Eaton. Optimal turbulent schmidt number for rans modeling of trailing edge slot film cooling. *Journal of Engineering for Gas Turbines and Power*, 137(7):072605–072605–8, 07/01 2015b. URL http://dx.doi.org/10.1115/1.4029206. 10.1115/1.4029206.

P. Martini, A. Schulz, and H.-J. Bauer. Film cooling effectiveness and heat transfer on the trailing edge cutback of gas turbine airfoils with various internal cooling designs. *Journal of Turbomachinery*, 128(1):196–205, February 1 2005a. doi: 10.1115/1.2103094.

P. Martini, A. Schulz, H. J. Bauer, and C. F. Whitney. Detached eddy simulation of film cooling performance on the trailing edge cutback of gas turbine airfoils. *Journal of Turbomachinery*, 128(2):292–299, February 1 2005b. doi: 10.1115/1.2137739.

F. R. Menter. Two-equation eddy-viscosity turbulence models for engineering applications. *AIAA Journal*, 32(8):1598–1605, 1994.

D. E. Metzger, H. J. Carper, and L. R. Swank. Heat transfer with film cooling near nontangential injection slots. *Journal of Engineering for Power*, 90(2):157–162, April 1968 1968. doi: 10.1115/1.3609155. URL http://dx.doi.org/10.1115/1.3609155.

S. Mhetras, J.-C. Han, and R. Rudolph. Effect of flow parameter variations on full coverage film-cooling effectiveness for a gas turbine blade. *Journal of Turbomachinery*, 134 (1):011004–011004, May 24 2011. doi: 10.1115/1.4003228.

R. J. Moffat. Describing the uncertainties in experimental results. *Experimental Thermal and Fluid Science*, 1(1):3–17, 1 1988. doi: http://dx.doi.org/10.1016/0894-1777(88)90043-X.

D. K. Mukherjee. Film cooling with injection through slots. *Journal of Engineering for Gas Turbines and Power*, 98(4):556–559, October 1 1976. doi: 10.1115/1.3446237.

A. Murata, S. Nishida, H. Saito, K. Iwamoto, Y. Okita, and C. Nakamata. Effects of surface geometry on film cooling performance at airfoil trailing edge. *Journal of Turbomachinery*, 134(5):051033–051033, May 31 2012. doi: 10.1115/1.4004828.

A. V. Murray, P. T. Ireland, T. H. Wong, S. W. Tang, and A. J. Rawlinson. High resolution experimental and computational methods for modelling multiple row effusion cooling performance. *International Journal of Turbomachinery, Propulsion and Power*, 3(1):4, 2018.

D. P. Narzary, K.-C. Liu, A. P. Rallabandi, and J.-C. Han. Influence of coolant density on turbine blade film-cooling using pressure sensitive paint technique. *Journal of Turbomachinery*, 134(3):031006–031006, July 14 2011. doi: 10.1115/1.4003025.

National Institute of Standards and Technology. Sulfur hexafluoride, 2016. `http://webbook.nist.gov/cgi/cbook.cgi?ID=C2551624&Units=SI`; accessed 24/11/2016.

K. Okada, M. Ono, T. Tomimura, T. Okuma, H. Konno, and S. Ohtani. Design and heat transfer characteristics of new plate heat exchanger. *Heat transfer-Japanese research*, 1(1):90–95, 1972.

M. K. Quinn, N. Gongora-Orozco, K. Kontis, and P. Ireland. Application of pressure-sensitive paint to low-speed flow around a u-bend of strong curvature. *Experimental*

Thermal and Fluid Science, 48(0):58–66, 7 2013. doi: http://dx.doi.org/10.1016/j.expthermflusci.2013.02.008.

A. P. Rallabandi, S.-J. Li, and J.-C. Han. Unsteady wake and coolant density effects on turbine blade film cooling using pressure sensitive paint technique. *Journal of Heat Transfer*, 134(8):081701–081701, June 5 2012. doi: 10.1115/1.4006748.

S. Ravelli and G. Barigozzi. Evaluation of rans predictions on a linear nozzle vane cascade with trailing edge cutback film cooling. In *ASME Turbo Expo 2013: Turbine Technical Conference and Exposition*, pages V03BT13A030–V03BT13A030. American Society of Mechanical Engineers, 2013.

S. Ravelli and G. Barigozzi. Application of unsteady cfd methods to trailing edge cutback film cooling. In *ASME Turbo Expo 2014*, Dusseldorf, Germany, 2014. ASME. GT2014-25435.

S. Ravelli and G. Barigozzi. Modelling the influence of vortex shedding on trailing edge cutback film cooling at different blowing ratios. In *ETC11: 11th European Conference on Turbomachinery Fluid Dynamics and Thermodynamics, Madrid (Spain), 23-27 March 2015*, pages 1–11, 2015.

W. C. Reynolds. *Thermodynamic properties in SI : graphs, tables, and computational equations for forty substances*. Stanford University, depart. of mechanical engineering, Stanford CA, 1979. ISBN 0917606051.

A. Richards. *University of Oxford Advanced Research Computing*. aug 2015. doi: 10.5281/zenodo.22558. URL `https://doi.org/10.5281/zenodo.22558`.

G. F. C. Rogers and Y. R. Mayhew. *Joule-Thomson coefficient*, chapter 7.4.4, pages 98–100. Engineering thermodynamics : work and heat transfer. Longman, Harlow, 4th edition, 1992. ISBN 0582045665.

Rolls-Royce. *The Jet Engine*. Rolls-Royce, London, 6th edition, 2005.

Rolls-Royce. Non statistical cooling air diagram high power, 10/02 2009.

Rolls-Royce. Trent xwb optimised for the airbus a350 xwb family, 10 June 2012. http://www.rolls-royce.com/Images/Trent%20XWB_tcm92-5753.pdf; accessed 08/08/2012.

G. Rosenblad and A. Kullendorff. Estimating heat transfer rates from mass transfer studies on plate heat exchanger surfaces, 1975.

J. E. Sargison. *Development of a Novel Film Cooling Hole Geometry*. PhD thesis, 2001. DPhil Thesis, University of Oxford, Oxford, United Kingdom.

A. J. Saul, P. T. Ireland, J. D. Coull, T. H. Wong, H. Li, and E. Romero. An experimental investigation of adiabatic film cooling effectiveness and heat transfer coefficient on a transonic squealer tip; turbo expo: Power for land, sea, and air, 2018. URL http://dx.doi.org/10.1115/GT2018-76207. TY: PROC; 10.1115/GT2018-76207.

A. F. Savostin and A. M. Tikhonov. Investigation of the characteristics of plate-type heating surfaces. *Thermal Engineering*, 17(9):113–117, 1970.

J. Stasiek, M. W. Collins, M. Ciofalo, and P. E. Chew. Investigation of flow and heat transfer in corrugated passages-i. experimental results. *International Journal of Heat and Mass Transfer*, 39(1):149–164, 1 1996. doi: 10.1016/S0017-9310(96)85013-7.

G. J. Sturgess. Design of combustor cooling slots for high film effectiveness: Part i-film general development. *Journal of Engineering for Gas Turbines and Power*, 108(2): 354–360, April 1 1986. doi: 10.1115/1.3239911.

G. J. Sturgess and G. D. Pfeifer. Design of combustor cooling slots for high film effectiveness: Part ii-film initial region. *Journal of Engineering for Gas Turbines and Power*, 108(2):361–369, April 1 1986. doi: 10.1115/1.3239912.

M. E. Taslim, S. D. Spring, and B. P. Mehlman. Experimental investigation of film cooling effectiveness for slots of various exit geometries. *Journal of Thermophysics and Heat*

Transfer, 6(2):302–307, 04/01; 2014/08 1992. doi: 10.2514/3.359. URL http://dx.doi.org/10.2514/3.359. doi: 10.2514/3.359; 12.

U.S. Department of Energy-National Energy Technology Laboratory (NETL) and D. G. Bogard. *Airfoil Film Cooling*, chapter 4.2.2.1. The Gas Turbine Handbook. National Energy Technology Laboratory, Morgantown, WV, 2006.

T. H. Wong, P. T. Ireland, and K. P. Self. Film cooling effectiveness measurements on engine representative trailing edge slots including cutback surface protuberances. In *11th European Turbomachinery Conference*, Madrid, Spain, 2015. ETC. ETC2015-254.

T. H. Wong, P. T. Ireland, and K. P. Self. Film cooling effectiveness measurements on trailing edge cutback surface and lands following novel cross corrugated slot geometry. In *ASME Turbo Expo 2016*, Seoul, South Korea, 2016a. ASME. GT2016-57371.

T. H. Wong, P. T. Ireland, and K. P. Self. Film cooling effectiveness downstream of trailing edge slots including cutback surface protuberances. *International Journal of Turbomachinery, Propulsion and Power*, 1(1):4, 2016b.

T. H. Wong, P. T. Ireland, and K. P. Self. Film cooling effectiveness downstream of optimised cross corrugated slot geometry with exit shaping. In *12th European Turbomachinery Conference*, Stockholm, Sweden, 2017. ETC. ETC2017-090.

Z. Yang and H. Hu. Study of trailing-edge cooling using pressure sensitive paint technique. *Journal of Propulsion and Power*, 27(3):700–709, 05/01; 2014/09 2011. doi: 10.2514/1.B34070. URL http://dx.doi.org/10.2514/1.B34070. doi: 10.2514/1.B34070; 01.

Z. Yang and H. Hu. An experimental investigation on the trailing edge cooling of turbine blades. *Propulsion and Power Research*, 1(1):36–47, 12 2012. doi: http://dx.doi.org/10.1016/j.jppr.2012.10.007.

J. B. Young and R. C. Wilcock. Modeling the air-cooled gas turbine: Part 1—general thermodynamics. *Journal of Turbomachinery*, 124(2):207–213, April 2002 2002a. doi: 10.1115/1.1415037. URL `http://dx.doi.org/10.1115/1.1415037`.

J. B. Young and R. C. Wilcock. Modeling the air-cooled gas turbine: Part 2—coolant flows and losses. *Journal of Turbomachinery*, 124(2):214–221, April 2002 2002b. doi: 10.1115/1.1415038. URL `http://dx.doi.org/10.1115/1.1415038`.

L. J. Zhang and R. S. Jaiswal. Turbine nozzle endwall film cooling study using pressure-sensitive paint. *Journal of Turbomachinery*, 123(4):730–738, February 1 2001. doi: 10.1115/1.1400113.

Y. Zhang, X. Yuan, and P. Ligrani. Film cooling effectiveness distribution on first-stage vane endwall with and without leading-edge fillets. *International Journal of Heat and Mass Transfer*, 66(0):642–654, 11 2013. doi: http://dx.doi.org/10.1016/j.ijheatmasstransfer.2013.06.065.

Appendices

Appendix A

Isenthalpic Expansion of Gases

A.1 Nitrogen

Figure A.1 shows a plot of pressure against enthalpy for nitrogen from Reynolds (1979). Point A marks the starting bottle pressure of $20\,\mathrm{MPa}$ at an ambient temperature of $293\,\mathrm{K}$. If the nitrogen is expanded isenthalpically to the mass flow controller feed pressure of $0.5\,\mathrm{MPa}$ marked as point B, the temperature drops by approximately $30\,\mathrm{K}$. As the coolant system is not adiabatic and there is heat transfer into the gas, the temperature is able to increase to point C. From this point, the further expansion of the gas through the mass flow controller to near ambient pressure at point D would result in a negligible change in temperature.

A.2 Carbon dioxide

Figure A.1 shows a plot of temperature against entropy for carbon dioxide from Reynolds (1979). Point A marks the starting bottle pressure of $5\,\mathrm{MPa}$ at an ambient temperature of $293\,\mathrm{K}$. If the carbon dioxide is expanded isenthalpically to the mass flow controller feed pressure of $0.5\,\mathrm{MPa}$ marked as point B, the temperature drops by approximately $75\,\mathrm{K}$ and also encroaches into the liquid-vapour mix region. If instead, the carbon dioxide is heated while it is expanded slowly to the intermediate reservoir pressure of

$0.7\,\mathrm{MPa}$ marked as point C, then there is no danger of the gas condensing within the coolant feed system. From this point, the further expansion of the gas through the mass flow controller to near ambient pressure at point D would result in a much more manageable temperature drop of approximately $7\,\mathrm{K}$. The gas is easily warmed back up to near ambient temperature through the rest of the coolant feed system up to the test section.

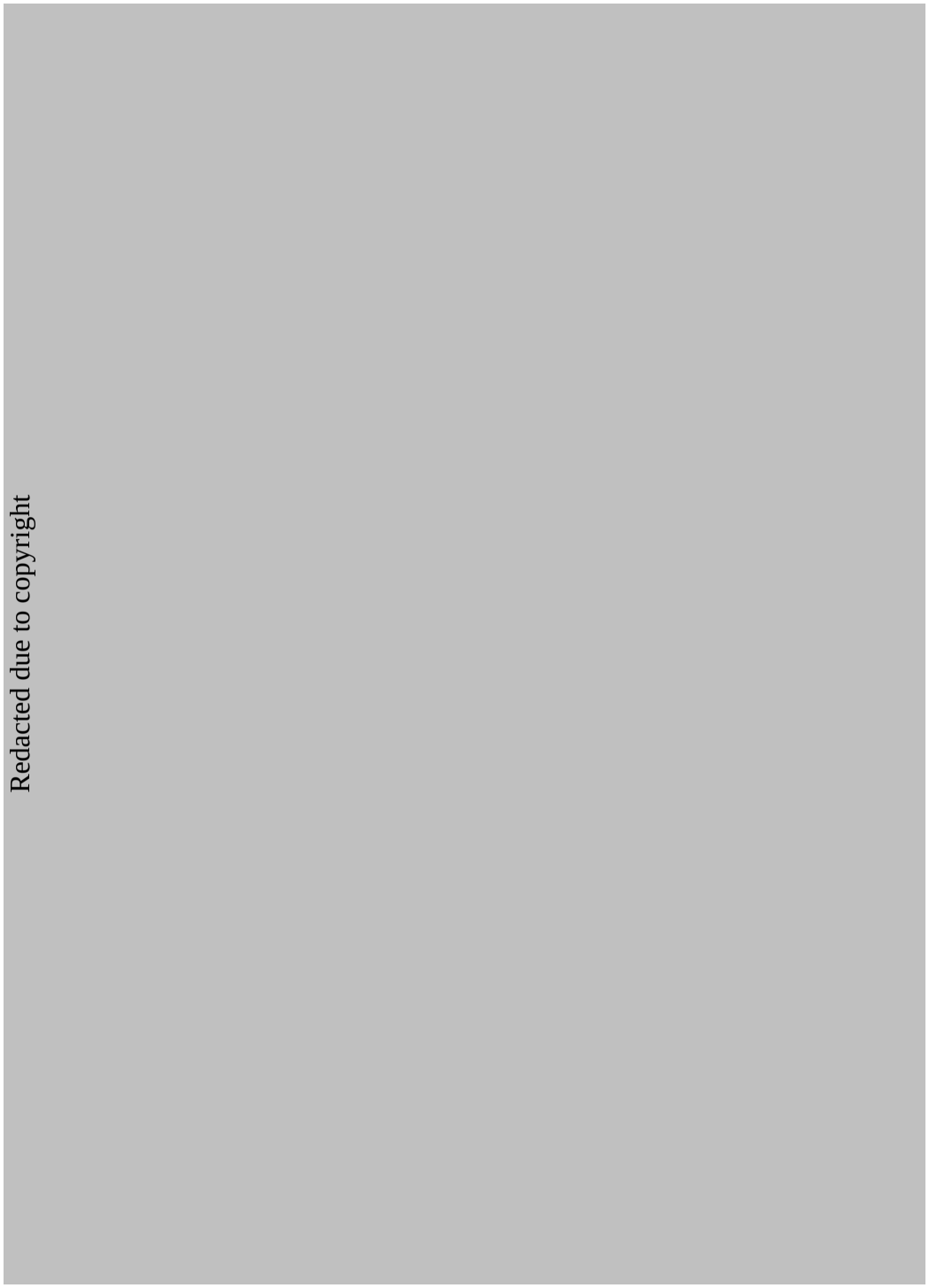


Figure A.1: Pressure-enthalpy chart for nitrogen (Reynolds, 1979)

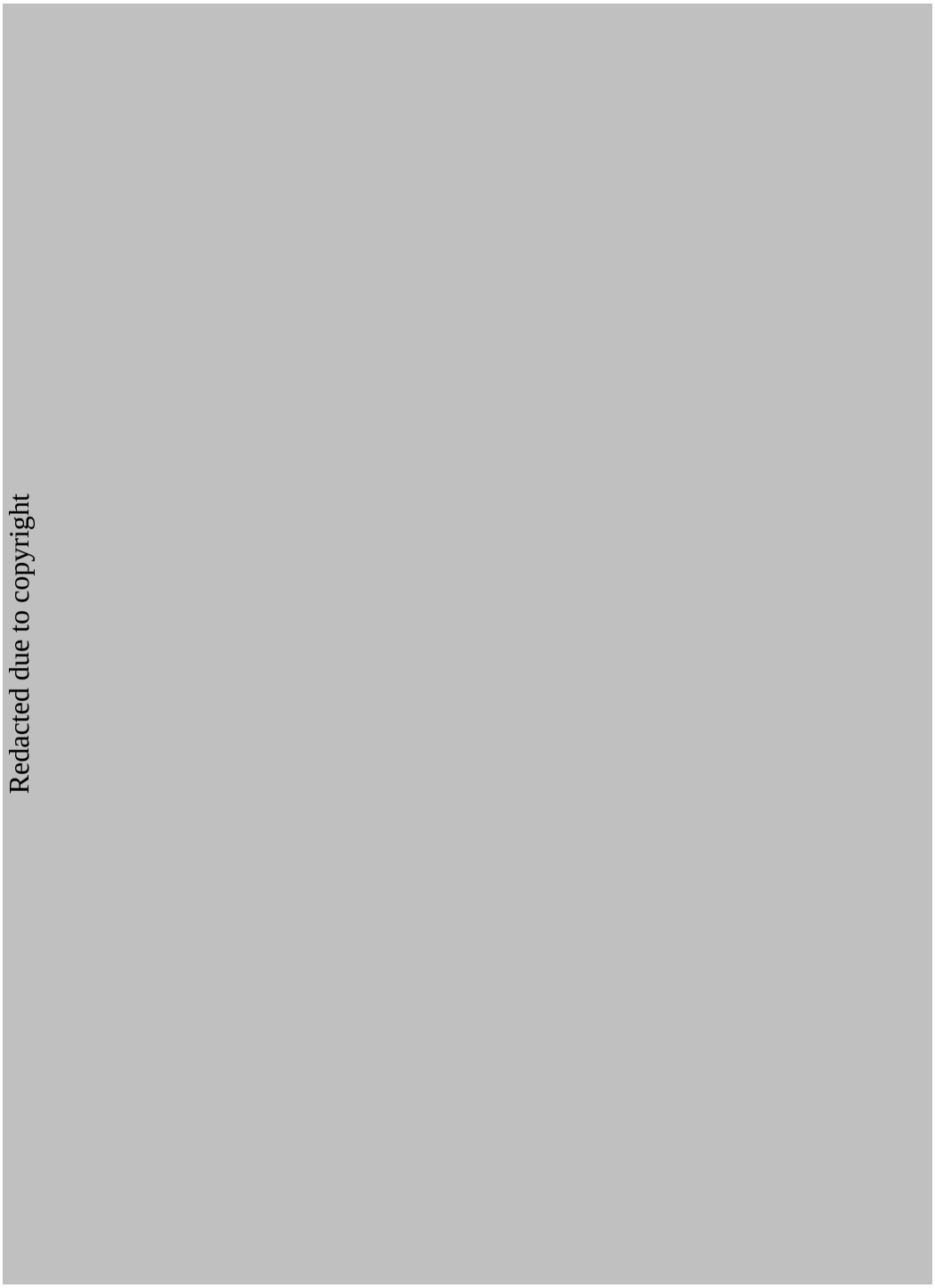


Figure A.2: Temperature-entropy chart for carbon dioxide (Reynolds, 1979)